Preface

This Special Issue represents a best paper collection from the successfully organized Women in Engineering workshop and Model-based Healthcare special sessions of the International Conference on Systems, Man, and Cybernetics (SMC), the flagship conference of the IEEE SMC Society held in Budapest from 9-12 October 2016.

SMC 2016 featured a total of 832 technical oral and poster presentations spread over 110 sessions, 3 workshops and 5 tutorials. The Model-based Healthcare I-II sessions and the Women in Engineering workshop involved 24 papers with high popularity within the conference. The current special issue titled "*The importance of modeling, analysis and control in both industrial and clinical applications*" includes the extended versions of the 14 best papers of the mentioned SMC 2016 special events.

The papers are supported by the *IEEE SMC Cyber-Medical Systems Technical Committee*. Nowadays, medical technological advancement and devices are firmly associated with engineering achievements. Therefore, intelligent and model-based applications are needed, robust enough to generalize its healthcare target, but individualized as well to personalize its applicability. In this way it could increase the quality of life of the patients, optimize therapy and hence, reduce treatment costs. This special issue provides adequate up-to-date applications of intelligent, model-based healthcare problems covering diabetes, cancer, cardiovascular systems and infection control.

The topic of control system plays a vital role in engineering and technology. For successful design of any physical control system modeling, analysis and simulation are important. Control strategies such as adaptive control, robust control, model based predictive control and fractional order control have brought significant improvements in the area of process control. These methods are of interest in applications dealing with uncertainties, constraints, memory effect, time delay, etc. In this special issue the importance and capabilities of control techniques in several areas of research will be provided to the community.

Artificial pancreas represents one of the most important biomedical engineering challenges of the last 15 years. The "closing the loop" problem in diabetes has many unsolved issues and is mainly discussed for type 1 (insulin dependent) diabetes patients. Alessandro Borri and his colleagues from Italy present in silico results for type 2 (non-insulin dependents) diabetic patients. The controller is developed based on an observer-based method without any information about the time course of insulinemia.

Fractional calculus is a relatively new topic in control and biomedical engineering. Dana Copot and her colleagues from Belgium compare classical impedance model with a fractional order one to estimate glucose concentrations. The clear benefit of capturing the dynamics of the measured impedance is demonstrated by the use of the fractional order impedance model.

The papers of the Physiological Controls Research Group of Óbuda University Hungary authored by Johanna Sápi and her colleagues, and by Tamás Ferenci and his colleagues present the latest results of the Tamed Cancer ERC StG grant. In the first paper the effectiveness of different drug delivery protocols is evaluated using in silico simulations. The results are compared with discrete-time controller-based treatments containing state feedback, setpoint control, actual state observer and load estimation. On the other hand, the paper of Tamás Ferenci et al. focuses on modeling the tumor growth under the targeted molecular therapy of antiangiogenesis with mixed-effect models. It is demonstrated that exponential model can be estimated in a robust manner, both at individual and at population-level by mixed effect model, while sigmoid-like growth curves are almost impossible to be estimated.

The work of Xuan Chen and her colleagues from Singapore is an extended version of their SMC paper awarded with the SMC 2016 Best Student Paper Award. A novel automated framework is presented to address the significant, but challenging task of multi-label brain tumor segmentation. The framework has clear advantages on performance and processing time compared to previous state-of-the-art approaches.

György Eigner’s paper from Hungary introduces a novel controller design approach dealing with the control of affine Linear Parameter Varying systems using the abstract mathematical properties of the LPV parameter space and classical state-feedback design. The method is demonstrated on a biomedical problem, diabetes mellitus.

Tun Wen Pai and his colleagues from Taiwan present their results in chronic heart failure clinical classification using Internet-of-Medical-Things devices and cloud computing technologies. The developed system can be customized on heart failure patients and the system is validated on several testing cases showing excellent performance and low cost.

Róbert Pethes and his colleagues from Hungary discuss infectious hospital agents. A simulation framework based on stochastic events is able to model wide range of infection spreading scenarios in the hospital environment.

Finally, the last biomedical related paper is connected to Rita Fleiner and her colleagues from Hungary and discusses indoor navigation possibilities in medical facilities for motion disabled persons. Two ontologies iLOC and hLOC are presented for supporting accessible free-text type indoor navigation in hospitals.

The remaining papers are focusing on industrial control applications. Xiaoyu Tan and his colleagues from Singapore present a cognitive engine based on the hybrid architecture for robot-assisted radio-frequency ablation system. It was demonstrated by ex-vivo experiments that the created engine provides surgical execution procedures correctly and it can be modified for other robot-assisted applications as well.

Dániel András Drexler’s paper from Hungary presents a closed-loop inverse kinematics algorithm to numerically approximate the solution of the inverse kinematics problem, a central problem of robotics. Simulations results show that second-order methods give the best results, but decreases stability margin. The latter is analyzed on different numerical integration techniques.

Eva Dulf and her colleagues’ paper from Romania discuss robust fractional order controllers for distributed systems using particle swarm optimization. Results are demonstrated on the complex chemical process of isotope separation columns cascade.

Carla Pinto from Portugal presents her paper in asymmetrically coupled fractional neurons. A fractional order model is proposed on the dynamics of two asymmetrically coupled Hodgkin-Huxley equations.

Silviu Folea and his colleagues from Romania and Belgium remains as well on the fractional order control topic. The paper uses a smart beam as a simulator for the airplane wings and a fractional order PD controller is designed for active vibration mitigation. The experimental results demonstrate that the designed controller can significantly improve the vibration suppression in smart beams.

Dr. Levente Kovács

Potential Benefits of Discrete-Time Controller-based Treatments over Protocol-based Cancer Therapies

Johanna Sápi, Dániel András Drexler, Levente Kovács

Research and Innovation Center of Óbuda University, Physiological Controls Group, Óbuda University, Kiscelli utca 82, H-1032 Budapest, Hungary
{sapi.johanna, drexler.daniel, kovacs.levente}@nik.uni-obuda.hu

Abstract: In medical practice, the effectiveness of fighting cancer is not only determined by the composition of the used drug, but determined by the administration method as well. As a result, having drugs with a suitable action profile is just a promising beginning, but without appropriate delivery methods, the therapy still can be ineffective. Finding the optimal biologic dose is an empirical process in medical practice; however, using controllers, an automated optimal administration can be determined. In this paper, we evaluate the effectiveness of different drug delivery protocols; using in silico simulations (like bolus doses, low-dose metronomic regimen and continuous infusion therapy). In addition, we compare these results with discrete-time controller-based treatments containing state feedback, setpoint control, actual state observer and load estimation.

Keywords: antiangiogenic therapy; maximum tolerated dose; bolus dose; low-dose metronomic regimen; continuous infusion therapy; optimal biologic dose; discrete-time control; state feedback; setpoint control; actual state observer; load estimation

1 Introduction

1.1 Biomedical Background

Tumor cells can appear in the human body after a somatic mutation. As tumor cells proliferate, the number of cells increase, and the tumor volume grows. This growth, however, is limited since blood supply is provided by the nearby capillaries, and if the tumor cells grow farther than the diffusion distance (150 μm), nutrition and oxygen access decrease. In order to overcome this problem, tumor cells need their own blood supply. There are two main ways to form new blood vessels. The formation of the first primitive vascular plexus is called vasculogenesis, while the formation of new blood vessels from the preexisting microvasculature is angiogenesis [1]. In the case of tumor growth, angiogenesis takes place, which is regulated by pro- and antiangiogenic factors. The most important proangiogenic factor is the vascular endothelial growth factor (VEGF) since it specifically regulates endothelial proliferation [2] which is essential for angiogenesis. Therefore, VEGF inhibition is an important therapeutic target [3]; and to control angiogenesis, anti-VEGF agents and other VEGF inhibitors are being used around the world [4]. However, the best angiogenic inhibition administration method is still unknown in clinical practice [5], thus an effective and automatic administration method is required.

1.2 Background of the Control Problem

We investigated a well-known tumor growth model under antiangiogenic therapy [6] and designed several continuous-time controllers like an LQ control method and state observer [7-9], flat control [10-12], modern robust control method [13-15], feedback linearization method [16] and adaptive fuzzy techniques [17]. However, with the current scientific knowledge, there is no medical device which can handle continuous infusion cancer therapy [18]; hence we designed a discrete-time control herein.

2 Tumor Growth Model

P. Hahnfeldt et al. created a model which describes tumor growth under angiogenic inhibition [6]. Assuming that after the injection, the level of the inhibitor in the bloodstream is equal to the amount of the injected inhibitor, the original third-order system was modified to a second-order system:

$$\dot{x}_1 = -\lambda_1 x_1 \ln\left(\frac{x_1}{x_2}\right) \tag{1}$$

$$\dot{x}_2 = b x_1 - d x_1^{2/3} x_2 - e x_2 g \tag{2}$$

$$y = x_1, \tag{3}$$

where the first state variable (x_1) is the tumor volume [mm^3], while the second state variable (x_2) is the volume of the vasculature of the tumor [mm^3]. The input of the model is the concentration of the injected inhibitor (g [mg/kg]). The first equation contains the λ_1 parameter which describes the tumor growth rate (1/day). The change of the vasculature volume depends on three effects: a) the tumor can stimulate the already existing capillaries to form new blood vessels by the process of sprouting (parameter b [1/day]), b) endothelial cell death causes volume loss in vasculature (parameter d [1/(day·mm^2)]), c) the administration of antiangiogenic drug causes volume loss in vasculature as well (parameter e [kg/(day·mg]). In the case of Lewis lung carcinoma, and using endostatin as antiangiogenic drug, the parameters are the following [1]: $\lambda_1 = 0.192$ 1/day, $b = 5.85$ 1/day, $d = 0.00873$ 1/day·mm^2, $e = 0.66$ kg/(day·mg).

3 Protocol-based Cancer Therapies

3.1 Cancer Protocols in the Light of the Dosage Problem

As it was discussed previously, there is no best way for antiangiogenic drug administration in clinical practice. There are three main methods which are used; however, both ones have advantages and disadvantages. Bolus dose (BD) administration means that the patient receives drug boluses on given days, and between the injections, the treatment has rest periods when there is no drug administration at all. The amount of injected dose can be the Maximum Tolerated Dose (MTD) or any lower dose. After an MTD injection, the treatment should include an extended rest period in order to avoid adverse events. Instead of bolus doses, anticancer drugs can be delivered over prolonged periods using low-doses, this therapy is called as Low-Dose Metronomic (LDM) regimen. Of course, in this case the rest periods can be shorter; but the real question is to find the Optimal Biologic Dose (OBD) which results in the best therapeutic efficacy. Finally, in clinical environment continuous infusion therapy is feasible (e.g. using mini-osmotic pumps), but there is no portable device yet. Clinical experiments have shown that low-dose administration therapies have better therapeutic efficacy than bolus dose injections, and continuous infusion therapies have even better results [19].

3.2 Simulation Results of the Protocol-based Cancer Therapies

The effect of bolus dose administration, low-dose metronomic regimen and continuous infusion therapy was investigated in silico, using the modified Hahnfeldt-model described by Eq. (1)-(3). The total administered inhibitor concentration is 300 mg/kg, and treatment period is 15 days in every simulation, in order to get comparable results. Simulations start from the lethal steady-state of the model when the initial value of tumor volume ($x_1(0)$) and vascular volume ($x_2(0)$) are $1.734 \cdot 10^4$ mm^3. Four different scenarios were examined [20] (left side of Figure 1).

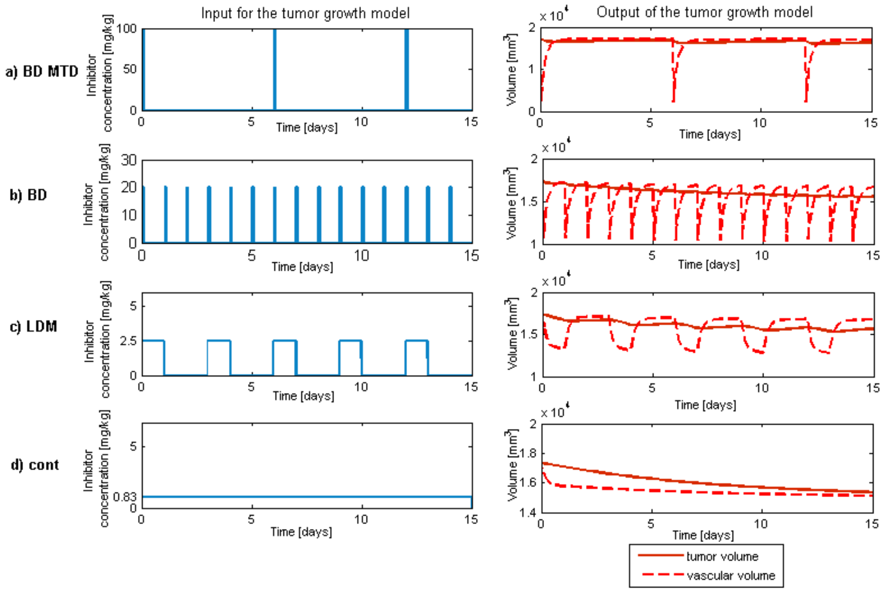

Figure 1

Protocol based therapies (treatment period is 15 days)

a) Therapy P1: bolus doses with maximum tolerated dose (BD MTD)

Therapy: 100 mg/kg bolus injected for one hour; treatment days: 1st, 6th and 12th days; rest periods: 5 days. Total inhibitor concentration: 300 mg/kg, steady state tumour volume: 16330 mm^3.

b) Therapy P2: bolus doses (BD)

Therapy: 20 mg/kg bolus injected for one hour; treatment days: every day of the therapy; rest periods: 23 hours. Total inhibitor concentration: 300 mg/kg, steady state tumour volume: 15580 mm^3.

c) Therapy P3: low-dose metronomic regimen (LDM)

Therapy: 2.5 mg/kg infusion administered for one day; treatment days: 1st, 4th ,7th, 10th, 13th days; rest periods: 2 days. Total inhibitor concentration: 300 mg/kg, steady state tumour volume: 15660 mm^3.

d) Therapy P4: continuous infusion therapy (cont)

Therapy: 0.8333 mg/kg/h continuous infusion administration during the whole therapy; without rest periods. Total inhibitor concentration: 300 mg/kg, steady state tumour volume: 15360 mm^3.

Therapy P1 (BD MTD). The therapy using bolus doses with maximum tolerated dose contains 100 mg/kg boluses which are injected for one hour. Treatment days are the 1st, 6th and 12th days (3 times); between these days, the therapy contains 5 days long rest periods.

Therapy P2 (BD). In this case lower bolus doses are used than the maximum tolerated dose. 20 mg/kg bolus is injected for one hour every day of the therapy (15 times). The treatment contains 23 hour rest periods.

Therapy P3 (LDM). Low-dose metronomic regimen is carried out with 2.5 mg/kg infusions which are administered for one day. Treatment days are the 1st, 4th ,7th, 10th and 13th days (5 times). The therapy contains 2 day rest periods.

Therapy P4 (cont). Continuous infusion therapy is carried out with 0.8333 mg/kg/h continuous infusion during the whole treatment, without rest periods.

The right side of Figure 1 depicts the outputs of the tumor growth model, using *Therapy P1 - Therapy P4* as inputs. Similarly to the clinical experimental results, simulations show that the less effective therapy is the bolus doses with maximum tolerated dose (BD MTD). Tumor volume reduction is not effective (steady state tumor volume is 16330 mm^3), and beside this, side-effects can occur and quality of life (QoL) of the patient decreases due to the therapy. Lower bolus doses (BD) cause continuous slight reduction of the tumor volume, however this is not significant (steady state tumor volume is 15580 mm^3). Another disadvantage of this method is the resulting high frequency oscillation-like characteristics of the vascular volume. Low-dose metronomic administration (LDM) has similar results as BD in terms of tumor volume reduction (steady state tumor volume is 15660 mm^3) and oscillation-like characteristics of the vascular volume; however, the oscillation frequency and amplitude are lower which can be more tolerable for the patient. The most effective treatment is the continuous infusion therapy (cont) since it results in the lower steady state tumor volume (15360 mm^3) and the change of the vascular volume is a smooth curve. In addition, due to the extremely low dosage, continuous infusion therapy has virtually no side-effects.

4 Discrete-Time Controller-based Treatments

The modified Hahnfeldt-model describes a nonlinear system, which has to be linearized due to controller design aspects. We applied operating point linearization in the $g_0 = 0$ operating point. The resulting LTI (linear time invariant) system using state space representation is

$$\dot{x} = Ax + Bu \tag{4}$$

$$y = Cx + Du, \tag{5}$$

where the matrices are

$$A = \begin{bmatrix} -\lambda_1 \log\left(\dfrac{x_1}{x_2}\right) - \lambda_1 & \lambda_1 \dfrac{x_1}{x_2} \\ b - \dfrac{2}{3} d \cdot x_1^{-\frac{1}{3}} \cdot x_2 & -d \cdot x_1^{\frac{2}{3}} \end{bmatrix} \tag{6}$$

$$B = \begin{bmatrix} 0 \\ -ex_2 \end{bmatrix} \tag{7}$$

$$C = \begin{bmatrix} 1 & 0 \end{bmatrix} \tag{8}$$

$$D = \begin{bmatrix} 0 \end{bmatrix}. \tag{9}$$

4.1 Discrete-Time Controller Design with State Feedback, Setpoint Control, Actual State Observer and Load Estimation

Taking into account a feasible discrete-time system, the state space equations are

$$x_{i+1} = A_d x_i + B_d u_i \tag{10}$$

$$y_i = Cx_i. \tag{11}$$

The controllability and observability matrices of the discrete-time system are

$$M_C = [B_d \quad A_d B_d \quad \dots \quad A_d^{\,n-1} B_d] \tag{12}$$

$$M_O = \begin{bmatrix} C \\ CA_d \\ \dots \\ CA_d^{\,n-1} \end{bmatrix}, \tag{13}$$

where n is the dimension of the state variables. Since for every nonzero operating point, the matrices are full rank, the system is controllable and observable in every operating point.

In order to find optimal solutions, we used the LQ control method as state feedback to minimize the tumor volume (x_1) using the lowest possible control signal. The discrete-time cost function containing the positive definite Q and R weighting matrices is

$$J(u) = \sum_{i=1}^{T} \left\{ x_i^{\,T} Q x_i + u_i^{\,T} R u_i \right\}. \tag{14}$$

As our aim was to minimize the square of the output ($x_1^2 = y^2$), the Q matrix is the following:

$$Q = C^T C. \tag{15}$$

The sought K feedback matrix of the discrete-time LQ problem can be found using the P solution of the Discrete Control Algebraic Ricatti Equation (DARE):

$$K = \left(R + B_d{}^T P B_d\right)^{-1} B_d{}^T P A_d \tag{16}$$

$$P = A_d{}^T P A_d - \left(A_d{}^T P B_d\right)\left(R + B_d{}^T P B_d\right)^{-1}\left(B_d{}^T P A_d\right) + Q. \tag{17}$$

For setpoint control, we assume that the reference signal is constant. The control structure is needed to be extended by two matrices (N_x and N_u) in order to use nonzero reference signal. The values of these matrices can be calculated as follows:

$$\begin{pmatrix} N_x \\ N_u \end{pmatrix} = \begin{bmatrix} A_d - I & B_d \\ C & 0 \end{bmatrix}^{-1} \begin{pmatrix} 0_{nxm} \\ I_m \end{pmatrix}, \tag{18}$$

where n is the dimension of the state variables, while m is the dimension of the inputs (and outputs).

As the vascular volume is non-measurable, we designed an actual state observer to estimate this state variable. We have verified that the matrix $M_o A_d$ is full rank, thus the discrete-time system is observable with an actual observer described by the following difference equation:

$$\hat{x}_i = F\hat{x}_{i-1} + Gy_i + Hu_{i-1}. \tag{19}$$

The F, H and G parameter matrices of the observer can be calculated as follows:

$$F = A_d - GCA_d \tag{20}$$

$$H = B_d - GCB_d \tag{21}$$

$$G = \left(\mathrm{e}_\mathrm{n}^\mathrm{T} M_c^{-1}\left(A_d^T, A_d^T C_d^T\right)\varphi_F\left(A_d^T\right)\right)^T, \tag{22}$$

where $\varphi_F(A_d{}^T)$ refers to the characteristic polynomial of the matrix F evaluated at the matrix $A_d{}^T$.

Assuming that a disturbance reduced to the input of the system can occur (load change), we designed load estimation as well. The system was extended by the disturbance modeled as a constant state-variable that adds up to the input of the original model. The state feedback and the setpoint control were designed for the original system; however, the actual state observer was designed for the extended system. As a consequence, the difference equation of the state observer is

$$\begin{pmatrix} \hat{x}_i \\ \hat{x}_{d\,i} \end{pmatrix} = \tilde{F}\begin{pmatrix} \hat{x}_{i-1} \\ \hat{x}_{d\,i-1} \end{pmatrix} + \tilde{G}y_i + \tilde{H}u_{i-1}, \tag{23}$$

where $\hat{x}_d$ is the estimation of the disturbance.

Figure 2 depicts the whole block diagram of the closed-loop discrete-time control system containing state feedback, setpoint control, actual state observer and load estimation. Please note that saturation is used before the input of the tumor model in order to avoid negative or too high input values due to physiological aspects.

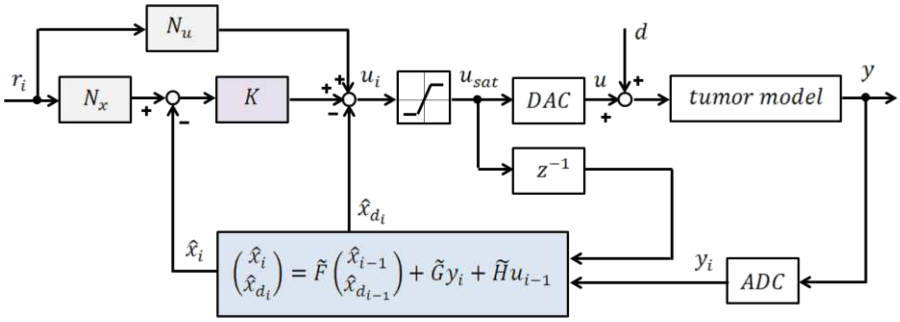

Figure 2

Block diagram of the discrete-time control containing state feedback, setpoint control, actual state observer and load estimation

4.2 Simulation Results of the Discrete-Time Controller-based Treatments

Using discrete-time controller, the treatment can contain bolus doses, low-dose metronomic parts and continuous periods as well. In order to get comparable results with the protocol based therapies, the treatment period was chosen to be 15 days. Parameters of the discrete-time controllers were chosen according to [21]. The operating point of the linearization is $x_1 = x_2 = 10$ mm^3, the R weighting matrix used in the design of the LQ control is 1. In order to get steady state tumor volumes close the protocol based cancer therapies' values, the reference signal is 13000 mm^3. Since protocol based cancer therapies do not have disturbance, the disturbance is 0% in the case of discrete-time controllers. Three different scenarios were examined in the light of the saturation level (left side of Figure 3).

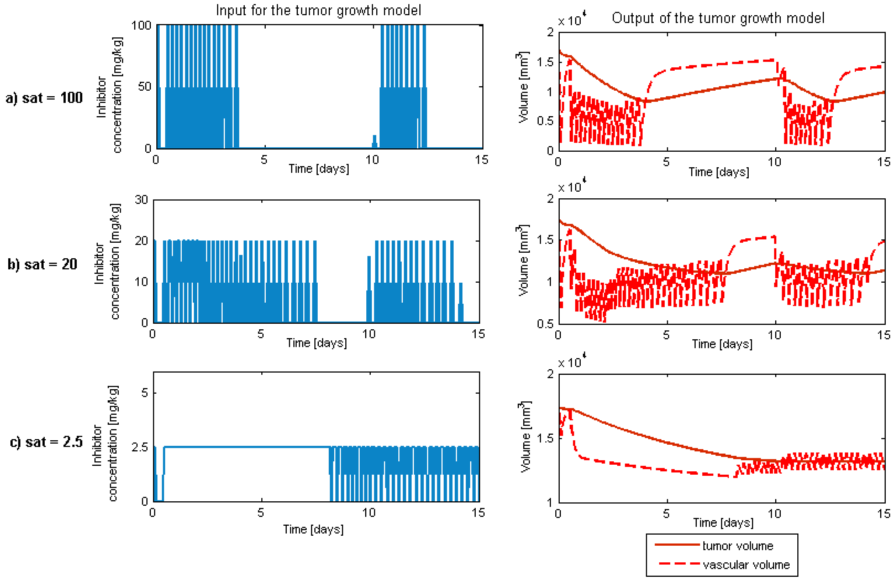

Figure 3

Discrete-time controller based therapies (treatment period is 15 days)

Parameters: operating point: 10 mm^3; *R*: 1; reference signal: 13000 mm^3; disturbance: 0%.

a) Therapy C1: saturation = 100 mg/kg

Total inhibitor concentration: 138 mg/kg, steady state tumour volume: 9870 mm^3.

b) Therapy C2: saturation = 20 mg/kg

Total inhibitor concentration: 56 mg/kg, steady state tumour volume: 11360 mm^3.

c) Therapy C3: saturation = 2.5 mg/kg

Total inhibitor concentration: 30 mg/kg, steady state tumour volume: 13153 mm^3.

Therapy C1 (sat = 100). The saturation level was chosen to be the maximum tolerated dose (*Therapy P1*). The control signal mostly contains MTD boluses; the administered boluses have lower amplitude only in a few cases. The treatment contains 3 rest periods, the longer one is approximately 6.5 days and it appears in the middle of the therapy.

Therapy C2 (sat = 20). This therapy has the same saturation level as *Therapy P2 (BD)*. Due to the lower saturation level compared to *Therapy C1*, this treatment has shorter rest periods; however, the characteristics of the treatments are similar. In the beginning of the therapy, bolus doses follow each other frequently for approximately 7.5 days, and in some cases the boluses are smaller than the level of saturation.

Therapy C3 (sat = 2.5). Finally, the saturation level was chosen to be equal to the input of the continuous infusion therapy (*Therapy P3*). The resulting treatment contains only one rest period in the very beginning of the treatment. After that a continuous administration can be obtained for approximately 8 days, which is followed by a phase where bolus doses follow each other frequently (the amplitude of these boluses is the saturation level in every case).

The right side of Figure 3 depicts the outputs of the tumor growth model, using *Therapy C1 - Therapy C3* as inputs. Using *Therapy C1*, the total inhibitor concentration is 138 mg/kg, which is the highest total drug administration among the discrete-time controller based therapies. The achieved “steady state”[1] tumor volume is 9870 mm^3 (since at the end of the treatment, an undershoot can be observed). The total inhibitor concentration in *Therapy C2* is 56 mg/kg, which is substantially lower in comparison with *Therapy C1*; however the steady state tumor volume is comparable (11360 mm^3). Finally, *Therapy C3* has resulted in the lowest total inhibitor concentration (30 mg/kg), and the achieved steady state tumor volume is 13153 mm^3 in this case.

Conclusions

The efficacy of the therapies are compared and evaluated based on the achieved total inhibitor concentrations and steady state tumor volumes (Figure 4). During the protocol based therapies, the same amount of inhibitor was administered in total. As a consequence, the comparison is quite trivial: the smaller the steady state tumor volume, the better the therapy. Bolus doses with maximum tolerated dose (BD MTD) is the less effective treatment; bolus doses with lower boluses (BD) and low-dose metronomic regimen (LDM) are better; however, the best method is the continuous infusion therapy (cont) from the protocol based therapies. Nevertheless, discrete-time controller based therapies show better performance regardless of the saturation value. The choice between these therapies depends on the medical preferences and constraints. Having a patient who can tolerate MTD, and knowing that the aim is the fastest tumor reduction, we have to choose 100 mg/kg saturation (sat = 100). If we would like to find a trade-off solution, 20 mg/kg saturation (sat = 20) is the most appropriate choice. However, if slower tumor reduction is desired and/or patient does not tolerate the inhibitor well, our choice is the 2.5 mg/kg saturation level (sat = 20).

[1] In fact, in most of the cases the output of the tumor growth model does not reach the steady state at the end of the simulation; however, as we would like to express the effectiveness of the control in terms of tumor reduction, we use the “steady state” for the final state of the investigated control and we specify its value.

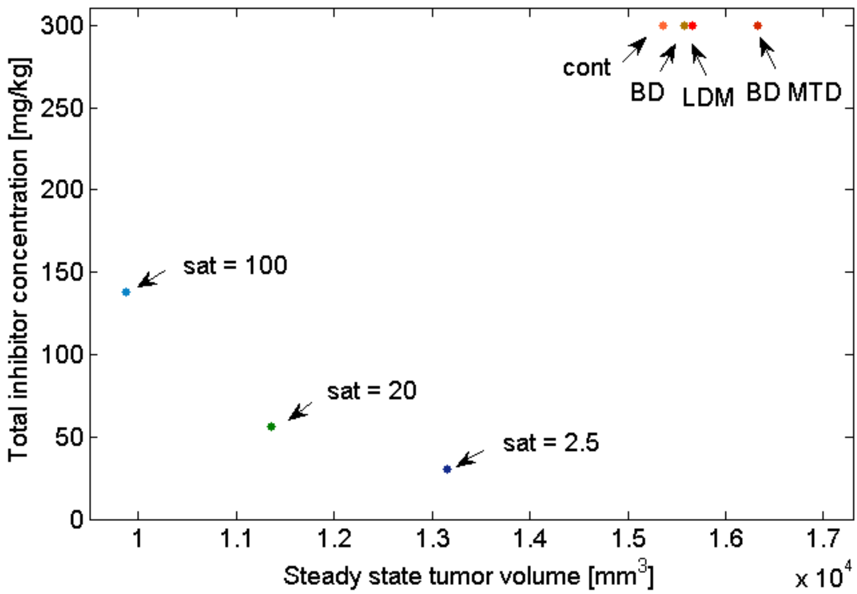

Figure 4

Comparison of the therapies as functions of total inhibitor concentration and steady state tumour volume

Protocol based therapies: bolus doses with maximum tolerated dose (BD MTD), bolus doses (BD), low-dose metronomic regimen (LDM), continuous infusion therapy (cont). Discrete controller based therapies: saturation: 100 mg/kg (sat = 100), saturation: 20 mg/kg (sat = 20), saturation: 2.5 mg/kg (sat = 2.5).

Acknowledgement

This project has received funding from the European Research Council (ERC) under the European Union's Horizon 2020 research and innovation programme (grant agreement No 679681).

References

[1] J. H. Distler, A. Hirth, M. Kurowska-Stolarska, R. E. Gay, S. Gay, O. Distler, "Angiogenic and Angiostatic Factors in the Molecular Control of Angiogenesis", *The Quarterly Journal of Nuclear Medicine*, Vol. 47(3), pp. 149-161, 2003

[2] N. Ferrara, "Vascular Endothelial Growth Factor and the Regulation of Angiogenesis", *Recent Prog Horm Res*, Vol. 55, pp. 15-35, discussion 35-36, 2000

[3] A. L. Harris, "Angiogenesis as a New Target for Cancer Control", *European Journal of Cancer Supplements*, Vol. 1, pp. 1-12, 2003

[4] S. Saha, M. K. Islam, J. A. Shilpi, S. Hasan, "Inhibition of VEGF: a Novel Mechanism to Control Angiogenesis by Withania Somnifera's Key Metabolite Withaferin A", *In Silico Pharmacol*, Vol. 29, pp. 1-11, DOI: 10.1186/2193-9616-1-11, eCollection 2013

[5] O. Distler, M. Neidhart, R. E. Gay, S. Gay, "The Molecular Control of Angiogenesis", *International Reviews of Immunology*, Vol. 21(1), pp. 33-49, 2002

[6] P. Hahnfeldt, D. Panigrahy, J. Folkman, and L. Hlatky, "Tumor Development under Angiogenic Signaling: A Dynamical Theory of Tumor Growth, Treatment Response, and Postvascular Dormancy", *Cancer Research*, Vol. 59, pp. 4770-4775, 1999

[7] D. A. Drexler, L. Kovács, J. Sápi, I. Harmati, Z. Benyó, "Model-based Analysis and Synthesis of Tumor Growth under Angiogenic Inhibition: a Case Study." *IFAC WC 2011 – 18th World Congress of the International Federation of Automatic Control*, pp. 3753-3758, August 2011, Milano, Italy

[8] J. Sápi, D. A. Drexler, I. Harmati, Z. Sápi, L. Kovács, "Linear State-Feedback Control Synthesis of Tumor Growth Control in Antiangiogenic Therapy," *SAMI 2012 – 10th IEEE International Symposium on Applied Machine Intelligence and Informatics*, pp. 143-148, January 2012, Herlany, Slovakia

[9] J. Sápi, D. A. Drexler, I. Harmati, Z. Sápi, L. Kovács, "Qualitative Analysis of Tumor Growth Model under Antiangiogenic Therapy – Choosing the Effective Operating Point and Design Parameters for Controller Design," *Optimal Control Applications and Methods*, Article first published online: 9 SEP 2015, DOI: 10.1002/oca.2196

[10] D. A. Drexler, J. Sápi, A. Szeles, I. Harmati, A. Kovács, L. Kovács, "Flat Control of Tumor Growth with Angiogenic Inhibition", *SACI 2012 – 6th IEEE International Symposium on Applied Computational Intelligence and Informatics*, pp. 179-183, May 2012, Timisoara, Romania

[11] D. A. Drexler, J. Sápi, A. Szeles, I. Harmati, L. Kovács, "Comparison of Path Tracking Flat Control and Working Point Linearization Based Set Point Control of Tumor Growth with Angiogenic Inhibition", *Scientific Bulletin of the "Politehnica" University of Timisoara, Transactions on Automatic Control and Computer Science*, Vol. 57 (71):(2), pp. 113-120, 2012

[12] A. Szeles, D. A. Drexler, J. Sápi, I. Harmati, L. Kovács, "Study of Modern Control Methodologies Applied to Tumor Growth under Angiogenic Inhibition", *IFAC WC 2014 – 19th World Congress of the International Federation of Automatic Control,* pp. 9271-9276, August 2014, Cape Town, South Africa

[13] A. Szeles, J. Sápi, D. A. Drexler, I. Harmati, Z. Sápi, and L. Kovács, "Model-based Angiogenic Inhibition of Tumor Growth using Modern Robust Control Method", *IFAC BMS 2012 – 8th IFAC Symposium on Biological and Medical Systems*, pp. 113-118, August 2012, Budapest, Hungary

[14] J. Sápi, D. A. Drexler, L. Kovács, "Parameter Optimization of H∞ Controller Designed for Tumor Growth in the Light of Physiological Aspects", *CINTI 2013 – 14th IEEE International Symposium on Computational Intelligence and Informatics*, pp. 19-24, November 2013, Budapest, Hungary

[15] L. Kovács, A. Szeles, J. Sápi, D. A. Drexler, I. Rudas, I. Harmati, Z. Sápi, "Model-based Angiogenic Inhibition of Tumor Growth using Modern Robust Control Method", *Computer Methods and Programs in Biomedicine*, Vol. 114, pp. 98-110, 2014

[16] A. Szeles, D. A. Drexler, J. Sápi, I. Harmati, Z. Sápi, L. Kovács, "Model-based Angiogenic Inhibition of Tumor Growth using Feedback Linearization", *CDC 2013 – 52nd IEEE Conference on Decision and Control*, pp. 2054-2059, December 2013, Florence, Italy

[17] A. Szeles, D. A. Drexler, J. Sápi, I. Harmati, L. Kovács, "Model-based Angiogenic Inhibition of Tumor Growth using Adaptive Fuzzy Techniques", *Periodica Polytechnica: Electrical Engineering and Computer Science,* Vol. 58:(1), pp. 29-36, 2014

[18] J. Sápi, L. Kovács, D.A. Drexler, P. Kocsis, D. Gajári, Z. Sápi, "Tumor Volume Estimation and Quasi-Continuous Administration for Most Effective Bevacizumab Therapy", *Plos One*, Vol. 10:(11), Paper e0142190. 20 p, 2015

[19] O. Kisker, CM. Becker, D. Prox, M. Fannon, R. D'Amato, E. Flynn, WE. Fogler, BK. Sim, EN. Allred, SR. Pirie-Shepherd, J. Folkman, "Continuous Administration of Endostatin by Intraperitoneally Implanted Osmotic Pump Improves the Efficacy and Potency of Therapy in a Mouse Xenograft Tumor Model", *Cancer Res*, Vol. 61(20), pp. 7669-7674, 2001

[20] J. Sápi, D. A. Drexler, L. Kovács, "Comparison of Protocol-based Cancer Therapies and Discrete Controller-based Treatments in the Case of Endostatin Administration", *SMC 2016 - IEEE International Conference on Systems, Man, and Cybernetics*, pp. 3830-3835, October 2016, Budapest, Hungary

[21] J. Sápi, D. A. Drexler, L. Kovács, "Discrete Time State Feedback with Setpoint Control, Actual State Observer and Load Estimation for a Tumor Growth Model", *SACI 2016 - IEEE 11th International Symposium on Applied Computational Intelligence and Informatics*, pp. 111-118, May 2016, Timisoara, Romania

An Automated Framework for Multi-label Brain Tumor Segmentation based on Kernel Sparse Representation

Xuan Chen[1], Binh P. Nguyen[3], Chee-Kong Chui[2], Sim-Heng Ong[1]

[1]Department of Electrical and Computer Engineering, National University of Singapore, 4 Engineering Drive 3, 117583, Singapore
[2]Department of Mechanical Engineering, National University of Singapore, 9 Engineering Drive 1, 117575, Singapore
[3]Centre for Computational Biology, Duke-NUS Medical School, 8 College Road, 169857, Singapore
xuan.chen@u.nus.edu, phubinh@ieee.org,
mpecck@nus.edu.sg, eleongsh@nus.edu.sg

Abstract: A novel automated framework is proposed in this paper to address the significant but challenging task of multi-label brain tumor segmentation. Kernel sparse representation, which produces discriminative sparse codes to represent features in a high-dimensional feature space, is the key component of the proposed framework. The graph-cut method is integrated into the framework to make a segmentation decision based on both the kernel sparse representation and the topological information of brain structures. A splitting technique based on principal component analysis (PCA) is adopted as an initialization component for the dictionary learning procedure, which significantly reduces the processing time without sacrificing performance. The proposed framework is evaluated on the multi-label Brain Tumor Segmentation (BRATS) Benchmark. The evaluation results demonstrate that the proposed framework is able to achieve compatible performance and better generalization ability compared to the state-of-the-art approaches.

Keywords: Brain tumor segmentation, kernel methods, superpixels, PCA, sparse coding, dictionary learning, graph-cuts

1 Introduction

Brain tumor refers to uncontrollable cell proliferation in the brain. Even though brain tumor is not a common disease, with prevalence of less than 0.1% in the western population, it results in high mortality [1]. The topic of brain tumor segmentation has long attracted researchers' attention because of its value in medical diagnosis and treatment planning. Brain tumor segmentation intends to separate tumors from non-tumor regions and classify brain tumor tissues according to predefined criteria [2]. Manual segmentation done by experts is possible but impractical, since it is tedious and time-consuming. Hence, semi-automated and automated approaches, which require less or even no human intervention, are practical alternatives.

Magnetic resonance (MR) imaging is preferable in brain imaging due its advantages of safety, better tissue contrast and fewer artifacts than computed tomography (CT). This emphasizes the significance of efficient and effective frameworks for brain tumor segmentation based on MR images. However, brain tumors exhibit a wide range in shape, size as well as location, and share intensities with normal brain regions in MR images. Besides, the structure of the tumor is usually complex. Therefore, much effort has been expended in the development of semi-automated or automated frameworks for brain tumor segmentation, especially multi-label brain tumor segmentation.

The past few decades have witnessed significant advances in the field of brain tumor segmentation. The approaches to brain tumor segmentation can be roughly classified into two categories: generative methods and discriminative methods. In generative methods, the anatomy and statistics of different brain tissues are explicitly modeled, while the features of task-relevant brain tissues are directly learned from training sets in discriminative methods [3]. Generative methods, although they have to deal with difficulties in modeling the prior knowledge of brain tissues and elaborate non-rigid registration, usually have better generalization ability on unseen images. Discriminative methods, which avoid the difficulties in modeling and registration, are sensitive to the amount and quality of training data.

The expectation-maximization (EM) algorithm usually plays an important role in the generative methods. Based on the statistics of the healthy brain, an outlier detection framework is proposed by Prastawa et al. [4] which treats brain tumor as outlier and generates model of tumors for subsequent EM segmentation. Menze et al. [5] incorporate multi-channel priors to augment the traditional atlas-based EM segmentation. Khotanlou et al. [6] introduce a two-step segmentation procedure, which includes tumor detection and initial segmentation refinement by fuzzy classification. Gooya et al. [7] describe a glioma growth model that is integrated with the inference of patient specific atlas to guides the EM-based segmentation.

Much research has been done in advancing discriminative methods. The classic level-set method [8, 9] is utilized due to its strength in following the change of object topology. The success of the random forest algorithm, which is essentially an ensemble classifier, in the multi-label Brain Tumor Segmentation (BRATS) challenge 2012 has boosted its popularity in the following years [10, 11].

The fact that sparse or compressible representations for signals and images are employed in some predefined or learned representation systems, also known as dictionaries, is the core of the well-known sparse coding algorithm. Compared to predefined dictionaries, learned dictionaries usually provide better sparse representations and hence more satisfying results [12]. Therefore, sparse coding and dictionary learning are commonly used together. Applications based on sparse representation using sparse coding and dictionary learning can be found in various tasks, e.g., image classification [13]. Instead of the explicit raw representation of data, kernel extension of sparse coding and dictionary learning work in an implicit, high-dimensional feature space to achieve more discriminative sparse representation. Kernel sparse representation has been utilized in the brain tumor segmentation task and its effectiveness in distinguishing tumor from normal brain regions has been demonstrated [14, 15]. However, multi-label brain tumor segmentation, which is more challenging compared to binary brain tumor segmentation, is not considered in their frameworks.

In this paper, we propose a fully automated framework based on kernel sparse representation for multi-label brain tumor segmentation. In the proposed framework, superpixels are used as basic processing units instead of traditional pixels [14] or patches [15]. A pixel-based framework involves much repeated effort in encoding similar pixels. In contrast, patches usually exhibit obvious inhomogeneity, though patch-based frameworks may be more efficient than their pixel-based counterparts. In the proposed framework, the sparse representation of each superpixel is generated in a high-dimensional feature space, where the nonlinear similarity among superpixels is more discriminative. Kernel dictionary learning is applied to learn class-specific dictionaries based on superpixel-level features including histogram and spatial location, while kernel sparse coding uses the learned dictionaries and features to generate a sparse representation for a given superpixel. The graph-cut method, which naturally take topological information into consideration, is employed in the framework. Kernel sparse representation, together with the topological information of brain tumor structure, is utilized by the graph-cut method to make the segmentation decision. The proposed framework is an enhanced version of the one introduced in our previous work [16] by including a PCA-based splitting component, named PCA-Split, to significantly speed up the processing procedure without affecting the accuracy. Furthermore, the new framework has slightly improved results. The idea of PCA-Split is driven by the fact that manipulation of a large matrix is of high computational cost. PCA-Split replaces the original training features with more compact and representative representations. Therefore, dominant features can be efficiently preserved, though the size of the training matrix is significantly decreased and hence processing time is reduced. The proposed framework is evaluated on 20 high-grade glioma (HGG) cases provided by the multi-modal Brain Tumor Segmentation Challenges 2013 (BRATS2013). Results shows the enhanced framework achieves comparable performance compared to the state-of-the-art approaches. In addition, it generalizes better on unseen images even though less training data is required.

The remainder of this paper is organized as follows. Section 2 provides an overview of the proposed framework for automated multi-label brain tumor segmentation. PCA-Split, kernel sparse representation and the graph-cut method, which are the three main components of the proposed framework, are discussed in Section 3-5. Evaluation results and comparison with the state-of-the-art approaches are reported in Section 6. The paper is concluded in Section 7.

2 Overview

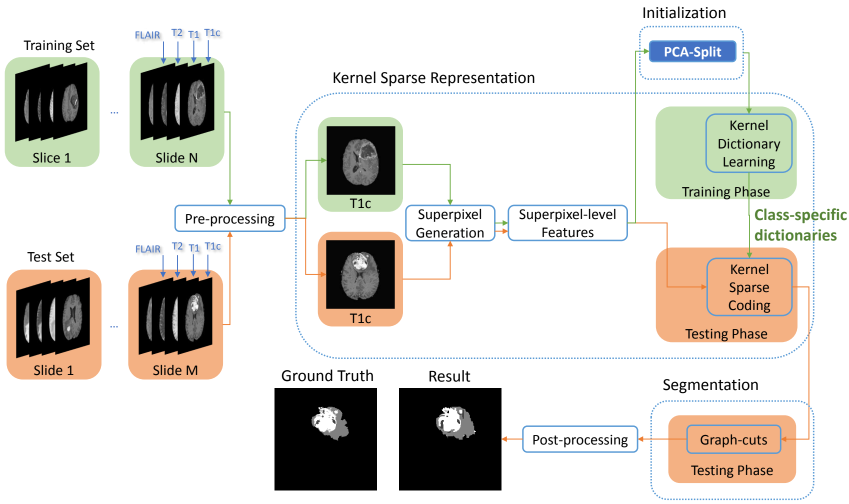

Figure 1
Overview of the proposed automated framework for multi-label brain tumor segmentation.

An overview of the proposed automated framework for multi-label brain tumor segmentation is shown in Figure 1. The proposed framework contains three main components: initialization with PCA-Split, kernel sparse representation and segmentation using graph-cuts. Given a set of training samples, PCA-Split initialization finds more compact and representative representations by splitting the set into a given number of subsets and replacing the raw representations with the centroids of each subsets. Kernel sparse representation consists of kernel dictionary learning and kernel sparse coding. In the training phase, kernel dictionary learning learns class-specific dictionaries based on superpixel-level features of brain tissues, which are used as representation systems for each task-relevant class. In the testing phase, kernel sparse coding generates optimal sparse codes for unseen testing samples according to the learned dictionaries and their superpixel-level features. The kernel sparse representation is then utilized in the graph-cut method to make pixel-wise segmentation decisions.

3 PCA-Split Initialization

Adequate and representative training samples are critical to the performance of learning-based approaches. However, manipulation of a large matrix is of high computational cost and the quality of the selected training samples is not guaranteed.

Algorithm 1 PCA-Split

Input: A input set $\mathbf{W} = [\mathbf{w}_i]_{i=1}^N$ and a desired number of subsets Q.
Task: Split a subset of the given input set with regard to its variance until the desired number of subsets is reached.
Initialize: Number of subsets $q = 1$, subsets $\mathbf{V} = [\mathbf{V}_1, ..., \mathbf{V}_i, ..., \mathbf{V}_q]$ and $\mathbf{V}_1 = \mathbf{W}$.
Procedure:
while $q \neq Q$ **do**
  for $\forall\, \mathbf{V}_i \subseteq \mathbf{V}$ **do**
    $\delta_i = \sum_{\{\forall j|\mathbf{w}_j \in \mathbf{V}_i\}} (\mathbf{w}_j - \boldsymbol{\mu}_i)^2$.
  end for
  Sort all subsets in descending order according to δ_i.
  Calculate covariance matrix $\boldsymbol{\Sigma}_1 = \sum_{\{\forall j|\mathbf{w}_j \in \mathbf{V}_1\}} (\mathbf{w}_j - \boldsymbol{\mu}_1)(\mathbf{w}_j - \boldsymbol{\mu}_1)^T$
  Find out eigenvector $\mathbf{eig}_{max}$ which corresponds to the largest eigenvalue.
  for all $j \in \{\forall j|\mathbf{w}_j \in \mathbf{V}_1\}$ **do**
    if $\langle (\mathbf{w}_j - \boldsymbol{\mu}_1), \mathbf{eig}_{max} \rangle < 0$ **then**
      $\mathbf{w}_j \in \mathbf{V}_{left}$
    else if $\langle (\mathbf{w}_j - \boldsymbol{\mu}_1), \mathbf{eig}_{max} \rangle \geq 0$ **then**
      $\mathbf{w}_j \in \mathbf{V}_{right}$
    end if
  end for
  $q \leftarrow q + 1$
  $\mathbf{V}_{q-1} \leftarrow \mathbf{V}_{left}$
  $\mathbf{V}_q \leftarrow \mathbf{V}_{right}$
  for $\forall\, \mathbf{V}_i \subseteq \mathbf{V}$ **do**
    $\boldsymbol{\mu}_i = \frac{\sum_{\{\forall j|\mathbf{w}_j \in \mathbf{V}_i\}} \mathbf{w}_j}{|\mathbf{V}_i|}$
  end for
end while
Output: subsets $\mathbf{V} = [\mathbf{V}_1, ..., \mathbf{V}_i, ..., \mathbf{V}_Q]$ and centroids $\mathbf{U} = [\boldsymbol{\mu}_1, ..., \boldsymbol{\mu}_Q]$

To address this problem, a principal-component-analysis-based (PCA-based) splitting technique is applied, which is named PCA-Split. The PCA-based splitting technique has been utilized in various applications, like codebook initialization for vector quantization [17] and hierarchical clustering [18]. The purpose of PCA-Split is, in each iteration, to find an optimal splitting plane with respect to the variance of a subset of the given data [17]. Splitting continues until the desired number of subsets is achieved. The centroid of each subset is used to represent all data samples that lie in the subset. The main properties of the subset are preserved by the centroid, while "outliers" are eliminated. In this way, more compact and representative representations of the dataset can be obtained.

The procedure of performing PCA-Split is described as follows. Given an input set $\mathbf{W} = [\mathbf{w}_i]_{i=1}^N$, PCA-Split starts with only one subset $\mathbf{V}_1$ which contains the entire input set. In each iteration, all subsets are sorted in descending order according to their representation distortions calculated by the formulation $\delta_q = \sum_{\forall j|\mathbf{w}_j \in \mathbf{V}_q}(\mathbf{w}_i - \boldsymbol{\mu}_q)^2$ with respect to the centroid $\boldsymbol{\mu}_q$. The subset with the largest representation distortion is then selected to be split. The optimal splitting plane is the eigenvector corresponding to the largest eigenvalue, which splits the subset into "left" and "right" groups. Hence the number of subsets is increased by one in each iteration until the preset number of subsets is reached.

The pseudo-code for PCA-Split is given in Algorithm 1, where $\langle \cdot, \cdot \rangle$ denotes the inner product, $\mathbf{X}^T$ the transpose of $\mathbf{X}$, $|\mathbf{X}|$ the number of elements in $\mathbf{X}$.

4 Kernel Sparse Representation

4.1 Extraction and Fusion of Superpixel-Level Features

Superpixels that contain pixels with similar perceptual meaning are the basic processing units in the proposed framework. The compact grouping of pixels is beneficial to the achievement of better kernel sparse representation and faster segmentation. The contour relaxed superpixel (CRS) algorithm [19] is utilized for superixel generation due to its flexibility in controlling the adaption to a complicated contour with a single parameter κ. MR imaging provides multi-modal information, like T1-weighted (T1), T2-weighted (T2), contrast-enhanced T1-weighted (T1c) and FLAIR, which help to enrich our understanding of brain tumors. Due to their higher spatial resolution and clearer display of brain tumor structure compared to other modalities, T1c images are used as the reference in the generation of superpixels. Superpixel generation is restricted to the brain area only to avoid unnecessary processing to the background area. CRS ($\kappa = 0.01$) partitions an input image into a set of superpixels $\mathbf{S} = [s_1, ..., s_t, ...s_T]$. In order to fully utilize the multi-modal information, the generated superpixel regions are applied to T1, T2 and FLAIR modalities.

Superpixel-level features are extracted based on the generated superpixel regions (Figure 2). For a superpixel s_t, 64-bin histograms from all four modalities are calculated, which are denoted as $\mathbf{h}_{t(c)}$ $(c \in \{\mathrm{T1}, \mathrm{T2}, \mathrm{T1c}, \mathrm{FLAIR}\})$. All histograms are normalized to have $\sum_{j=1}^r \mathbf{h}_{t(c)}(j) = 1$, where r is the number of pixels located in superpixel s_t, to prevent bias induced by the difference in number of pixels. In addition to histograms, spatial locations of superpixels are taken into consideration. The spatial location of superpixel s_t is defined as its centroid $\mathbf{l}_t = (x_t, y_t)$. The mean values of positions of all pixels in superpixel s_t in the x-axis normalized by the width of the image and y-axis normalized by the height of the image correspond to the values of x_t and y_t respectively. Therefore, the learned dictionaries are able to simultaneously model both features including histogram and spatial location.

The proposed framework, instead of working on the raw representation of data, generates kernel sparse representation in a high-dimensional, implicit feature space $\mathscr{F}$.

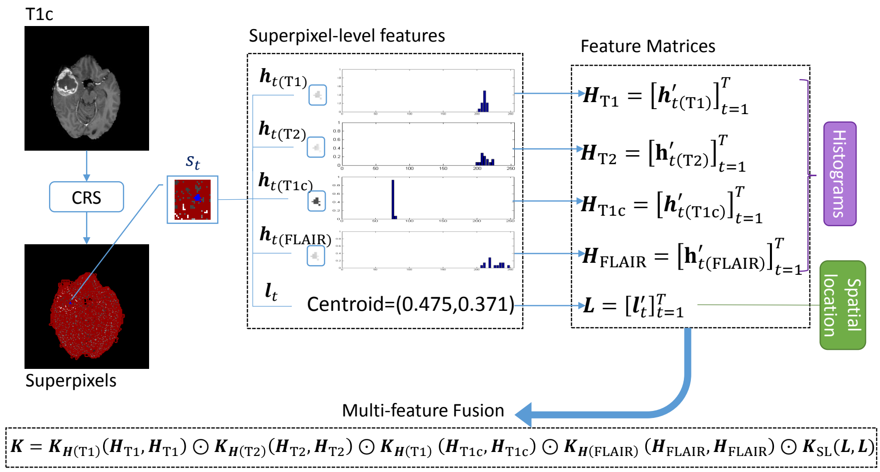

Figure 2
Extraction and fusion of superpixel-level features.

Nonlinear similarities in $\mathscr{F}$ between samples are considered, which are more discriminative compared to the linear similarity in the original space. In order to map the raw representation to the feature space $\mathscr{F}$, a nonlinear transformation $\Phi(\cdot)$ is applied. Hence, nonlinear similarity between two samples $\mathbf{x}$ and $\mathbf{x}'$ can be measured by the inner product $\Phi(\mathbf{x})^T\Phi(\mathbf{x}')$. Nevertheless, $\Phi(\cdot)$ can be intractable in the high-dimensional, even infinite-dimensional, feature space $\mathscr{F}$ [14]. To address this problem, the kernel trick is adopted, which replaces the intractable inner product $\Phi(\mathbf{x})^T\Phi(\mathbf{x}')$ with a known kernel function $\mathscr{K}$. With the knowledge of the kernel and the samples, nonlinear similarity can always be calculated even though the explicit formulation of $\Phi(\cdot)$ is not known. To proceed with the replacement, the chosen kernel function should satisfy Mercer's theorem [20]. The well-known radial basis function (RBF) kernel is selected in our framework. The definition of the RBF Kernel is $\mathscr{K}(\mathbf{x},\mathbf{y}) = \exp(-\|\mathbf{x}-\mathbf{y}\|^2/2\sigma^2)(\sigma = 1.5)$.

Given two matrices $\mathbf{X} = [\mathbf{x}_i]_{i=1}^N$ and $\mathbf{X}' = [\mathbf{x}_i']_{i=1}^M$, a Gramian matrix $\mathbf{K}(\mathbf{X},\mathbf{X}') \in \mathbb{R}^{N\times M}$ is defined such that its (n,m)-entry $\mathbf{K}_{n,m}$ corresponds to the nonlinear similarity $\mathscr{K}(\mathbf{x}_n,\mathbf{x}_m')$ between the n^{th} element of $\mathbf{X}$ and the m^{th} element of $\mathbf{X}'$. All extracted superpixel-level features are arranged in column vector manner into their corresponding feature matrices (Figure 2). Specifically, in the training phase, the raw representations of all features are substituted by the centroids of subsets obtained by applying PCA-Splits to their corresponding feature matrices with a specified number of substes Q. For histogram feature matrices, Gramian matrices $\mathbf{K}_{H(c)}$ $(c \in \{\mathrm{T1},\mathrm{T2},\mathrm{T1c},\mathrm{FLAIR}\})$ are obtained to represent the nonlinear similarities in a specific modality, while a Gramian matrix $\mathbf{K}_{SL}$ is calculated for that of spatial location. $\mathbf{K}_{H(c)}$ $(c \in \{\mathrm{T1},\mathrm{T2},\mathrm{T1c},\mathrm{FLAIR}\})$ and $\mathbf{K}_{SL}$ are denoted as the following formulations:

$$
\begin{aligned}
\mathbf{K}_{H(c)}(i,j) &= \exp\left(-\frac{\|\mathbf{h}_{i(c)}-\mathbf{h}_{j(c)}\|_2^2}{2\sigma^2}\right) \\
\mathbf{K}_{\mathrm{SL}}(i,j) &= \exp\left(-\frac{\|\mathbf{l}_i-\mathbf{l}_j\|_2^2}{2\sigma^2}\right)
\end{aligned}
\tag{1}
$$

Not only the sparse representation benefits from the kernel trick, the use of the the kernel trick also facilitate the fusion of multi-features such that all the Gramian matrices can be combined in an elegant way by simple Hadamard product. The combination yields an ensemble matrix $\mathbf{K}$, i.e., $\mathbf{K} = \mathbf{K}_{H(\mathrm{T1})} \odot \mathbf{K}_{H(\mathrm{T2})} \odot \mathbf{K}_{H(\mathrm{T1c})} \odot \mathbf{K}_{H(\mathrm{FLAIR})}$. Learning of dictionary based on the ensemble Gramian matrix is more efficient and effective since all five features are captured at one time. For simplicity, the rest of the paper only focuses on the ensemble Gramian matrix for the generation of kernel sparse representation, rather than the five Gramian matrices individually.

4.2 Kernel Sparse Coding and Kernel Dictionary Learning

Given a set of input data $\mathbf{Y} = [\mathbf{y}_i]_{i=1}^N, \mathbf{y}_i \in \mathbb{R}^M$, the goal of dictionary learning is to obtain an optimal overcomplete dictionary $\mathbf{D} \in \mathbb{R}^{M\times K}$ to well model the given data $\mathbf{Y}$, so that each element $\mathbf{y}_i \in \mathbf{Y}$ can be approximated by a linear combination of only a few dictionary atoms $\mathbf{d}_k, (k = 1,2,...,K)$ via a code $\mathbf{x}_i \in \mathbb{R}^K$. The code $\mathbf{x}_i$ is sparse since only a few entries are non-zero. The objective function of dictionary learning is given by:

$$
(\hat{\mathbf{X}}, \hat{\mathbf{D}}) = \arg\min_{\mathbf{X,D}} \|\mathbf{Y} - \mathbf{D}\mathbf{X}\|_F^2 \; s.t. \; \|\mathbf{x}_i\|_0 \le T_0, \forall i \tag{2}
$$

where $\mathbf{X} = [\mathbf{x}_i]_{i=1}^N$, $\|.\|_F$ is the Frobenius norm, $\|.\|_0$ denotes the ℓ_0 norm and T_0 the sparsity level, which indicates the maximum number of non-zero entries in a sparse code $\mathbf{x}_i$.

Upon obtaining the dictionary, $\mathbf{D}$ is fixed and sparse coding finds the optimal sparse representation $\mathbf{X}'$ for the testing data $\mathbf{Y}'$ based on the learned dictionary $\mathbf{D}$. The optimization problem of sparse coding is expressed as:

$$
(\hat{\mathbf{X}}') = \arg\min_{\mathbf{X}'} \|\mathbf{Y}' - \mathbf{D}\mathbf{X}'\|_F^2 \; s.t. \; \|\mathbf{x}_i'\|_0 \le T_0, \forall i \tag{3}
$$

To adapt the original optimization problem of sparse coding and dictionary learning into feature space $\mathscr{F}$, a nonlinear transformation $\Phi(\cdot)$ is applied to both the data matrix. Therefore, the kernel extensions of dictionary learning and sparse coding are formulated as equations (4) and (5) respectively:

$$
(\hat{\mathbf{X}}, \hat{\mathbf{D}}) = \arg\min_{\mathbf{X,D}} \|\Phi(\mathbf{Y}) - \Phi(\mathbf{D})\mathbf{X}\|_F^2 \; s.t. \; \|\mathbf{x}_i\|_0 \le T_0, \forall i \tag{4}
$$

$$
(\hat{\mathbf{X}}') = \arg\min_{\mathbf{X}'} \|\Phi(\mathbf{Y}') - \Phi(\mathbf{D})\mathbf{X}'\|_F^2 \; s.t. \; \|\mathbf{x}_i'\|_0 \le T_0, \forall i \tag{5}
$$

where $\Phi(\mathbf{Y}) = [\Phi(\mathbf{y}_i)]_{i=1}^N$, $\Phi(\mathbf{Y}') = [\Phi(\mathbf{y}'_i)]_{i=1}^P$ and $\Phi(\mathbf{D}) = [\Phi(\mathbf{d}_i)]_{i=1}^K$.

The dictionary in $\mathscr{F}$ can be represented by the linear combination of the input data (i.e., $\Phi(\mathbf{D}) = \Phi(\mathbf{Y})\mathbf{A}$), since all dictionary atoms lie in the linear span of the input data [12]. $\mathbf{A} \in \mathbb{R}^{N\times K}$ is an atom representation dictionary and the optimal $\mathbf{A}$ is directly related to the best dictionary $\mathbf{D}$ that can be achieved. The formulation of kernel dictionary learning and kernel sparse coding can be re-written as equations (6) and (7) respectively:

$$(\hat{\mathbf{X}}, \hat{\mathbf{A}}) = \arg\min_{\mathbf{X,A}} \|\Phi(\mathbf{Y}) - \Phi(\mathbf{Y})\mathbf{A}\mathbf{X}\|_F^2 \ s.t. \ \|\mathbf{x}_i\|_0 \leq T_0, \forall i \tag{6}$$

$$(\hat{\mathbf{X}}') = \arg\min_{\mathbf{X}'} \|\Phi(\mathbf{Y}') - \Phi(\mathbf{Y})\mathbf{A}\mathbf{X}'\|_F^2 \ s.t. \ \|\mathbf{x}'_i\|_0 \leq T_0, \forall i \tag{7}$$

A kernel extension of the K-SVD type dictionary learning algorithm [12] is adopted in our framework. Since learning of dictionary iteratively alternates between kernel sparse coding and kernel dictionary learning until predefined criteria are met or maximum iteration number is reached, we only focus on the optimization of kernel dictionary learning (i.e., equation (6)) for simplicity.

In the kernel sparse coding step, the atom representation dictionary $\mathbf{A}$ is assumed to be known and fixed. The sparse codes matrix $\mathbf{X}$ can be found by minimizing the approximation error $\|\Phi(\mathbf{Y}) - \Phi(\mathbf{Y})\mathbf{A}\mathbf{X}\|_F^2$ subject to the sparsity constraint $\|\mathbf{x}_i\|_0 \leq T_0, \forall i$. The penalty term can be decomposed and written as:

$$\|\Phi(\mathbf{Y}) - \Phi(\mathbf{Y})\mathbf{A}\mathbf{X}\|_F^2 = \sum_{i=1}^{N} \|\Phi(\mathbf{y}_i) - \Phi(\mathbf{Y})\mathbf{A}\mathbf{x}_i\|_2^2 \tag{8}$$

Now, the "big" problem is separated into N "small" optimization problems:

$$\min_{\mathbf{x}_i} \|\Phi(\mathbf{y}_i) - \Phi(\mathbf{Y})\mathbf{A}\mathbf{x}_i\|_2^2 \ s.t. \ \|\mathbf{x}_i\|_0 \leq T_0 \tag{9}$$

To facilitate optimization, the objective function is reconstructed with kernel function $\mathscr{K}$ to avoid the unknown nonlinear transformation $\Phi(\cdot)$:

$$\min_{\mathbf{x}_i} \mathscr{K}(\mathbf{y}_i, \mathbf{y}_i) - 2\mathbf{K}(\mathbf{y}_i, \mathbf{Y})\mathbf{A}\mathbf{x}_i + \mathbf{x}_i^T \mathbf{A}^T \mathbf{K}(\mathbf{Y,Y})\mathbf{A}\mathbf{x}_i \ s.t. \ \|\mathbf{x}_i\|_0 \leq T_0 \tag{10}$$

With the help of the kernel trick, this optimization problem can be solved by the classic orthogonal matching pursuit (OMP) algorithm [21].

Once the sparse codes matrix is calculated, we update the all dictionary atoms according to the projection error. In other words, kernel dictionary learning, with the fixed $\mathbf{X}$, searches for a new atom representation dictionary $\mathbf{A}$ to minimize $\|\Phi(\mathbf{Y}) - \Phi(\mathbf{Y})\mathbf{A}\mathbf{X}\|_F^2$.

First, the penalty term is rewritten as:

$$\|\Phi(\mathbf{Y}) - \Phi(\mathbf{Y})\sum_{j=1}^{K} \mathbf{a}_j \mathbf{x}_j^R\|_F^2 = \|\Phi(\mathbf{Y})(\mathbf{I} - \sum_{j\neq k} \mathbf{a}_j \mathbf{x}_j^R) - \Phi(\mathbf{Y})(\mathbf{a}_k \mathbf{x}_k^R)\|_F^2 \tag{11}$$

where $\mathbf{a}_k$ and $\mathbf{x}_k^R$ correspond to the k^{th} column of $\mathbf{A}$ and the k^{th} row of $\mathbf{X}$ respectively. Contribution made by the k^{th} dictionary atom to the estimated sample can be obtained from $\mathbf{a}_k\mathbf{x}_k^R$. For simplicity, we denote $\mathbf{E}_k = \mathbf{I} - \sum_{j \neq k} \mathbf{a}_j \mathbf{x}_j^R$, which represents the approximation error between the estimated and original samples when the k^{th} dictionary atom is removed.

As can be seen in equation (11), the pair of unknown variables $(\mathbf{a}_k, \mathbf{x}_k^R)$ is expected to be found to minimize the approximation error. This can be solve by the best rank-1 approximation. Due to their trivial contribution to the optimization problem, columns related to zero entries of $\mathbf{x}_k^R$ in $\mathbf{E}_k$ and $\mathbf{a}_k\mathbf{x}_k$ are removed, which yields $\mathbf{E}_k^{Re}$ and $\mathbf{a}_k\mathbf{x}_k^{Re}$ respectively ($\mathbf{x}_k^{Re}$ containing only non-zero weights of $\mathbf{x}_k^R$). Singular value decomposition (SVD) is applied to $\mathbf{E}_k^{Re}$ and $\mathbf{a}_k\mathbf{x}_k^{Re}$ instead of $\mathbf{E}_k$ and $\mathbf{a}_k\mathbf{x}_k^R$ to preserve the specified sparsity level and reduce computational cost.

The SVD decomposes $\Phi(\mathbf{Y})\mathbf{E}_k^{Re}$ into three parts:

$$\Phi(\mathbf{Y})\mathbf{E}_k^{Re} = \mathbf{U}\boldsymbol{\Sigma}\mathbf{V}^T \tag{12}$$

Equating $\Phi(\mathbf{Y})\mathbf{a}_k\mathbf{x}_k^{Re}$ to the rank-1 matrix, which corresponds to the largest singular value $\sigma_1 = \boldsymbol{\Sigma}(1,1)$ of $\Phi(\mathbf{Y})\mathbf{E}_k^{Re}$, gives the solution to the best rank-1 approximation.

$$\Phi(\mathbf{Y})\mathbf{a}_k\mathbf{x}_k^{Re} = \mathbf{u}_1\sigma_1\mathbf{v}_1^T \tag{13}$$

where $\mathbf{u}_1$ and $\mathbf{v}_1$ are the first columns of $\mathbf{U}$ and $\mathbf{V}$ corresponding to σ_1 respectively. Thus, the solution can be calculated from the equations below:

$$\begin{aligned} \Phi(\mathbf{Y})\mathbf{a}_k &= \mathbf{u}_1 \\ \mathbf{x}_k^{Re} &= \sigma_1\mathbf{v}_1^T \end{aligned} \tag{14}$$

However, it is impractical to perform SVD on $\Phi(\mathbf{Y})\mathbf{E}_k^{Re}$ since the explicit formulation of $\Phi(\cdot)$ is unknown. Consequently, the kernel trick should be used again such that the eigen decomposition of $\mathbf{E}_k^{ReT}\Phi(\mathbf{Y})^T\Phi(\mathbf{Y})\mathbf{E}_k^{Re}$, which is $\mathbf{V}\boldsymbol{\Delta}\mathbf{V}^T$, is calculated to infer the unknown variables. As a result, $\mathbf{V}$ is obtained and σ_1 can be deduced by $\sigma_1 = \sqrt{\boldsymbol{\Delta}(1,1)}$. An analytical solution is possible when the term for σ_1 is substituted into equation (14):

$$\mathbf{a}_k = \sigma_1^{-1}\mathbf{E}_k^{Re}\mathbf{v}_1 \tag{15}$$

In each iteration, all the atoms of $\mathbf{A}$ are updated according to the manner stated above followed by the search for new sparse codes based on the new dictionary. This process alternates between kernel dictionary learning and kernel dictionary learning till some preset conditions are satisfied.

5 Graph-Cuts

The pixel-wise segmentation decision is made by the graph-cut method based on both kernel sparse representation and topological information of the brain structures. The task requires the proposed framework to classify pixels into five specific classes, which are non-tumor (label=0), necrotic core (label=1), edema (label=2), non-enhancing core (label=3) and enhancing core (label=4). For each class, a dictionary is learned by applying kernel dictionary learning to a set of training samples as described in Section 4. These dictionaries should be able to model their own classes well since they are optimized for the particular purpose, even though they fail to approximate well the rest of the classes.

For a test superpixel s_t, the proposed framework computes five sparse codes $\mathbf{x}_0, \mathbf{x}_1, \mathbf{x}_2, \mathbf{x}_3$ and $\mathbf{x}_4$ with respect to the five dictionaries. The approximation errors between the input sample s_t and the five approximations are denoted by $e_0^{s_t}, e_1^{s_t}, e_2^{s_t}, e_3^{s_t}$ and $e_4^{s_t}$, and measured by:

$$e_i^{s_t} = \|\Phi(\mathbf{y}^{s_t}) - \Phi(\mathbf{D}_i)\mathbf{x}_i^{s_i}\|_2^2,\ i = 0, 1, 2, 3, 4 \tag{16}$$

Segmentation based on kernel sparse representation does not take topological information of the brain structure into consideration. The graph-cut method, which naturally incorporates topological information, is a possible remedy. We propose a variant graph-cuts [22, 23] to better adapt to our application. A graph should be constructed to proceed with the variant graph-cuts. To facilitate graph construction, a superpixel is first ungrouped into a set of pixels which form the superpixel. Then these pixels are given the same approximation errors as the superpixel they belong. The image is represented by a array which contains all its pixels $\mathbf{z} = (z_1, ..., z_l ..., z_L)$, assuming there are L pixels in total. The approximation errors assigned to pixel z_l are denoted by $e_i^{z_l} (i = 0, 1, 2, 3, 4)$. These pixels, besides the approximation errors, contains extra information in terms of different gray-level intensities in multimodalities. For pixel z_l, gray-level intensities in the four modalities are defined as $g_{\mathrm{T1}}^{z_l}, g_{\mathrm{T2}}^{z_l}, g_{\mathrm{T1c}}^{z_l}$ and $g_{\mathrm{FLAIR}}^{z_l}$.

The energy function of graph-cuts is expressed by:

$$E(f) = \sum_{\{p,g\} \in \mathscr{N}} V_{p,q}(f_p, f_q) + \sum_{p \in \mathscr{P}} D_p(f_p) \tag{17}$$

where f is a label in a finite label set $\mathscr{L}$, $\{p, q\}$ a pair of pixels in the pixel set $\mathscr{P}$, and $\mathscr{N}$ a set of neighboring pixels. The first term in equation (17) is known as the smoothness term, which encourages pairwise smoothness while preserving label discontinuity on boundaries. The data term is the name given to the second term, which measures the fit of label f to the observed data p.

Typically, the data term is formulated with negative log-likelihood. According to the previous discussion, if a test sample belongs a specific class, the smallest approximation error can be achieve when the dictionary learned for this class is used in kernel sparse coding. Therefore, the kernel sparse representation generated in the previous step is utilized in the data term as the measurement of label appropriateness as shown below:

$$\sum_{l=1}^{L} D_{z_l}(f_{z_l}) = \sum_{l=1}^{L} log(e_{f_{z_l}}^{z_l}) \tag{18}$$

The smoothness term is defined as:

$$\sum_{\{z_l,z_q\}\in\mathcal{N}} V_{z_l,z_q}(f_{z_l},f_{z_q}) = \theta \sum_{\{z_l,z_q\}\in\mathcal{N}_4} [f_{z_l} \neq f_{z_q}] \exp - \beta \|z_l - z_q\|_2^2 \tag{19}$$

where θ is a constant controlling the degree of discontinuity preserving, $\mathcal{N}_4$ indicates 4-way connectivity and $[\cdot]$ is a indicator function taking value 1 for true prediction or 0 for false prediction. θ is empirically set to 50 according to the preliminary experiments. The Euclidean distance between pixel z_l and z_q is given by:

$$\|z_l - z_q\|_2^2 = \sum_c (g_c^{z_l} - g_c^{z_q})^2, \; c \in \{\mathrm{T1}, \mathrm{T2}, \mathrm{T1c}, \mathrm{FLAIR}\} \tag{20}$$

Though θ only has the control on overall smoothness, we have another parameter β to prevent the tendency of being over-smooth on boundaries between different classes. β is computed by:

$$\beta = (2 < \|z_l - z_q\|_2 >)^{-1} \tag{21}$$

where $< \cdot >$ denotes expectation over $\mathcal{N}_4$ neighborhood.

The optimization of the variant graph-cuts, depending on nonlinear feature similarity and topological information, provides the best label configurations for all pixels. We use the GCMex - MATLAB wrapper to implement the proposed variant graph-cuts [23, 24, 25].

6 Experiment and Discussion

The proposed framework is evaluated on 20 real HGG cases in the training set of BRATS2013 with two-fold cross validation (CV). In the training phase, the superpixels collected from the training set for each of the five classes (i.e., non-tumor(0), necrotic core(1), edema(2), non-enhancing core(3) and enhancing-core(4)) are initialized for kernel dictionary learning by PCA-Split. The desired number of subsets Q is empirically set to 512 considering the trade-off between good segmentation result and less processing time. As a result, the dictionaries of the five task-relevant classes are learned from their corresponding 512 PCA-Split centroids. For kernel dictionary learning and kernel sparse coding, we fix the number of dictionary atoms to 200 and the sparsity level to 5. The framework is implemented on MATLAB using a computer with Intel processor (i7-3930K, 3.20GHz) and 32GB of RAM.

The following three regions are segmented and used for evaluation:

- Region 1: complete tumor (label 1+2+3+4)
- Region 2: tumor core (label 1+3+4)
- Region 3: enhancing core (label 4)

The performance of the proposed framework is reported via the Dice similarity coefficient, Jaccard index and sensitivity [3] on the aforementioned three regions.

Even though the BRATS2013 dataset has been pre-processed with skull-striping and co-registration, obvious intensity bias can still be observed. The intensity bias can significantly worsen the segmentation accuracy since superpixel-level histograms are intensively used in our framework. This requires further pre-processing steps including bias field correction and intensity inhomogeneity correction. T2 and FLAIR are exempted from bias field correction due to the fact that the correction decreases their contrast. N4ITK [26] tool in Slicer3D is used for bias field correction, while intensity inhomogeneity is adjusted by a learning-based two-step standardization [27].

The segmentation result output directly from graph-cuts can be noisy. Therefore, binary morphological processing and connected component analysis are applied as post-processing steps.

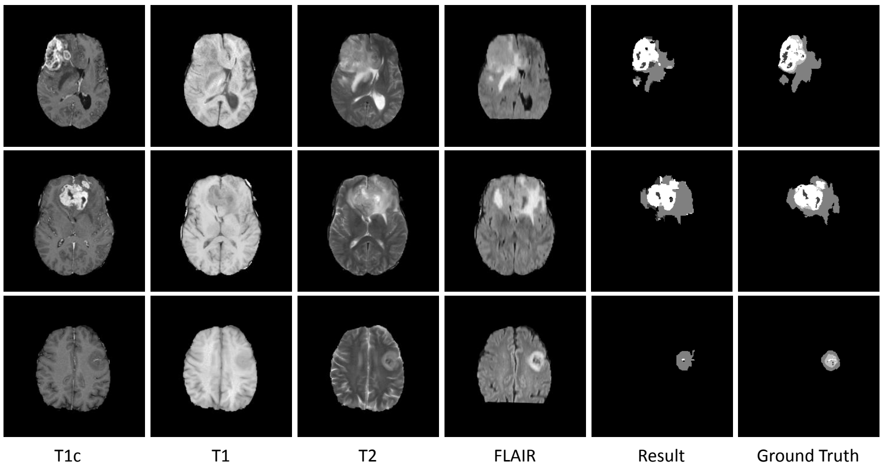

Figure 3
Three segmentation examples of the proposed framework. First column to sixth column correspond to T1c images, T1 images, T2 images, FLAIR images, segmentation results and ground truths respectively. The first row shows one slice of patient009, while the second row is a slice of patient015. The bottom row demonstrates the performance of the proposed framework on the worst case-patine012.

Several segmentation examples generated by the proposed approach are shown in Figure 3. In addition, we report the averages and standard deviations of the Dice similarity coefficient, Jaccard index and sensitivity that achieved by the proposed framework in Table 1. The performance of our previous method [16] is also concluded in Table 1. For Region 2 and Region 3, we report the performance twice, one including patient012 while the other excluding patient012, since the peculiarity of patient012 significantly worsens the overall performance as can be seen from Table 1. The reason why both our frameworks fail to give good segmentation results for patient012 is probably because of the similar intensities shared by the non-enhancing core and the edeme in all four modalites. Moreover, the tumor of patient012 mainly consists of non-enhancing core and edema, which makes it extremely difficult for our approaches to make good segmentation decision. Hence,

Table 1
Evaluation of performance on BRATS 2013 training cases (HGG)

	Dice				Jaccard				Sensitivity			
	previous		proposed		previous		proposed		previous		proposed	
	mean	std	mean	std	mean	std	mean	std	mean	std	mean	std
Region 1	81.1	9.3	81.1	9.6	69.2	12.5	69.1	12.9	81.9	13.6	82.3	14.1
Region 2	62.9	17.6	63.3	22.1	48.0	17.3	49.5	21.0	69.3	22.4	71.1	25.2
Region 2(*)	65.3	14.2	66.5	17.1	50.0	15.2	52.0	18.2	72.4	18.2	74.8	19.6
Region 3	69.7	17.2	70.4	19.6	55.6	17.8	57.1	19.6	70.1	22.5	71.2	24.5
Region 3(*)	71.9	14.4	73.4	14.8	57.7	15.5	59.7	16.2	72.9	19.2	74.5	20.0

* denotes the scores are calculated excluding the result of patient0012.

the proposed framework easily mistakes the non-enhancing core for the edema and results in very low scores in both Region 2 and Region 3. The average processing time for one slice required by our previous framework and the proposed framework are 8 seconds and 30 seconds. The comparison between our previous framework and the proposed framework in terms of performance (Table 1) and processing time clearly reveals the advantages of the proposed framework over the previous one. The proposed framework, with exactly the same training and test set configuration, achieves comparable scores in Region 1 and slightly outperforms the previous one in both Region 2 and Region 3. The proposed framework (8 seconds) requires less than one third of the average execution time for one slice of the previous method (30 seconds).

We also show in Table 2 the performances of three state-of-the-art discriminative approaches [28, 29, 30] evaluated on the same dataset. Scores are directly extracted from their published papers. This table is for reference only due to the lack of their training and testing set configurations. Nevertheless, we can conclude that our proposed approaches achieves competitive performance compared to the state-of-the-art approaches. In addition, better generalization ability of the proposed framework is observed when we compare the CV type used in our framework to those in their approaches (Table 3). This means, the proposed framework achieves comparable performance with much less training cases, but still perform well on more unseen images.

Conclusions

A novel automated framework for multi-label brain tumor segmentation is proposed in this paper. As an enhanced version of our previous framework in [16], the proposed framework has advantages in both performance and processing time. PCA-Split initialization provides compact and representative training samples for kernel dictionary learning, which significantly reduce training and processing time without scarifying good models for related classes. Kernel sparse representation based on kernel dictionary learning and kernel sparse coding is utilized in the graph-cut method together with the topological information of brain structure to arrive at a segmentation decision. The results show that the proposed framework gives a comparable performance while better generalization ability is observed when compared to the state-of-the-art discriminative approaches.

We plan to include topological information in the generation of sparse representation as an extra regularization term, instead of optimizing sparse representation and graph-cuts separately, such that jointly optimization can be achieved and hence better sparse representation and result are expected.

Table 2
Performance of state-of-the-art methods

	Dice						Jaccard						Sensitivity					
	Approach 1		Approach 2		Approach 3		Approach 1		Approach 2		Approach 3		Approach 1		Approach 2		Approach 3	
	mean	std	mean	std	mean	std	mean	std	mean	std	mean	std	mean	std	mean	std	mean	std
Region 1	73.4	—	79.0	17.0	80.2	12.4	59.8	—	—	—	68.4	15.3	85.7	—	—	—	85.9	12.6
Region 2	60.8	—	60.0	26.0	69.1	22.0	48.5	—	—	—	56.1	21.2	67.8	—	—	—	71.9	26.2
Region 3	63.5	—	53.0	25.0	69.8	24.7	50.8	—	—	—	57.8	23.2	66.8	—	—	—	68.0	27.0

Table 3
CV Type used in the state-of-the-art approaches

	Approach 1	Approach 2	Approach 3
CV Type	20-fold	Leave-one-out	5-fold

Approach 1 is proposed by Buendia et al.[28], Approach 2 is proposed by Cordier et al.[29] and Approach 3 is proposed by Meier et al.[30]

References

[1] Stefan Bauer, Roland Wiest, Lutz-P Nolte, and Mauricio Reyes. A survey of MRI-based medical image analysis for brain tumor studies. *Physics in Medicine and Biology*, 58(13):R97, 2013.

[2] Nelly Gordillo, Eduard Montseny, and Pilar Sobrevilla. State of the art survey on MRI brain tumor segmentation. *Magnetic Resonance Imaging*, 31(8):1426–1438, 2013.

[3] Bjoern H Menze, Andras Jakab, Stefan Bauer, Jayashree Kalpathy-Cramer, Keyvan Farahani, Justin Kirby, Yuliya Burren, Nicole Porz, Johannes Slotboom, Roland Wiest, et al. The multimodal brain tumor image segmentation benchmark (BRATS). *IEEE Transactions on Medical Imaging*, 34(10):1993–2024, 2015.

[4] Marcel Prastawa, Elizabeth Bullitt, Sean Ho, and Guido Gerig. A brain tumor segmentation framework based on outlier detection. *Medical Image Analysis*, 8(3):275–283, 2004.

[5] Bjoern H Menze, Koen Van Leemput, Danial Lashkari, Marc-André Weber, Nicholas Ayache, and Polina Golland. A generative model for brain tumor segmentation in multi-modal images. In *Proceedings of International Conference on Medical Image Computing and Computer-Assisted Intervention (MICCAI 2010)*, pages 151–159. 2010.

[6] Hassan Khotanlou, Olivier Colliot, Jamal Atif, and Isabelle Bloch. 3D brain tumor segmentation in MRI using fuzzy classification, symmetry analysis and spatially constrained deformable models. *Fuzzy Sets and Systems*, 160(10):1457–1473, 2009.

[7] Ali Gooya, Kilian M Pohl, Michel Bilello, Luigi Cirillo, George Biros, Elias R Melhem, and Christos Davatzikos. GLISTR: glioma image segmentation and registration. *IEEE Transactions on Medical Imaging*, 31(10):1941–1954, 2012.

[8] Aaron E Lefohn, Joshua E Cates, and Ross T Whitaker. Interactive, GPU-based level sets for 3D segmentation. In *Proceedings of International Conference on Medical Image Computing and Computer-Assisted Intervention (MICCAI 2003)*, pages 564–572, 2003.

[9] Sean Ho, Lizabeth Bullitt, and Guido Gerig. Level-set evolution with region competition: automatic 3-D segmentation of brain tumors. In *Proceedings of IEEE International Conference on Pattern Recognition*, volume 1, pages 532–535, 2002.

[10] Ezequiel Geremia, Bjoern H Menze, Nicholas Ayache, et al. Spatial decision forests for glioma segmentation in multi-channel MR images. In *the MICCAI Challenge on Multimodal Brain Tumor Image Segmentation (BRATS 2012)*, volume 34, pages 14–17, 2012.

[11] S Reza and KM Iftekharuddin. Multi-class abnormal brain tissue segmentation using texture. In *the MICCAI Challenge on Multimodal Brain Tumor Image Segmentation (BRATS 2013)*, pages 38–42, 2013.

[12] Hien Nguyen, Vishal M Patel, Nasser M Nasrabadi, and Rama Chellappa. Kernel dictionary learning. In *Proceedings of IEEE International Conference on Acoustics, Speech and Signal Processing (ICASSP 2012)*, pages 2021–2024, 2012.

[13] Jinjun Wang, Jianchao Yang, Kai Yu, Fengjun Lv, Thomas Huang, and Yihong Gong. Locality-constrained linear coding for image classification. In *Proceedings of IEEE Conference on Computer Vision and Pattern Recognition (CVPR 2012)*, pages 3360–3367, 2010.

[14] Jayaraman J Thiagarajan, Karthikeyan Natesan Ramamurthy, et al. Kernel sparse models for automated tumor segmentation. *International Journal on Artificial Intelligence Tools*, 23(3), 2014.

[15] Jeon Lee, Seung-Jun Kim, Rong Chen, and Edward H Herskovits. Brain tumor image segmentation using kernel dictionary learning. In *Proceedings of IEEE International Conference on Engineering in Medicine and Biology Society (EMBC 2015)*, pages 658–661. IEEE, 2015.

[16] Xuan Chen, Binh P. Nguyen, Chee-Kong Chui, and Sim-Heng Ong. Automated brain tumor segmentation using kernel dictionary learning and superpixel-level features. In *Proceedings IEEE International Conference on Systems, Man, and Cybernetics (SMC 2016)*, page [to appear], Budapest, Hungary, 9–12 Oct 2016. IEEE.

[17] Jens Schneider and Rüdiger Westermann. Compression domain volume rendering. In *Proceedings of IEEE International Conference on Visualization (VIS 2003)*, pages 293–300, 2003.

[18] Mark Pauly, Markus Gross, and Leif P Kobbelt. Efficient simplification of point-sampled surfaces. In *Proceedings of IEEE International Conference on Visualization (VIS 2002)*, pages 163–170, 2002.

[19] Christian Conrad, Matthias Mertz, and Rudolf Mester. Contour-relaxed superpixels. In *International Workshop on Energy Minimization Methods in Computer Vision and Pattern Recognition*, volume 8081, pages 280–293, 2013.

[20] Nello Cristianini and John Shawe-Taylor. *An introduction to support vector machines and other kernel-based learning methods*. Cambridge University Press, 2000.

[21] Yagyensh Chandra Pati, Ramin Rezaiifar, and PS Krishnaprasad. Orthogonal matching pursuit: Recursive function approximation with applications to wavelet decomposition. In *Proceedings of The Twenty-Seventh Asilomar Conference on Signals, Systems and Computers*, pages 40–44, 1993.

[22] Carsten Rother, Vladimir Kolmogorov, and Andrew Blake. Grabcut: Interactive foreground extraction using iterated graph cuts. In *ACM Transactions on Graphics (TOG)*, volume 23, pages 309–314, 2004.

[23] Yuri Boykov, Olga Veksler, and Ramin Zabih. Fast approximate energy minimization via graph cuts. *IEEE Transactions on Pattern Analysis and Machine Intelligence*, 23(11):1222–1239, 2001.

[24] Vladimir Kolmogorov and Ramin Zabih. What energy functions can be minimized via graph cuts? *IEEE Transactions on Pattern Analysis and Machine Intelligence*, 26(2):147–159, 2004.

[25] Yuri Boykov and Vladimir Kolmogorov. An experimental comparison of min-cut/max-flow algorithms for energy minimization in vision. *IEEE Transactions on Pattern Analysis and Machine Intelligence*, 26(9):1124–1137, 2004.

[26] Nicholas J Tustison, Brian B Avants, et al. N4ITK: improved N3 bias correction. *IEEE Transactions on Medical Imaging*, 29(6):1310–1320, 2010.

[27] László G Nyúl, Jayaram K Udupa, and Xuan Zhang. New variants of a method of MRI scale standardization. *IEEE Transactions on Medical Imaging*, 19(2):143–150, 2000.

[28] Patricia Buendia, Thomas Taylor, Michael Ryan, and Nigel John. A grouping artificial immune network for segmentation of tumor images. In *the MICCAI Challenge on Multimodal Brain Tumor Image Segmentation (BRATS 2013)*, pages 1–5, 2013.

[29] Nicolas Cordier, Bjoern Menze, Hervé Delingette, and Nicholas Ayache. Patch-based segmentation of brain tissues. In *the MICCAI Challenge on Multimodal Brain Tumor Image Segmentation (BRATS 2013)*, pages 6–17, 2013.

[30] Raphael Meier, Stefan Bauer, Johannes Slotboom, Roland Wiest, and Mauricio Reyes. A hybrid model for multimodal brain tumor segmentation. In *the MICCAI Challenge on Multimodal Brain Tumor Image Segmentation (BRATS 2013)*, pages 31–37, 2013.

Novel LPV-based Control Approach for Nonlinear Physiological Systems

György Eigner

Physiological Controls Research Center
Research and Innovation Center of Óbuda University
Kiscelli u. 82, H-1032 Budapest, Hungary
eigner.gyorgy@nik.uni-obuda.hu

Abstract: The current paper introduces a novel controller design approach dealing with the control of affine Linear Parameter Varying (LPV) systems using the abstract mathematical properties of the LPV parameter space and classical state-feedback design. By the designed controller structure the parameter dependent LPV system mimics a given selected reference LTI system reaching given performance specifications originally prescribed for the reference LTI system. Further, the actual feedback gains are calculated by comparison to the reference control gains - thus, realizing a "relative control". The method is demonstrated on given nonlinear biomedical problems with simulation results under MATLAB.

Keywords: LPV model; Affine LPV; qLPV; Physiological control

1 Introduction

Nonlinear controller design is a challenging task even using current increased computational power. Although the physical reality is mostly nonlinear, the most widely used controller design approaches are based on linear controller design methodologies providing particular solutions around the favorable operating range of the original systems. In the last decade, different controller design solutions appeared trying to describe and handle the whole operation range of the nonlinear systems based on optimization, iteration or else and they exploited the possibilities of the increased numerical calculation capacities [1].
The recently developed Robust Fixed Point Transformation (RFPT)-based controller design [2] uses inverse kinematics and dynamics to accurately approximate the system to be controlled and formalize the control task as a fixed point problem. If the conditions are satisfied through the convergence of Cauchy series in the Banach-space the controller adapts itself to the requirements of the system along the predefined performance specification [2].
Significant direction is the usage of the Lyapunov stability theorems combined with Linear Parameter Varying (LPV) methodology, as the conditions of the stability are

defined as Linear Matrix Inequalities (LMI) and the solutions, namely, the appropriate controllers can be calculated through advanced LMI-optimization tools [3]. This direction is represented by the Tensor Product (TP) transformation based controller design which originates from the Fuzzy theorem and uses the LPV-LMI optimization methods [4].
The current research work focuses to an other direction, namely, how can be used the mathematical properties of the LPV parameter space in controller design regarding the classical state feedback control in such a way that the completed controller structure handles the LPV system and through the original nonlinear system. This approach does not require convex LMI optimization neither inverse kinematics, however, it can provide global stability.
The paper is structured, as follows: first we introduce the affine LPV systems and the classical state feedback approaches; after, we present the proposed novel control scheme; then the method is demonstrated via a nonlinear biomedical problems; finally, we conclude the results of the research.

2 Affine LPV Configuration

The affine LPV configuration originates from the Linear-Time Invariant (LTI) and Variant (LTV) systems. The classical state-space representation of an LTI system can be described as:

$$\begin{aligned} \dot{x}(t) &= Ax(t) + Bu(t) + Ed(t) \\ y(t) &= Cx(t) + Du(t) + D_2d(t) \end{aligned} , \tag{1}$$

where $A(t) \in \mathbb{R}^{n\times n}$ is the state matrix, $B(t) \in \mathbb{R}^{n\times m}$ and $E(t) \in \mathbb{R}^{n\times l}$ are the control and disturbance input matrices, $C(t) \in \mathbb{R}^{p\times n}$ is the output matrix, $D(t) \in \mathbb{R}^{p\times m}$ and $D_2(t) \in \mathbb{R}^{p\times l}$ are the input and disturbance feed-forward matrices. The $x(t) \in \mathbb{R}^n$, $u(t) \in \mathbb{R}^m$, $d(t) \in \mathbb{R}^l$ vectors are the state, control and disturbance input vectors.
Similar to LTI systems, the parameter dependent affine LPV systems can be described easily with their general state-space representation:

$$\begin{aligned} \dot{x}(t) &= A(p(t))x(t) + B(p(t))u(t) + E(p(t))d(t) \\ y(t) &= C(p(t))x(t) + D(p(t))u(t) + D_2(p(t))d(t) \end{aligned} . \tag{2}$$

In this case, each matrix is a function of the parameter vector $p(t) \in \mathbb{R}^k$, which is a k-dimensional real time function and the elements of it are the scheduling variables - the preliminary selected functions of the given nonlinear system [3]. Thus, this configuration allows to handle the nonlinear system as a linear one by hiding the nonlinearity of the system inside the scheduling variables. Hence, by the use of LPV systems linear controller design methodologies can be applied on the nonlinear systems itself.
Among different representation of LPV systems, in the affine case the scheduling parameter is a function of the a state / states and these dependencies can be described

as follows [3]:

$$\begin{array}{ll} A(p(t)) = A_0 + \sum_{i=1}^{k} p_i(t)A_i & B(p(t)) = B_0 + \sum_{i=1}^{k} p_i(t)B_i \\ E(p(t)) = E_0 + \sum_{i=1}^{k} p_i(t)E_i & C(p(t)) = C_0 + \sum_{i=1}^{k} p_i(t)C_i \\ D(p(t)) = D_0 + \sum_{i=1}^{k} p_i(t)D_i & D_2(p(t)) = D_{2,0} + \sum_{i=1}^{k} p_i(t)D_{2,i} \end{array} . \tag{3}$$

3 State Feedback and Gain-Scheduling Control

The idea of optimal state feedback control for LTI systems originates from the 1960s when the cost function based optimization appeared in modern control engineering. Over decades, different cost functions and feedback gain calculation techniques appeared like quadratic regulation, energy minimization, time minimization or tracking error minimization, etc. [5]. Regarding to LPV systems the first generation of gain scheduling control techniques were developed in the late 1990s [6, 7].
In case of state feedback control, the control signal occurs in the following form:

$$u(t) = -Kx(t) \ , \tag{4}$$

where $K \in \mathbb{R}^{m \times n}$ is the feedback gain matrix. K can be designed via different iteration-based methods. For example, in case of Linear-Quadratic (LQ) control, the control input of (4) minimizes the following cost function [8]:

$$J(u) = \int_0^{\infty} \left(x^T Qx + u^T Ru + 2x^T Nu\right) dt \ , \tag{5}$$

and the optimal gain K can be calculated by solving the control algebraic Ricatti equation [8]:

$$\begin{array}{l} A^T X + XA - (XB+N)R^{-1}(B^T X + N^T) + Q = 0 \\ K = R^{-1}(B^T S + N^T) \end{array} . \tag{6}$$

The optimal K gain provides better control performances through pole-placement of LTI systems. In general, this configuration modifies the open-loop A_{open} state matrix into $A_{closed} = A_{open} - BK$ via (4). The poles of the characteristic equation can be calculated, as follows:

$$\mid I\lambda - A + BK \mid = 0 \ . \tag{7}$$

In gain-scheduling control, which is a natural choice in case of affine LPV system, the optimal gain becomes parameter dependent [6]:

$$u(t) = -K(p(t))x(t) \ . \tag{8}$$

The class of $p(t)$ dependent controllers of (8) are similar with the class of $p(t)$ dependent system of (2). Since, the continuous controller design is impossible,

the reasonable choice is to divide the k dimensional parameter space into different slices. Hence, different controllers have to be designed for each slice and these controllers can handle the occurring LTI systems inside these slices. The drawback is the high computational capacity, complex switching schedule (as $p(t)$ varies over time) and the necessary advanced methods providing global stability.
Instead of this natural, however sometimes unmanageable configuration, the polytopic model configuration and polytopic controller design spread out in control engineering [3, 9–11].
In politopic cases, the number of necessary controllers are reduced. If, the parameter space is handled as a vector space and the occurring LTI systems ("system trajectory") are inside a given region of the vector space, a convex hull can be designed, which wraps the system trajectory. As a result, it is enough to design specified number of controllers to the determining point of the p-space. Thus, if the convexity properties are fulfilled, the resulting controller (as convex combination of the designed controllers) can handle each occurring LTI system inside the polytope [10, 11]. The benefits of these methods are the drawbacks at the same time: the necessary deep mathematical knowledge and understanding, high computational capacity. The global stability is only particularly true, i.e. if the system trajectory does not exit from the convex hull (the value of $p(t)$ cannot be higher or lower than the predefined values) [11, 12].

4 Novel, Specific Control Scheme

We have previously investigated the opportunities of using the mathematical properties of the parameter space in order to define norm-based performance markers for LPV systems and examined the general properties of models used in diabetes researches [11]. However, these properties can be observed in large number of physiological systems, as well:

- Input(s) are not affected by nonlinearities and do not have direct inputs-outputs connection (D and D_2 are persistent in time and zero matrices)
- Output(s) are not affected by nonlinearities
- Since the nonlinearities do not affect the inputs and the outputs, it is not necessary to select their elements as scheduling parameters, which means that B and C are independent from the parameter vector p; moreover, these are usually time-independent
- The nonlinearities only appear in the state matrix $A(p(t))$ regarding to the nonlinear system dynamics, nonlinear cross effects and nonlinear coupling; the patient variabilities mostly occur in the elements of A.

The necessity, which originally brought to life the LPV methods and theories was to handle the nonlinear systems as linear ones. Thus, each element of the time-dependent and nonlinear A should be selected as scheduling variable.

In our previous study [11], we have shown that every parameter dependent LPV system can be equivocally determined by the belonging parameter vector if the above statements are fulfilled. In other words, each p parameter vector (a point in the parameter space) belongs to an underlying LTI system $S(p)$, further, each $S(p)$ is equivocally determined by its corresponding p parameter vector.

4.1 Investigated LPV Model Class

Our investigation focuses on LPV systems that have parameter dependent elements only in their $A(p(t))$, as follows:

$$\begin{aligned} \dot{x}(t) &= A(p(t))x(t) + Bu(t) + Ed(t) \\ y(t) &= Cx(t) + Du(t) + D_2 d(t) \end{aligned} \quad . \tag{9}$$

If the parameter vector is persistent in time, the belonging parameter dependent LPV system can be simplified to an LTI system. Moreover, the vary of $p(t)$ realizes the system trajectory, which consist of infinite number of LTI systems. In this case, each points in the parameter space equivocally determines an underlying LTI system. This property allows to define different norms in the parameter space on the parameter vectors, however, most of them can be interpreted on the underlying LTI system.

In this study, we deal with this specific model class and the proposed controller design method is valid on this particular group of models (mostly true in case of physiological systems).

4.2 Mathematical Background

Definition 1. *Similarity of matrices [13]: A quadratic, $n \times n$ matrix A is similar to a matrix B, if an invertible C matrix exists that $A = C^{-1}BC$. Notation: $A \sim B$.*

The definition above has wide range of applications. Two of them can be found in the following theorems [13, 14]:

Theorem 1. *Similarity invariance of the determinants of matrices: If $A \sim B$, then $|A| = |B|$.*

Proof. Let $A \sim B$, namely, $A = C^{-1}BC$. Then $|A| = |C^{-1}BC| = |C^{-1}||B||C| = |B|$, since $|C||C^{-1}| = 1$ [13]. □

Theorem 2. *If $A \sim B$, then the characteristic polynomials of the matrices and thus, the eigenvalues and the geometric and algebraic multiplicities of the eigenvalues of the matrices are the same.*

Proof. Let $A \sim B$, namely, $A = C^{-1}BC$. Then $A - \lambda I = C^{-1}BC - \lambda C^{-1}IC = C^{-1}(BC - \lambda IC) = C^{-1}(B - \lambda I)C$, namely, $A - \lambda I \sim B - \lambda I$ [13]. □

These mathematical tools can be used to define eigenvalues equality rules for state feedback systems.

4.3 The Completed Feedback Gain Matrix

Let us define the compact form of (9):

$$\begin{pmatrix} \dot{x}(t) \\ y(t) \end{pmatrix} = \begin{pmatrix} A(p(t)) & B & E \\ C & D & D_2 \end{pmatrix} \begin{pmatrix} x(t) \\ u(t) \\ d(t) \end{pmatrix} = S(p(t)) \begin{pmatrix} x(t) \\ u(t) \\ d(t) \end{pmatrix} \quad , \tag{10}$$

where $S(p(t)) \in \mathbb{R}^{(n+p)\times(n+m+l)}$. When p is persistent in time, (10) simplifies to a LTI system, which is represented by S of (11).

$$\begin{pmatrix} \dot{x}(t) \\ y(t) \end{pmatrix} = S \begin{pmatrix} x(t) \\ u(t) \\ d(t) \end{pmatrix} \quad . \tag{11}$$

Each LPV system is dependent from the parameter vector $p(t)$, which may vary in time. As we mentioned earlier, this variation realizes a system trajectory $S(p(t))$ in the parameter space, which consist of infinite number of LTI systems. These LTI systems appear over time, during the variation of $p(t)$. The only difference between the occurred LTI systems are the different belonging parameter vectors, if the aforementioned requirements - each nonlinearity causing and time variant terms and variables have to be selected as scheduling parameter in order to avoid underlying differences, the nullspace problem, etc. [11] - are fulfilled.

From state feedback design point of view, without gain scheduling or other advanced techniques that would mean the need of infinite number of optimal gains to handle the occurring LTI systems (in continuous time), which is obviously impossible. However, if we want to apply the linear state feedback controller design techniques on the given LPV system, we can utilize this property, namely, the difference between the occurring LTI systems are only the values of the belonging parameter vectors.

In order to embed the "difference" into the controller scheme, we applied the results of our previous study [11]. In this study, we concluded that it is possible to use 2-norm based difference interpreted on the space of the parameter vector to define dissimilarities between LTI systems, which belong to given parameter vectors. For example, in case of two points a and b in the parameter space represented by "persistent" parameter vectors, the 2-norm based difference among these is:

$$e = ||p_a - p_b|| \quad . \tag{12}$$

This difference marker allows the description of the difference between arbitrary points in the parameter space, in other words, the dissimilarities among different belonging LTI system (e.g. in the above mentioned case the dissimilarity between $S(p_a)$ and $S(p_b)$. Moreover, it is possible to use $e(t)$ as a function of time, when we describe the difference between a reference point p_{ref} and the $p(t)$ and of course the dissimilarity between the belonging underlying LTI systems, $S(p_{ref})$ and $S(p(t)$.

In the followings a $2D$ parameter space example is presented: having two scheduling variables $p(t) \in \mathbb{R}^2$. During the operation of the system, the $p(t)$ varies over time from $p_{act}(t_0)$ to $p_{act}(t_n)$. It is possible to describe the 2-norm based difference between the reference point p_{ref} and actual parameter vector p_{act} (and actual dissimilarity between $S(p_{ref})$ and $S(p(t))$ by $e(t)$.

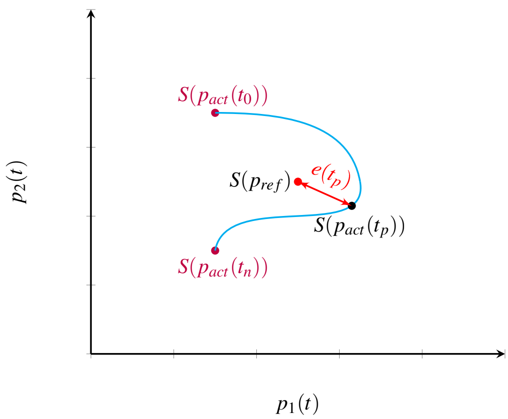

Figure 1
$2D$ example of the interpretation of the 2-norm based difference between a reference point (reference system) and the actual $p(t)$ (actual LTI system $S(p(t))$).

Let us define a reference point in the parameter space p_{ref}, which serves as the reference parameter vector and S_{ref} as its corresponding LTI reference system. Consequently classical state feedback design can be applied on S_{ref}. Generally, the goal of controller design in such methodologies is to provide optimal feedback gains as a result of an integral optimization process. The appearing optimal feedback gain has to stabilize the system, and to reach better properties for the system to be controlled. This should be done by the new poles of characteristic equation. Let us consider that K_{ref} is an eligible and optimal gain for the S_{ref} LTI system. In this case, the modified state matrix of the state-feedback reference system will be $A(p_{ref}) - BK_{ref}$ and the eigenvalues λ_{ref} can be calculated via solving the characteristic equation:

$$\mid I\lambda_{ref} - (A_{ref} - BK_{ref}) \mid = \mid I\lambda_{ref} - A_{ref} + BK_{ref} \mid = 0 \quad . \tag{13}$$

In the parameter space, each underlying parameter dependent LTI system $S(p)$ is unequivocally determined by its belonging parameter vector p. If, the dissimilarity between the parameter dependent LTI systems can be described by the 2-norm based difference of the parameter vectors (as we have seen earlier), then it is possible to use this connection to define such kind of unique, completed state feedback controller, which is designed for the reference LTI system $S(p_{ref})$; however, it can deal with each occurring LTI system $S(p(t))$ during operation. Moreover, if this completed controller can provide stability and good performance criteria for the reference system $S(p_{ref})$, it can provide the same properties for each occurring $S(p)$ (and the LPV system $S(p(t))$). On the other hand, that means that, if we have a nonlinear system, we can transform it to an LPV system and with this approach, we can design a controller handling this LPV and in ultimate sense, the nonlinear system itself.

First of all, we consider that the LPV system is in the form of (10); thus, only the state matrix $A(p(t))$ is parameter dependent. Let consider the closed-loop system matrix as follows:

$$A(p(t)) - B(K_{ref} + Ke(t)) \ , \tag{14}$$

where $e(t)$ is the 2-norm based difference between the p_{ref} and $p(t)$ and $K_{m \times n}$ is a continuously calculable gain. At this point, two main considerations are needed. The first, that this configuration has to provide the stability, namely, the state matrix (14) of the newly defined closed-loop system should have eigenvalues with negative real parts. The second, this criteria can be satisfied, if we apply a specific form of the above defined Theorem (1)-(2).

Let $A_{ref} + BK_{ref} \sim A(p(t)) - B(K_{ref} + Ke(t))$, which means that the eigenvalues of the two matrices are equal $\lambda(p_{ref}) = \lambda(p(t))$ at $\forall p(t)$, if $\lambda(p(t))$ is the eigenvalues of $(A(p(t)) - B(K_{ref} + Ke(t)))$. This is only possible, if the similarity transformation matrix is the $I_{n \times n}$ unity matrix. Namely, $A_{ref} - BK_{ref} = I^{-1}(A(p(t)) - B(K_{ref} + Ke(t)))I$, i.e. the introduced completed gain has to provide the "smoother" similarity, but also the "strict" equality criteria. Shortly, the proposed completed feedback gain $K_{ref} + Ke(t)$ has to provide the equality of not just the eigenvalues $\lambda(p_{ref}) = \lambda(p(t))$, but also the equality of the matrices, as well:

$$A_{ref} - BK_{ref} = A(p(t)) - B(K_{ref} + Ke(t)) \ . \tag{15}$$

4.4 Consequences, Controller Design and Limitations

Let us consider that $p(t)$ can be measured or estimated. In this case, the only unknown in matrix in (15) is K. By rearranging (15), the K can be calculated at every $p(t)$:

$$K = \frac{B^{-1}(A_{ref} - BK_{ref} - A(p(t)) + BK_{ref})}{e(t)} = \frac{B^{-1}(A_{ref} - A(p(t)))}{e(t)} \tag{16}$$

In this way:

$$\begin{aligned} &A(p(t)) - B(K_{ref} + Ke(t)) = \\ &A(p(t)) - B\left(K_{ref} + \frac{B^{-1}(A_{ref} - BK_{ref} - A(p(t)) + BK_{ref})}{e(t)} e(t)\right) \ , \end{aligned} \tag{17}$$

such a controller structure appears, which can provide that the LPV system $S(p(t))$ is going to behave as the feedback controlled LTI reference system $S(p_{ref})$ itself, regardless from the actual value of $p(t)$. Shortly, the LPV system will mimic the feedback controlled reference LTI system.

Figure 2 demonstrates the completed control loop in compact form - which is necessary to realize this idea in practice. Since, we considered that $p(t)$ can be measured or estimated, the 2-norm based difference is available at any time.

At this point, we can summarize the main steps which are needed in order to realize the proposed controller design method:

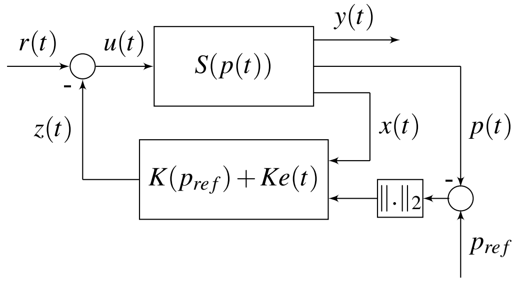

Figure 2
Feedback control loop with completed gain

1. Realize and validate the LPV models in appropriate form (from the original nonlinear model),
2. Select the reference point p_{ref}, which determines $S(p_{ref})$ reference system in accordance to the needs of reality; namely, the selection of such a reference LTI $S(p_{ref})$ system is needed, which can provide the best operating results from the given application point of view.
3. State feedback controller design via linear controller design method in order to realize the optimal K_{ref} gain for the $S(p_{ref})$ system.
4. Design of the eligible controller scheme, including the appropriate form of (16).
5. Realize of the control environment.

Through the above mentioned points, the controller design is possible and easy to handle. This novel method may provide another controller design possibility then gain scheduling or LPV-LMI based approaches, but have limitation as well:

1. In this point, we summarized the considerations so far, which are needed in order to use this controller design approach: the nonlinear system should be given in form of (10) or has to be transformed to this term; only the $A(p(t))$ can be parameter dependent in (10); $p(t)$ should be measurable or estimable; $S(p_{ref})$ should be a well selected reference LTI system from the given application point of view. Each nonlinear system which is state-space represented, can be transformed to the form of (10), if the nonlinearities are connected to the selected state variables.
2. The invertibility of B is a key point. Generally, $B_{n\times m}$ is not a square matrix and occasionally contains dependent linearly columns, as well. Here we have three cases: (*i*) B is square matrix and invertible; (*ii*) B is not a square matrix, however, does not contain linearly dependent columns; (*iii*) B is not square matrix and does contain linearly dependent columns. In the first (*i*) case, B is invertible and (16) can be used to calculate K. For the second (*ii*) case, if B is not a square matrix, but linearly independent, the left hand side matrix multiplication of B with B^T can be a solution. In this manner, the completion

of (15)-(16) is necessary, as follows:

$$\begin{aligned} &A_{ref} - BK_{ref} = A(p(t)) - B(K_{ref} + Ke(t)) \\ &(A_{ref} - BK_{ref} - A(p(t)) + BK_{ref}) = BKe(t)) \\ &B^T(A_{ref} - A(p(t))) = B^T BKe(t)) \\ &K = \frac{(B^T B)^{-1} B^T (A_{ref} - A(p(t)))}{e(t)} \end{aligned} , \tag{18}$$

where the $B^T B$ term becomes now a square matrix and without linear dependency among the columns of it is invertible. The most unfavorable case is the third (*iii*) case when B is not a square matrix and does have linearly dependency. In this case, $B^T B$ may be singular. However, with other techniques like singular value decomposition (SVD) [14], $B^T B$ can be approximated or through Gram-Schmidt orthogonalization method [15], the $B^T B$ can be transformed such that the linear dependency can be eliminated. However, if these techniques are not usable the K in form of (16) cannot be calculated, only BK can be calculated.

3. The third important point is the question of singularity. When the reference point p_{ref} and the actual parameter vector $p(t)$ are equal to each other, $e(t) = 0$, which causes that K of (16) becomes infinite. In order to avoid this situation in practice, a condition should be embedded into the calculation of K via (19):

$$K = \begin{cases} 0 & \text{if } -\varepsilon < e(t) < \varepsilon \\ \dfrac{B^{-1}(A_{ref} - A(p(t)))}{e(t)} & \text{otherwise} \end{cases} , \tag{19}$$

where ε is a real number. If, $e(t) = 0$ it means $p_{ref} = p(t)$ and $S(p_{ref}) = S(p(t))$; in other words, for those LTI systems where $p(t)$ is near to p_{ref}, namely, $S(p(t))|_{-\varepsilon<e(t)<\varepsilon}$ we apply only the K_{ref} feedback gain. However, the goal is to avoid singularity, hence ε can be as small as numerically does not cause problems during the calculations. Rationally, the K_{ref} gain is the optimal gain for $S(p_{ref})$ LTI system. In the small "environment" of $S(p_{ref})$, when $S(p(t))$ is near to equal $S(p_{ref})$, the K_{ref} is able to handle the system $S(p(t))|_{-\varepsilon<e(t)<\varepsilon}$ (provide stability, etc.), however, approximation error can be occur.

In the following section, we demonstrated the proposed methodology in case of different models between various circumstances.

5 Case Studies

Two different control examples are examined on nonlinear models to demonstrate the applicability of the presented method. The examinations are made alongside the aforementioned main steps:

1. Realization and validation of valid LPV models in appropriate form
2. Design of the eligible controller scheme

3. Realization of the control environment

5.1 Control of a Simple Nonlinear System

First the demonstration is done on a simply "academic"'nonlinear system without input-output limitations, where each state variables can be considered outputs as well. The system dynamics are described with the following equations:

$$\begin{aligned} \dot{x}_1(t) &= x_1(t)x_2(t) + u_1(t) \\ \dot{x}_1(t) &= -2x_2(t) + 4\sqrt{x_3(t)}x_2(t) + u_2(t) \\ \dot{x}_1(t) &= -2x_3(t) + u_3(t) \end{aligned} \quad . \tag{20}$$

Selecting $x_1(t)$ and $\sqrt{x_3(t)}$ as scheduling variables, i.e. $p(t) = [x_1(t), \sqrt{x_3(t)}]^T$ the equation can be written in form of (9):

$$\begin{pmatrix} \dot{x}_1(t) \\ \dot{x}_2(t) \\ \dot{x}_3(t) \end{pmatrix} = A(p(t)) \begin{pmatrix} x_1(t) \\ x_2(t) \\ x_3(t) \end{pmatrix} + B \begin{pmatrix} u_1(t) \\ u_2(t) \\ u_3(t) \end{pmatrix} \quad , \tag{21}$$

where $A(p(t)), B, C$ and D are, if the output is x_1:

$$A(p(t)) = \begin{bmatrix} 0 & 0 & 0 \\ 0 & -2 & 0 \\ 0 & 0 & -2 \end{bmatrix} + \begin{bmatrix} 0 & 1 & 0 \\ 0 & 0 & 0 \\ 0 & 0 & 0 \end{bmatrix} p_1(t) + \begin{bmatrix} 0 & 0 & 0 \\ 4 & 0 & 0 \\ 0 & 0 & 0 \end{bmatrix} p_2(t) \tag{22}$$

and

$$B = \begin{bmatrix} 1 & 0 & 0 \\ 0 & 1 & 0 \\ 0 & 0 & 1 \end{bmatrix} \quad C = \begin{bmatrix} 1 & 0 & 0 \end{bmatrix} \quad D = \begin{bmatrix} 0 & 0 & 0 \end{bmatrix} \ . \tag{23}$$

We considered that there is no disturbance in the system. Considering $p_{ref} = [-1, 1]^T$ the reference point, the underlying LTI state matrix $A_{p_{ref}}$ becomes:

$$A_{p_{ref}} = \begin{bmatrix} 0 & -1 & 0 \\ 4\sqrt{1} & -2 & 0 \\ 0 & 0 & -2 \end{bmatrix} \ . \tag{24}$$

The eigenvalues of $A_{p_{ref}}$ are $\lambda_{ref} = [-1 \pm 1.7321i, -2]$ meaning that the reference LTI system is stable. However, the higher imaginary parts may cause higher oscillations in the answer of the system.

In order to realize the completed controller structure, the last missing part is the reference gain K_{ref}, the optimal feedback gain for $S(p_{ref})$. We found that the rank of the controllability matrix was 3, i.e. the system is controllable ($n = 3$). We designed an LQ regulator via the MATLAB embedded *lqr* order. Our goal was to only to introduce the completed controller design method; hence, we did not focus on the selection of Q and R. Thus, we applied a standard rule during selection of Q and R:

$Q = C^T C$ and $R = I_m$ (unity matrix). In the given circumstances we concluded that the reference feedback gain was equal to:

$$K_{ref} = \begin{bmatrix} 0.436 & -0.1 & 0 \\ -0.1 & 0.0469 & 0 \\ 0 & 0 & 0 \end{bmatrix} . \tag{25}$$

With this K_{ref}, the eigenvalues of the closed-loop reference state matrix $A(p_{ref}) - BK_{ref}$ are $\lambda_{ref,closed} = [-1.2415 \pm 1.7439i, -2]$, which means that with this Q and R the K_{ref} causes only a small improvement in the eigenvalues (smaller real and imaginary parts).

We have applied reference compensation, namely set-point control to determine the steady state values of the states. However, as $A(p(t))$ is parameter dependent and vary in time, the necessary compensator has to follow these changes. The parameter dependent compensator matrices can be calculated as follows [8]:

$$\begin{bmatrix} A(p(t)) \\ B \end{bmatrix} \begin{bmatrix} N_x \\ N_u \end{bmatrix} = \begin{bmatrix} O_{n\times m} \\ I_m \end{bmatrix} \rightarrow \begin{bmatrix} N_x \\ N_u \end{bmatrix} = \begin{bmatrix} A(p(t)) \\ B \end{bmatrix}^{-1} \begin{bmatrix} O_{n\times m} \\ I_m \end{bmatrix} , \tag{26}$$

where $O_{n\times m}$ is the zero matrix, while I_m the unity matrix. The applied reference was persistent in time, with values of $r = [10, 15, 14]^T$ and the initial state values were $x_0 = [20, 20, 20]^T$. In order to avoid singularity during calculation of K, we applied $\varepsilon = 1e-5$ limit ($-1e-5 < e(t) < 1e-5 \rightarrow K = K_{ref}$, otherwise K is calculated as in (16).

Results can be seen on Fig. 3. The upper left figure shows the changing of the state variables of the reference LTI system $S(p_{ref})$ in time, while the top right figure shows the changing of the state variables of the LPV system $S(p(t))$ in time. The lower left diagram shows the error between the system. Since, the order is 1e-14, only numerical calculation error can be seen between the systems during operation. The lower right diagram shows the parameter space. The p_{ref} is the reference parameter vector, the $p_{par,start}$ and $p_{par,end}$ is the starting and ending points of $p(t)$ parameter vector.

One can see that the completed controller works well and the parameter dependent LPV system mimics the behavior of the reference LTI system regardless from the variation of $p(t)$ over time.

5.2 Control of Nonlinear Compartment Model

In this example we demonstrated our controller solution in case of physiological compartmental models with high nonlinearities. Compartmental modeling is extremely useful and widely used in modeling of physiological systems [16]. Since, this example system can be handled as a physiological system, we tried the operation of the controller with ”high” saturations.

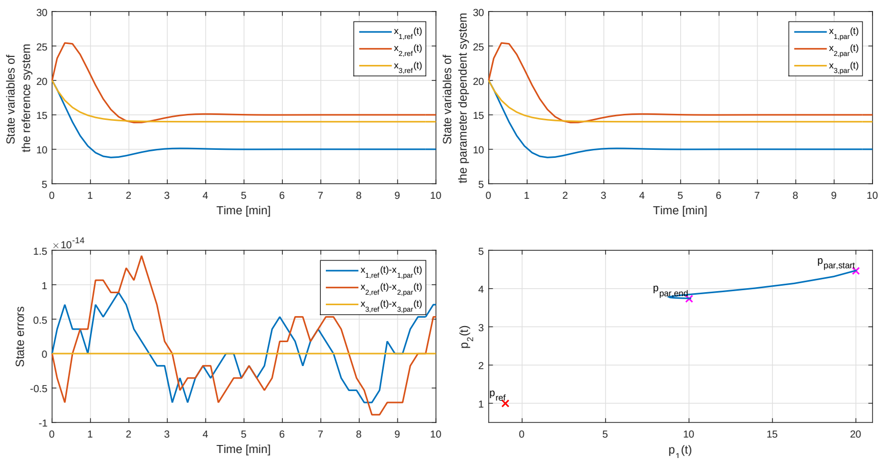

Figure 3
Result of the simulations

Consider an arbitrary compartmental model given by the following equations:

$$\begin{aligned} \dot{x_1}(t) &= -k\frac{x_1(t)}{1+ax_1(t)} + bx_2(t) - c(x_2(t)+z)x_1(t) + \frac{u_1(t)}{V_1} \\ \dot{x_2}(t) &= -k\frac{x_2(t)}{(1+dx_2(t))} - bx_2(t) + \frac{u_2(t)}{V_2} \end{aligned}, \tag{27}$$

where $a = 0.4$ [L/mmol], $b = 0.1$ [1/min], $c = 0.5$ [1/min], $d = 0.005$ [L/mmol], $k = 0.8$ [1/min], $z = 0.1$ [mmol/L], V_1=2 [L] and V_2=1 [L]. The $x_1(t)$ and $x_2(t)$ are the states and u_1 and u_2 [mmol/min] are the inputs. The model has three nonlinearities: the natural degradations of the compartments are loaded with Michaelis-Menten-type saturations and x_2 has a coupling to an output of x_1. Figure 4 shows the graphical representation of the model.

The selected scheduling variables are $p = \left[\frac{k}{1+ax_1(t)}, x_2(t)+z, \frac{k}{1+dx_2(t)}\right]^T$. Similarly to (20)-(21), the state-space representation of the LPV system can be written, as follows (x_1 and x_2 are considered outputs as well):

$$\begin{aligned} \begin{pmatrix} \dot{x}_1(t) \\ \dot{x}_2(t) \end{pmatrix} &= A(p(t)) \begin{pmatrix} x_1(t) \\ x_2(t) \end{pmatrix} + B \begin{pmatrix} u_1(t) \\ u_2(t) \end{pmatrix} \\ A(p(t)) &= \begin{bmatrix} 0 & b \\ 0 & -b \end{bmatrix} + \begin{bmatrix} -1 & 0 \\ 0 & 0 \end{bmatrix} p_1(t) + \begin{bmatrix} 0 & 0 \\ -c & 0 \end{bmatrix} p_2(t) + \begin{bmatrix} 0 & 0 \\ 0 & -1 \end{bmatrix} p_3(t) \quad . \\ B &= \begin{bmatrix} 1/V_1 & 0 \\ 0 & 1/V_2 \end{bmatrix} \quad C = \begin{bmatrix} 1 & 1 \end{bmatrix} \quad D = \begin{bmatrix} 0 & 0 \end{bmatrix} \end{aligned} \tag{28}$$

The selected reference parameter vector is $p_{ref} = [0.6667, 0.6, 0.64]^T$ (where $[x_{1,d}, x_{2,d}]^T =$

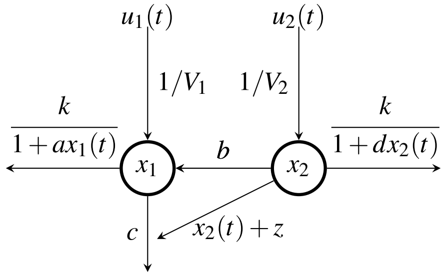

Figure 4
Nonlinear compartmental model

$[0.5, 0.5]^T$). At the reference point, the $A(p_{ref})$ is equal to:

$$A(p_{ref}) = \begin{bmatrix} -0.6697 & 0.1 \\ 0 & -0.74 \end{bmatrix} . \tag{29}$$

and the eigenvalues of the $A(p_{ref})$ are $\lambda = [-0.6697, -0.74]^T$, i.e. the reference LTI system is stable, however, the poles are close to zero. The rank of the controllability matrix is 2, i.e. the reference LTI system is controllable ($n = 2$). We used the MATLAB *care* order to design the K_{ref} gain beside $Q = I_2$ (unity matrix) and $R = 0.01I_2$. The obtained result is:

$$K_{ref} = \begin{bmatrix} 8.7493 & 0.058 \\ 0.1161 & 9.2883 \end{bmatrix} . \tag{30}$$

This K_{ref} provides that the eigenvalues of the closed-loop reference state matrix $A(p_{ref}) - BK_{ref}$ are $\lambda_{ref,closed} = [-5.046, -10.0267]^T$ - which is a good improvement, since the new eigenvalues are much far from zero. The completed controller structure will provides that the parameter dependent LPV system's closed-loop state matrix will be equal to $\lambda_{ref,closed}$ regardless from the actual value of $p(t)$. From here, K can be calculated at each iteration as (19).
We applied the same reference compensation as in the previous example. In order to realize this, we used (26) to calculate the compensator matrices at each iterations during operation. The selected reference levels were $r = [8, 7]^T$, the initial states $x_0 = [20, 10]^T$ and the selected bound in order to avoid singularity was $\varepsilon = 1e-5$ during calculation of K based on (19).
The results can be seen on Fig. 5. The upper left diagram shows the change of the state variables of the reference LTI system $S(p_{ref})$ over time, while the upper right diagram represents the simulation results over time of the state variables of the parameter dependent LPV system $S(p(t))$. The difference (error) between them is represented by the lower left diagram. However, as the $p(t)$ varies over time (as the lower right diagram shows), there is only numerical difference between the states of $S(p_{ref})$ and $S(p(t))$. That means, the LPV system and indirectly, the original nonlinear system, precisely mimics the behavior of the reference LTI system over time. Since, the given example is a physiological one, we tried the accuracy of the proposed controller structure, if there is a saturation on the control input, which

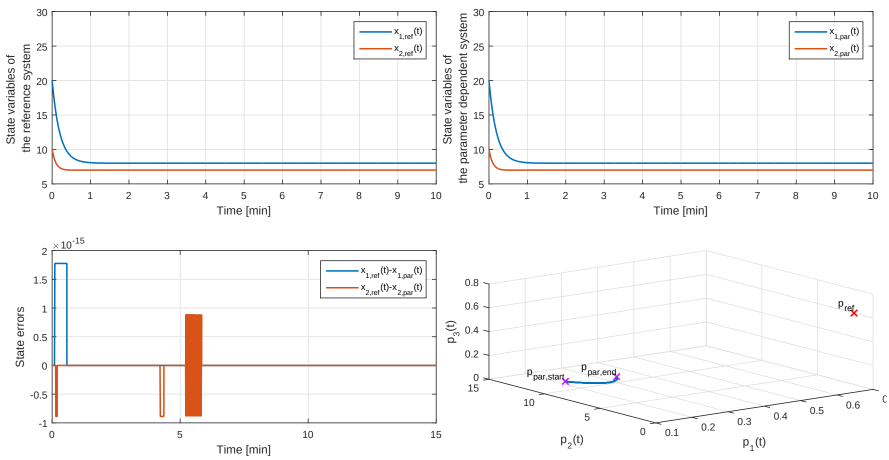

Figure 5
Results of the simulation without control input saturations

does not allow the occurrence of physiological not relevant control inputs (control inputs only can be positive or has to be higher than a given amount). We have found that the results are different than the previous case, which mostly come from that fact, that the selected scheduling variables are dependent from the actual values of the states. Namely, the state variables are coupled to the $S(p(t))$ through the $p(t)$. However, we did not use any saturation on the values of the state variables to compensate the effect of the saturation.
Figure 6 represents this latter scenario, when saturation is applied. Each parameter turned to be the same during the simulation, except that we consider that the input signal cannot be negative at all. The results shows that there is a difference between the states of $S(p_{ref})$ and $S(p(t))$ over time. However, the controller can handle the situation and can provide stable control for $S(p(t))$. The difference is slowly decreasing and the state variables reach the predefined reference levels.

Conclusions

In this paper we introduced a novel LPV-based controller design approach. This method provides a mixture of classical, optimal state-feedback control and a supplementary control, which is based on the 2-norm difference between parameter vectors (and belonging parameter dependent LTI systems) of the LPV parameter space. The main advantage of the proposed controller structure is that it is sufficient to design a reference controller for a reference LTI system and the actual, necessary control action, over time, will be determined by comparison to this reference controller through algebraic manipulations. Moreover, the LPV system will mimic the behavior of the reference system over time, requiring an appropriately selected reference LTI system. The completed controller can thus guarantee the stability of the system. Moreover, it is enough to determine performance specifications only for the reference LTI system - due to the completed controller forces, the LPV system will aquire these specifications, as well.

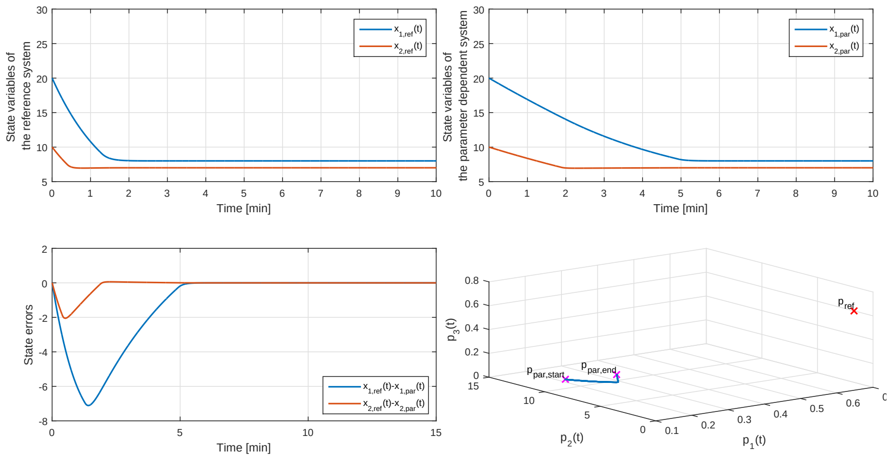

Figure 6
Results of the simulation with control input saturations

Acknowledgement

Gy. Eigner thankfully acknowledge the support of the Robotics Special College of Óbuda University. The research was supported by the Research and Innovation Center of Óbuda University.

References

[1] W. S. Levine. *The Control Engineering Handbook*. CRC Press, Taylor and Francis Group, Boca Raton, 2nd edition, 2011.

[2] J. K. Tar, J. F. Bitó, L. Nádai, and J. A. T. Machado. Robust Fixed Point Transformations in Adaptive Control Using Local Basin of Attraction. *ACTA Polytechnica Hungarica*, 6(1):21–37, 2009.

[3] A. P. White, G. Zhu, and J. Choi. *Linear Parameter Varying Control for Engineering Applicaitons*. Springer, London, 1st edition, 2013.

[4] P. Baranyi, Y. Yam, and P. Varlaki. *Tensor Product Model Transformation in Polytopic Model-Based Control*. Series: Automation and Control Engineering. CRC Press, Boca Raton, USA, 1st edition, 2013.

[5] R. S. Burns, editor. *Advanced Control Engineering*. Butterworth-Heinemann, Oxford, UK, 1st edition, 2001.

[6] D. J. Leith and W. E. Leithead. Survey of gain-scheduling analysis design. *International Journal of Control*, 73:1001–1025, 1999.

[7] D.W. Gu, P.H. Petkov, and M.M. Konstantinov. *Robust Control Design with Matlab*. Springer, London, UK, 2nd edition, 2013.

[8] W. S. Levine, editor. *The Control Engineering Handbook*. CRC Press, Taylor and Francis Group, Boca Raton, USA, 2 edition, 2011.

[9] O. Sename, P. Gáspár, and J. Bokor. Robust control and linear parameter varying approaches, application to vehicle dynamics. volume 437 of *Lecture Notes in Control and Information Sciences*. Springer-Verlag, Berlin, 2013.

[10] L. Kovács, B. Benyó, J. Bokor, and Z. Benyó. Induced l_2-norm minimization of glucose–insulin system for type I diabetic patients. *Comput. Meth. Prog. Bio.*, 102(2):105 – 118, 2011.

[11] Gy. Eigner, J. K. Tar, I. Rudas, and L. Kovács. LPV-based quality interpretations on modeling and control of diabetes. *ACTA Polytechnica Hungarica*, 13(1):171 – 190, 2016.

[12] J. Kuti, P. Galambos, and P. Baranyi. Minimal volume simplex (mvs) convex hull generation and manipulation methodology for tp model transformation. *Asian Journal of Control*, 2015. submitted.

[13] F. Wettl. *Linear Algebra [in Hungarian]*. Budapest University of Technology and Economy, Faculty of Natural Sciences, Budapest, Hungary, 1nd edition, 2011.

[14] R. A. Beezer. *A First Course in Linear Algebra*. Congruent Press, Washington, USA, version 3.40 edition, 2014.

[15] J. K. Tar, L. Nádai, I. Felde, and I. J. Rudas. *Advances in Robot Design and Intelligent Control: Proceedings of the 24th International Conference on Robotics in Alpe-Adria-Danube Region (RAAD)*, chapter Cost Function-Free Optimization in Inverse Kinematics of Open Kinematic Chains, pages 137–145. Springer International Publishing, 2016.

[16] J. D. Bronzino and D. R. Peterson, editors. *The Biomedical Engineering Handbook*. CRC Press, Boca Raton, USA, 4th edition, 2016.

Clinical Feature Classification for Chronic Heart Failure and Construction of a Safe Mechanism for Rehabilitation using Internet-of-Medical-Thing Devices

Shao-Jie Hsu, Shih-Syun Lin, Tun-Wen Pai

Department of Computer Science and Engineering, National Taiwan Ocean University, No. 2, Peining Rd., Keelung 202, Taiwan
e-mail: twp@mail.ntou.edu.tw

Chao-Hung Wang, Min-Hui Liu

Heart Failure Research Center, Division of Cardiology, Department of Internal Medicine, Chang Gung Memorial Hospital (Keelung), No. 222, Maijin Rd., Keelung 204, Taiwan
e-mail: bearty@cgmh.org.tw

Chi-Wen Cheng

Division of Cardiology, Department of Internal Medicine, Chang Gung Memorial Hospital (Keelung), No. 222, Maijin Rd., Keelung 204, Taiwan
e-mail: chyiwen@cgmh.org.tw

Dong-Yi Chen

Division of Cardiology, Department of Internal Medicine, Chang Gung Memorial Hospital (Linkou), No. 5, Fuxing St., Taoyuan 333, Taiwan
e-mail: dongyi70@cgmh.org.tw

Kuo-Li Pan

Division of Cardiology, Department of Internal Medicine. Chang Gung Memorial Hospital (Chiayi), No. 6, Sec. West, Jiapu Rd., Puzih City, Chiayi 613, Taiwan
e-mail: q12070@cgmh.org.tw

Shyh-Ming Chen

Division of Cardiology, Department of Internal Medicine, Chang Gung Memorial Hospital (Kaohsiung), No. 123, Dapi Rd., Kaohsiung 833, Taiwan
e-mail: syming99@cgmh.org.tw

Abstract: Heart failure (HF) is a complex syndrome without an objective definition. It has become a serious problem in public health policies because of the increased prevalence, high cost of treatment, frequent re-hospitalization and high mortality. Neither strict standards for HF classification nor single-type treatments are currently available. The non-specific clinical symptoms make diagnosis at early stages difficult, leading to deterioration and hospitalization. The use of advanced medical techniques and newly developed medicines may decrease mortality, but many HF patients still have a low quality of life because of insufficient muscular endurance and limited activities. Recent reports have shown that exercise programs contribute to the recovery of cardiac functions and improve clinical results for most HF patients. However, excessive, intense exercise may increase the risk of death, particularly for cardiac-related patients. In this study, different HF types are categorized and a safe, customized mechanism for self-exercise training integrating Internet-of-Medical-Thing devices and cloud computing technologies is proposed. The detected biometric features of the HF patients are linked to the personal communication devices of the patients and doctors, a cloud server system and the hospital medical information system. The proposed system mainly collects heart rate and metabolic equivalent features in a real-time manner from the Internet-of-Medical-Thing devices worn by patients. Measured data are dynamically compared to customized maximum limitations that are defined by rehabilitation physicians according to the patient's cardio-pulmonary exercise testing record in the hospital. A prototype system was successfully developed and validated with several test cases and showed excellent performance at an affordable cost. The proposed mechanism provides a customized platform for HF patients to pursue a better quality of life, based on prognostic exercise prescription using a safe self-exercise training mechanism.

Keywords: chronic heart failure; ejection fraction; heart rate; metabolic equivalent; Internet-of-Medical-Thing

1 Introduction

1.1 Epidemiology and Symptom of Heart Failure

Heart failure (HF) is a complex, irreversible, costly, and high-mortality disease that is becoming an increasing health problem affecting public health policies worldwide. Epidemiologic studies have described the critical social burden of HF because of its high prevalence, frequent rehospitalization rates, and high healthcare costs [1]. For example, more than 5 million people reportedly suffer from HF in the United States, and more than 30 billion dollars are required for medical treatment of HF patients each year [2]. The prevalence of HF in the Taiwanese population is as high as 16% for elderly people (age greater than 65 years) and annual reports of health statistics have shown that heart-related diseases have become the second leading cause of death in recent years [3]. Similar to that in other countries, the health budget burden from frequent rehospitalization caused by HF-related diagnoses is significantly increased. The cost of hospitalization for HF patients has increased by an average of 5.5% over the past decade in Taiwan. This may be because of the success of thrombolysis and intravascular stent therapies, which have greatly increased the survival rates of myocardial infarction patients in recent years. However, all heart-related diseases and most chronic diseases can progressively become an epidemic of heart failure and create a major public health problem worldwide [4]. Despite the development of advanced medications and surgical therapies for HF patients, HF remains a progressive, irreversible, and ultimately fatal disease over a short period because of poor prognosis.

The general symptoms of HF are associated with progressive conditions of fatigue and dyspnea, and limit the daily activities of patients, resulting in serious invisible disabilities [5]. However, the symptoms of HF are not obvious at earlier stages, and patients often ignore common symptoms such as asthma or breathing problems. Thus, HF patients at risk are frequently reluctant to seek medical assistance until they are in serious conditions or in a late-stage. Another challenge is that HF symptoms are quite variable, such as abnormal breathing conditions, dyspnea, fatigue, leg edema, difficulty sleeping, loss of appetite, coughing with phlegm or mucus foam, memory loss, and confusion. HF is a complex syndrome without a simple objective definition and is easily misdiagnosed like other chronic diseases, limiting the opportunity for early therapies.

1.2 Major Categories of HF Disease

Accurate diagnosis of HF enables appropriate management and greater benefit from early treatment for HF patients. In this study, we initially divided HF patients into five major groups including systolic, diastolic, valvular, atrial fibrillation, and non-specified HF types. Systolic HF is very common in male patients and those with ischemic heart diseases [6]. Clinically, we used an ejection fraction (EF) of 50% in the left ventricle as a threshold [7]. Valvular heart disease is characterized by damaged conditions or a defect in one of the four heart valves: mitral and aortic valves in the left heart and tricuspid and pulmonary valves in the right heart. Normal functioning valves ensure that blood flows with proper force, direction, and time. In valvular type heart disease, the valves become too narrow and hardened (stenotic) to open fully, or are unable to close completely (incompetent).

A stenotic valve forces blood to flow back to the adjacent heart chamber, while an incompetent valve leaks blood back into the previous chamber [8]. To compensate for the poor pumping action, the heart muscle enlarges and thickens, thereby losing elasticity and efficiency. Diastolic HF is ascribed to the natural effect of aging on the heart. It is mainly caused by the stiffening of heart muscles, which can prevent the patient's heart from properly filling with blood [9]. Diastolic HF may not reduce the ejection fraction compared to systolic HF patients. In diastolic HF, the left ventricle may pump well during the systole; however, it does not fill with enough blood during the diastole. A patient's ventricle may have a normal EF, but an insufficient amount of blood is pumped out. As a result, the ventricle pumps out less blood with each beat. The criteria for the diagnosis of diastolic HF remain imprecise, making it difficult to conduct valid clinical trials of treatment. The problem is compounded by the fact that systolic and diastolic HF commonly coexist when patients present with many ischemic and non-ischemic etiologies of HF. Narrowly defined, diastolic HF has often been defined as "heart failure with normal systolic function" (i.e. LVEF is greater than 50%) [10]. In this study, we also adopted an EF of 50% as a criterion in accordance with pulmonary edema and congestion conditions from chest X-ray examination reports to identify diastolic HF cases. Atrial fibrillation (AF) appears with abnormal heart rhythm and can be characterized and diagnosed as rapid and irregular beating through an electrocardiogram device [11]. AF is strongly associated with heart failure, coronary artery disease, valvular heart disease, diabetes mellitus, and hypertension. Normally, findings from 12-lead electrocardiogram can confirm the diagnosis of AF; hence, patients with an annotated ICD-9 code of 42731 can be directly confirmed as having AF. The remaining HF patients not satisfying the criteria described above can be categorized into a non-specified HF group, as there are many subtypes that must be further defined according to various combination syndromes.

1.3 Cardiac Rehabilitation for HF Patients

Once the major HF types are accurately identified, proper medications and surgical treatments can be applied. In addition to traditional therapies, exercise prescription may improve health conditions in both psychological and physiological aspects. A recent report revealed that intervened exercise training programs for HF patients achieved a 35% reduction in the risk of death and 28% reduction for both all-cause mortality and hospitalization [12]. This additional cardiac rehabilitation can be considered as a preventive medical prescription and will reduce the symptoms of HF patients, including enhanced endothelial cell functions of blood vessels [13], improved exercise tolerance by increasing muscle oxygen uptake efficiency [14], reducing sympathetic nerve activities [15], and reducing inflammation [16]. It is also recommended by the American Heart Association and European Society of Cardiology that all stabilized HF patients should be advised to participate in exercise training therapies [5].

However, clinical trials of exercise intensity, frequency, duration, type of exercise equipment, and exercise protocols should be customized for each HF patient, based on cardio-pulmonary exercise testing (CPX) assessments [17]. CPX is a common and noninvasive measuring procedure used in clinical practice which to provide precise and reliable assessment of various factors in response to maximal aerobic capacity including cardiac and pulmonary measurements. As customized maximal fitness levels are instructed by rehabilitation physicians, long-term and self-training activities can be performed at home according to the exercise prescription. Although regular exercise can help to improve survival rates of HF patients, high-intensity exercises may also increase the risk of sudden death. Hence, a proper or safe mechanism for self-training at home is very important for HF patients.

1.4 Internet of Medical Things and Two Adopted Biometric Features

Internet of Things (IoT) is a network connecting various physical devices that allow objects to collect or exchange data from each other. Among the IoT application areas, the medical care application referred to as the Internet of Medical Things (IoMT) has gained attention and can be constructed by connecting healthcare wearable devices, enabling doctors to remotely supervise and diagnose patient conditions [18]. In this study, we adopted bracelet devices and propose a safe mechanism for HF patient self-training programs. By wearing a bracelet and collecting both heart rate (HR) and metabolic equivalent (MET) data, this system can automatically send an warning message to patients, doctors, and healthcare assistants simultaneously if a dangerous event occurs. In addition, the system can detect whether the user is at risk of HF symptoms by comparing her/his biometric values with those of normal healthy people. Once the user is identified as a potential HF patient, the system offers a pre-registration function of instant notification message to the users. Particularly, when a user is at a critical status according to the collected health bracelet data, the developed system will immediately send out urgent notifications to doctors, family, or caregivers to prevent dangerous consequences.

When patients are diagnosed with HF and categorized as having a specific type of HF, doctors may advise patients to participate in rehabilitation training to recover cardiac function. However, in order to prevent over-exercising, rehabilitation professionals perform the CPX test for individual evaluation of exercise intensity limits. Two major biometric features are applied in our developed system, including peak oxygen uptake (VO_2max) and heart rate (HR). VO_2max can be transferred to corresponding metabolic equivalent (MET) by dividing by 3.5 and patient weight (kg). One unit of MET is defined as an energy consumption of 3.5 mL oxygen per kilogram per minute or defined as the rate of energy produced per unit surface area of an average person seated at rest [19]. Different exercise intensities reflect different MET values. For example, the physical activity of walking at a general speed is approximately equal to an MET value of 3.6 and jogging activity is close to an MET value of 7. Thus, higher METs indicate greater exhaustion. In this designed system, the maximum limitations for endurance or resistance trainings for HF patients were initially set as either 40-80% of maximum MET (Vo_2max/weight/3.5) or maximum predicted HR (220 minus age in years). When either condition is exceeded, the warming mechanism will be activated for safety monitoring.

This paper is organized as follows. Section 2 describes the procedures of feature extraction from medical documents and corresponding statistics. Section 3 introduces a newly proposed safe mechanism for self-exercise training program and all module functions, and Sections 4 presents our conclusions.

2 Medical Records and Feature Extraction

2.1 Data Sources and Feature Extraction

This study analyzed a total of 103,114 HF patients collected from four divisions of Chang Gung Memorial Hospital (CGMH) in Taiwan (IRB:105-0504C), including the Keelung (22,664), Linkou (42,052), Chiayi (15,662), and Kaohsiung (22,736) divisions. At least one hospitalization or outpatient medical record annotated with an ICD-9 of 428 or 42731 is required, and both ultrasound (M22) and chest X-ray (75-011) examination reports for each HF patient from years 2004 to 2013 are basic requirements for HF type categorization. Under such limitations, only 62,159 patients remained for classification in this study, including Keelung (16,694), Linkou (13,649), Chiayi (13,474), and Kaohsiung (18,342). According to the general rules shown in Table 1, we divided the HF patients into five major categories including systolic, diastolic, valvular, AF, and non-specified types. After the data screening processes, only 42% of HF patients could be primarily classified into the first four types including systolic, diastolic, valvular, or AF categories. Based on this low percentage, HF is indeed, a complex disease with complicated symptoms. More than 50% of HF patients require additional criteria to specifically identify the myocardial abnormalities associated with valve, pericardium, endocardium, heart rhythm and conduction issues.

Table 1
Criteria for classified HF types

HF type	Classified rule
Systolic	EF lower than 50%
Valvular	Mitral Regurgitation / Mitral Stenosis / Aortic Regurgitation / Aortic Stenosis been classified as moderate to severe or SEVERE
Diastolic	EF higher than 50% and reported edema or congestion in patient's Chest X-rays examination report
Atrial fibrillationC{PX	Annotated with ICD-9 code of 42731
Non-specified	Not been classified as systolic, valvular, diastolic type

2.2 Data Extraction Method

Regular expression was used to extract features from all of the collected clinical documents. To evaluate ultrasound test reports, we applied regular expression to examine all associated features, including patient EF values, valvular conditions (mitral stenosis, mitral regurgitation, aortic stenosis, aortic regurgitation), left ventricular end-diastolic dimension, left ventricular end-systolic dimension, interventricular septal end diastolic dimension, left ventricular end diastolic posterior wall dimension, aortic root, left atrial dimension, the ratio of early transmittal flow velocity and early mitral annular velocity. In addition, the system analyzed reports of patient chest X-rays examination simultaneously to determine whether the keywords of "edema" or "congestion" conditions were annotated within the documents. If the patient had participated in CPX testing, the VO_2max values were also retrieved to set exercise training limitations.

2.3 Data Analysis and Statistics

To identify additional features of HF patients, we categorized HF patient into five groups as described above and further clustered each group into several subgroups according to different genders and age intervals. The experiments were performed by analyzing hospitalization medical documents for HF patients within different age intervals. Statistical analysis showed that male patients in systolic, diastolic, valvular, and AF types were 2, 4, 6, and 4 years younger than female patients, respectively. However, this was not obvious for the cluster of non-specified HF patients. Additionally, the average age of hospitalization of valvular and diastolic

HF patients was higher than for other subgroups. In Figure 1, the Venn diagram shows the relationship between clustered patients for the five HF types in CGMH. Based on the defined criteria, there was some overlap between populations with different comorbidities among diastolic, valvular, systolic, and AF types. The largest HF group in CGMH was the systolic type. However, the non-specified HF population accounted for more than 50% of patients; the number of non-canonical forms of diastolic HF is increasing because of the aging society in most developed countries. More diastolic HF subtypes are expected to be defined and categorized in the near future.

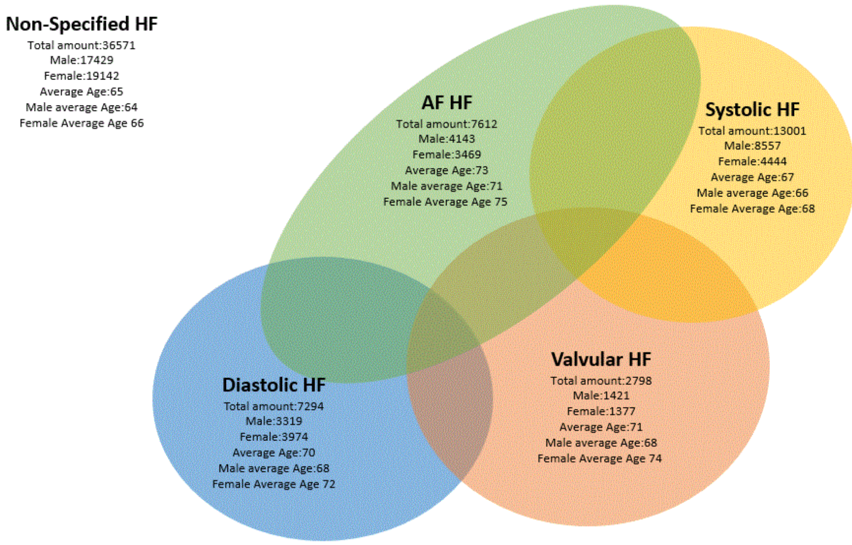

Figure 1
Venn diagram of number statistics of each HF type in four divisions of CGMH, Taiwan

3 A Safe Mechanism Design for Self-Exercise Training

3.1 System Mechanism

The proposed mechanism is divided into three modules. The first module includes a raw medical database analytical server and medical information systems. The raw medical database of HF patients from CGMH and healthy people were collected and analyzed for reference clusters. The server side connects with the hospital information systems and provides emergency messages to doctors as well as providing exercise prescriptions including MET and corresponding HR limitations for patients. The second module is designed for end users. After downloading the application (APP), users are required to provide personal information such as gender, age, and weight for the default settings designed in the next module. After wearing a wireless health bracelet device, the system begins to detect and record the METs and HRs of users and the bracelet connects to the APP through Bluetooth. According to the IoMT mechanism, the APP transmits physical data to cloud servers each minute based on the Message Queuing Telemetry Transport messaging protocol, a lightweight protocol for connecting with remote locations through limited network bandwidth. The final module is a cloud server for managing and analyzing the transmitted data. After receiving data from the APP, the designed system constructs a personal dataset including time, heart rate, and MET values, and the registered patient's identifier and corresponding time feature are applied as the super key for storage in the cloud database for a specific user. The integrated system configuration is shown in Figure 2. The cloud server analyzes retrieved personal data and compares them with the customized prescription limitations of the maximum MET and HR thresholds. When the physical MET/HR values exceed one of the two ranging limitations (40–80% of MET peak or maximum predicted HR = 220 – age in years [20]), the system immediately sends a warning message to notify the patients to reduce exercise intensities. When the remote healthcare system is combined with the hospital information system, doctors can remotely monitor and inspect the patient's MET/HF values by comparison with her/his CPX testing guidelines.

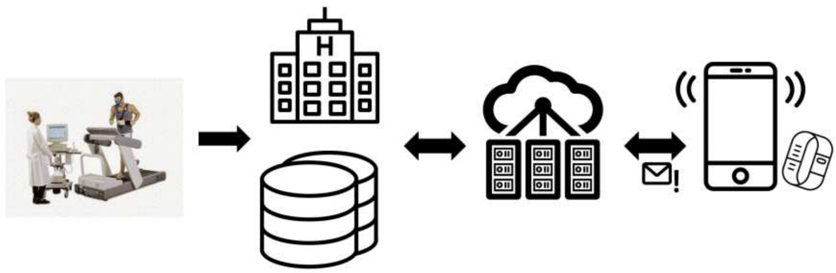

Figure 2

System configuration and data flow. The left sub-figure represents cardio-pulmonary exercise testing (CPX) assessments. The detected personal CPX testing records is recorded in the database server located in the hospital medical information center (the second sub-figure from left). The rightest sub-figure shows the wireless health bracelet device for biometric feature detection and a smartphone device for data transfer. The collected biometric features from HF patients are sent to the cloud server for real-time evaluation (the third sub-figure from left). The cloud server also takes responsibility for sending warning messages to appropriate recipients through Short Message Service (SMS).

3.2 Construction of Peak Limitations from Standard Reference Curves

Peak limitations for both MET and HR parameters for different ages and genders were constructed for two healthy male and female groups. These two sets of peak limitation bounding boxes in MET vs. HR measurements were obtained by transforming the original figure of peak VO_2 (mL/min) vs. age (years) as defined by Fleg *et al.* [21].

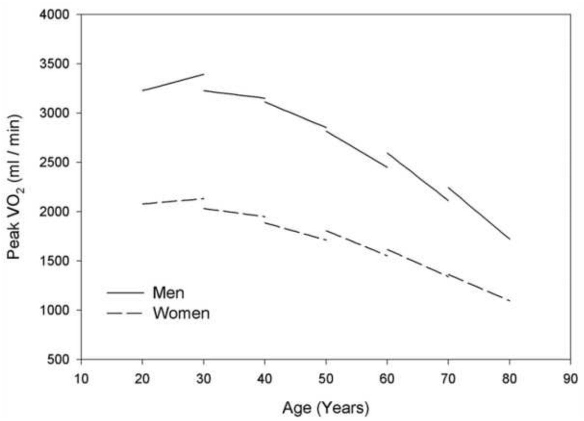

(a)

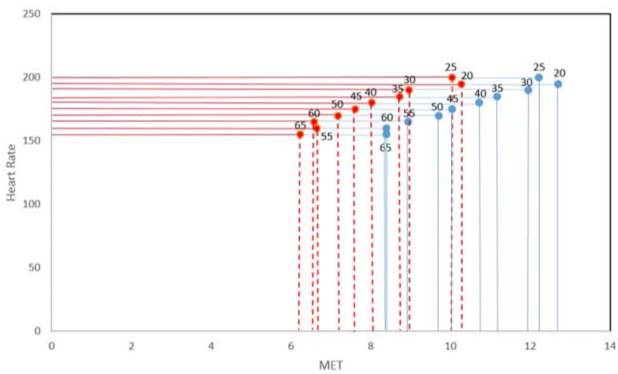

(b)

Figure 3

Standard reference curve transformation and construction for data calibration. (a) Peak VO_2 (mL/min) vs. age (years) defined by American Heart Association (Reprinted from Fleg *et al.* [21]); (b) Transformed standard peak VO_2 vs. age to maximum limitation of MET/HR as safety bounding boxes for various ages/gender. Red dotted bounding boxes for female and blue solid bounding boxes for male. Corresponding ages are shown in the upper-right corners.

The original figure is reprinted in Figure 3(a) and the transformed corresponding boundaries are shown in Figure 3(b). Maximum MET values were obtained by dividing peak VO_2 (mL/min) by 3.5 and the average weight (kg) of the healthy people, and corresponding HR values were obtained by subtracting age in years from 220. Thus, two sets of limitation bounding boxes for both males and females were obtained as shown in Figure 3(b). It should be noted that each bounding box represents a set of default maximum limitations for HF patients with the same age and gender. Once an HF patient wears the IoMT device for self-exercise training, all collected MET and HR values will be evaluated in a real-time manner and compared to her/his own customized limitations assigned by rehabilitation physicians. If there is no clear definition by a physician, the general rules of setting initial maximum limitations for an HF patient are used with a range of 40-80% of peak MET and 220 – age in years for HR parameter according to the HF patient's age and gender. Thus, every HF patient will have a customized maximum limitation region for monitoring safety.

3.3 Exercise Training Statistics for HF Patients

A total of 1035 HF patients with CPX testing records from the CGMH database were retrieved from 4 divisions. Six attributes including sex, age, weight, maximum heart rate achieved, MET and CPX testing limitations were retrieved from their corresponding medical documents. Only 728 male and 327 female entries were retrieved for analysis, as the CPX testing equipment were limited and only a proportion (1.6%) of HF patients were qualified and willing to accept exercising training. Because of the general symptoms of dyspnea and fatigue, most HF patients are reluctant to participate in rehabilitation programs, even if they understand that exercise training may postpone rehospitalization and reduce the risk of mortality. This is particularly true for the elderly, who are the major population of HF patients. Only partial distributions of CPX testing results are shown in Figure 4(a). Different clusters represent the conditions of HF patients and healthy people: right green triangle cluster for healthy group with age ranging from 25 to 35 years; middle yellow circle cluster for HF patients with age ranging from 25 to 35 years; left red diamond shape cluster for HF patients with age from 55 to 65 years. Healthy and young groups clearly cluster to the right locations within the MET vs. HR measurements. In this study, the average number of CPX tests conducted was 1.5 times per person among the 1035 HF patients, and the maximum testing record was five. Here, we display a case of an HF patient who attended 5 exercise training in Keelung CGMH, and the trained sequential conditions are shown in Figure 4(b). The patient's maximum MET and HR measurements were clearly, significantly improved. This condition was true for all HF patients. Hence, we suggest that after the stable conditions of HF patients are confirmed by doctors and rehabilitation physicians, the patients should be advised to consistently perform self-training at home. For these cases, the proposed safe mechanism using IoMT bracelets should be considered.

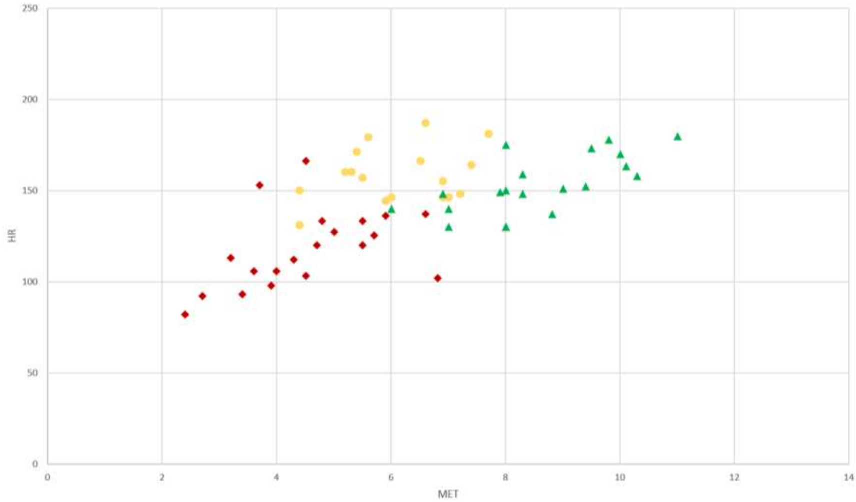

(a)

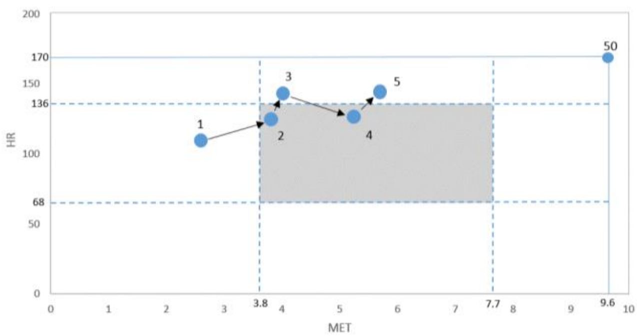

(b)

Figure 4

CPX testing measurements from collected data. (a) Different clusters of HF patients and healthy people: right green triangles for healthy group (age from 25 to 35 years); middle yellow circles for HF patients (age from 25 to 35 years); left red diamond shape dots for HF patients (age from 55 to 65 years); (b). An example HF patient with 5 exercise training data, sequentially. The maximum limitation box (solid lines) derived from healthy people is shown, and the conditions of the patient improved following the MET/HR measurements and move towards those of healthy people.

3.4 Warning Functions

Because of the sudden, urgent, and fatal characteristics of HF patients, the proposed warning mechanism is categorized into three different types. The first warning function is designed for users who have not been previously diagnosed with HF or any cardio-related symptoms. The system provides corresponding maximum limitation bounding boxes obtained from a healthy group of people. If the data are collected from a user after exercise training and all data points are relatively lower and distant from the default bounding box, she/he should be very careful about her/his heart conditions. This rough clustering and warning message may help people who are unaware that their heart conditions are already at a high-risk level. The second warning function is designed for HF patients as a secure monitoring mechanism. Based on the patient's exercise training conditions, rehabilitation physicians provide exercise prescription advice regarding maximum limitations of MET and HR references. If patients surpass the restriction levels after any self-training exercises, the server will send an instant warning message to the patient to remind her/him to lower the exercise intensity. The third warning messages are designed for an emergency condition when the user's heartbeat rate suddenly decreases to a predetermined low level; the system will send out an instant message to her/his doctors and family for emergency treatment. This mechanism is designed for serious HF patients who exercise alone.

Conclusions

Accurate classification of HF types may enable doctors to make better decisions regarding surgical and medication treatments for their HF patients. Here, we analyzed medical documents from non-intrusive ultrasound and X-ray examination records to determine the features of EF values, valvular conditions, edema, congestion, and ICD-9 codes for AF. Using straightforward classification rules, we effectively increased the diagnosis accuracy of HF types for providing proper prognostic healthcare. In addition, evaluating CPX testing performance may assist HF patients in understanding their rehabilitation limitations and function as guidelines for self-exercise training programs at home. To avoid increased cardiovascular mortality risk, particularly when HF patients perform exercise training without rehabilitation professionals aside, a safer mechanism is desired, which is successfully provided in this study. The proposed application system sets parameters for maximum MET and HR measurements either from a rehabilitation physician's exercise prescription or from default settings obtained from controlled healthy groups. A real-time monitoring system retrieves both MET and HR features from users' bracelets and provides an efficient and effective mechanism of sending warning messages to the patients when maximum limitations are exceeded. If the conditions are extremely severe for the HF patient, a warning message will also be sent to their family, doctors and/or caregivers.

According to the distributions of MET/HR features for HF patients, the CPX testing conditions of HF patients are significantly lower than for healthy people, and these clustered MET/HR features can be applied as reference indicators for HF symptom detection. Using appropriate protocols for exercise training programs, HF patients can enhance their heart conditions and improve their quality of life by consistently participating in rehabilitation therapies. This proposed warning mechanism applies not only to HF patients, but also to users who may be unaware of their HF symptoms. Additionally, the application mechanism used in this study is applicable for different disease targets, such as, diagnosis, classification and early warning models for various chronic diseases. In summary, we propose a safe system that collects MET and HR values through IoMT bracelets and designed default safety regions of MET vs. HR for HF patients of different age, gender and weight to, monitor self-training programs. We expect to provide users with an effective warning mechanism through bracelet devices and perform automatic detection and prevention for both HF patents and healthy people.

Though the prototype of the proposed warning system is successfully implemented herein, a field experimental test should be applied to verify the performance of the proposed system. A large-scale field experiment project is currently in progress. To assure that appropriate steps are performed, to protect the rights and welfare of humans participating as the subjects in our study, we have raised a research program to the Institutional Review Board (IRB) for approval. When IRB reviews and approves our research program, we will start to randomize all collected subjects into treatment and control groups, and the experimental outcomes and usage behavior between these two groups will be carefully compared. Meanwhile, in addition to the detected features of MET and HR from self-trained patients, we will try to discover possible associations between the measured features and the classified HF types. New biometric features from the IoMT devices will be considered and adopted in this study, if they are effective and stable. According to the confirmed relationship between measurable features and HF groups, we will try to organize the best customized default settings for each individual HF patient.

Acknowledgement

This work is supported by Ministry of Science and Technology, Taiwan, R.O.C. (MOST 104-2321-B-019-009 to T.-W. Pai and MOST 105-2634-E-019-001 to Lin) and Chang Gung Memorial Hospital, Keelung, Taiwan (CMRPG2C0351 to C.-H. Wang).

References

[1] O. S. Ogah, S. Stewart, O. E. Onwujekwe, A. O. Falase, S. O. Adebayo, T. Olunuga and K. Sliwa, "Economic Burden of Heart Failure: Investigating Outpatient and Inpatient Costs in Abeokuta, Southwest Nigeria," *PLoS One,* Vol. 9, No. 11, pp. e113032, 2014

[2] R. L. Page, J. A. Joglar, M. A. Caldwell, H. Calkins, J. B. Conti, B. J. Deal, N. A. Estes, 3rd, M. E. Field, Z. D. Goldberger, S. C. Hammill, J. H. Indik, B. D. Lindsay, B. Olshansky, A. M. Russo, W. K. Shen, C. M. Tracy and S. M. Al-Khatib, "2015 ACC/AHA/HRS Guideline for the Management of Adult Patients With Supraventricular Tachycardia: A Report of the American College of Cardiology/American Heart Association Task Force on Clinical Practice Guidelines and the Heart Rhythm Society," *J Am Coll Cardiol*, Sep 16, 2015

[3] A.-J. Hsiao, L.-H. Chen, and T.-H. Lu, “Ten Leading Causes of Death in Taiwan: A Comparison of Two Grouping Lists,” *Journal of the Formosan Medical Association*, Vol. 114, Issue 8, pp. 679-680, 2014

[4] L. N. Aminde, A. Dzudie, and A. P. Kengne, “Prevalent Diabetes Mellitus in Patients with Heart Failure and Disease Determinants in Sub-Saharan Africans having Diabetes with Heart Failure: a Protocol for a Systematic Review and Meta-Analysis,” *BMJ Open*, Vol. 6, No. 2, pp. e010097, 2016

[5] P. Ponikowski, A. A. Voors, S. D. Anker, H. Bueno, J. G. F. Cleland, A. J. S. Coats, V. Falk, J. R. González-Juanatey, V.-P. Harjola, E. A. Jankowska, M. Jessup, C. Linde, P. Nihoyannopoulos, J. T. Parissis, B. Pieske, J. P. Riley, G. M. C. Rosano, L. M. Ruilope, F. Ruschitzka, F. H. Rutten, P. Meer, "2016 ESC Guidelines for the Diagnosis and Treatment of Acute and Chronic Heart Failure: The Task Force for the Diagnosis and Treatment of Acute and Chronic Heart Failure of the European Society of Cardiology (ESC) Developed with the special contribution of the Heart Failure Association (HFA) of the ESC." *European heart journal*, 2016

[6] M. Davies, F. Hobbs, R. Davis, J. Kenkre, A. K. Roalfe, R. Hare, D. Wosornu, R. J. Lancashire, “Prevalence of Left-Ventricular Systolic Dysfunction and Heart Failure in the Echocardiographic Heart of England Screening Study: a Population-based Study,” *Lancet*, Vol. 358, No. 9280, pp. 439-44, 2001

[7] B. A. Borlaug and W. J. Paulus, “Heart Failure with Preserved Ejection Fraction: Pathophysiology, Diagnosis, and Treatment,” *Eur Heart J*, Vol. 32, No. 6, pp. 670-9, 2011

[8] B. Iung, G. Baron, E. G. Butchart, F. Delahaye, C. Gohlke-Barwolf, O. W. Levang, P. Tornos, J. L. Vanoverschelde, F. Vermeer, E. Boersma, P. Ravaud and A. Vahanian, “A Prospective Survey of Patients with Valvular Heart Disease in Europe: The Euro Heart Survey on Valvular Heart Disease,” *Eur Heart J*, Vol. 24, No. 13, pp. 1231-43, Jul, 2003

[9] Z. H. Chen, Y. R. Jiang, J. Q. Peng, J. W. Ding, S. Li, J. Yang, H. Wu and J. Yang, “Clinical Effects of Combined Treatment by Optimal Dose of Furosemide and Spironolactone on Diastolic Heart Failure in Elderly Patients,” *Exp Ther Med,* Vol. 11, No. 3, pp. 890-894, 2016

[10] M. F. Jimenez-Navarro, J. M. Garcia-Pinilla, A. M. Trujillo and E. de Teresa Galvan, “Treatment of Heart Failure due to Systolic Dysfunction,” *Rev Esp Cardiol*, Vol. 6 Suppl. F, pp. 46-52, 2006

[11] A. J. Camm, P. Kirchhof, G.Y.H. Lip, U. Schotten, I. Savelieva, S. Ernst, I. C. Van Gelder, N. Al-Attar, G. Hindricks, B. Prendergast, H. Heidbuchel, O. Alfieri, A. Angelini, D. Atar, P. Colonna, R. De Caterina, J. De Sutter, A. Goette, B. Gorenek, M. Heldal, S. H. Hohloser, P. Kolh, J.-Y. Le Heuzey, P. Ponikowski, F. H. Rutten, “Guidelines for the Management of Atrial Fibrillation: the Task Force for the Management of Atrial Fibrillation of the European Society of Cardiology (ESC) *European Heart Journal*, 31(19), 2369-429, 2010

[12] W. M. Mampuya, “Cardiac Rehabilitation Past, Present and Future: An Overview,” *Cardiovascular Diagnosis and Therapy* 2(1), pp. 38-49, 2012

[13] D. Fischer , S. Rossa, U. Landmesser, S. Spiekermann, N. Engberding, B. Hornig, H. Drexler, “Endothelial Dysfunction in Patients with Chronic Heart Failure is Independently Associated with Increased Incidence of Hospitalization, Cardiac Transplantation, or Death,” *Eur Heart Journal*, Vol. 26(1), pp. 65-69, 2005

[14] R. Hambrecht, E. Fiehn, J. Yu, J. Niebauer, C. Weigl, L. Hilbrich, V. Adams, U. Riede, G. Schuler, “Effects of Endurance Training on Mitochondrial Ultrastructure and Fiber Type Distribution in Skeletal Muscle of Patients With Stable Chronic Heart Failure,” *J Am Coll Cardiol*, Vol. 29(5), pp. 1067-1073, 1997

[15] P. J. Mueller, “Exercise Training and Sympathetic Nervous System Activity: Evidence for Physical Activity Dependent Neural Plasticity,” Clin Exp Pharmacol Physiol, Vol. 34(4), pp. 377-384, 2007

[16] J. A. Woods, K. R. Wilund, S. A. Martin, and B. M. Kistler, “Exercise, Inflammation and Aging,” Aging Dis., Vol. 3(1), pp. 130-140, 2012

[17] G. J. Balady, R. Arena, K. Sietsema, J. Myers, L. Coke, G. F. Fletcher, D. Forman, B. Franklin, M. Guazzi, M. Gulati, S. J. Keteyian, C. J. Lavie, R. Macko, D. Mancini, R. V. Milan, ”Clinician’s Guide to Cardiopulmonary Exercise Testing in Adults: A Scientific Statement from the American Heart Association,”. *Circulation*, Vol. 122, pp. 191-225, 2010

[18] C. Doukas and I. Maglogiannis, "Bringing IoT and Cloud Computing towards Pervasive Healthcare," IEEE Proceedings of the Sixth International Conference Innovative Mobile and Internet Services in Ubiquitous Computing (IMIS), pp. 922-926, 2012

[19] M. Jette, K. Sidney, G. Blumchen, “Metabolic Equivalents (METS) in Exercise Testing, Exercise Prescription, and Evaluation of Functional Capacity,” Clin. Cardiol, Vol. 13, pp. 555-565, 1990

[20] G. F. Fletcher, P. A. Ades, P. Kligfield, R. Arena, G. J. Balady, V. A. Bittner, L. A. Coke, J. L. Fleg, D. E. Forman, T. C. Gerber, M. Gulati, K. Madan, J. Rhodes, P. D. Thompson, M. A. Williams; American Heart Association Exercise, Cardiac Rehabilitation, and Prevention Committee of the Council on Clinical Cardiology, Council on Nutrition, Physical Activity and Metabolism, Council on Cardiovascular and Stroke Nursing, and Council on Epidemiology and Prevention, “Exercise standards for testing and training: a scientific statement from the American Heart Association,” Circulation, Vol. 128(8), pp. 873-934, 2013

[21] J. L. Fleg, C. H. Morrell, A. G. Bos, L. J. Brant, L. A. Talbot, J. G. Wright, E. G. Lakatta, “Accelerated Longitudinal Decline of Aerobic Capacity in Healthy Older Adults,” Circulation, Vol. 112(5), pp. 674-82, 2005

Sampled-data Observer-based Glucose Control for the Artificial Pancreas

Alessandro Borri[1], Pasquale Palumbo[1], Costanzo Manes[2], Simona Panunzi[1], Andrea De Gaetano[1]

[1] CNR-IASI Biomathematics Laboratory, Italian National Research Council (CNR), 00168 Rome, Italy

[2] DISIM Department, University of L'Aquila, 67100 L'Aquila, Italy

{alessandro.borri, simona.panunzi, andrea.degaetano}@biomatematica.it, pasquale.palumbo@iasi.cnr.it, costanzo.manes@univaq.it

Abstract: Artificial Pancreas (AP) is an expression referred to a set of techniques for the closed-loop control of the plasma glucose concentration by means of exogenous insulin administration in diabetic patients. Diabetes comprises a group of metabolic disorders characterized by high blood sugar levels over a prolonged period, due to pancreas failure to produce enough insulin and/or insulin resistance, so that higher amounts of insulin are usually required in order to keep glycemia in a safe range. In this work, we face the problem of glucose control for a class of Type-2 diabetic patients, in the presence of sampled glucose measurements and without any information about the time course of insulinemia. A compact physiological model of the glucose-insulin system is reviewed, then an observer (based on this model) is designed to estimate the insulin trajectory from the glucose samples. Finally, a feedback control law (based on the reconstructed state) is designed to deliver exogenous intra-venous insulin to each individual. Simulations have been performed in-silico on models of virtual patients, whose parameters are tuned according to real data, and aim at validating the method in the presence of parameter variations and quantization errors.

Keywords: Diabetes, Artificial Pancreas, Glucose Control, Observers, Feedback Systems

1 Introduction

In the past twenty years, with the improvement in technology allowing both direct measurement of glucose concentrations in the interstitium (or signals strongly correlated with it) and the availability of miniaturized hormonal pumps with acceptable autonomy, weight and precision of delivery, the automatic, closed-loop control of glycemia has become a real possibility. Together with the opening of technological opportunities there has naturally been the emergence of the need for theoretical analysis of the control algorithms to be employed in the practical industrial applications. This heterogeneous collection of devices, techniques, technology and theory, is known under the umbrella term “Artificial Pancreas” (AP). The main approach (though not the only one) to the regulation of the levels of glucose in blood has been the administration of carefully titrated amounts of the hormone insulin [1–3], which is notably completely lacking in Type-1 Diabetes Mellitus (T1DM) patients. Insulin promotes the uptake of glucose by peripheral tissues (particularly muscle and adipose tissue) and inhibits the release of autonomously synthesized glucose (from glycogen or other precursors) in the liver and kidney. Insulin is naturally formed in pancreatic beta cells, which are destroyed by the autoimmune processes typically characterizing the development of T1DM. To this lack of endogenous insulin, traditional medical therapy supplies with the administration of human or human-like hormone intravenously (IV) or subcutaneously (SC). The relevance of this topic is determined by the fact that T1DM affects approximately the 1% of the world population, with a huge impact on health expenditure by industrialized countries. While not so dramatic in its onset as T1DM, adult-onset or Type-2 Diabetes Mellitus (T2DM) also represents a huge burden on the health system due to the fact that its prevalence is not only vastly greater than that of T1DM (about 10 times as frequent), but also that T2DM incidence is increasing, to epidemic proportions, due to the spreading of excessively rich dietary habits from western to emerging Countries. In T2DM, the original defect consists in a lack of effect of insulin (“insulin resistance”): the hormone is initially secreted in higher than normal amounts by the pancreas, in an attempt to correct hyperglycemia resulting from insulin resistance. With the progression of disease, however, glucose toxicity and possibly other factors determine first a relative, then an absolute deficiency of insulin secretion, with an accelerated worsening of the individual conditions and the development of the clinical picture of frank diabetes mellitus. In this situation, the patient undergoes a progressive step-up of the therapeutic measures employed, going from simple dieting and increase in physical exercise, to oral hypoglycemic agents of different kinds to supplemental insulin therapy.

In this framework, the theory on the artificial control of glycemia has had to address a number of problems, stemming from the nonlinear and delayed insulin response [4,5], the availability of observations on glucose only, and the high variability of the insulin determinations that can be obtained with radio-immunological methods [6]. One fruitful way to address these problems has been through the shift from modelless to model-based control algorithms, in which the controller is synthesized using the model equations themselves. It is clear that, in this procedure, the smaller, the more general, the easier to implement, and the more robust the physiological model is, the better the resulting characteristics of the controller will be. It is clear therefore that the physiological model used to interpret the data and realize the controller must be relatively small and have easily identifiable parameters; it must, in other words, be a “compact” model [14], possibly even allowing to find an analytical solution to the control problem. In order to validate the controller based on the compact model, however, some “extended” model of the same physiological system must be used, more realistic, with parameters taken from the literature or decided upon by physicians to represent the kind of patients under investigation. In this way, the possible control strategies can be directly simulated and tested in silico.

We will use as a compact model a Delay-Differential Equations (DDE) model we have previously published [7, 8], which has been demonstrated to exhibit much better properties than alternative "minimal" models [13], and which we have already used in several different situations [9–12]. It must be noticed that the use of DDE-based glycemia-control algorithms can be equally well applied to both T1DM and T2DM patients, where in the latter case pancreatic Insulin Delivery Rate (IDR) also needs to be modelled, and in which IDR exhibits random variability [5]. Previous work published on this DDE model include having demonstrated that it can be used to safely control glycemia down to normal levels in T2DM subjects [9] and having validated observer-based controls against a widely known extended model [10], while current research effort is being dedicated to new therapeutic insulin dosing approaches for T2DM patients [16].

The goal of the present work is to consider the problem of controlling glycemia based upon sampled measurements. Unlike most of the contributions having appeared in the literature so far, we will assume not only non-availability of serum insulin determinations, but also the availability of glycemia measurements only at discrete sampling times, as it happens in the Continuous Glucose Monitoring (CGM) [17] technique of patient surveillance, which is the motivating reason of the present analysis. The observer we will use is constructed as shown in Cacace et al. [18, 19]. In contrast with previous work [9], we will therefore not assume glycemia to be measurable over continuous time. Strictly speaking, Cacace's construction cannot be applied when the compact model is delayed, so we limit our analysis to the situation in which the delay in insulin response is small (shorter than one minute). The control algorithm, based on the estimated state, will deliver exogenous intra-venous insulin continuously, with changes in insulin administration rate happening at sampling times. In order to make our simulations more realistic, we introduce further real-life complications, such as quantization (modeling the possible lack of accuracy of the instrument as well as the analog-to-digital and digital-to-analog conversion processes) both in the measurement and in the control phases.

The paper is structured as follows: in Section 2, we review some theoretical results about observer-based closed-loop control methods; in Section 3, we describe a model of the glucose-insulin system in terms of ordinary differential equations; in Section 4, we apply the methods described in Section 2 to the glucose-insulin model to find a control strategy (in terms of exogenous insulin rate) aiming at tracking desired glucose trajectories; Section 5 illustrates preliminary in-silico validation results for the described framework, obtained in an experimental setup utilizing data coming from real patients. Some final remarks and comments on future work conclude the article.

2 Review of Observer-based Closed-Loop Control Design

Consider a system of nonlinear differential equations in the form

$$\begin{cases} \dot{x}(t) &= f(x(t)) + g(x(t))u(t), \qquad t \geq 0 \\ y(t) &= c(x(t-\delta(t))), \qquad t \geq \Delta \end{cases} \tag{1}$$

where $x(t) \in \mathbb{R}^n$ denotes the state vector, $\dot{x}(t) := \frac{dx(t)}{dt}$ is its time derivative, $u(t) \in I\!R$ is the input function, $y(t) \in I\!R$ is the measured output, $\delta(t) \in [0,\Delta]$ is the output time-varying measurement delay (known), $x_0 \in I\!R^n$ is the initial state, $g(x)$ and $f(x)$ are C^∞ vector fields and $c(x)$ is a C^∞ function.

The problem of asymptotic state observation consists in the design of a causal system producing a vector variable $\hat{x}(t)$, which is called *observed state*, asymptotically converging to the real state $x(t)$ (i.e., $\|x(t)-\hat{x}(t)\| \to 0$), from the knowledge of the pair $(u(t), y(t))$. Such a system is called an *asymptotic observer*; additionally, it is said to be an *exponential observer* if there exist $\mu > 0$ and $\alpha > 0$ such that

$$\|x(t)-\hat{x}(t)\| \leq \mu\, e^{-\alpha t} \|x(0)-\hat{x}(0)\|, \tag{2}$$

for any $x(0)$ and $\hat{x}(0)$ in $\mathbb{R}^n$.

With the aim of designing such an observer, we first define the drift-observability map $z = \phi(x)$, stacking the first n Lie derivatives (from 0 to $n-1$) of the output function $c(x)$ along the drift vector field $f(x)$, and its Jacobian $Q(x)$, as

$$z = \begin{bmatrix} z_1 \\ z_2 \\ \vdots \\ z_n \end{bmatrix} = \phi(x) := \begin{bmatrix} h(x) \\ L_f c(x) \\ \vdots \\ L_f^{n-1} c(x) \end{bmatrix}, \qquad Q(x) := \frac{\partial \phi(x)}{\partial x}. \tag{3}$$

The observer in [18, 19], also reviewed in [20], takes the following expression:

$$\dot{\hat{x}}(t) = f(\hat{x}(t)) + g(\hat{x}(t))u(t) + e^{-\eta\delta(t)} Q^{-1}(\hat{x}(t)) K \big\{ y(t) - c(\hat{x}(t-\delta(t))) \big\}, \tag{4}$$

where the gain matrix K assigns the n eigenvalues of $(A-KC)$ so that the estimation error $x(t)-\hat{x}(t)$ asymptotically vanishes, with

$$A := \begin{bmatrix} 0_{(n-1)\times 1} & I_{(n-1)\times(n-1)} \\ 0 & 0_{1\times(n-1)} \end{bmatrix}, \quad C \ := \begin{bmatrix} 1 & 0_{1\times(n-1)} \end{bmatrix}, \tag{5}$$

and $\eta > 0$ is a design parameter, whose role is to assign a larger weight to the more recent measurements with respect to the older ones.

Under some technical hypotheses (including, in particular, uniform Lipschitz drift-observability and uniform input boundedness), if the system has full relative degree, it is possible to demonstrate the following theorem, establishing the exponential convergence to zero of the observation error.

Theorem 1. [19] Given the system (1), with $\delta(t) \in [0,\Delta]$, for any assigned $\eta > 0$, there exists K and a positive $\bar{\Delta}$ such that the system in (4) is a global exponential observer for the system in (1), provided that $\Delta < \bar{\Delta}$, with η being the estimation error decay rate (namely, (2) holds with $\alpha = \eta$ and some $\mu > 0$).

We remark that the previous result allows to employ the observer (4) if the sampling interval is smaller than or equal to Δ. If this is not the case, as shown in [19], a chain of sampled observers can be built.

In order to close the control loop, an input-output linearization approach is adopted, assuming that the relative degree of the system is n (see, e.g., [22]). The observability map dynamics in (3) rewrites:

$$\dot{z} = \frac{\partial \phi(x)}{\partial x}\dot{x} = Q(x)(f(x) + g(x)u). \tag{6}$$

We impose the virtual input $v := \dot{z}_n = L_f^n c(x) + L_g L_f^{n-1} c(x)u$, in order to obtain the linearizing feedback law:

$$u = \frac{v - L_f^n c(x)}{L_g L_f^{n-1} c(x)}. \tag{7}$$

The virtual input v needs to be chosen with the aim of tracking desired trajectories for the closed-loop system. To this end, a smooth reference output signal $y_{ref}(t)$ is defined, along with the vector of its first n time derivatives

$$z_{ref}(t) = \begin{bmatrix} z_{1,ref}(t) \\ z_{2,ref}(t) \\ \vdots \\ z_{n,ref}(t) \end{bmatrix} = \begin{bmatrix} y_{ref}(t) \\ \dot{y}_{ref}(t) \\ \vdots \\ y_{ref}^{(n-1)}(t) \end{bmatrix},$$

and defining $e := z - z_{ref}$, the error equation is

$$\dot{e} = Ae + B(v - \dot{z}_{n,ref}), \qquad \text{with} \quad B := \begin{bmatrix} 0_{(n-1)\times 1} \\ 1 \end{bmatrix}.$$

Since the Brunovsky pair (A,B) is reachable, it is sufficient to set

$$v = He + \dot{z}_{n,ref} \tag{8}$$

to guarantee the exponential convergence to zero of the linearized error dynamics, with rate determined by the n eigenvalues of matrix $(A + BH)$, assigned by means of H.

As a final remark, we notice that the control law reported in Eq. (7)–(8) is a continuous state-feedback control strategy, which depends on the continuous state $x(t)$, which is usually not available, except for its estimate $\hat{x}(t)$ provided by the observer (4). So, it is possible to restate the control law in (7)–(8) in terms of a feedback from the reconstructed state, but this is not guaranteed to work, in general, in the non-linear case, although local convergence results exist in the literature. In the linear case, instead, the separation principle would guarantee the asymptotic convergence of the output $y(t)$ to its reference value $y_{ref}(t)$.

3 A Continuous-Discrete Model of the Glucose-Insulin System

Continuous-discrete models refer to physical continuous-time systems with measurements acquired at discrete sampling times. These models often appear in clinical/medical applications like those related to the Artificial Pancreas, with control design problems related to the lack of a continuous stream of output data. According to [19], discrete measurements can still be formalized by means of a continuous-time output function. To this end, for a sampling sequence $\{t_i\}$ and assuming to measure plasma glucose concentration $G(t_i)$, the piecewise-constant output function $y(t)$ defined as

$$y(t) = G(t_i) \qquad t \in [t_i, t_{i+1}), \quad i = 0, 1, \ldots$$

can be restated as a *delayed* output in the equivalent form

$$y(t) = G(t - \delta(t)) \qquad t \geq 0, \tag{9}$$

where the delay $\delta(t)$ within any two consecutive sampling instants is time-varying:

$$\delta(t) = t - t_i, \qquad t \in [t_i, t_{i+1}), \quad i = 0, 1, \ldots, \tag{10}$$

with $t_0 = 0$. The sampling interval has a uniform upper bound equal to $\Delta := \max_i (t_{i+1} - t_i)$.

As shown in the previous section, this formal setting of the model output function allows to design exponential observers and observer-based control laws, which have been recently exploited also in the context of the artificial pancreas [9, 10, 21]. To this end, we consider a modified version of the DDE model presented in [7, 8] and exploited in [9, 10], which contains an explicit discrete delay modeling the secondary insulin released for varying plasma glucose concentration. Since we need to restate into the form of Eq. (1), the delay of the glucose-stimulated insulin production rate is neglected. This fact clearly limits the proposed feedback control law applicability and refers to further developments of the mathematical theory possibly including time-delay systems. Nonetheless, this work aims at showing the proof of concept of an observer-based control law in such continuous-discrete systems.

In absence of delay, the equations of model [7, 8] are particularized as follows:

$$\begin{cases} \frac{dG(t)}{dt} &= -K_{xgi}G(t)I(t) + \frac{T_{gh}}{V_G}, \\ \frac{dI(t)}{dt} &= -K_{xi}I(t) + \frac{T_{iGmax}}{V_I}h\big(G(t)\big) + u(t), \end{cases} \quad t \geq 0 \tag{11}$$

with initial conditions $G(0) = G_0$, $I(0) = I_0$, where:

- $G(t)$ is the glucose concentration in the plasma at time t $[mM]$;
- $I(t)$ is the insulin concentration in the plasma at time t $[pM]$;
- K_{xgi} is the rate of glucose uptake by tissues per unit of plasma insulinemia $[min^{-1}pM^{-1}]$;
- T_{gh} is the net balance between hepatic glucose output and zero-order glucose tissue uptake $[min^{-1}(mmol/KgBW)]$;
- V_G is the apparent distribution volume for glucose $[L/kgBW]$;
- K_{xi} is the apparent linear insulin clearance rate $[min^{-1}]$;
- T_{iGmax} is the maximal second-phase insulin release rate $[min^{-1}(pmol/kgBW)]$;
- V_I is the apparent insulin distribution volume $[L/kgBW]$;
- $h(\cdot)$ is a nonlinear function representing the endogenous pancreatic Insulin Delivery Rate (IDR) as

  $$h(G) = \frac{(G/G^*)^\gamma}{1+(G/G^*)^\gamma},$$

  where γ (dimensionless) denotes the progressiveness of the pancreas reaction to circulating glucose concentrations and G^* [mM] is the glucose concentration at which the insulin release reaches half of its maximal rate;
- $u(t)$ is the exogenous intra-venous insulin delivery rate at time t, which takes the role of control input $[pM/min]$.

The model in (11) enjoys some interesting properties:

- it is statistically robust, in that its parameters are statistically identifiable with very good precision by means of standard perturbation experiments, such as the Intra-Venous Glucose Tolerance Test (IVGTT) [7, 13];
- it is a compact model, in the sense that according to a "minimal" set of independent parameters, it allows to very well resemble the physiology of the glucose/insulin kinetics [7];
- it is mathematically consistent, in that exhibits satisfactory properties of the solutions [8]; in particular: positivity, boundedness, and a unique positive stable equilibrium.

Identification issues and statistical robustness of this model are discussed in [7], whilst the work [8] exhaustively treats its structural properties and the qualitative behavior of its solutions.

4 The Artificial Pancreas

We now apply the control design methodology illustrated in Section 2 to the glucose-insulin model described in Section 3. By restating in the vector form $x(t) = [x_1(t), x_2(t)]^T =$

$[G(t), I(t)]^T$ the already defined state variables, a compact expression in the form (1) is obtained for (10)–(11):

$$\begin{cases} \dot{x}(t) &= f(x(t)) + Bu(t), \qquad t \geq 0 \\ y(t) &= Cx(t-\delta(t)), \qquad t \geq \Delta \\ \delta(t) &= t - t_i, \quad t \in [t_i, t_{i+1}), \quad i = 0, 1, ... \end{cases} \tag{12}$$

where

$$f(x) = \begin{bmatrix} f_1(x) \\ f_2(x) \end{bmatrix} = \begin{bmatrix} -K_{xgi}x_1x_2 + \frac{T_{gh}}{V_G} \\ -K_{xi}x_2 + \frac{T_{iGmax}}{V_I}h(x_1) \end{bmatrix},$$

$$\delta(t) \in [0, \Delta], \qquad B = [0 \quad 1]^T, \qquad C = [1 \quad 0].$$

The drift-observability map $z = \phi(x)$ and its Jacobian are

$$z = \begin{bmatrix} z_1 \\ z_2 \end{bmatrix} = \phi(x) := \begin{bmatrix} Cx \\ Cf(x) \end{bmatrix} = \begin{bmatrix} x_1 \\ f_1(x) \end{bmatrix} = \begin{bmatrix} x_1 \\ -K_{xgi}x_1x_2 + \frac{T_{gh}}{V_G} \end{bmatrix}, \tag{13}$$

$$Q(x) := \frac{\partial \phi(x)}{\partial x} = \begin{bmatrix} 1 & 0 \\ -K_{xgi}x_2 & -K_{xgi}x_1 \end{bmatrix}, \tag{14}$$

where invertibility is guaranteed for $x_1 \neq 0$.

The observer equation in (4) is

$$\dot{\hat{x}}(t) = f(\hat{x}(t)) + Bu(t) + e^{-\eta\delta(t)}Q^{-1}(\hat{x}(t))K\{y(t) - C\hat{x}(t-\delta(t))\}, \tag{15}$$

where the eigenvalues $\lambda_1 < 0$, $\lambda_2 < 0$ of $(A - KC)$ are assigned by means of $K = \begin{bmatrix} -(\lambda_1+\lambda_2) \\ \lambda_1\lambda_2 \end{bmatrix}$ with the aim of ensuring the exponential convergence to zero of the error $x(t) - \hat{x}(t)$, and where $A = \begin{bmatrix} 0 & 1 \\ 0 & 0 \end{bmatrix}$.

By explicitly rewriting $\hat{x}(t) = [\hat{x}_1(t), \hat{x}_2(t)]^T = [\hat{G}(t), \hat{I}(t)]^T$, for all times $t \in [t_i, t_{i+1})$ and $i = 0, 1, ...$, the observer (4) is component-wise rewritten as

$$\begin{cases} \frac{d\hat{G}(t)}{dt} = -K_{xgi}\hat{G}(t)\hat{I}(t) + \frac{T_{gh}}{V_G} + e^{-\eta\delta(t)}(\lambda_1+\lambda_2)(G(t_i) - \hat{G}(t_i)), \\ \frac{d\hat{I}(t)}{dt} = -K_{xi}\hat{I}(t) + \frac{T_{iGmax}}{V_I}h\big(\hat{G}(t)\big) + u(t) + e^{-\eta\delta(t)}\frac{K_{xgi}(\lambda_1+\lambda_2)\hat{I}(t) - \lambda_1\lambda_2}{K_{xgi}\hat{G}(t)}(G(t_i) - \hat{G}(t_i)). \end{cases} \tag{16}$$

The technical assumptions of Theorem 1 are fulfilled for the glucose-insulin system in (10)–(11), which ensures that the observation error exponentially vanishes.

We now detail the algorithm of glucose control. The observability map evolution in (13) rewrites:

$$\dot{z} = \begin{bmatrix} \dot{z}_1 \\ \dot{z}_2 \end{bmatrix} = \frac{\partial \phi(x)}{\partial x}\dot{x} = Q(x)(f(x)+Bu) = \begin{bmatrix} 1 & 0 \\ -K_{xgi}x_2 & -K_{xgi}x_1 \end{bmatrix} \begin{bmatrix} f_1(x) \\ f_2(x)+u \end{bmatrix}$$
$$= \begin{bmatrix} 1 & 0 \\ -K_{xgi}x_2 & -K_{xgi}x_1 \end{bmatrix} \begin{bmatrix} z_2 \\ -K_{xi}x_2 + \frac{T_{iGmax}}{V_I}h(x_1)+u \end{bmatrix}, \tag{17}$$

so one obtains

$$\begin{cases} \dot{z}_1 & = z_2, \\ \dot{z}_2 & = -K_{xgi}x_2\Big(-K_{xgi}x_1x_2 + \frac{T_{gh}}{V_G}\Big) + K_{xgi}x_1\Big(K_{xi}x_2 - \frac{T_{iGmax}}{V_I}h(x_1)\Big) - K_{xgi}x_1u. \end{cases} \tag{18}$$

We now get the linearizing feedback law by setting $\dot{z}_2 := v$ to obtain

$$u = K_{xi}x_2 - \frac{T_{iGmax}}{V_I}h(x_1) - \frac{v + K_{xgi}x_2(-K_{xgi}x_1x_2 + \frac{T_{gh}}{V_G})}{K_{xgi}x_1} \tag{19}$$

which is computable for positive glycemias x_1, in agreement with the Jacobian matrix $Q(x)$ in (14) being invertible.

The reference glycemia trajectory is

$$y_{ref}(t) = G_{ref}(t) = G_d + (G_b - G_d)e^{-\lambda t},$$

with $\lambda > 0$, and its goal is to lead the glycemia of an individual from a high basal value G_b of a subject to a lower healthier value G_d. By defining

$$z_{ref} = \begin{bmatrix} z_{1,ref} \\ z_{2,ref} \end{bmatrix} := \begin{bmatrix} y_{ref} \\ \dot{y}_{ref} \end{bmatrix},$$

its dynamics is readily computed:

$$\dot{z}_{ref}(t) = \begin{bmatrix} \dot{z}_{1,ref}(t) \\ \dot{z}_{2,ref}(t) \end{bmatrix} = \begin{bmatrix} z_{2,ref}(t) \\ \dot{z}_{2,ref}(t) \end{bmatrix} = \begin{bmatrix} -\lambda(G_b - G_d)e^{-\lambda t} \\ \lambda^2(G_b - G_d)e^{-\lambda t} \end{bmatrix}.$$

The error $e := z - z_{ref}$ is described by the equation

$$\dot{e} = \begin{bmatrix} \dot{z}_1 - \dot{z}_{1,ref} \\ \dot{z}_2 - \dot{z}_{2,ref} \end{bmatrix} = \begin{bmatrix} z_2 - z_{2,ref} \\ v - \dot{z}_{2,ref} \end{bmatrix} = Ae + B(v - \dot{z}_{2,ref}).$$

Finally, we assign

$$v = He + \dot{z}_{2,ref} \tag{20}$$

to guarantee the convergence to zero of the linearized error dynamics, whose convergence rate is determined by the eigenvalues $\lambda_3 < 0$, $\lambda_4 < 0$ of matrix $(A+BH)$, assigned by $H = \begin{bmatrix} -\lambda_3\lambda_4 \\ (\lambda_3+\lambda_4) \end{bmatrix}^T$.

As discussed at the end of Section 2, in the spirit of separation principle, we restate Eqs. (19)–(20) in terms of a control from the estimated state, leading to the following continuous feedback law

$$u = \max\left\{0, K_{xi}\hat{x}_2 - \frac{T_{iGmax}}{V_I}h(\hat{x}_1) - \frac{H(\hat{z}-z_{ref}) + \dot{z}_{2,ref} + K_{xgi}\hat{x}_2(-K_{xgi}\hat{x}_1\hat{x}_2 + \frac{T_{gh}}{V_G})}{K_{xgi}\hat{x}_1}\right\} \tag{21}$$

where $\hat{z} := \begin{bmatrix} \hat{x}_1 \\ f_1(\hat{x}) \end{bmatrix}$, and $\hat{x} = \begin{bmatrix} \hat{x}_1 \\ \hat{x}_2 \end{bmatrix} = \begin{bmatrix} \hat{G} \\ \hat{I} \end{bmatrix}$ is the output of the observer in (16). We remark that the possibility of a negative exogenous insulin rate in (21) is formally inhibited.

5 In-silico Evaluation

We here evaluate the performance of the techniques illustrated in the previous sections in a non-ideal experimental context. We start from the data obtained from 3 healthy subjects, whose samples of glucose and insulin are included in the data collected in [7]. Some anthropometric data for these subjects are summarized in Table 1. Each individual underwent an Intra-Venous Glucose Tolerance Test (IVGTT), according to which a glucose bolus is administered intra-venously after an overnight fasting period, and then plasma glucose and serum insulin concentration are sampled for the following 3 hours, at varying sampling time. IVGTT is also considered among the most affordable and commonly used perturbation procedures used to estimate insulin sensitivity. Measurements of glycemia and insulinemia from this experiment are used to identify the parameters of the ODE model (11), which is coincident with the DDE model in [7], [8] in the particular case $\tau_g = 0$. As a matter of fact, as already mentioned before, just subjects with negligible delay in the glucose action on pancreatic IDR are considered, following the sample-based approach in [19], and in absence of theoretical results for this method when applied to systems expressed by delayed differential equations.

After the identification phase, since some of the considered subjects are pre-diabetic and not diabetic, we artificially perturbate the parameters in order to simulate a potential natural progression of the disease towards diabetes (see also [9]). In particular, we reduced the insulin resistance (up to about $K_{xgi} < 10^{-4}$) and the pancreatic glucose sensitivity T_{iGmax}, to then recompute some of the other parameters via the algebraic steady-state conditions obtained from the model in Eq. (11). In more details, the basal values of glycemia G_b and insulinemia I_b, representing the equilibria of (11) in absence of exogenous insulin administration ($u = 0$), are obtained from:

$$\begin{cases} K_{xgi}V_G G_b I_b &= T_{gh}, \\ K_{xi}V_I I_b &= T_{iGmax}h\big(G_b\big). \end{cases}$$

Table 2 collects the parameter values for the three individuals. Note that the parameters of each model are assumed to be known (up to some uncertainty) in the

Table 1
Numerical values of some anthropometric parameters
(in the respective units of measurement) for the 3 patients considered.

Parameter	**Patient 1**	**Patient 2**	**Patient 3**
Sex	Male	Female	Female
Age [years]	32	26	27
Height [m]	1.69	1.57	1.56
Body Weight [kg]	68	48	57
Body Mass Index [kg/m^2]	23.81	19.47	23.42

Table 2
Model parameters values (and units of measurement)
used in the in-silico evaluation.

Parameter	**Patient 1**	**Patient 2**	**Patient 3**
G_b	8.96	8.78	8.44
I_b	27.82	24.04	7.04
K_{xgi}	$7.45 \cdot 10^{-5}$	$9.96 \cdot 10^{-5}$	$5.39 \cdot 10^{-5}$
T_{gh}	0.0025	0.0027	0.0003
V_G	0.13	0.13	0.10
K_{xi}	0.10	0.06	0.25
T_{iGmax}	1.39	0.75	0.94
V_I	0.24	0.25	0.25
γ	2.30	2.52	1.52
G^*	9	9	9

construction of the artificial pancreas *tailored* to the particular patient, in the spirit of the so-called *personalized medicine* approach.

In addition to the hypotheses dealt with in the theoretical part, we consider a more realistic simulation setting and assume a quantization error both in the measuring and in the control procedure, accounting for the processes of analog-to-digital and digital-to-analog conversion in digital devices. Quantization steps of 0.1 mM for the glycemia measurements and $20 pM/min$ for the exogenous Insulin Delivery Rate (IDR) are assumed, respectively. Accordingly, quantization errors affect the initial values of the observer-based controller. The sampling time of the glycemia measurements is assumed constant and equal to $t_{i+1} - t_i = \Delta$, for all observations i, so that we can write more simply $t_i = i \cdot \Delta$, with $\Delta = 5$ [min], which is a typical value for many Continuous-Glucose-Monitoring (CGM) devices currently available on the market [23]. We also assume that control samples are held for the same interval, without any phase shifts.

The Artificial Pancreas is designed by considering the individual parameters for each patient in Table 2, but an additional random uncertainty (up to $\pm 5\%$) is considered with respect to the real values. The parameter η in (16) is set equal to 5, the target glycemia is equal to $G_d = 5$ mM, the decay rate is $\lambda = 1/30$. The same closed-loop eigenvalues for all patients are set: $\lambda_1 = -0.8$, $\lambda_2 = -1.6$, $\lambda_3 = -1$,

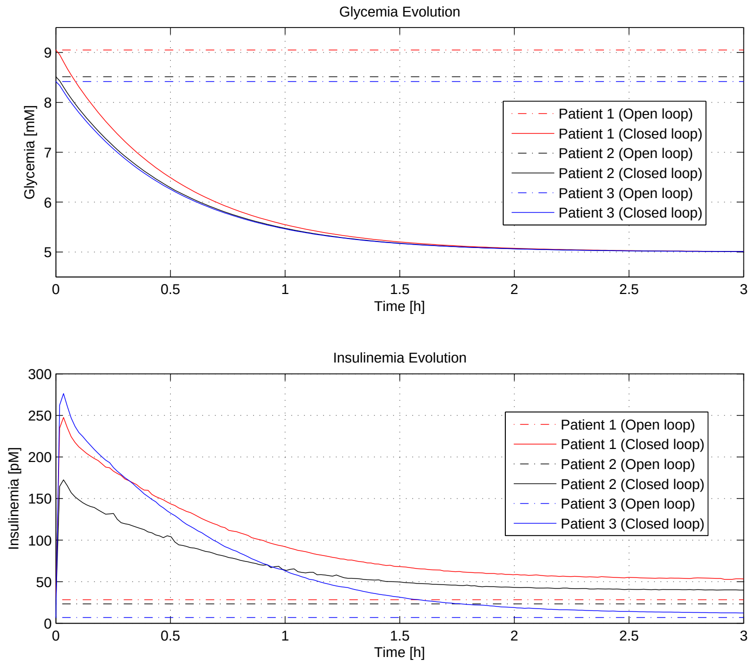

Figure 1
Top panel: trajectories of glycemia for 3 virtual patients: basal values (dash-dotted lines) and patients controlled by means of the Artificial Pancreas (solid lines).
Bottom panel: trajectories of insulinemia for 3 virtual patients: basal values (dash-dotted lines) and patients controlled by means of the Artificial Pancreas (solid lines).

$\lambda_4 = -0.5$, uniquely determining the values of the observer gain K in (4) and the control gain H in (21).

Figures 1 and 2 illustrate the results in terms of glycemia and insulinemia trajectories, glucose percent error and IDR input. We note that the glucose trajectories (Fig. 1, top panel) monotonically decrease towards the target value G_d, which is reached, in all the subjects, within the experiment time horizon (3 hours). Correspondingly, the insulinemia trajectory (Fig. 1, bottom panel) shows an initial peak (exceeding 150 pM for the three patients), to then recover towards levels below the 50-pM value. Higher values of insulinemia (patient 3) correspond to higher exogenous insulin infusions (Fig. 2, bottom panel). In spite of the different parameters and initial conditions, the error falls below 10% (with respect to the target glycemia G_d) within about 1 hour for all the patients (Fig. 2, top panel), due to the common choice of the closed-loop eigenvalues.

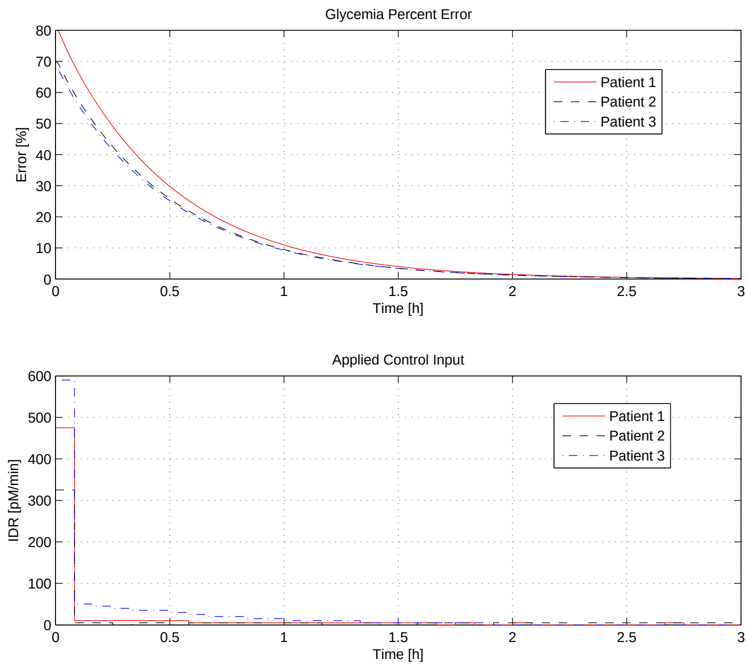

Figure 2
Top panel: glycemia percent error for the 3 virtual patients.
Bottom panel: exogenous IDR input for the 3 virtual patients.

Discussion and Further Work

In this work, we proposed a solution to a glucose control problem with partial/inaccurate information, in the direction of the development of the so-called Artificial Pancreas. After a general review of nonlinear output-feedback techniques, we considered a compact existing model constituted by nonlinear ordinary differential equations, which is known to represent adequately the evolution of the glucose-insulin system in people in which the apparent delay in the pancreatic second-phase insulin secretion can be approximately neglected. In this context, we designed an observer, which estimates the continuous dynamics of glucose and insulin from sparse measurements of glycemia. Then, the loop was closed by designing a feedback law from the observer state, and actuated in terms of exogenous insulin delivery, with the goal of tracking a proper trajectory of glycemia. A preliminary in-silico evaluation of the proposed methods has been performed on virtual patients whose parameters have been computed starting from real data, in a non-ideal simulation setup including quantization and parameter variations. The obtained results highlight that the approach can constitute a promising tool for studying and realizing an Artificial Pancreas in more realistic scenarios. In view of this goal, research studies will focus in the future on the validation of the techniques illustrated in this paper in the context of more comprehensive models (such as [15]), to better understand the way a real patient would react to the proposed treatment. In addition, formal extensions of the observer-based control to more general cases (state delays, discretized input and output) are under investigation.

References

[1] S.A. Weinzimer, G.M. Steil, K.L. Swan, J. Dziura, N. Kurtz, W.V. Tamborlane, *Fully automated closed-loop insulin delivery versus semiautomated hybrid control in pediatric patients with type 1 diabetes using an artificial pancreas*, Diabetes care, 31(5), 934-939, 2008.

[2] A.M. Albisser, B.S. Leibel, T.G. Ewart, Z. Davidovac, C.K. Botz, W. Zingg, H. Schipper, R. Gander, *Clinical control of diabetes by the artificial pancreas*, Diabetes, 23(5), 397-404, 1974.

[3] K. Zarkogianni, E. Litsa, K. Mitsis, P.-Y. Wu, C.D. Kaddi, C.-W. Cheng, M.D. Wang, K.S. Nikita, *A Review of Emerging Technologies for the Management of Diabetes Mellitus*, IEEE Trans. Biomed. Eng., 62(12), 2735-2749, 2015.

[4] A. Makroglou, J. Li, and Y. Kuang, *Mathematical models and software tools for the glucose-insulin regulatory system and diabetes: An overview*, Appl. Numer. Math., 56, 559-573, 2006.

[5] P. Palumbo, S. Ditlevsen, A. Bertuzzi, and A. De Gaetano, *Mathematical modeling of the glucose-insulin system: A review*, Math. Biosci., 244, 69-81, 2013.

[6] P. Palumbo, P. Pepe, S. Panunzi, and A. De Gaetano, *Recent results on glucose-insulin predictions by means of a state observer for time-delay systems*, "Predic-

tion Methods for Blood Glucose Concentration: Design, Use and Evaluation", H. Kirchsteiger, J. Jørgensen, E. Renard and L. Del Re Editors, Springer, 2015.

[7] S. Panunzi, P. Palumbo, and A. De Gaetano, *A discrete single delay model for the intra-venous glucose tolerance test*, Theor. Biol. Med. Model., 4, 2007.

[8] P. Palumbo, S. Panunzi, and A. De Gaetano, *Qualitative behavior of a family of delay-differential models of the glucose-insulin system*, Discrete Contin. Dyn. Syst. Ser. B., 7(2), 399-424, 2007.

[9] P. Palumbo, P. Pepe, S. Panunzi, and A. De Gaetano, *Time-Delay Model-Based Control of the Glucose-Insulin System, by Means of a State Observer*, Eur. J. Control, 6, 591-606, 2012.

[10] P. Palumbo, G. Pizzichelli, S. Panunzi, P. Pepe, and A. De Gaetano, *Model-based control of plasma glycemia: Tests on populations of virtual patients*, Math. Biosci., 257, 2-10, 2014.

[11] P. Palumbo, P. Pepe, S. Panunzi, A. De Gaetano, Closed-loop glucose control: application to the Euglycemic Hyperinsulinemic Clamp, in *Proc. 52nd Conf. Decision and Control*, Dec. 2013, 4461–4466.

[12] P. Palumbo, G. Pizzichelli, P. Pepe, S. Panunzi, A. De Gaetano, Closed-loop control scheme for the Euglycemic Hyperinsulinemic Clamp: validation on virtual patients, in *Proc. 19th IFAC World Congress of Automatic Control*, 2088–2093, Cape Town, South Africa, 2014.

[13] S. Panunzi, A. De Gaetano, G. Mingrone, G., *Advantages of the single delay model for the assessment of insulin sensitivity from the intravenous glucose tolerance test.*, Theoretical Biology & Medical Modelling, 7, 9, 2010.

[14] F. Chee, T. Fernando, *Closed loop control of blood glucose*, Berlin, Heidelberg, Springer-Verlag, 2007.

[15] C. Dalla Man, R. Rizza, and C. Cobelli, *Meal simulation model of the glucose insulin system* IEEE Transactions on Biomedical Engineering, 54(10), 1740–1749, 2007.

[16] C.R. Gaz, A. De Gaetano, C. Manes, P. Palumbo, A. Borri , S. Panunzi, *Effective Control of Glycemia using a Simple Discrete-delay Model*, IFAC World Congress 2017, Toulouse, France, 2017 (to appear).

[17] W.V. Tamborlane, R.W. Beck, B.W. Bode, B. Buckingham, H.P. Chase, R. Clemons, et al., *Continuous glucose monitoring and intensive treatment of type 1 diabetes*, The New England journal of medicine, 359(14), 1464-1476, 2008.

[18] F. Cacace, A. Germani, and C. Manes, *An observer for a class of nonlinear systems with time varying observation delay*, Syst. Control Lett., 59, 305–312, 2010.

[19] F. Cacace, A. Germani, and C. Manes, *A chain observer for nonlinear systems with multiple time-varying measurement delays*, SIAM J. Control and Optim., 52.3, 1862-1885, 2014.

[20] A. Borri, F. Cacace, A. De Gaetano, A. Germani, C. Manes, P. Palumbo, S. Panunzi, P. Pepe, *Luenberger-like Observers for Nonlinear Time-Delay Systems with Application to the Artificial Pancreas*, IEEE Control Systems Magazine, 2017 (conditionally accepted).

[21] L. Kovács, B. Pálancz, B. Zoltán, *Design of Luenberger Observer for Glucose-Insulin Control via Mathematica*, Proceedings of the 29th Annual International Conference of the 28th IEEE EMBS, 624-627, 2007.

[22] A. Isidori, *Nonlinear control systems*, Springer Science & Business Media, 1995.

[23] D.B. Keenan, J.J. Mastrototaro, G. Voskanyan, G.M. Steil, *Delays in Minimally Invasive Continuous Glucose Monitoring Devices: A Review of Current Technology*, Journal of diabetes science and technology, 3.5, 1207–1214, 2009.

Infectious Hospital Agents: A HAI Spreading Simulation Framework

Róbert Pethes, Tamás Ferenci, Levente Kovács

Research and Innovation Center of Óbuda University, Physiological Controls Group, Óbuda University, Budapest, Hungary
Email: pethes.robert@phd.uni-obuda.hu, {ferenci.tamas, kovacs.levente}@nik.uni-obuda.hu

Abstract: Infectious Hospital Agents (IHA) is an individual-based simulation framework that is able to model wide range of infection spreading scenarios in the hospital environment. The simulations are agent-based simulations driven by stochastic events, the evolution of the model is tracked in discrete time. Our aim was to build a general, customisable and extensible simulation environment for the domain of Hospital-Associated Infections (HAIs). The system is designed in Object Oriented fashion, and the implementation is in C++. In this paper, the authors describe the motivations and the background of the framework, sketch the conceptual framework, and present a demonstration example.

Keywords: Healthcare-Associated Infections; Hospital simulation; Agent-based simulation

1 Introduction

Hospital-associated infections (HAI) are infections that patients get while receiving treatment in healthcare settings. In practice, HAIs are often identified as antibiotic-resistant bacteria, such as Methicillin Resistant Staphylococcus Aureus (MRSA), Clostridium difficile, Drug-resistant Streptococcus pneumonia and Vancomycin Resistant Enterococci (VRE). Antibiotic resistance is the ability of bacteria to resist the effects of an antibiotic [1]. It occurs when bacteria change in a way that reduces the effectiveness of drugs to cure or prevent infections. The molecular mechanism of the resistance development is a complex process, and the most frequent type of resistance is acquired and transmitted via the conjugation of plasmid [2]. Furthermore, the emergence of multidrug-resistant (MDR) bacteria strains increases the seriousness of the problem. According to these facts, it is easy to see that the treatment of these infections are very costly [3] and complicated, that is the reason why prevention gets great emphasis. Surveillance, outbreak investigation and interruption, HAI prevention are included in hospital infection control. In infection control, it is essential to understand the dynamics of infection spreading, and to predict the effects of the interventions against HAIs. Mathematical modelling and simulations can help the infection control professionals to improve their understanding of these complex processes, and make better decisions.

Primarily, our aim was to build a simulation framework that is able to simulate a wide range of infection spreading scenarios, but we are faced with the problem, that the spreading process and the infection control processes highly depend on the other hospital processes. Therefore we have to simulate the hospital processes at the same level, what is a difficult problem in itself.

1.1 Pathogen Sources and Transmission Routes

In this section, we review the possible pathogen sources and the pathogen transmission routes. Studies have shown that the primary transmission pathway is the patient – healthcare worker (HCW) – patient route [4,5]. In other words, the HCWs transmit the pathogens via their hands. Pittet et al. [4] identified the 5 main steps of pathogen transmission via healthcare workers' hands (the pathogen sequence steps) and the evidence supporting each step. The steps are the following:

1. Pathogens are present on the patient's skin or in the patient's immediate environment.
2. Transfer of pathogens to HCW's hands.
3. Pathogens must survive on HCW's hands for at least several minutes.
4. Hand decontamination (hand washing/rubbing or hand antisepsis) by the healthcare worker must be inadequate or omitted entirely.
5. The HCW's contaminated hand(s) must come into direct contact with another patient or with a fomite in direct contact with the patient.

In the prevention of HAI transmission, our aim is to break this sequence. Of course the patient to patient and HCW to HCW routes are also important, if we investigate the spread of an airborne diseases, such as influenza. There are some special cases, when we have to consider the patient to patient routes also: when the probability that two patients come into direct contact is not negligible, such as in a pediatric ward. A contaminated environment may also be a source of pathogens in hospitals. For example strains of MRSA can survive and remain viable on dust particles or skin scales for many weeks and months [6], and it is also proven that low densities of MRSA can initiate infections [7]. As we have mentioned in the previous subsection, antibiotic resistant pathogens can emerge caused by the selective pressure of antibiotics, but more commonly, newly admitted patients can carry these pathogens to the hospital [8,9].

1.2 Infection Control Measures

Infection control measures are all the interventions against HAIs that a hospital can use to prevent the infections. In this section we briefly overview the most common infection control measures:

- Hand hygiene: Obviously, hand hygiene is one of the most important infection control measures [4, 5]. There are two main factors when we are talking about hand hygiene: compliance and the quality of hand decontamination. In brief, the first one refers to the frequency of hand washing/rubbing, the second refers to the quality of it.
- Staff cohorting: This is a method to restrict the transmission network. If we assign a caregiver to a subgroup of patients, we can eliminate the transmission of the pathogen (via the HCW's hand) between patient groups. In other word, we can decrease the role of the 2nd and 5th steps of the transmission sequence discussed before.
- Patient isolation: This is another way to restrict the transmission network. If a patient is found to be colonized or infected, then isolation is justifiable. In this case, there are special hygiene and precaution rules for the HCW who enters or leaves the room of the isolated patient. However, patient isolation is very costly and often practically impossible as the number of colonized/infected patients are increasing.
- Surveillance: a collection of methods for collecting every information regarding the epidemic process. This can contain a lot of data acquisition methods: swabbing (microbiological sampling) at admission, periodically repeated swabbing of the patients, tracking the patients' temperature chart, illness records, computing the risk factors, etc. The result of the surveillance can be used to ordain special interventions, such as isolation. Recently, there is a new trend to use information technology tools for monitoring hand hygiene compliance and quality [10], and Lehotsky et al. showed that direct, personal feedback can reduce the rate of inadequate hand rubbing [11].
- Patient decolonization: We suppose that patients are persistent carriers after colonization, and this fact has an important role in the pathogen transmission sequence. For example, patients can carry MRSA on their skin, nose or injured skin, therefore they act as a constant source for MRSA transmission [12]. MRSA eradication can be effectively done by using mupirocin and chlorhexidline for decolonization [13].
- Antibiotic usage protocols: antibiotic usage in hospitals has a key role in emergence and spread of HAIs [14], and the applied protocol has a great impact [15].
- Cleaning and sterilization.

1.3 Hospital Simulations

The effective operation of hospitals is a key issue for society, and the optimization of the operation of hospitals is an important question in the practical Operational Research/Management Science. The " optimality" has different viewpoints, and the resulting healthcare service directly affects the lives of many people. However, hospitals are complex systems, and it is very hard to find an optimal plan to manage hospital resources, and predict the effects of the interventions or the change of the environment. A hospital can be also seen as a queuing system, but the direct use of queuing analytic theory is very hard [16]. One tool, that can help, is computer simulation. A simulation is a simplified replica of a real-world system, and can be used to evaluate "what-if?" scenarios before applying the changes. The most common hospital simulation methods [17] are Discrete Event Simulation (DES), System Dynamics (SD) and Agent-Based Simulation (ABS). DES is applied to model systems that change their states dynamically, stochastically, in discrete time intervals. It is particularly applicable for systems that have queuing structure. System Dynamics is a method of simulating continuous systems. It works on a set of differential equations. In this method, we usually examine cohorts rather than individuals. SD models are more appropriate for studying the interrelationship between elements of the systems. In an Agent-Based Simulation, there are autonomous objects called agents, who are living in an environment and interact with each other.

1.4 Modelling and Simulations in Infection Control

The most important model types in HAI modelling and simulation are compartment-based and agent-based models [18–20]. In a compartment-based model, the population is divided into groups (compartments), and the number of agents of each compartment are tracked in the model. Each compartment represents a stage of the infection history. The most common compartments are Susceptible (S), Exposed (E), Infectious (I) and Recovered or removed (R). Different combinations of these compartments lead to different model structures, and the usual model structures, depending on the aims and the level of details are: S-I, S-I-S, S-I-R and S-I-R-S. Inside a compartment, we suppose homogeneous mixing of the agents. After the compartments are decided, one can define the governing equations of the model therefore the compartment models are given by closed mathematical equations. These equations can be differential or stochastic equations, and since the nature of the system is highly stochastic and the population size in a hospital is relatively low, therefore the latter one is more common. (Compartment models therefore are very similar to System Dynamics discussed in the previous subsection).

In the agent-based simulations of HAI spreading, the agents are patients and HCWs, and the interactions are the treatments. The model is driven by discrete (usually stochastic) events. A model like this can be used to predict the effect of the interventions, and therefore, it can support decision making. In an ABS we can investigate models where the population is inhomogeneous, and we can define any interaction that we can represent with a computer program. Therefore, we have greater flexibility in the modelling compared to the compartment-based models, but this flexibility has a price [21]: the simulation time can be very long due to the complexity, the validation of the model is much more difficult, and in addition, it is very hard to plug an agent-based model into an estimation method to estimate the model parameters from recorded time series.

In this paper our focus is on agent-based models. Ferrer et al. [22] built a model that combines the operational and the epidemiological perspectives to size-up the effect of understaffing and overcrowding in an Intensive Care Unit (ICU). In their model they have taken into account the work schedule, sick leaves, workload, fatigue and occupation state of HCWs. Milazzo et al. [21] tested the effect of spatial and personnel cohorting. In [23] the spread of influenza like illness was simulated. The model contains the immunity of the patients and the spatiality of the ward (emergency ward), and they tested the effect of infection control policies. Meng et al. [24] built a transmission model based on patient to patient transmission routes, and tested the effect of admission and repeat screening tests, shorter test turnaround time, isolation, and decolonisation. Lee et al. [25] investigated the effect of an MRSA outbreak in a region (Orange Country, California) containing multiple hospitals, they modelled patient movement and the MRSA spreading between the institutions. Hernbeck et al. [26] tracked the motion of HCWs and the patient-HCW, HCW-HCW interactions using sensor network. They have built an agent-based simulation on the resulting hospital society network, and investigated the effect of peripatetic HCWs (having large and diverse set of contacts) on the spread of HAIs.

2 The Elements of The Conceptual Model

Our aim was to build an extensible and robust simulation framework to be able to model a wide range of different hospital infection spreading scenarios. These models are infection spreading processes embedded into a hospital simulation. During the design, we have identified, (1) the main hospital processes affecting the infection spreading, (2) then the elements of the infection spreading, and finally (3) the interaction points with each other. The identified processes of (1) - (3) are together what we call conceptual model.

2.1 Hospital Processes

The basic organization unit of the hospital is the ward. There are two types of individuals: patients and healthcare workers. We do not deal with visitors, because our primary interests are HAIs (but the model is open: we can extend it with visitors). The patients belong to a specific ward, but the caregivers can work in multiple wards.

The identified hospital processes are the following:

1. The admission process: the arrival of new patients to a hospital ward. New patients can arrive from outside (other hospital, community) or from an another ward of the hospital. Since the characteristic of each ward can be very different. Therefore, the admission pattern of each ward can be different in the same hospital.

2. The discharge of patients: the removal of the patients from the ward. In this framework, we determine (sample from a predefined distribution) the Length-

of-Stay (LOS) value of each patient at admission, and if the LOS is elapsed, the patient will be removed from the ward. In some cases, the LOS value can change later: for example, if a patent become infected, the LOS value will be increased.

3. Treatment scheduling: every HCW has a list of the treatments that she/he can perform, and at admission, a list of treatments (demand for treatments) is assigned to each patient. Every treatment demand has an urgency value between 0 and 1 (which can change in time). The treatment scheduling process assigns one (or more, if it is necessary) available HCW(s) to the patients according to the treatments urgency, and also determines the length of the treatment duration (sample from a predefined distribution). The treatment demands list of the patients can also change later, again, in case of infection, the infected patients need more care. In the conceptual model, we do not fix any scheduling method.

4. Treatment processing: The treatment scheduler generates patient-HCW assignments, and assigns a treatment and a treatment duration for each pair. In this step, the HCWs perform the treatment.

2.2 The Infection Spreading Process

We suppose that there can be multiple pathogen types in the hospital, and an individual can be clean, colonized or infected for each of the pathogen types. Colonization means that the pathogen's strains are in the different parts of the host's body, but she/he is asymptomatic. In contrast, if somebody is infected, she/he has symptoms, which means sickness. We suppose that patients are reservoirs. Therefore, if a patient becomes colonized, she/he remains colonized (unless we do not do a complete decolonization), but HCWs are not reservoirs, so for HCWs we define maximum colonization time.

We have identified the following elements of the spreading process:

1. Admission colonization: a newly admitted patient can be colonized or infected by one or more pathogens. The admission colonization process decides if an admitted patient is colonized/infected or not.

2. Transmission process: the pathogen transmission from one agent to another. The transmission routes can be: patient to HCW, HCW to patent, HCW to HCW, patient to patient, environment to patient, environment to HCW, patent to environment and HCW to environment. Pathogen transmission or colonization does not mean infection, it means only that the pathogen moves from one agent to another.

3. Infection process: the process when a colonized patient become infected and has symptoms. If a patient becomes infected, then it can increase the LOS and the number of treatment demands.

4. The infection control measures are sub-processes or modifiers of the previ-

ously defined processes. For example hand washing/rubbing is performed in the treatment processing part, staff cohorting strategy modifies the treatment scheduler, surveillance can be part of almost all of the main processes.

3 Implementation Issues

Infectious Hospital Agents is an agent-based programming simulation framework, where the agents are patients and HCWs. The design is in object-oriented fashion and the elements of the sketched conceptual model are implemented via (abstract) classes. We have tried to create a very general and extensible software design, and gave different implementations for each of the elements. These pre-implemented classes can be used as building blocks to set up different simulation scenarios. One can find the details of the object-oriented design in [27]. The implementation is in C++, and for generating differently distributed random numbers, we use the Boost.Random [28] library. We can retrieve all the events, statistics and transmission networks from the implemented event-oriented bookkeeping.

4 An Example

Here we present a demonstration simulation example, which is created with the IHA framework. This example is very simple, and some parameter values are not verified, but it can give an insight to the system, and some guidance about the parametrization. We simulate a hypothetical ICU-like ward, with the following properties:

- Only one ward.
- Pathogen: MRSA.
- Simulate only colonization.
- Do not use any infection control measure.
- Only one treatment type with averaged properties.
- Transmission routes: only patient-to-HCW and HCW-to-patient.
- Time unit is minute, time step: 10 minutes.
- The treatment scheduler is a priority based scheduler, where the priorities are the treatment urgency values. If the priorities are the same, it uses random selection.

Model parametrization:

- Admission process: It is a common assumption in hospital simulations, that the admission process is a Poission-process [16]. In this example we use this assumption, and set the admission process to a Poission-process with rate 1/180. Therefore, the mean time between two successive patient arrivals is

180 minutes.

- The Length-of-Stay distribution: Statistical parameter fitting methods shows that Lognormal, Weibull and Gamma distributions fit best to LOS empirical data [29]. Here we use the lognormal distribution to sample the LOS values of the patients. The lognormal distribution is a continuous probability distribution of a random variable, whose logarithm is normal distributed. The density function of the lognormal distribution is: $\ln\mathcal{N}(x;\mu,\sigma) = \frac{1}{x\sigma\sqrt{2\pi}}\exp\left[-\frac{(\ln x-\mu)^2}{2\sigma^2}\right]$, where μ and σ are the mean and standard deviation of the variable's natural logarithm. Setting $\mu = 1.3205061822$ and $\sigma = 0.3627345555$, we get that $E[LOS] = 4$ days and $SD[LOS] = 1.5$ days.

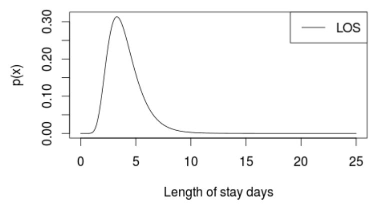

Figure 1
LOS density function

If we plot the probability density function of the LOS values (Figure 1), we can observe that it is an asymmetric heavy tailed distribution, and on the right side of the mean, the decreasing of the plot is not so steep, expressing the fact that greater LOS values may occur with a small, but not negligible probability.

- The probability of admission colonization set to 0.15 according to [30].
- It is a common assumption that the treatment duration is exponentially distributed [16], but it is a huge simplification, and it is hard to find a good parameter value. In this example, we set the parameter value of the exponential distribution to 1/10, expressing that the expected value of the treatment length is 10 minutes. However, this parameter is the weakest part of this example.
- The pathogen transmission probability is set to 0.05 according to [22]. In a more accurate model, the pathogen transmission probability should depend on the contact length, but here, as seen previously, our knowledges about the treatment duration length is inappropriate, therefore we do not use the time dependent model. Using fixed transmission probability, we can ensure that the treatment length does not have a direct effect to the infection spreading process, unless it is not too high.
- Treatment frequency: 8 times a day.
- HCW decolonization period: 1 day.

The length of the simulation was 120 days, but we have omitted the first 20 days to avoid the initial transients. We have run the simulation independently 100 times, and obtained the result time series by averaging these 100 independent runs: the number of patients in the ward (Figure 2a), the number of colonized patients (Figure 2b), the number of newly colonized patients (Figure 2c) and the rate of the colonized patients (Figure 2d). The number of colonized patients are the number of patients who were colonized at admission plus the number of newly colonized patients. The average number of newly colonized patients for this 100 day period is 17.08.

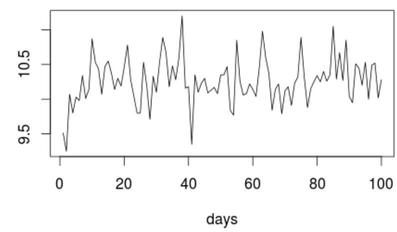

(a)
Average number of patients

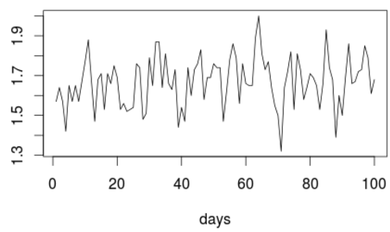

(b)
Average number of colonized patients

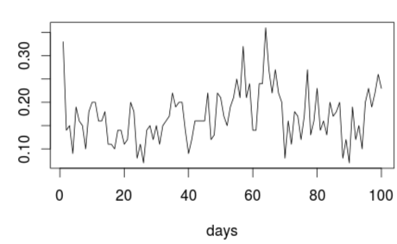

(c)
Average number of newly colonized patients

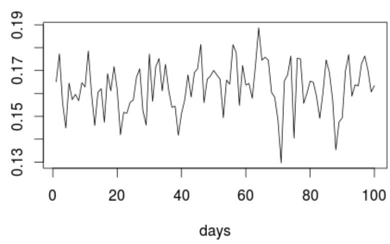

(d)
Rate of colonized patients

Figure 2
The simulation results: averaged time series

In the second part of the example, we study the effect of changing the pathogen transmission probability to the accumulated number of newly colonized patients in the ward. For this reason, we fix every parameter, except the transmission probability, and an $S = \{0.005, 0.01, 0.02, 0.03, 0.04, ..., 0.15\}$ test value set for the transmission probability. For each $p \in S$, we set the pathogen transmission probability to p, ran the simulation 100 times, and computed the average accumulated number of newly colonized patients, and additionally the average accumulated number of colonized patients. The results are summarized in Table 1 and in Figure 3. If p is small, then practically there are no newly colonized patients in the ward, because we assume that the HCWs are not reservoirs, and the probability that there is a pathogen transmission from a colonized patient to a HCW and the same HCW passes on the pathogen to an another uncolonized patient in a 24 hours length time interval (the maximum colonization time for a HCW is set to 24 hours) is very small. In this case, the admission colonization process keeps the pathogen in the ward. As we increase the transmission probability, the number of newly colonized patients are increasing (as we expect), and the rate of newly colonized patients is rising in the total number of colonized patients, and about $p = 0.11$, the number of newly colonized patients reaches the number of patients who were colonized at admission (supposing that the probability that a patient is colonized at admission is 0.15).

Table 1
Results of testing the model in different transmission probabilities

Transmission probability	Colonized patients	Newly colonized patients
0.005	154.42	0.52
0.01	154.54	1.03
0.02	156.83	3.85
0.03	158.62	6.1
0.04	162.55	11.72
0.05	166.78	17.08
0.06	175.16	28.91
0.07	186.53	44.28
0.08	195.66	56.92
0.09	211.38	75.94
0.1	228.16	99.53
0.11	257.84	135.36
0.12	279.73	162.45
0.13	306.92	195.87
0.14	336.84	229.11
0.15	358.41	255.19

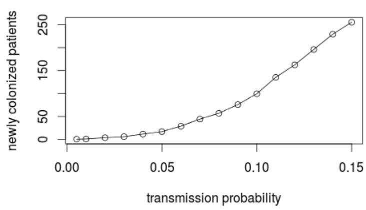

Figure 3
Newly colonized patients in function of transmission probability

Finally we investigate the impact of changing the admission colonization probability parameter to the accumulated number of colonized and newly colonized patients.

Here, we fix the transmission probability to 0.07 (We use higher transmission probability, to scale up the effect of the change in the admission colonization probability), set the rest of the parameters as before, and test the system setting the admission colonization probability to $\{0.05, 0.01, 0.02, ..., 0.17, 0.2\}$. As before, we run the simulations for each of the values of the admission colonization probability 100 times, and obtain the results by averaging the time series. The result are gathered in Table 2 and shown in Figure 4 and Figure 5. We can see in the figures, that the number of colonized patients and the number of newly colonized patients increase more or less linearly when we increase the probability of admission colonization, as it is expected.

Table 2
Results of testing the model against different admission colonization probabilities

Admission colonization	Colonized patients	Newly colonized patients
0.005	6.67	1.68
0.01	13.06	3.68
0.02	26.15	7.41
0.03	37.09	9.17
0.04	49.1	11.06
0.05	60.3	13.46
0.06	74.19	16.91
0.07	86.52	19.89
0.08	100.81	24.87
0.09	115.44	29.89
0.1	128.77	33.53
0.11	140.31	36.31
0.12	152.32	38.09
0.13	163.93	40.44
0.14	176.42	43.19
0.15	186.53	44.28
0.16	198.63	46.55
0.17	209.7	47.23
0.2	243.83	51.74

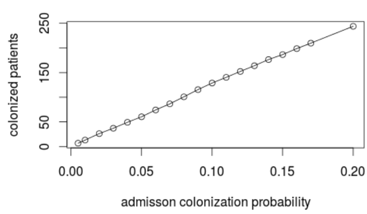

Figure 4
Colonized patients in function of admission colonization probability

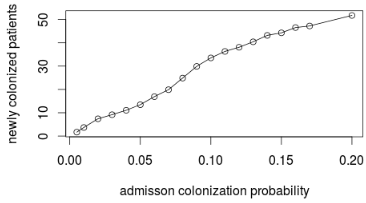

Figure 5
Newly colonized patients in function of admission colonization probability

5 Discussion

In this paper we have described the motivations and the background of the IHA simulation framework, presented the conceptual model, and a simple example of the usage of the framework. In the conceptual model, we have identified the main hospital processes affecting the spreading process, we have described the elements of the spreading process, and the way how the hospital processes and the spreading process interact with each other. According to these, we can see, that the spreading process is embedded deeply inside the hospital, and any change of these processes can cause huge change in the other processes. Here, we have excluded a lot of factors from the model, for example: the role of visitors, roster pattern of the HCWs etc., however the conceptual model and the simulation framework are open and extensible. The described work here is a tool development for future research.

5.1 Future Work

From software development perspective, we have to work on the validation of our system, because the complexity of the software requires the usage of same systematic software validation method. From modelling perspective, we have to extend the framework with more precise implementation of each sub-processes. Here, we highlight some of them:

- It is a common assumption that the admission of patients is a Poission-process [16]. In practice often that is not the case. When we use Poission-process, we implicitly suppose that the following conditions are true [31]:
  1. The probability of more than one arrivals in a short Δt length time interval is low ($o(\Delta t)$).
  2. The $p(\Delta t)$ probability that at least one patient arrives in a Δt time interval is "almost linear" function of Δt, ($p(\Delta t) = a\Delta t + o(\Delta t)$).
  3. The interarrival times (times between two successive arrivals) are independent random variables.

  Here a is a positive constant and o is the common asymptotic notion: $f(x) \in$

$o(g(x))$ means $\lim_{x\to\infty}\frac{f(x)}{g(x)}=0$ The consequence of these assumptions is that the arrival process is a Poission-process. However, as mentioned in [16], these conditions are often not met. For example, sometimes several patients arrive in an Emergency Department (ED) at the same time (several people injured in the same car accident), which clearly violates the condition (1), or the probability of new patient arrivals could depend on the previous arrivals when ED is close to its capacity, which contradicts to condition (3), or the average arrival rate varies during a day, etc. These phenomena may directly effect the infection spread, for example the sudden increase of the load on the HCWs may decrease the hand hygiene compliance, causing higher transmission rate. Consequently, to be able to make the arrival process more precise, we have to create more accurate statistical models, and collect more data to support these models.

- The duration of the patient-HCW contacts is an important factor in the transmission process, since obviously the transmission probability increases with the contact time. However, there is a lack of statistical results about the treatment durations. One way to fix this problem is observing the proximity patterns of the agents in the hospital: collecting data about who is close to whom at what time. This kind of information is invaluable, when we want to study the spreading phenomenon, not only to build statistics about the contact durations. For example, the SocioPatterns project has developed a platform that allows physical proximity measurements using wearable sensors based on radiofrequency identification devices (RFID) [32]. The human body acts as a shield for the radiofrequency signals, therefore the sensors record only contacts when the individuals are facing each other, and thus a contact can be considered as indicative of communication and contact between the individuals. Using these sensors, the temporal proximity networks of patients [33], school children [34], and conference attendees [35] have been successfully recorded.
- If we have statistics concerning the contact durations, we can build and apply different time-dependent transmission models.
- There is a lot of question about the infection process itself. What is the probability, that a colonized patient become infected? Clearly, it depends on not only the pathogen, but also the patient. This probability is very different for a patient in a regular Emergency Department from a patient after immunosuppressive therapy in a transplantation institute. Furthermore, how does the infection increases the LOS of the treatment and treatment demand? These questions lead to the modelling of the immunity of the patients.

Acknowledgement

The research was supported by European Research Council Starting Grant (ERC-StG 679681). Tamás Ferenci was supported by UNKP-16-4/III New National Excellence Program of the Ministry of Human Capacities.

References

[1] CDC, Get Smart: Know When Antibiotics Work. http://www.cdc.gov/getsmart/community/about/antibiotic-resistance-faqs.html.

[2] Alfonso J Alanis. Resistance to antibiotics: are we in the post-antibiotic era? *Archives of medical research*, 36(6):697–705, 2005.

[3] Eyal Zimlichman, Daniel Henderson, Orly Tamir, Calvin Franz, Peter Song, Cyrus K Yamin, Carol Keohane, Charles R Denham, and David W Bates. Health care–associated infections: a meta-analysis of costs and financial impact on the us health care system. *JAMA internal medicine*, 173(22):2039–2046, 2013.

[4] Didier Pittet, Benedetta Allegranzi, Hugo Sax, Sasi Dharan, Carmem Lúcia Pessoa-Silva, Liam Donaldson, John M Boyce, et al. Evidence-based model for hand transmission during patient care and the role of improved practices. *The Lancet infectious diseases*, 6(10):641–652, 2006.

[5] Benedetta Allegranzi and Didier Pittet. Role of hand hygiene in healthcare-associated infection prevention. *Journal of Hospital Infection*, 73(4):305–315, 2009.

[6] A Rampling, S Wiseman, L Davis, AP Hyett, AN Walbridge, GC Payne, and AJ Cornaby. Evidence that hospital hygiene is important in the control of methicillin-resistant staphylococcus aureus. *Journal of Hospital Infection*, 49(2):109–116, 2001.

[7] SJ Dancer. The role of environmental cleaning in the control of hospital-acquired infection. *Journal of hospital Infection*, 73(4):378–385, 2009.

[8] Kepler A Davis, Justin J Stewart, Helen K Crouch, Christopher E Florez, and Duane R Hospenthal. Methicillin-resistant staphylococcus aureus (mrsa) nares colonization at hospital admission and its effect on subsequent mrsa infection. *Clinical Infectious Diseases*, 39(6):776–782, 2004.

[9] John A Jernigan, Amy L Pullen, Laura Flowers, Michael Bell, and William R Jarvis. Prevalence of and risk factors for colonization with methicillin-resistant staphylococcus aureus at the time of hospital admission. *Infection Control & Hospital Epidemiology*, 24(06):409–414, 2003.

[10] Tamás Haidegger, Viktor Varga, Ákos Lehotsky, Péter Róna, Róbert Pethes, Péter Szerémy, László Szilagyi, Tamás Ferenci, and Levente Kovács. Information technology tools employed in infection control. In *Computational Intelligence and Informatics (CINTI), 2015 16th IEEE International Symposium on*, pages 339–344. IEEE, 2015.

[11] Ákos Lehotsky, László Szilágyi, Tamás Ferenci, Levente Kovács, R Pethes, György Wéber, and Tamás Haidegger. Quantitative impact of direct, personal feedback on hand hygiene technique. *Journal of Hospital Infection*, 91(1):81–84, 2015.

[12] Tatiana V Gurieva, Martin CJ Bootsma, and Marc JM Bonten. Decolonization of patients and health care workers to control nosocomial spread of methicillin-resistant staphylococcus aureus: a simulation study. *BMC infectious diseases*, 12(1):302, 2012.

[13] Heidi SM Ammerlaan, Jan AJW Kluytmans, Heiman FL Wertheim, Jan L Nouwen, and Marc JM Bonten. Eradication of methicillin-resistant staphylococcus aureus carriage: a systematic review. *Clinical Infectious Diseases*, 48(7):922–930, 2009.

[14] Erika MC D'Agata, Pierre Magal, Damien Olivier, Shigui Ruan, and Glenn F Webb. Modeling antibiotic resistance in hospitals: the impact of minimizing treatment duration. *Journal of theoretical biology*, 249(3):487–499, 2007.

[15] Hong-Rui Sun, Xinxin Lu, and Shigui Ruan. Qualitative analysis of models with different treatment protocols to prevent antibiotic resistance. *Mathematical biosciences*, 227(1):56–67, 2010.

[16] A Kolker. Queuing analytic theory and discrete events simulation for healthcare: right application for the right problem, 2010.

[17] Murat M Gunal. A guide for building hospital simulation models. *Health Systems*, 1(1):17–25, 2012.

[18] Hajo Grundmann and B Hellriegel. Mathematical modelling: a tool for hospital infection control. *The Lancet infectious diseases*, 6(1):39–45, 2006.

[19] Esther van Kleef, Julie V Robotham, Mark Jit, Sarah R Deeny, and William J Edmunds. Modelling the transmission of healthcare associated infections: a systematic review. *BMC infectious diseases*, 13(1):1, 2013.

[20] Tan N Doan, David CM Kong, Carl MJ Kirkpatrick, and Emma S McBryde. Optimizing hospital infection control: the role of mathematical modeling. *Infection Control & Hospital Epidemiology*, 35(12):1521–1530, 2014.

[21] L Milazzo, James L Bown, A Eberst, G Phillips, and JW Crawford. Modelling of healthcare associated infections: a study on the dynamics of pathogen transmission by using an individual-based approach. *Computer methods and programs in biomedicine*, 104(2):260–265, 2011.

[22] Jordi Ferrer, Maëlle Salmon, and Laura Temime. Nosolink: an agent-based approach to link patient flows and staff organization with the circulation of nosocomial pathogens in an intensive care unit. *Procedia Computer Science*, 18:1485–1494, 2013.

[23] Marek Laskowski, Bryan CP Demianyk, Julia Witt, Shamir N Mukhi, Marcia R Friesen, and Robert D McLeod. Agent-based modeling of the spread of influenza-like illness in an emergency department: a simulation study. *IEEE Transactions on Information Technology in Biomedicine*, 15(6):877–889, 2011.

[24] Yang Meng, Ruth Davies, Katherine Hardy, and Peter Hawkey. An application of agent-based simulation to the management of hospital-acquired infection. *Journal of Simulation*, 4(1):60–67, 2010.

[25] Bruce Y Lee, Sarah M McGlone, Kim F Wong, S Levent Yilmaz, Taliser R Avery, Yeohan Song, Richard Christie, Stephen Eubank, Shawn T Brown, Joshua M Epstein, et al. Modeling the spread of methicillin-resistant staphylococcus aureus (mrsa) outbreaks throughout the hospitals in orange county, california. *Infection Control & Hospital Epidemiology*, 32(06):562–572, 2011.

[26] Thomas Hornbeck, David Naylor, Alberto M Segre, Geb Thomas, Ted Herman, and Philip M Polgreen. Using sensor networks to study the effect of peripatetic healthcare workers on the spread of hospital-associated infections. *Journal of Infectious Diseases*, page jis542, 2012.

[27] Pethes Róbert, Ferenci Tamás, and Kovács Levente. Infectious hospital agents: an individual-based simulation framework. In *Systems, Man, and Cybernetics (SMC), 2016 IEEE International Conference on*, pages 3434–3439. IEEE, 2016.

[28] Jens Maurer, D Abrahams, B Dawes, and R Rivera. Boost random number library, 2004.

[29] Alfio Marazzi, Fred Paccaud, Christiane Ruffieux, and Claire Beguin. Fitting the distributions of length of stay by parametric models. *Medical care*, 36(6):915–927, 1998.

[30] Werner C Albrich and Stephan Harbarth. Health-care workers: source, vector, or victim of mrsa? *The Lancet infectious diseases*, 8(5):289–301, 2008.

[31] Samuel Karlin and Howard E Taylor. *A first course in stochastic processes*. Academic press, 1975.

[32] Ciro Cattuto, Wouter Van den Broeck, Alain Barrat, Vittoria Colizza, Jean-François Pinton, and Alessandro Vespignani. Dynamics of person-to-person interactions from distributed rfid sensor networks. *PloS one*, 5(7):e11596, 2010.

[33] Lorenzo Isella, Mariateresa Romano, Alain Barrat, Ciro Cattuto, Vittoria Colizza, Wouter Van den Broeck, Francesco Gesualdo, Elisabetta Pandolfi, Lucilla Ravà, Caterina Rizzo, et al. Close encounters in a pediatric ward: measuring face-to-face proximity and mixing patterns with wearable sensors. *PloS one*, 6(2):e17144, 2011.

[34] Juliette Stehlé, Nicolas Voirin, Alain Barrat, Ciro Cattuto, Lorenzo Isella, Jean-François Pinton, Marco Quaggiotto, Wouter Van den Broeck, Corinne Régis, Bruno Lina, et al. High-resolution measurements of face-to-face contact patterns in a primary school. *PloS one*, 6(8):e23176, 2011.

[35] Juliette Stehlé, Nicolas Voirin, Alain Barrat, Ciro Cattuto, Vittoria Colizza, Lorenzo Isella, Corinne Régis, Jean-François Pinton, Nagham Khanafer, Wouter Van den Broeck, et al. Simulation of an seir infectious disease model on the dynamic contact network of conference attendees. *BMC medicine*, 9(1):1, 2011.

Indoor Navigation for Motion Disabled Persons in Medical Facilities

Rita Fleiner[1], Barnabás Szász[2], Gabriella Simon-Nagy[1], András Micsik[3]

[1]Department of Applied Informatics, John von Neumann Faculty of Informatics, Óbuda University, Bécsi út 96/b, 1034 Budapest, Hungary
{fleiner.rita; nagy.gabriella}@nik.uni-obuda.hu

[2]Faculty of Informatics, University of Debrecen, Kassai út 26, 4028 Debrecen, Hungary

[3]Department of Distributed Systems, Institute for Computer Science and Control, Hungarian Academy of Sciences, Lágymányosi u. 11, 1111 Budapest, Hungary,
andras.micsik@sztaki.mta.hu

Abstract: A data model is presented in the form of ontology which includes the indoor location description of hospitals, the indoor navigation features and the accessibility attributes for people with motion disabilities. The possible use of the ontology is demonstrated by outlining some RDF data excerpt, OWL definitions and SPARQL queries for the navigation features of future applications.

Keywords: Linked Open Data; ontology; indoor navigation; medical facility; accessibility

1 Introduction

Linked Open Data (LOD) [1] is a well-known method of publishing and interlinking open structured data on the Web so that computers can read it automatically. This method enables data from different sources to be connected and queried; connections can be created by utilizing links contained in datasets that refer to other datasets. The standard data model for Linked Open Data is Resource Description Framework (RDF). In RDF, data is structured as triples in the form of subject, predicate and object, which is called a statement. SPARQL is an RDF query language, designed to retrieve and manipulate data stored in RDF format.

In our previous works we developed general methods for indoor wayfinding. In this paper we address the special case of navigating inside the building of a medical facility. This means that the navigation task is defined between points of interest (POIs), rooms or departments of a hospital building as starting and end points. We also take notice of the accessibility features of building parts to support navigation for the motion disabled visitors and patients. To accomplish this, we allow description of several features of corridors and rooms that are significant in terms of accessibility, such as distance, number of stairs, and the presence or absence of barriers and assistance features in the building.

Outdoor navigation is widely available nowadays, and helps people to find a place while driving or walking or using public transport. This type of navigation is usually based on a map and coordinates provided by GPS. Inside buildings, however, a navigation system has to cope with more complex routes and lacks the use of GPS signals. Most of the current solutions require special and expensive hardware for indoor positioning. Instead of relying on an indoor coordinate system, our approach follows the natural way, how people give route advice to each other, telling which landmarks to pass in sequence to reach the destination. Requisites for our navigation method are kept as inexpensive and simple as possible. The solution should scale up to large buildings, like hospitals. In our work we exploit Linked Data and SPARQL for building flexible APIs providing location and routing information.

The complexities of the requirements demanded a data model developed as a formal ontology, which also helps to apply the Linked Data principles to the published data. During the ontology development our aim was to design a 4-star vocabulary described in the guidelines [2].

The aim of the paper is to provide a data model in the form of two ontologies: iLOC [3] and hLOC [4]. The iLOC ontology describes the indoor navigation features and the accessibility attributes for people with motion disabilities, the hLOC contains the indoor location description of hospitals, including supportive services typically found in medical facilities.

The rest of the paper is organized as follows. In Section 2, we describe research fields that are related to the topic and in Section 3, usage examples are presented that the suggested model should satisfy. In Section 4, the ontology achieving accessible indoor navigation is explained. In Section 5, the ontology of indoor location description of hospitals is introduced. Section 6, shows examples for SPARQL queries and OWL definitions using the developed ontologies.

2 Related Work

Linked datasets rely on vocabularies, schemas or ontologies. There were several attempts to provide indoor navigation ontologies. Worboys [5] provided a general overview of the state of the art, and defines a top level taxonomy to classify indoor models into semantic and spatial categories. Semantic indoor space models represent entity types, their properties and relationships. Topological models are concerned with the connectivity within a space. Geometrical models add quantification of distance and finally hybrid or multilayered models provide combined features of all the above.

OntoNav [6] is a semantic indoor navigation system and an ontological framework of handling routing requests. OntoNav navigates the users inside floors and buildings, but it does not provide navigation instructions within rooms, while in case of a large hall with several entrances it is useful to have routes inside the hall as well. The underlying INO ontology is unavailable, furthermore, it has most of the required implicit knowledge about selecting best paths and avoiding obstacles built into the path-finding algorithms, not into the ontology.

ONALIN [7] provides routing for individuals with various needs and preferences; it takes the ADA (American Disability Act) standards, among other requirements, into consideration. Buildings are modeled as hallway networks, and feasible routes can be identified for users having specific constraints. ONALIN uses pre-computed variants of hallway networks for each possible set of disabilities, and then runs path search algorithms on the selected hallway network.

Scholz and Schabus [8] created an indoor navigation ontology for the movement of production assets in a production environment, to support autonomous navigation in the indoor space. Production assets pass through steps of a workflow, and for each step the suitable equipment is found and the best route to the equipment is calculated. Details of route calculation are not given, but it is done with a tailor-made algorithm considering asset properties such as size or special handling instructions.

Geodint [9] uses standard shortest path algorithm in a derived graph model for navigation. None of the above ontologies is accessible at the moment of writing this paper. However, some parts of the conceptual semantic model were reused from these earlier work inspiring the hierarchy of classes. The main difference in our approach compared to the mentioned related work is the use of standard (or de facto standard) query languages and reasoning for the computation of routes. In this way we can keep the computation generic and use the model (the ontology) to describe all necessary knowledge for various types of route calculations. Thus, the need to design and implement a specialized route search algorithm for each domain and scenario can be avoided.

SNOMED CT [10] is one of the most comprehensive medical ontologies, consisting of more than 316.000 classes organized in a hierarchical structure. It is maintained and regularly updated by IHTSDO[1], the latest version was released in

[1] International Health Terminology Standards Development Organisation, http://www.ihtsdo.org/

September 2015. SNOMED CT contains terminology for the human body, medical procedures, pharmaceutical products, and also the logical and physical organization of healthcare facilities. The structured collection of hospital departments and room types has proven to be very useful in the process of constructing indoor navigation for medical buildings. SNOMED CT does not exist in RDF format, therefore we could not utilize it directly.

Several single-city navigation applications can be found that enable wayfinding for wheelchair users. Also, there are maps with accessibility information on public buildings. However, few applications provide a comprehensive solution for the differently abled to navigate in most cities. Perhaps the best-known international project is Wheelmap.org, an OpenStreetMap-based solution. Wheelmap concentrates on the needs of wheelchair users. Therefore, the color signs for locations are as follows: green color shows buildings that are fully wheelchair-accessible; yellow means partial accessibility; red signs show places that are not accessible for wheelchair users. The map also shows accessible toilets, based on the following criteria: the doorway's inner width is at least 90 cm, clear inner space is at least 150 x 150 cm, it has a wheelchair-height toilet seat, folding grab rails and accessible hand basin. [11]

Benner and Karimi [12] examined available ontologies (including INO and ONALIN) for pedestrian wayfinding and navigation, and found that there is a lack of generic approach for disability, existing solutions cover only parts of the whole spectrum. They suggest to focus more on the semantics of accessibility of the built environment.

Several countries have laws to ensure equal access to public services by the means of enforcing accessible building structures. These rules can be included in civil rights laws, or in architectural regulations. An example for the former case is the Americans with Disabilities Act of 1990 (ADA) in the USA, that regulates public buildings including medical facilities to be accessible for persons with motion (and other types of) disabilities. [13] In Hungary, the government regulation about national settlements planning and building requirements (OTÉK) orders the newly built and renovated public buildings to be accessible for wheelchair users by providing alternatives to stairs (slopes or stairlifts or elevators), the doorways with inner width of at least 90 cm, and accessible toilets. [14]

3 Usage Examples

Medical services are typically organized in several departments, each department located at different parts or on different floors of the hospital building. Departments usually include multiple medical-purposed rooms, such as examination and treatment, operating, or diagnostic imaging rooms, and also some non-medical rooms and services. Visitors, patients and medical staff may look for an actual room, a category of rooms (e.g. a toilet nearby), a department without the aim for a specific room, or just a location offering some services like an ATM or a vending machine.

The following use-case examples demonstrate the requirements for navigation in a medical facility:

The simplest case is when a person wants to get from one point of interest to another, for example finding a way from the building entrance to the room number 312. The navigation instructions should be simple and easy to follow: take the elevator to the third floor, go to the left in the corridor until you get to the vending machine, then look for the room number 312 nearby.

A somewhat more complicated situation arises when the visitor has incomplete information about their goal. A good example for this is a patient with an appointment for a heart checkup. He knows the name of the doctor (let us say Dr. Heart) and the department, which is outpatient adult cardiology in this case, but not the exact room number. A useful navigation application could offer two different options at this point: either navigate the patient to the information desk or the nurse station of the cardiology department, or offer a list of the rooms in that department with detailed information, so that the patient can find Dr. Heart's office in the list.

Another example can be a visitor looking for a toilet. In this case, the exact room number is irrelevant; the navigation should provide directions toward the nearest toilet available for visitors (as opposed to toilets of ensuites belonging to inpatients rooms, or toilets reserved for the personnel).

The user of the navigation application initializes the search based on the names of services or departments. However, the naming conventions differ from country to country, and sometimes even among hospitals of the same area. To support hospital navigation successfully, the ontology must accommodate these differences. The following examples provide some insight into the problematic cases.

The co-location of different services can result in compound names for departments: in Hungary, gynecology departments are mostly co-located with obstetrics and neonatal care, therefore they have a common name for the three services (another example is the frequent co-location of dermatology and genitourinary care). On the other hand, there are departments with generalized names and area of care such as Internal medicine, but some hospitals provide separate departments for different specialties like cardiology or gastroenterology.

The route search should consider various parameters of the corridors, doors and other building parts to accommodate the special needs of the differently abled, e.g. wheelchair users, or the elderly with motion difficulties. When initializing the query, the user gives the starting point and the goal as well as the accessibility preferences for the route. These preferences should be finely tuned to the person's needs, including the maximum distance they have to walk without a resting opportunity, the number of stairs, or the angle of slopes.

For example, a person using a wheelchair has to avoid stairs, and can only travel between floors by elevator. They also need wide-enough doors to cross, and a route without high door thresholds, and steep slopes. But different kinds of wheelchairs (e.g. an electric wheelchair) can travel through passages of different steepness, and even a standard wheelchair can travel different steepness routes depending on the direction (e.g. rolling up or down the slope). A wheelchair user can overcome some smaller barriers with help.

An elderly person using a walking cane may only want to walk less or climb as few stairs as possible, but it is not impossible for them to get through obstacles on the way.

The support of the staff of the medical facility (e.g. students, medical residents, ambulance personnel) is also among our aims. Therefore, navigation has to extend to staff-only rooms such as laboratories. However, the restricted access to these locations (e.g. door only passable using an RFID card) has to be described in the ontology and considered in the route search as a parameter.

4 iLOC Ontology

In this section the iLOC ontology is presented, which provides indoor location description of a general building, navigation method inside a building and accessibility attributes for people with disabilities. The iLOC ontology was designed in such a way that it can be extended easily by additional ontologies to serve environment specific use cases.

Figures 1 and 2 show the main classes as ovals and the most significant object properties as arrows between the classes. Classes defined in this ontology are using the *iloc* prefix, classes and properties used from other ontologies are prefixed with their own and such classes are marked with dashed line. Dotted arrows mark the subclass relationships between the classes.

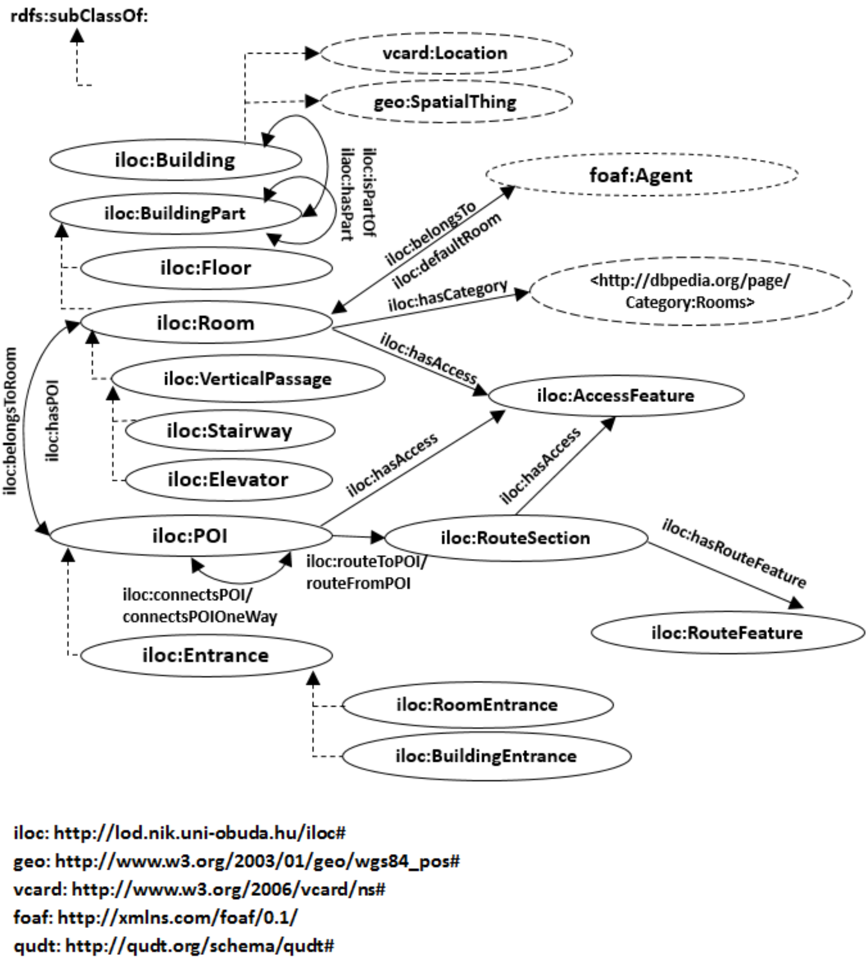

Figure 1
iLOC ontology

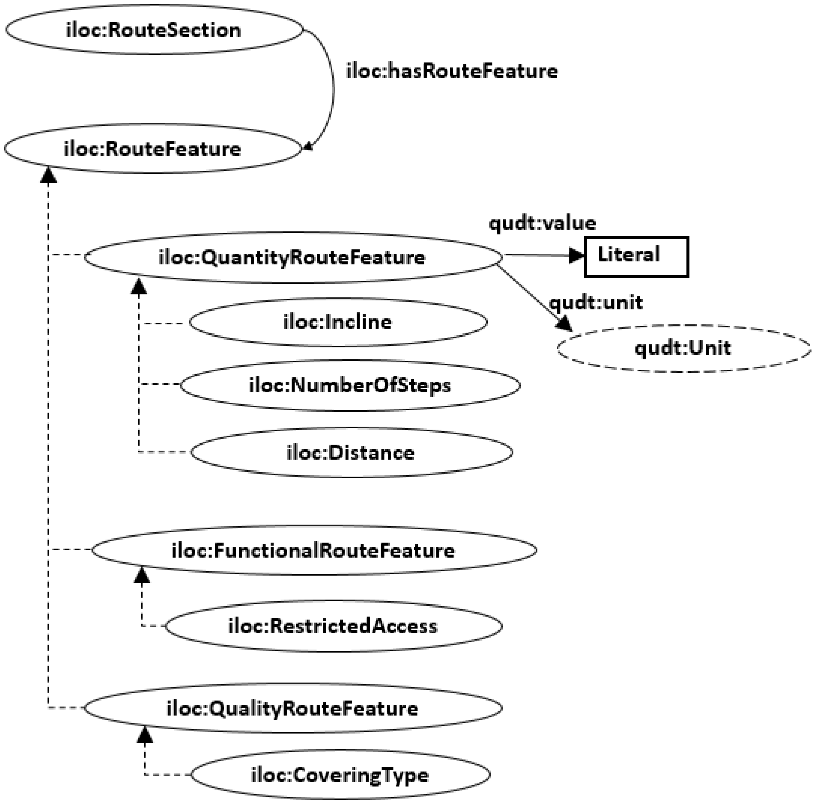

Figure 2
iLOC:RouteFeature and its subclasses

The iLOC ontology has three main classes: *Building*, *BuildingPart* and *POI*. *Building* class is a subclass of vcard:Location and geo:SpatialThing, in this way the address and the latitude, longitude coordinates can be assigned to its instances. *Building* entities have internal structure that the ontology aims to describe. *BuildingPart* provides an abstract concept to the different parts of the internal structure of a building. It has two subclasses: *Floor* and *Room*. A *Floor* entity represents an actual floor of a building. The *Room* class has a subclass *VerticalPassage* with special meaning for indoor navigation, its instances connect different *Floor* entities. *VerticalPassage* has two further subclasses: *Elevator* and *Stairway*.

The *isPartOf* object property, and its inverse property *hasPart* express hierarchical structural relationships within the building, e.g. a specific *Room* entity can be in *isPartOf* relation with a specific *Floor* entity. A *Room* instance is not tied to a specific floor directly, as there are examples when room height and floor height do not match and the room has entrances on multiple floors. Another example is an

Elevator or *Stairway* instance that can belong also to multiple floors. The solution is that a specific *Room* instance can be assigned to more floors with the *isPartOf* property.

Additional environment specific ontologies can define further *Room* subclasses for shopping malls, universities and other use cases; hLOC is such an ontology for hospital environments. The environment specific subclasses do not play a special role in the navigation process; they can act as custom filters to select specific type of rooms. In most cases, at the beginning of the navigation the exact starting point or target point is not exactly known by the user, a potential list of rooms can support the user's choice. So the classification of the rooms can help to narrow down the potential list of rooms to a convenient length.

Room entities might belong to *foaf:Agent* entities, represented with the *belongsTo* property. With this property, *Room* instances can belong to specific organizations, and also to certain persons. In the hospital environment for example, in this way we can represent the location of a room in a department, or the linkage of a room to a certain person. Domain ontologies should define the necessary organization-type subclasses. A default *Room* instance might be assigned to a specific *foaf:Organization* entity with the *defaultRoomOf* property. This may be useful, if one has limited knowledge about the actual room he/she is looking for, only the specific organization is known (e.g. the department name in a hospital). Entities of the *Room* class can be classified into further external categories by the *hasCategory* property which can point to room categories defined in DBpedia[2].

The *POI* (Point of Interest) class plays an important role in the navigation process supported by iLOC. An indoor route is built up by a consecutive sequence of *POI* instances, where adjacent *POI* entities are connected with the *connectsPOI* property. In iLOC the *POI* class has one subclass: *Entrance*, which is further specified as *RoomEntrance* and *BuildingEntrance*. The *Entrance* instances have the special meaning of defining the connections between rooms or the entry point to buildings. Constraints in the ontology require that each building and room should have at least one entrance and a room entrance should belong to exactly two rooms. Similarly, to the class *Room*, additional *POI* subclasses can be defined in environment specific ontologies. Examples for *POI* class instances are statues, bank automats, display boards or vending machines.

The *connectsPOI* describes a direct route between two *POI* instances, the navigation route between two connected POIs is taken for granted. The *connectsPOIOneWay* is the asymmetric parent property of the *connectsPOI* property. It describes one-way routes between points. A navigation route is defined by a series of named and connected POIs. This approach supports

[2] http://wiki.dbpedia.org/

instructions like: “Cross the building entrance. Pass by the display board. Go to the stairs. Go to the 4th floor. Pass by the bank automat. Look for Room 407.” The *hasPOI* property and its inverse property (*belongsToRoom)* express *POI* and *Room* relationships, a specific *Room* entity contains a given *POI* entity.

The *RouteSection* class represents a traversable path between two connected POIs. When defining a *RouteSection* instance its endpoint POIs must be specified. Route sections can be described by various attributes, among these there exist qualitative (e.g. covering type), quantitative (e.g. length, width, number of steps and incline) and functional descriptors or constraints (e.g. restricted access). It follows that certain accessibility constraints (e.g. usable for wheelchairs) can be inferred from certain route properties, but they can also be specified by manual entries on the basis of human decisions.

Extra information about route and disability profiles can be added to a RouteSection instance with the help of the *RouteFeature* and *AccessFeature* classes. The role of the *RouteFeature* class is to add extra descriptions to *RouteSection* instances that can be used in patient customized wayfinding queries. As shown in Figure 2, *RouteFeature* class has three direct subclasses *QuantityRouteFeature*, *QualityRouteFeature* and *FunctionalRouteFeature*, which can have further subclasses. *QuantityRouteFeature* subclasses (e.g. *Distance, Incline* or *NumberOfSteps*) contain instances having unit properties and numeric values as well. The QUDT ontology[3] can be used in providing generic measures and units to reuse. *QualityRouteFeature* subclasses (e.g. *CoveringType*) contain instances that describe specific qualities of the route sections. *FunctionalRouteFeature* subclasses (e.g. *RestrictesAccess*) contain instances adding extra information about the funcionality of the route. The *hasRouteFeature* property establishes the connection between the *RouteSection* and the *RouteFeature* classes. With the above property class hierarchy our aim is to present an extensible property framework, and not to give a complete and final solution for route descriptors.

The *AccessFeature* class represents different disabilities that require special features to traverse a *RouteSection* entity or to use a *Room* or *POI* instance. As we focused on supporting people with motion disabilities, the following instances were defined for the AccessFeature class for representing different accessibility needs: *Wheelchair*, *EWheelchair* (for electronic wheelchair), *WheelchairWHelp* (for wheelchair with help), *Stretcher* and *Stroller*. *RestrictedAccess* instance was introduced to represent areas where permission is required for the access. In the future additional instances can be added to the list in order to widen the accessibility features. The *hasAccess* property can be used to associate a specific disability constraint to a *RouteSection*, *Room* or *POI* instance.

[3] http://qudt.org/schema/qudt#

5 hLOC Ontology

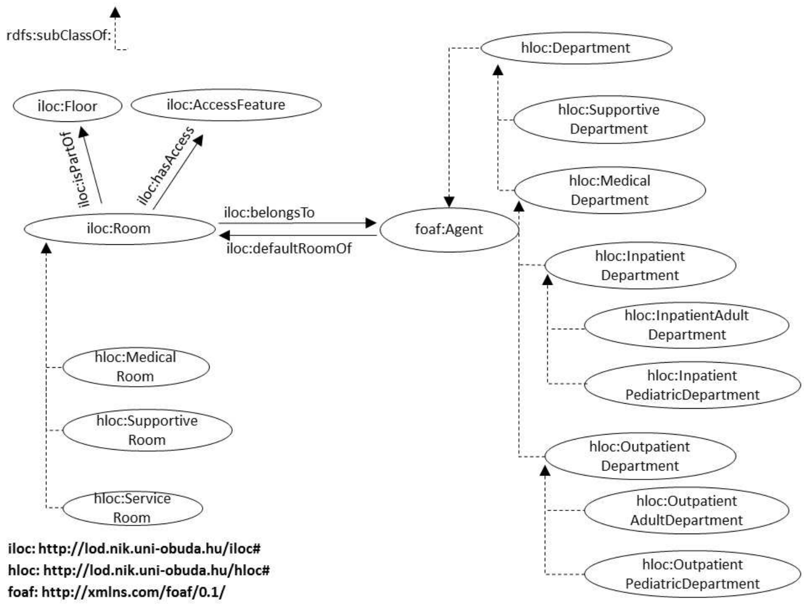

Figure 3
hLOC ontology

Hospitals have a number of room types and other building features that are typical of medical service facilities. For an ontology to support indoor hospital navigation, it has to contain descriptions of medical purpose locations.

iLOC does not have these specifics, however, it can be extended to provide support for indoor environments with special requirements. hLOC is an extension over iLOC that enables its usage in hospitals and to provide navigation support for people with motion disabilities. This ontology uses the prefix *hloc*.

The overview of the hLOC ontology is shown in Figure 3. The hLOC ontology extends iLOC with semantic classifications for hospital indoor structure. One of these is the definition of three iloc:Room subclasses in compliance with the room categories in the hospital environment. These are the classes: *MedicalRoom*, *SupportiveRoom* and *ServiceRoom*.

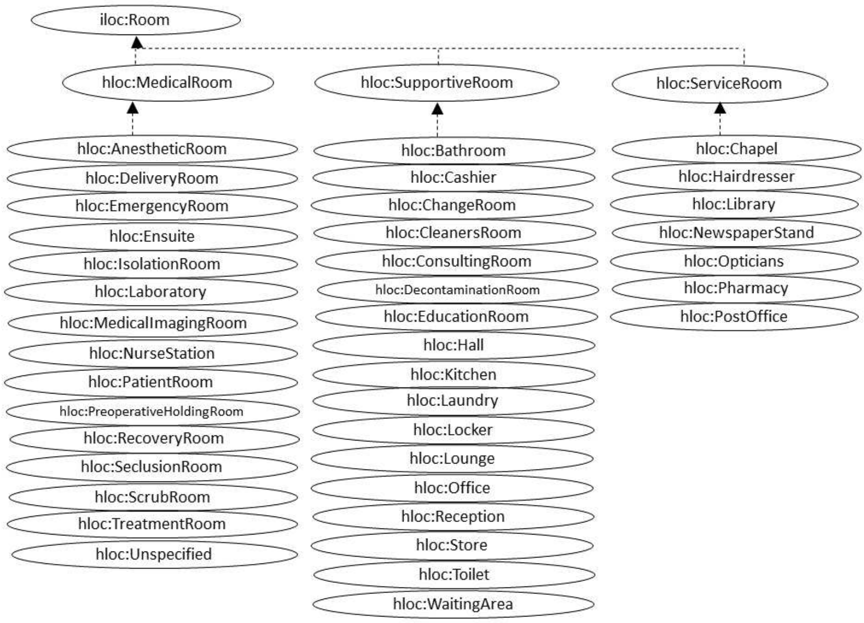

Figure 4
iLOC Room subclasses in hLOC

The subclasses of the MedicalRoom class cover medicine-specific room types like medical imaging rooms, operating and emergency rooms or ensuites for patients staying permanently in the hospital. Supportive rooms are also necessary for the daily operation of the hospital but not direct scenes of medical procedures. Examples of SupportiveRoom subclasses can be: DecontaminationRoom, Kitchen, Toilet, Office and so on. A service room can be any optional, convenience type service provided in the building of the hospital, such as a chapel, shop, pharmacy or post office.

In Figure 4 we give a recommendation for the list of iloc:Room subclasses (falling under *MedicalRoom*, *SupportiveRoom* and *ServiceRoom*) based on [10, 15].

The hLOC ontology also contains the class *hloc:Department* as the subclass of foaf:Organization. The hloc:Department has two direct subclasses: *SupportiveDepartment* and *MedicalDepartment*. MedicalDepartment can be further classified according to the following features: inpatient or outpatient, and adult or pediatric. Inpatient departments provide care for people in need of long-term medical assistance. Therefore, they contain ensuite type medical rooms to accommodate patients. Outpatient departments are specialized in shorter medical procedures, where the patient is able to go home after treatment.

Both inpatient and outpatient departments can be either for adults or children. In this way we get the following subclasses: *InpatientPediatricDepartment*, *InpatientAdultDepartment*, *OutpatientPediatricDepartment* and *OutpatientAdultDepartment*.

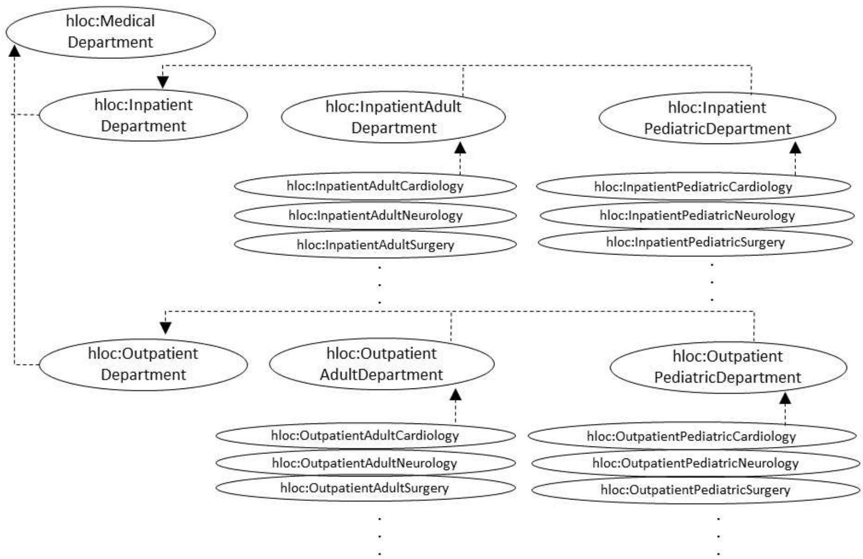

Figure 5
Examples for Medical Department subclasses

The recommended complete list (made by studying the SNOMED CT taxonomy and the structure of several prestigious hospitals in Hungary and abroad) for Medical Department names is the following:

Addiction Services, Anesthesiology, Andrology, Cardiology, Clinical Laboratory, Critical Care, Dentistry, Dermatology, Diagnostic Imaging, Dietetics, Emergency, Endocrinology, Gastroenterology, Genetics, Genitourinary Medicine, Gynecology, Hematology, Hepatology, Immunology, Internal Medicine, Microbiology, Nephrology, Neurology, Neonatology, Obstetrics, Oncology, Ophthalmology, Orthopedics, Otolaryngology, Palliative Care, Pathology, Physiotherapy, Plastic Surgery, Psychiatry, Psychology, Respirology, Radiology, Rehabilitation, Rheumatology, Sports Medicine, Surgery, Toxicology, Trauma, Urology.

The exact name for a certain MedicalDepartment subclass arises as follows: [Inpatient | Outpatient] ‖ [Adult | Pediatric] ‖ [MedicalDepartment_name]. For example, for the term *Neurology, InpatientPediatricNeurology* is generated as an *InpatientPediatricDepartment* subclass. Figure 5 shows some examples for Medical Department subclasses following the structure of the hLOC ontology.

6 Evaluation

In this section data excerpts, OWL definitions and SPARQL queries are presented to demonstrate the possibilities of the developed ontologies. The following excerpt describes RouteSection, POI and Room instances:

```
@prefix iloc: <http://lod.nik.uni-obuda.hu/iloc/iloc#> .
@prefix rdfs: <http://www.w3.org/2000/01/rdf-schema#> .
@prefix foaf: <http://xmlns.com/foaf/0.1/> .

:RS014 a iloc:RouteSection;

iloc:hasAccess iloc:Stretcher;

iloc:hasRouteFeature [

        a iloc:NumberOfSteps;

        qudt:value 1.]

iloc:hasRouteFeature [

        a iloc:Distance;

        qudt:value 21;

        qudt:unit qudt:meter .]

iloc:routeFromPOI :CoffeMachine002;

iloc:routeToPOI :EntranceOfRoom203.


:CoffeMachine002 a iloc:POI;

rdf:label "Coffe machine on the 2nd floor"@en;

iloc:belongsToRoom :Hallway2ndFloor ;

iloc:connectsPOI :EntranceOfRoom203,

    :EntranceOfRoom202,

    :EntranceOfToilet2ndFloorLadies.


:EntranceOfRoom203 a iloc:Entrance;

rdf:label "Entrance of Room 203"@en;

iloc:belongsToRoom :Hallway2ndFloor ;

iloc:belongsToRoom :Room203 ;

iloc:connectsPOI :CoffeMachine002,

    :EntranceOfRoom202,

    :EntranceOfToilet2ndFloorLadies.
```

```
:Room203 a iloc:Room;
rdf:label "Room 203"@en;
iloc:belongsTo hloc:InpatientAdultDepartment ;
iloc:defaultRoomOf ex:InstitueOfCardiology ;
iloc:hasAccess iloc:WheelChair;
iloc:hasPOI :EntranceOfRoom203.
```

We can define the list of tolerable route features for wheelchair users and for visitors as RouteFeature subclasses: WheelChairAccessibleFeature and VisitorAccessibleFeature. Using the Protégé syntax for OWL restrictions, we can then write a definition for Wheelchair Accessible RouteSection individuals as follows:

```
WheelChairAccessibleRouteSection ≡ RouteSection and ( hasRouteFeature only
WheelChairAccessibleFeature)

VisitorAccessibleRouteSection ≡ RouteSection and ( hasRouteFeature only
VisitorAccessibleFeature)
```

Finally, if we have calculated a Route individual referring to all included RouteSections with the object property sections, the reasoner can automatically classify a route into a visitor accessible route using this class definition:

```
VisitorAccessibleRoute ≡ sections only VisitorAccessibleRouteSection
```

SPARQL 1.1 supports property path queries that can be used in wayfinding queries. It does not return what the path is nor the length of the shortest path - only whether there is such a path. By probing against different path lengths, this limitation can be overcome by a query similar to the following, which returns the shortest route (routes with the least steps) between <room1> and <room2> (with maximum length of three steps for brevity):

```
SELECT ?distance ?start ?p1 ?p2 ?p3 ?end WHERE {
  BIND (<room1> AS ?start ).
  BIND (<room2> AS ?end).
  ?p1 iloc:belongsToRoom ?start.
  ?p1 iloc:connectsPOI ?p2.
  ?p2 iloc:connectsPOI ?p3.
  ?plast iloc:belongsToRoom ?end.
  FILTER (?p3 = ?plast || ?p2 = ?plast || ?p1 = ?plast )
  BIND (if( ?p3 = ?plast , 3, if( ?p2 = ?plast , 2, if( ?p1 = ?plast , 1, -
1))) AS ?distance)
} ORDER BY ?distance LIMIT 1
```

Future SPARQL versions might better support such path queries by enabling access to the length of the path or to the specific elements of a route. OpenLink Virtuoso[4] has an extension for SPARQL with a transitive closure operator. The following SPARQL query using this extension provides the same result as the previous example:

```
SELECT ?step ?link WHERE {
  BIND (<poi1> AS ?start ).
  BIND (<poi2> AS ?end).
  ?start iloc:connectsPOI ?end OPTION(TRANSITIVE, t_no_cycles,
t_shortest_only, t_in(?start), t_out(?end), t_step (?start) as ?link,
t_step('step_no') as ?step, t_direction 3 ).
}
```

Gremlin [16], as a graph traversal language, is a functional language. The purpose of the language is to enable a human user to easily define a traversal, which is a tree of functions called steps, and thus, program a Gremlin machine. The following Gremlin code fragment provides the same result as the previous examples:

```
start = g.v(<room1>)

end = g.v(<room2>)

start.as('x').dedup().out('iloc:connectsPOI').loop('x')

  { it.loops < 3 && !it.path.contains(it.object) &&

    it.object != end }

.path.filter{it.last()==end}[0]
```

Although SPARQL is able to query longer path, not all implementation is capable to deliver results. Experiments were carried out with Apache Marmotta[5] and Virtuoso triplestores and also with Gremlin traversing engine. In some cases, Marmotta produced long response times in finding routes, queries were returning results in a wide range of 1-10 s. Virtuoso was significantly faster with its non-standard extension. The best performance was measured with the Gremlin traversing engine, queries were returning results in the 150-250 ms range.

Conclusions

In this paper we presented two ontologies iLOC and hLOC for supporting accessible free-text type indoor navigation in hospitals. The possible use of the ontologies was demonstrated by presenting SPARQL queries that future applications can build on to provide these navigation features. According to the classification of Worboys, iLOC with the extension of hLOC represents a hybrid indoor model since they contain semantic, topological and geometrical features as well, in the form of entity information, connectivity and distance descriptions.

4 https://virtuoso.openlinksw.com

5 http://marmotta.apache.org

The research contributions of the paper include the new ontological model of wayfinding which enables the use of SPARQL or Gremlin and inferencing for the calculation of indoor routes. This generic approach makes it possible to compute routes of different details, include third party local data into route finding and to apply various preferential and capability-based filtering for calculated routes. While previous approaches used specially constructed algorithms for wayfinding and disability specific concepts were built into the navigation ontologies, in our case it was possible to separate the generic task of navigation from concrete constraints on disabilities and building specific features. Furthermore, the domain of navigation in hospitals was investigated, and iLOC was extended with the novel hLOC ontology providing a wide range of way-finding functionality dedicated for hospitals.

References

[1] Berners-Lee, T. (2006) Linked Data-Design Issues, http://www.w3.org/DesignIssues/LinkedData.html

[2] Janowicz, K., Hitzler, P., Adams, B., Kolas, D., and Vardeman II, C. (2014) Five Stars of Linked Data Vocabulary Use. Semantic Web, 5(3) 173-176

[3] Szász, B., Fleiner, R., Micsik, A. and Simon-Nagy, G. (2016) iLOC – An Indoor Ontology, http://lod.nik.uni-obuda.hu/iloc/iloc-20161107.owl

[4] Fleiner, R., Simon-Nagy, G. and Szász, B. (2016) hLOC – A Hospital Ontology, http://lod.nik.uni-obuda.hu/hloc/hloc.owl

[5] Worboys, M. (2011, November) Modeling Indoor Space. In Proceedings of the 3rd ACM SIGSPATIAL International Workshop on Indoor Spatial Awareness (pp. 1-6) ACM

[6] Anagnostopoulos, C., Tsetsos, V., and Kikiras, P. (2005) OntoNav: A Semantic Indoor Navigation System. In 1st Workshop on Semantics in Mobile Environments (SME05) Ayia

[7] Dudas, P. M., Ghafourian, M., and Karimi, H. (2009, May) ONALIN: Ontology and Algorithm for Indoor Routing. In Mobile Data Management: Systems, Services and Middleware, 2009. MDM'09. Tenth International Conference on (pp. 720-725) IEEE

[8] Scholz, J., and Schabus, S. (2014, September) An Indoor Navigation Ontology for Production Assets in a Production Environment. In International Conference on Geographic Information Science (pp. 204-220) Springer International Publishing

[9] Matuszka, T., Gombos, G., and Kiss, A. (2013) A New Approach for Indoor Navigation Using Semantic Webtechnologies and Augmented Reality. In Virtual Augmented and Mixed Reality. Designing and Developing Augmented and Virtual Environments (pp. 202-210) Springer Berlin Heidelberg

[10] SNOMED CT. Systematized Nomenclature of Medicine - Clinical Terms, http://purl.bioontology.org/ontology/SNOMEDCT

[11] Wheelmap.org. How does Wheelmap work?, https://community.wheelmap.org/en/about/how-to-map/

[12] Benner, J. G., Karimi, H. A. Accessible Wayfinding Ontologies for People with Disabilities. Extended Abstract for the RDWG Online Symposium on Accessible Way-Finding Using Web Technologies, 3 December 2014

[13] The Americans with Disabilities Act of 1990 and Revised ADA Regulations Implementing Title II and Title III, http://www.ada.gov/2010_regs.htm

[14] 253/1997. (XII. 20.) Korm. rendelet az országos településrendezési és építési követelményekről - Akadálymentesítésre vonatkozó kivonat, Mozgáskorlátozottak Egyesületeinek Országos Szövetsége (MEOSZ), www.meosz.hu/doc/p26-2otek_segedlet.doc

[15] Department of Human Services, Victoria. (2004, November) Design Guidelines for Hospitals and Day Procedure Centres http://www.healthdesign.com.au/vic.dghdp/dghdp_content/guidelines/dghdp_part_b_complete_20_377.pdf

[16] Rodriguez, M. A. (2015, October) The Gremlin Graph Traversal Machine and Language (invited talk) In Proceedings of the 15th Symposium on Database Programming Languages (pp. 1-10) ACM

Cognitive Engine for Robot-assisted Radio-Frequency Ablation System

Xiaoyu Tan[1], Chin-Boon Chng[1], Bin Duan[1], Yvonne Ho[1], Rong Wen[2], Xuan Chen[3], Kah-Bin Lim[1] and Chee-Kong Chui[1]

[1] Department of Mechanical Engineering, National University of Singapore, 9 Engineering Drive 1, 117575, Singapore

[2] Planning and Operation Management, Singapore Institute of Manufacturing Technology (SIMTech), 2 Fusionopolis Way, 138634, Singapore

[3] Department of Electrical and Computer Engineering, National University of Singapore, 4 Engineering Drive 3, 117583, Singapore

xiaoyu_tan@u.nus.edu, e0015042@u.nus.edu, duanbin@u.nus.edu, yvonne.yw.ho@u.nus.edu, wenr@SIMTech.a-star.edu.sg, xuan.chen@u.nus.edu, limkahbin@nus.edu.sg, mpecck@nus.edu.sg

Abstract: In order to develop an efficient and user-friendly supervisory system for robot-assisted radio-frequency ablation of liver tumors, we proposed and developed a new cognitive engine. This novel framework, based on a hybrid architecture. This novel system can generate and supervise entire surgical procedures, which are readable for both operators and computers, by applying semantic methods. The entire prototype is constructed by ontology and operated by SPARQL query language in JAVA. According to ex-vivo phantom experiments, the cognitive engine provides surgical execution procedures correctly for the radio-frequency ablation surgical system. The proposed cognitive engine can be modified for many other robot-assisted applications.

Keywords: cognitive engine; radio-frequency ablation; needle insertion; surgical robots

1 Introduction

Recently, semantic approaches have been applied extensively in multiple applications designed to improve the intelligence in communication between operators and robots [1] [2]. Moreover, these robots can take advantage of semantic approaches in catering to different operational circumstances. Typically, these methods are constructed by ontology as a supervisory system with a readable experience database that is accessible for both human and computers (or processors) [3]. Hence, by recording the experience of the robots' operation into a knowledge database and querying operation procedures based on task-specific requirements, the effectiveness and efficiency of robotic implementation will be dramatically enhanced [4].

In this paper, a framework for a cognitive engine is proposed, to supervise an image-guide, robot-assisted, radio-frequency ablation surgical system as reported in [5] [6]. The cognitive engine can supervise and generate complete and unique surgical procedures from a knowledge database depending on the patient specific requirements and available surgical instruments. By constructing the cognitive engine in a semantic approach, the entire surgical system will be easily operated to perform similar surgical tasks. During or after the surgical operation, the knowledge can be updated automatically or manually to the cognitive engine, providing more options to satisfy patients and surgeons requirements for future surgeries.

The chosen language of a cognitive engine should be readable by both operators and processors. It should also be able to demonstrate the logical relationship between variant objectives. Hence, Web Ontology Language (OWL) is best suited for the task of constructing the knowledge database. OWL is developed from the Extensible Markup Language (XML) which is a widespread language used in website development [7]. By using Protégé [8], which is an OWL creation software, the semantic knowledge base can be easily established and the logical relationship can also be simplified. OWL is supported by multiple applications for performing various artificial intelligence tasks [9] [10]. Hence, the usage of OWL ensures the applicability of the knowledge database construction with other low-level control systems. By implementing the inbuilt semantic reasoning functions, Protégé can provide information for retrieval. However, the base retrieval system cannot be customized and is insufficient for the development of a cognitive engine. Therefore, SPARQL query language is utilized via a JAVA platform to enable semantic reasoning in the cognitive engine [11] [12] [13].

The proposed cognitive engine can perform semantic information recording, within an OWL knowledge database and semantic retrieval, through SPARQL query language. By combining these two functions, the cognitive engine can build specific surgical plans based on patients, surgeons or robotic instrument specifications. This paper reports our latest results since our cognitive engine was presented in the IEEE SMC 2016 conference [42]. As the knowledge database is expanded, the cognitive engine will provide more options for similar surgical operations. The cognitive engine can also be modified for other robot-assisted procedural applications.

2 Literature Review

2.1 Cognitive Architecture

The main objective of the application of cognitive architecture is to imitate the cognition function of animals and human when they encounter variable circumstances [14]. Cognitive science is, therefore, the foundation of related research in cognitive architectures, and it covers language, perception, memory, attention, reasoning and emotion [15]. For constructing a cognitive architecture, memory and reasoning are two crucial parts of the architecture.

The cognitive architecture, which is also called cognitivist architecture, can be realized by multiple methods [16]. These methods construct cognitivist architecture from a diverse stance of the nature of cognitive functions. There are three outstanding cognitive architecture paradigms – symbolic, emergent and hybrid.

2.1.1 Symbolic Architecture

The symbolic cognitive approaches are achieved by symbolic information processing representation systems. Symbolic architecture transforms the states and behaviors into symbolic representation and manipulating these representations to enhance the interaction and adaptation. During the expansion of the knowledge database, the effectiveness of symbolic architecture operation will increase [17]. The symbolic architecture also shows potential in artificial intelligent related research. In most of the symbolic architectures, researchers focus on how to create an artificial cognitive system with symbolic representation and make the whole system understandable by humans.

A cognitive vision system was developed to observe the traffic situation through videos based on symbolic architectures [18]. During several levels of processing, the videos which contains traffic information was transformed into symbolic representation in Situation Graph Trees (SGTs). This information was updated automatically during the operation. More methods have since been developed to translate SGTs into other logical relationships for other applications [19] [20].

This architecture was also implemented for decision making. One well-known method is dynamic decision networks [21], which is an extension of Bayesian Belief Networks. By combining the symbolic architecture in the network structure, the system can perform recognition, reasoning and learning. However, it involves too many manual tasks during system operation, which can be very time-consuming [22]. Moreover, the symbolic architecture can also be unstable in the handling noisy data [23].

2.1.2 Emergent Architecture

Emergent approaches are constructed by taking different stances on the nature of cognition. As researchers would like to utilize this architecture to imitate the real-time response features in cognition, this architecture is widely applied in dynamic systems and self-organizing systems [23]. These structures are supervised by a cognitive agent cell which can detect the environment in real-time and determine meaningful information for responses [24]. Typically, the quality of detection depends on the choice and installation of the sensors and how the emergent architecture is implemented with the sensor data in the cognitive cell [24].

There are two categories of emergent architecture: connectionist models and dynamic systems models. Connectionist models are built by a parallel structure which can perform non-symbolic methods to achieve specific relationships rather than using logical methods [25]. Dynamic systems models are also wildly used in artificial intelligence and can perform self-organization to arrange information and behaviors in an orderly manner, especially for larger groups of data [26].

Although the emergent architecture can provide correct real-time analysis, some of these procedures remain meaningless for human operators. These procedures cannot be presented in a semantic way for human understanding, during operation [27]. Hence, this architecture is not suitable for developing a supervision system for surgical robots which requires distinct objectives for each simple action.

2.1.3 Hybrid Architecture

Hybrid architecture is a combination between symbolic architecture and emergent architecture. By utilizing semantic reasoning approaches and non-symbolic approaches, to enhance the operational efficiency, the systems with hybrid architecture are usually designed to implement specific strategies under disparate circumstance [27].

Numerous studies have been conducted based on hybrid architectures [28] and introduced a practical way to perform semantic reasoning in norm compliance. By analyzing the logical relationship between various agents and normative behaviors, the authors constructed a normative layer, through which, by applying semantic reasoning, the procedure of taking norms at run-time, can be supervised and modified [28].

Hybrid architectures are also exploited in service, trade, and industrial applications. “Roboearth” robotic system is a typical service robotic system [2], capable of supervising multiple service robots at the same time. For individual service robots, they are capable of performing basic service tasks individually through fixed operating commands. However, these procedures are time-consuming because the invariable control commands contain repetitive actions such as repeated registration and recognition. After applying semantic approaches, individual robots can perform the service tasks automatically and upload their knowledge and experience on "Roboearth" cloud engine [29]. If other robots are requested to do the similar tasks, they will query the cloud engine and get initial information such as objectives and their positions [30].

Some industrial applications are also introduced in recent research. For example, human-machine interaction and industrial assembly were enhanced by applying semantic descriptors in system described in [1] [31]. This system can assist normal workers to learn and manipulate complex industrial robots. Under the assistance of semantic descriptors, workers can perform complicated assembling tasks in a shorter time. A new platform which can enhance the accuracy of manufacturing device testing is also reported in [32]. This platform which is named VirCA (Virtual Collaboration Arena), combines Virtual Reality (VR) and semantic approaches to establish a user-friendly human-machine interface. After applying VirCA in solving practical manufacturing issues, VirCA shows high reliability and efficiency in technical training [32].

Other applications which combine hybrid architectures have been recently reported. An ontology model-based method is introduced to provide medical assistance for cardiovascular disease diagnosis [43]. One breast tumor diagnosis system is also reported to reduce the normally manual classification error, by performing self-validating cerebellar model neural networks [44]. More ontology-based methods are also reported in recent research to enhance the evaluation for visualization [45] and realize the multilingual information retrieval in recommendation system [46] which shows the strength of ontology for organizing the information and performing specific information searching.

Although the systems discussed above, execute simple or several tasks, they do not fully explore the potential of applying semantic approaches under hybrid architecture in their current state. As hybrid architectures can store and share the experience for various applications and respond to different environments based on properties reasoning, this structure is worth exploring and has formed the basis of our proposed cognitive engine, for robot-assisted surgical system.

2.2 Radio-frequency Ablation Needle Insertion System

For performing large and multiple liver tumors ablation with high accuracy, consistency and efficiency, the Image-guide Radio-frequency Ablation (RFA) Surgical Robotic System [5] [6] was developed to implement minimally invasive ablation surgery based on commonly used clinical RF needles. This surgical robotic system incorporates several components including medical image processing, surgery pre-planning, KINECT-based vision registration and a needle insertion robot with a remote-center mechanism (RCM). The full system which is shown in Fig. 1 has been presented in the IEEE SMC 2016 conference [42].

Before the surgery, detailed diagnosis of patient, including clear computed tomography (CT) scan, is obtained. Based on the CT images, surgeons will begin the pre-operative planning with medical image processing to segment tumor areas, followed with the determination a single insertion point (SIP) on the patient's skin and planning various needle insertion trajectories through the SIP. KINECT-based vision registration will be performed to map the trajectories to the surgical robotic coordinate system. During the surgical operation, the surgical robot with spherical mechanism executes these trajectories through SIP to reach multi-targets to achieve the required surgical outcomes.

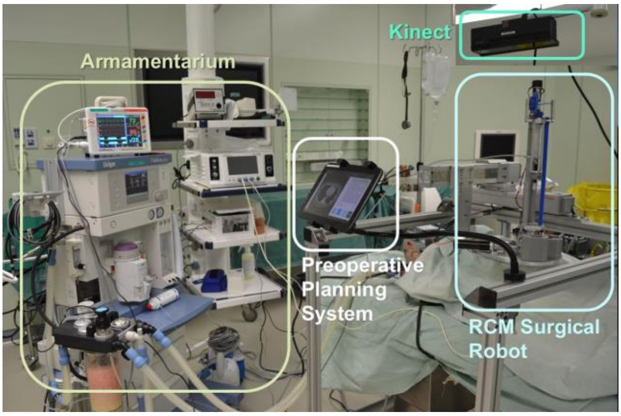

Figure 1
Image-guide Radio-frequency Ablation Surgical Robotic System

This surgical procedure could dramatically reduce the patient's blood loss and improve postsurgical recovery [5] [6]. However, this system requires substantial preparation time, during pre-operative planning. There is clearly a need for a more efficient framework.

3 Architecture of Cognitive Engine

The proposed cognitive engine is a supervisory intelligent cell used to generate semantic action sequences for guiding low-level control and provide an understandable semantic reference for pre-operative planning. This cognitive engine is constructed in OWL, by protégé software [7] [8]. Compared with other languages, which are widely used in semantic approaches such as DARPA Agent Markup Language (DAML) [32] and Simple HTML Ontology Extension (SHOE) [33], OWL is able to emphasize the semantic logical relationship with more facilities [32]. For semantic information retrieval, we apply SPARQL query language through the JAVA platform. The framework of surgical robot supervised by a cognitive engine is shown in Fig. 2.

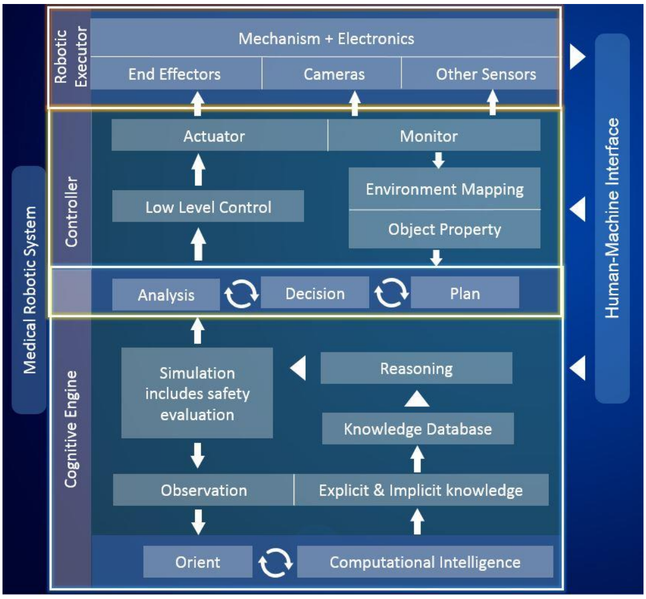

Figure 2
The framework of surgical robot supervised by a cognitive engine

During pre-operative planning, surgeons will import representative information such as objective titles into the cognitive engine for semantic reasoning. The cognitive engine will query the knowledge database and provide available surgery procedures with these keywords for selection. These procedures contain reliable analysis, decisions and operation guiding plan depending on the stored knowledge with acquired information from environment mapping and objective properties. However, this semantic reasoning procedure is designed to be accessible and manually revisable through the human-machine interface which is shown in Fig. 3 for safety consideration. Hence, flexible semantic reasoning is an essential part of the cognitive engine.

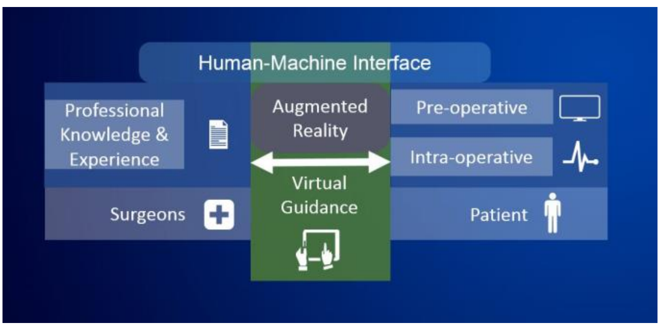

Figure 3
The human-machine interface during surgical robots operation

In order to verify safety and feasibility, the retrieved surgical procedures are first evaluated by embedded simulation testing. If the simulation results show that the risk level of performing retrieved surgical procedures on the assigned patient is relatively low, the cognitive engine will accept and send these procedures to the low-level control system for future surgical operations. Moreover, the overall processes of the simulation is also reviewed by the surgeons. Based on their judgment, surgeons and operators can modify the results of the simulation, which includes all decisions and plans.

For experience recording and knowledge storage, computational intelligence methods could be implemented to assist in extracting explicit and implicit knowledge from surgeons and operators. Therefore, their professional medical knowledge and surgical experience could be recorded manually or automatically in the knowledge database. Due to the usage of ontology, the knowledge base can be hosted with online servers which is extremely helpful for knowledge sharing [2] [29].

From the framework described above, the cognitive engine can offer specific reasoning by accompanying unique properties such as the quantity, shape and positions of liver tumors, patients' physical quality, and medical instruments. These customized surgical procedures are expressed in semantic approaches which are readable for both human operators and processors. Hence, compared with other surgical robotics systems [34] [35], the cognitive engine is sufficiently user-friendly in operation, which greatly decreases training times.

Comparing the "Roboearth" semantic representation [2], which applies repetitive properties to reflect relationships between individual actions, our semantic architecture is (1) established by relationships between main classes and actions and (2) is easily reconstructed, spread and exchanged, because they are linked to the main class, individually, using different properties.

4 Implementation of Cognitive Engine

An ex-vivo phantom experiment is designed to verify the feasibility of two significant features in our cognitive engine: property-specific reasoning and human-like communication.

Typically, for RFA surgical treatment, surgeons will prepare various types of RF needles to satisfy the treatment requirements of liver tumors with different shapes and distributions. Disparate RF needles can achieve highly different clinical effects during ablation operation [39] [40].

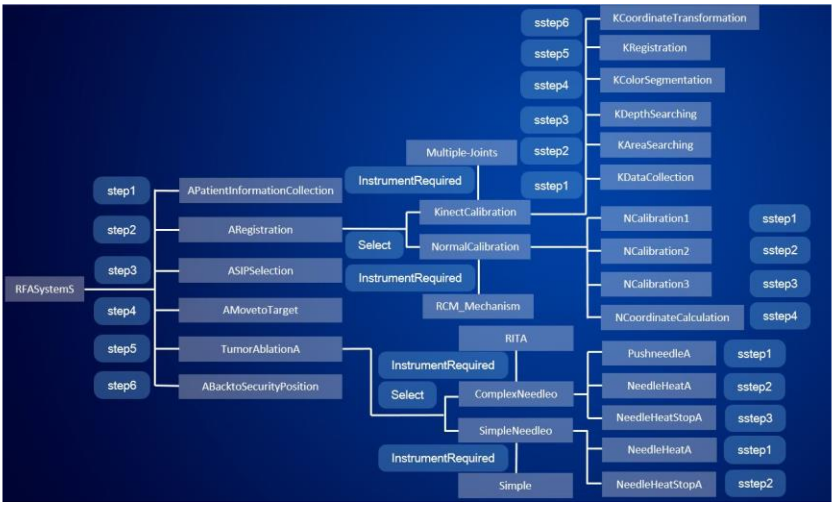

Figure 4
The architecture of semantic action representation

A single RF electrode, which performs RFA through the top area of a typically long needle, was selected in our previous study [6]. This electrode is the first choice for small size liver tumor ablation with a small elliptic ablation area and is known to improve post-operative recovery [39]. The singular structure contributes to the high accuracy that the single RF electrodes can achieve in operation. However, for large liver tumor elimination, surgeons normally choose the four-tine RF probe to generate a larger ablation area in order to guarantee a high probability of complete ablation.

We developed two registration methods for surgical robots with different mechanism designs. Our study was based on a Remote-Center Mechanism (RCM) mounted on two motorized linear x-y slides [6]. Hence, it was easy to fulfill the required degrees of freedom for a "targeting feature point" registration method in calculating the transformation matrix. However, for other surgical systems which are not moving along the x-axis, y-axis, and z-axis, such as da Vinci Surgical Robot System [41], a KINECT-based registration method was also developed in our previous study. With the variety of surgical robots and various ablation needles, the adjustments between each method in pre-operative planning can be very time-consuming.

This experiment is designed to recognize properties such as ablation needles and types of surgical robots automatically and offer an acceptable semantic action sequence for surgical robots manipulation. Due to the hybrid architecture, robots will execute the semantic action sequence in the form of programmed commands. The actual operation of low-level control is not within the scope of this paper.

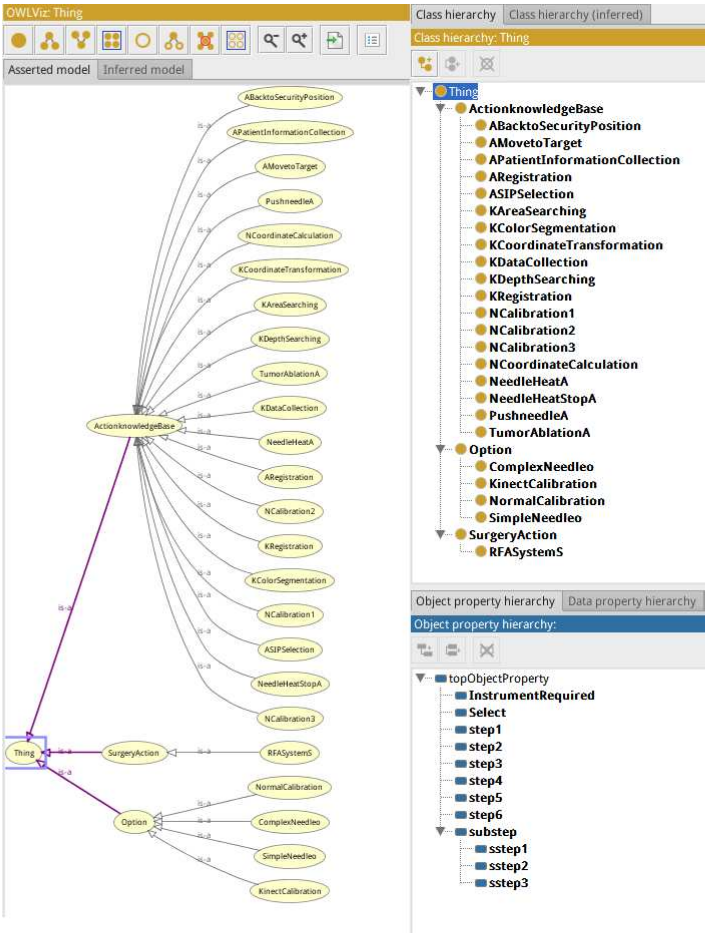

Figure 5

The architecture of semantic action representation in ontology knowledge database

From the architecture of action representation shown in Fig. 4, all of the surgical operation information is recorded into OWL as the subclass of superclass “RFASystemS”. This information includes mechanism description (“Instruments”), available selections (“selection”), available surgery types (“SurgeryAction”) and all action steps (“ActionknowledgeBase”). Properties such as “Step1” and “SStep1” are used to connect two classes in knowledge in order to construct the logical relationship. So, technically, the entire ontology knowledge database is built up by numerous triplet components (class-property-class). For reasoning, SPARQL query language is implemented by Jena library on JAVA platform. The finished ontology knowledge database is shown in Fig. 5.

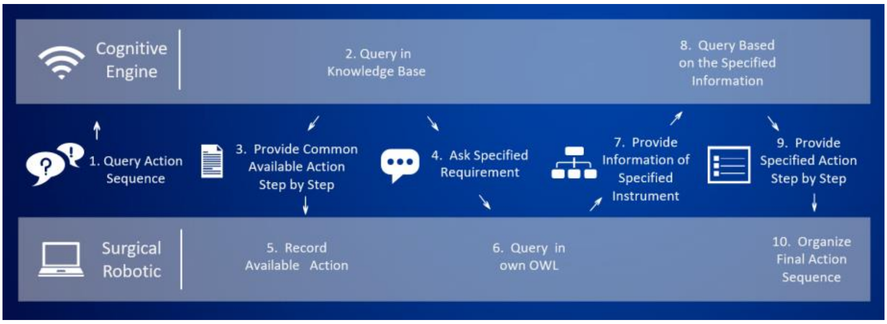

Figure 6
The execution flows of cognitive engine

Having two independent OWL files, with different recorded instruments, the cognitive engine will use the properties obtained from querying and offer different action sequence. Execution of the cognitive engine is shown in Fig. 6. Surgeons will input the initial information into the cognitive engine to query the action sequence from the knowledge database. Then, the cognitive engine will respond and provide commonly available repetitive actions sequences, with the instrument request. Subsequently, the surgical robot will record all information and query specific instruments from its own OWL database. After the information acquisition, the cognitive engine will offer all available action sequences that are suitable for the appointed surgical robots.

5 Results and Discussion

The experiment was implemented with two individual OWL files which indicated specific requirements of medical instruments and different surgical robots. For the first group, the cognitive engine should offer the correct action sequence with single RF electrode and normal registration method. Conversely, for the second group, the cognitive engine should offer the corresponding action sequence with the four-tine RF probe and Kinect registration method.

The experimental results are shown in Fig 7. The cognitive engine provided different action sequences based on specific requirements from multi-aspect.

In this experiment, cognitive engine generated a relatively simple action sequence with normal calibration steps in the first group from “rfa:NormalCalibration” which contains four simplex steps: “rfa:NCalibration1”, “rfa:NCalibration2”, “rfa:NCalibration3” and “rfa:NCoordinateCalculation”. For ablation steps which involve the application of single RF electrode, the cognitive engine provided corresponding steps from “rfa:SimpleNeedleo” which has two sub-actions: “rfa:NeedleHeatA” and “rfa:NeedleStopA”.

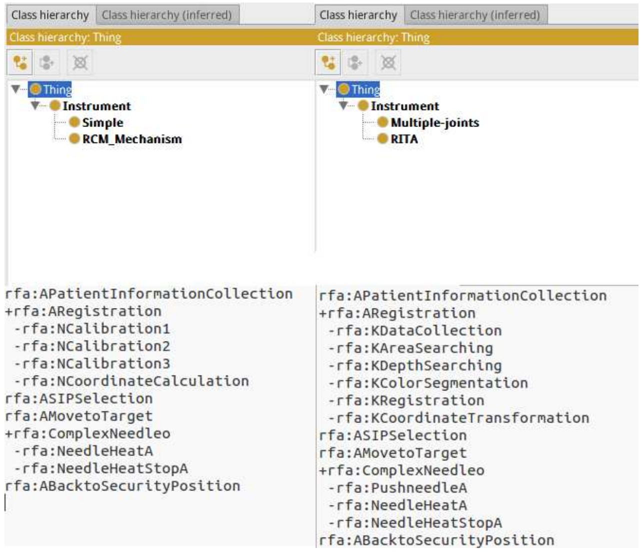

Figure 7

The results of cognitive engine experiment

For the second group, the cognitive engine created a more complex action sequence for Kinect calibration from “rfa:KinectCalibration” with six correct individual actions: “rfa:KDataCollection”, “rfa:KAreaSearching”, “rfa:KDepthSearching”, “rfa:KColorSegmentation”, “rfa:KRegistration” and “rfa:KCoordinateTransformation”. For ablation steps, because of applying four-tine RF probe which needs one more action to spread the needle, cognitive engine regulated the steps from “rfa:ComplexNeedleo” with three sub-actions: “rfa:PuchNeedleA”, “rfa:NeedleHeatA” and “rfa:NeedleHeatStopA”.

The cognitive engine indeed provides the correct action sequence for different surgical robots with various medical instruments. There are several advantages of applying cognitive engine for surgical robots:

The first advantage is property-specific reasoning. Due to the application of OWL in knowledge database construction, the logical relationship between specific properties and action list could be emphasized in a semantic way. Through performing the information retrieval with the SPARQL query language, the cognitive engine will provide an acceptable execution sequence based on corresponding properties. Similar to animals and human cognition nature, they give various responses when encountering different environments [38].

Another advantage is human-like communication. Not only that the tasks and objectives could be represented in OWL form, the robots could present themselves similarly. A comprehensive description of robots is extremely helpful for knowledge exchange because the feasibility of variable programming is easily verified based on the individual hardware and software requirement (properties) recorded in OWL [36] [37]. Therefore, this process imitates human communication when they exchange information with each other because learning and sharing depend on their personal details.

The third advantage is the understandable language for both human and robots. We choose OWL which is a good semantic method to construct the entire cognitive engine. For human operators, information which is in the form of readable words and sentences indicates every single procedure in surgical operations. However, for processors, this information will be linked to programmable commands for low-level control operation.

The fourth advantage is knowledge storage and sharing. Although some steps in performing similar tasks are varying, most of the steps are the same. Hence, we need to record only the different information from each surgical task which is linked by specific properties individually. For repetitive actions and steps, the cognitive engine will retrieve and organize them through the knowledge database. The application of OWL which is developed by web developing language XML/RDF [13] makes the knowledge database compatible with most web applications. As a consequence, the knowledge can be easily shared on the internet platform.

Conclusion

In this paper, we presented the framework of our cognitive engine which was developed as a "hybrid" architecture, with semantic approaches. The Cognitive Engine is designed to implement property-specific surgical operations and store surgical experience or professional medical knowledge in a knowledge database for repetitive usage. The implementation of ontology also makes the entire content readable for both operators and processors. From the experimental results, the cognitive engine can adapt to perform RFA needle insertion therapy with different surgical robots and various medical instruments.

The Cognitive Engine shows remarkable potential in applications for supervising multiple robots and enhancing human-robot interaction. Some industrial applications have also been introduced in recent research. The proposed Cognitive Engine could be modified to assist the interaction with sophistical robots in dedicated work cells to develop, repair or refinish highly sophisticated and personalized products. The semantic approach can be easily integrated with available virtual simulation technologies to provide an intelligent work cell.

In the future, we will investigate various computational intelligence methods and their deployment within the Cognitive Engine to enhance the effectiveness of knowledge organization for other surgical operations. We will also explore other control methods for surgical robots, to achieve a better connection between the Cognitive Engine and lower level control mechanisms.

Acknowledgement

Clinical inputs from A/Prof S Chang, Department of Surgery and Dr. J Peneyra, Comparative Medicine Centre, National University of Singapore are acknowledged. The last author wishes to acknowledge the insightful discussions on intelligent manufacturing with colleagues in the Advanced Manufacturing Institute, AIST Tsukuba, Japan.

References

[1] A. Perzylo, N. Somani, S. Profanter, M. Rickert, and A. Knoll, "Toward Efficient Robot Teach-in and Semantic Process Descriptions for Small Lot Sizes," in Robotics: Science and Systems (RSS), Workshop on Combining AI Reasoning and Cognitive Science with Robotics, Rome, Italy, 2015

[2] N. Somani, C. Cai, A. Perzylo, M. Rickert, and A. Knoll, "Object Recognition using Constraints from Primitive Shape Matching," in Advances in Visual Computing. Springer, 2014, pp. 783-792

[3] O. Zweigle, R. van de Molengraft, R. d'Andrea, and K. Häussermann, "Roboearth: Connecting Robots Worldwide," in Proceedings of the 2nd International Conference on Interaction Sciences: Information Technology, Culture and Human. ACM, 2009, pp. 184-191

[4] H. Knublauch, R. W. Fergerson, N. F. Noy, and M. A. Musen, "The Protégé OWL Plugin: An Open Development Environment for Semantic Web Applications," in The Semantic Web–ISWC 2004. Springer, 2004, pp. 229-243

[5] L. Yang, R. Wen, J. Qin, C.-K. Chui, K.-B. Lim, and S. K.-Y. Chang, "A Robotic System for Overlapping Radiofrequency Ablation in Large Tumor Treatment," Mechatronics, IEEE/ASME Transactions on, Vol. 15, No. 6, pp. 887-897, 2010

[6] B. Duan, R. Wen, C.-B. Chng, W. Wang, P. Liu, J. Qin, J. L. Peneyra, S. K.-Y. Chang, P.-A. Heng, and C.-K. Chui, "Image-guided Robotic System for Radiofrequency Ablation of Large Liver Tumor with Single Incision," in Ubiquitous Robots and Ambient Intelligence (URAI), 2015 12th International Conference on. IEEE, 2015, pp. 284-289

[7] D. L. McGuinness, F. Van Harmelen et al., "Owl Web Ontology Language Overview," W3C Recommendation, Vol. 10, No. 10, p. 2004, 2004

[8] Knublauch, Holger, et al. "The Protégé OWL Plugin: An Open Development Environment for Semantic Web Applications." International Semantic Web Conference. Springer Berlin Heidelberg, 2004

[9] Doan, AnHai, et al. "Ontology Matching: A Machine Learning Approach."Handbook on Ontologies. Springer Berlin Heidelberg, 2004, 385-403

[10] Buitelaar, Paul, Philipp Cimiano, and Bernardo Magnini. "Ontology Learning from Text: An Overview." Ontology Learning from Text: Methods, Evaluation and Applications 123 (2005): 3-12

[11] S. Bechhofer, “Owl: Web Ontology Language,” in Encyclopedia of Database Systems. Springer, 2009, pp. 2008-2009

[12] J. Perez, M. Arenas, and C. Gutierrez, “Semantics and Complexity of ´sparql,” in International Semantic Web Conference, Vol. 4273, Springer, 2006, pp. 30-43

[13] I. Horrocks, P. F. Patel-Schneider, H. Boley, S. Tabet, B. Grosof, M. Dean et al., “Swrl: A Semantic Web Rule Language Combining Owl and Ruleml,” W3C Member Submission, Vol. 21, p. 79, 2004

[14] D. T. Willingham, “Ask the Cognitive Scientist,” Newsletter, Vol. 26, 2013

[15] Thagard, Paul, Cognitive Science, The Stanford Encyclopedia of Philosophy (Fall 2008 Edition), Edward N. Zalta (ed.)

[16] D. Vernon, G. Metta, and G. Sandini, “A Survey of Artificial Cognitive Systems: Implications for the Autonomous Development of Mental Capabilities in Computational Agents,” IEEE Transactions on Evolutionary Computation, Vol. 11, No. 2, p. 151, 2007

[17] E. Hollnagel and D. D. Woods, “Cognitive Systems Engineering: New Wind in New Bottles,” Int. J. Human-Computer Studies, Vol. 51, pp. 339-356, 1999

[18] H.-H. Nagel, “Steps toward a Cognitive Vision System,” AI Mag., Vol. 25, No. 2, pp. 31-50, 2004

[19] M. Arens and H.-H. Nagel, “Quantitative Movement Prediction based on Qualitative Knowledge about Behaviour,” KI-Zeitschrift Künstliche Intelligenz, Special Issue on Cognitive Computer Vision, pp. 5-11, Apr. 2005

[20] M. Arens and H. H. Nagel, M. Jarke, J. Koehler, and G. Lakemeyer, Eds., “Representation of Behavioral Knowledge for Planning and Plan Recognition in a Cognitive Vision System,” in Proc. 25th German Conf. Artif. Intell. (KI-2002), Aachen, Germany, Sep. 2002, pp. 268-282

[21] B. Neumann and R. Möller, “On Scene Interpretation with Description Logics,” in Cognitive Vision Systems: Sampling the Spectrum of Approaches, H. I. Christensen and H.-H. Nagel, Eds. Berlin, Germany: Springer-Verlag, 2005, LNCS, pp. 235-260

[22] R. Möeller, B. Neumann, and M. Wessel, “Towards Computer Vision with Description Logics: Some Recent Progress,” in Proc. Integration of Speech and Image Understanding, Corfu, Greece, 1999, pp. 101-115

[23] P. Langley, J. E. Laird, and S. Rogers, “Cognitive Architectures: Research Issues and Challenges,” Cognitive Systems Research, Vol. 10, No. 2, pp. 141-160, 2009

[24] G. Sandini, G. Metta, and D. Vernon, “Robotcub: An Open Framework for Research in Embodied Cognition,” in Proc. IEEE-RAS/RSJ Int. Conf. Humanoid Robots (Humanoids 2004), 2004, pp. 13-32

[25] D. A. Medler, “A Brief History of Connectionism,” Neural Computing Surveys, Vol. 1, pp. 61-101, 1998

[26] R. Reiter, Knowledge in Action: Logical Foundations for Specifying and Implementing Dynamical Systems. Cambridge, MA: MIT Press, 2001

[27] A. J. Butt, N. A. Butt, A. Mazhar, Z. Khattak, and J. A. Sheikh, “The Soar of Cognitive Architectures,” in Current Trends in Information Technology (CTIT), 2013 International Conference on. IEEE, 2013, pp. 135-142

[28] M. B. van Riemsdijk, L. A. Dennis, M. Fisher, and K. V. Hindriks, “Agent Reasoning for Norm Compliance: a Semantic Approach,” in Proceedings of the 2013 International Conference on Autonomous Agents and Multi-Agent Systems. International Foundation for Autonomous Agents and Multiagent Systems, 2013, pp. 499-506

[29] D. Hunziker, M. Gajamohan, M. Waibel, and R. D’Andrea, “Rapyuta: The Roboearth Cloud Engine,” in Robotics and Automation (ICRA), 2013 IEEE International Conference on. IEEE, 2013, pp. 438-444

[30] M. Tenorth, A. C. Perzylo, R. Lafrenz, and M. Beetz, “Representation and Exchange of Knowledge about Actions, Objects, and Environments in the Roboearth Framework,” Automation Science and Engineering, IEEE Transactions on, Vol. 10, No. 3, pp. 643-651, 2013

[31] S. Profanter, A. Perzylo, N. Somani, M. Rickert, and A. Knoll, “Analysis and Semantic Modeling of Modality Preferences in Industrial Humanrobot Interaction,” in IEEE/RSJ International Conference on Intelligent Robots and Systems (IROS), 2015

[32] U. Yadav, G. S. Narula, N. Duhan, V. Jain, and B. Murthy, “Development and Visualization of Domain Specific Ontology using Protege,” Indian Journal of Science and Technology, Vol. 9, No. 16, 2016

[33] J. Heflin and J. Hendler, “A Portrait of the Semantic Web in Action,” Intelligent Systems, IEEE, Vol. 16, No. 2, pp. 54-59, 2001

[34] Surgical, Intuitive. "The da Vinci Surgical System." Intuitive Surgical Inc., Sunnyvale, CA, available at: http://www.intuitivesurgical.com (2013)

[35] Chitwood Jr, W. Randolph, et al. "Robotic Surgical Training in an Academic Institution." Annals of Surgery 234.4 (2001): 475-486

[36] R. Mendoza, B. Johnston, F. Yang, Z. Huang, X. Chen, and M.-A. Williams, "Oboc: Ontology-based Object Categorisation for Robots," in International Conference on Computational Intelligence, Robotics and Autonomous Systems. Massey University Press, 2007

[37] L. Kunze, T. Roehm, and M. Beetz, "Towards Semantic Robot Description Languages," in Robotics and Automation (ICRA), 2011 IEEE International Conference on. IEEE, 2011, pp. 5589-5595

[38] J. R. Anderson, Cognitive Psychology and its Implications. WH Freeman/Times Books/Henry Holt & Co, 1990

[39] I. A. Chang and U. D. Nguyen, "Thermal Modeling of Lesion Growth with Radiofrequency Ablation Devices," Biomedical Engineering Online, Vol. 3, No. 1, p. 27, 2004

[40] S. Tungjitkusolmun, S. T. Staelin, D. Haemmerich, J.-Z. Tsai, H. Cao, J. G. Webster, F. T. Lee Jr, D. M. Mahvi, and V. R. Vorperian, "Threedimensional Finite-Element Analyses for Radio-Frequency Hepatic Tumor Ablation," Biomedical Engineering, IEEE Transactions on, Vol. 49, No. 1, pp. 3-9, 2002

[41] Maeso, Sergio, et al. "Efficacy of the Da Vinci Surgical System in Abdominal Surgery Compared with that of Laparoscopy: a Systematic Review and Meta-Analysis." Annals of Surgery, Vol. 252, No. 2, pp. 254-262, 2010

[42] X. Tan, C.-B. Chng, B. Duan, Y. Ho, R. Wen, X. Chen, K.-B. Lim and C.-K. Chui, "Design and Implementation of a Patient-Specific Cognitive Engine for Robotic Needle Insertion," in System, Man, and Cybernetics (SMC), 2016 IEEE International Conference on. IEEE, 2016 [to appear]

[43] Sram, Norbert, and Márta Takács. "An Ontology Model-based Minnesota Code." Acta Polytechnica Hungarica 12.4 (2015)

[44] Guan, Jian-sheng, et al. "Breast Tumor Computer-aided Diagnosis using Self-Validating Cerebellar Model Neural Networks." Acta Polytechnica Hungarica 13.4 (2016)

[45] Machová, Kristína, et al. "Ontology Evaluation Based on the Visualization Methods, Context and Summaries." Acta Polytechnica Hungarica 13.4 (2016)

[46] Pham, Xuan Hau, et al. "Ontology-based Multilingual Search in Recommendation Systems." Acta Polytechnica Hungarica 13.2 (2016)

Closed-Loop Inverse Kinematics Algorithm with Implicit Numerical Integration

Dániel András Drexler

Physiological Controls Research Center, Research and Innovation Center of Óbuda University, Óbuda University, Hungary
drexler.daniel@nik.uni-obuda.hu

Abstract: The closed-loop inverse kinematics algorithm is a numerical approximation of the solution of the inverse kinematics problem, which is a central problem of robotics. The accuracy of this approximation, i.e. the convergence of the numerical solution to the real solution can be increased by increasing the value of a feedback gain parameter. However, this can lead to unstable operation if the stability margin is reached. The accuracy of the closed-loop inverse kinematics algorithm is increased here by replacing the numerical integration with second-order and implicit numerical integration techniques. The application of implicit Euler, explicit trapezoid, implicit trapezoid and the weighted average method is considered, and an iteration is presented to calculate the implicit solutions. Simulation results show that implicit second-order methods give the best results. However, they decrease the stability margin due to the iteration required to calculate the implicit solution. The stability margin of the algorithms with different numerical integration techniques is analyzed, and it turns out that the implicit trapezoid method has the most desirable properties.

Keywords: differential inverse kinematics; numerical integration; explicit Euler; implicit Euler; explicit trapezoid; implicit trapezoid; theta method; weighted average method

1 Introduction

In robotics, finding the motion of the robot joints that results in the predefined motion of the end effector of the robot is a central problem, called the inverse kinematics problem. The solution of this problem lies in the inversion of nonlinear geometric transformations (that are nonlinear in the joint variables of the robot), and we can only find symbolic solution in special cases (for special robot architectures), see e.g. [1–3]. Thus in general, we need to use numerical techniques to solve the inverse kinematics problem; the most widely used approaches that can be used in real-time are based on the Jacobian of the robot [4]. This Jacobian defines a linear relationship for fixed joint variables between the joint velocities and the end effector velocities, thus given the desired end effector velocities, we can calculate the necessary joint velocities by solving a system of linear equations defined by the Jacobian.

In the implementation of the Jacobian-based inverse kinematics algorithm, first we discretize the problem in time, solve the linear system of equations, and finally integrate the joint variables using a numerical integration technique. The most common numerical integration technique used in the literature is the explicit Euler method (see e.g. [5–7]). The Jacobian-based solution of the inverse kinematics problem is usually called the differential inverse kinematics algorithm.

Since the differential inverse kinematics algorithm is a numerical approximation of the solution, it has a tracking error. The tracking performance can be improved by adding a constant multiple of the tracking error to the desired end effector velocity, this constant will be called the feedback gain, and the algorithm with nonzero feedback gain will be referred to as the closed-loop inverse kinematics (CLIK) algorithm (see e.g. [8]), being presented in Section 2. The tracking error can be decreased by increasing the value of the feedback gain. However, there is an upper limit for that depending on the sampling time (for the proof see [8]); if the feedback gain exceeds this limit, then the algorithm becomes unstable. The maximal value of this limit is $2/T_s$ with T_s being the sampling time used at the discretization, if the initial tracking error is small enough, which implies that this also gives an upper limit for the tracking performance.

The tracking performance of the CLIK algorithm can be further increased if we replace the numerical integration with second-order methods, as it was shown, e.g. in [9–11]. Second-order, explicit trapezoid method was proposed in [9], while implicit methods with an algorithm to calculate the implicit solutions were proposed in [10, 11]. In [11], explicit Euler, implicit Euler, explicit trapezoid and implicit trapezoid methods were implemented and compared to each other, and it turned out that the trapezoid methods yield better performance, and the implicit trapezoid method has the best performance properties.

The implicit trapezoid method does the integration using the average of the velocities from the explicit and implicit Euler methods. This can be generalized further by using the convex combination of these velocities, this is called the ϑ-method (or weighted average method) in the literature [12]. Note that these methods are usually used to solve partial differential equations, and for specific problems it was shown that among all convex combinations, the average gives the best tracking performance; we show the same here with simulations in Section 4.

The implicit Euler, explicit trapezoid, implicit trapezoid and ϑ-methods and their application in the CLIK problem are explained in Section 3. The iterative algorithm to calculate the implicit solutions is also expounded in Section 3, where the conditions on the convergence of the iteration are also given. The application of the algorithms is demonstrated using simulations in Section 4, where the results from the known explicit and the proposed implicit methods are compared.

The maximal value of the feedback gain parameter in the CLIK algorithm is examined using simulations with different numerical integration techniques. It turns out that the stability margin is close to $2/T_s$ for the explicit and implicit trapezoid methods. However, the CLIK algorithm becomes unstable for smaller feedback gain if implicit Euler method is used for numerical integration. For the weighted average method, the stability margin depends on the weighting parameter ϑ. Theoretical upper limits for the stability margins are also given symbolically for these algorithms in Section 3 that are verified in Section 4 with the simulations. The simulation results show that the implicit trapezoid method has the best performance, and the stability margin for the feedback gain, if the implicit trapezoid method is used, is very close to the stability margin of the CLIK algorithm using the explicit Euler method that was used in [8].

2 Closed-Loop Inverse Kinematics Algorithm

We will denote the vector of joint variable functions with θ, whose ith component θ_i is the joint variable of the $i$the joint of the manipulator. θ is a function that maps the value of the joint variables (angles or displacements depending on the type of the joints) for each positive time instant. We denote the forward kinematics mapping by f, i.e. $f(\theta)$ is the end effector pose (position and orientation). Suppose that the orientation is represented as a vector, e.g. the components of the vector are rotations around the basis vectors of a fixed spatial frame. Let the desired end effector pose be x_d, while the desired end effector velocity be $\dot{x}_d$. Denote the Jacobian of the mapping f at the joint variable θ by $J(\theta)$, i.e. $\dot{x} = J(\theta)\dot{\theta}$.

We are looking for the joint variable function θ_d such that

$$f(\theta_d) = x_d \tag{1}$$

holds. This implies that for the velocities the expression

$$\dot{x}_d = J(\theta_d)\dot{\theta}_d \tag{2}$$

holds as well.

First, we discretize the problem in time, i.e. consider the functions θ and x_d in discrete time instants $t = kT_s$ with k being a nonnegative integer, while T_s being the sampling time. Define the discretized functions as $\theta[k] := \theta(kT_s)$ and $x_d[k] := x_d(kT_s)$. After the discretization, the velocities become differences, i.e. $\Delta\theta[k] := \dot{\theta}(kT_s)$ and $\Delta x_d[k] := \dot{x}_d(kT_s)$.

The discretized version of (2) is thus

$$\Delta x_d[k] = J(\theta_d[k])\Delta\theta_d[k], \quad k = 0, 1, 2, \ldots \tag{3}$$

The differential inverse kinematics algorithm is based on solving a linear system of equations

$$\Delta x_d[k] = J(\theta[k])\Delta\theta[k], \quad k = 0, 1, 2, \ldots \tag{4}$$

to acquire $\Delta\theta[k]$, followed by a numerical integration

$$\theta[k+1] = \theta[k] + \alpha\Delta\theta[k] \tag{5}$$

to update the joint variable vector. The numerical integration used in (5) is the explicit Euler method [13]. Since (4) only describes velocities, but the goal is to track the desired path, i.e. to minimize the difference between the elements of the series $f(\theta[0]), f(\theta[1]), f(\theta[2]), \dots$ and $x_d[0], x_d[1], x_d[2], \dots$, it is necessary to take the tracking error $x_d[k] - f(\theta[k])$ into consideration as well. We add this feedback term after multiplication with the feedback parameter α to the desired velocities, so that (4) becomes

$$\Delta x_d[k] + \alpha(x_d[k] - f(\theta[k])) = J(\theta[k])\Delta\theta[k], \quad k = 0, 1, 2, \dots \tag{6}$$

thus the joint variable difference $\Delta\theta[k]$ is calculated as

$$\Delta\theta[k] = J^{\#}(\theta[k])\left(\Delta\theta[k] + \alpha(x_d[k] - f(\theta[k]))\right) \tag{7}$$

where the $J^{\#}$ denotes the (generalized) inverse of the Jacobian. This algorithm is called the CLIK algorithm that has better tracking performance than the differential inverse kinematics algorithm without the feedback term. The performance of the algorithm increases, i.e. the speed of the convergence of the series $f(\theta[0]), f(\theta[1])$, $f(\theta[2])$ to the series $x_d[0], x_d[1], x_d[2], \dots$ becomes faster as α is increased, until the stability margin is reached, at which point the algorithm becomes unstable, thus the increase of the performance by changing the feedback parameter is limited. However, further increase in the tracking performance can be achieved by replacing the numerical integration step (5) by a different technique [9–11] that will be discussed in the upcoming sections.

We supposed that the task is to achieve the desired position and orientation of the end effector of the manipulator. However, the task can be more specific, for example only the position or the orientation of the end effector is considered, or the robot moves only in a plane (i.e. it is a planar manipulator). In this case, the functions x_d and f can be described such that they map to the space relevant to the specific task, we will call this space the task space. Similarly, we can define the Jacobian of the new function f that maps to the task space, we will call this Jacobian the task Jacobian. The sum of the desired velocity and the feedback term defined in the task space will be called the task vector and denoted by $t(\theta[k], k)$, where the first argument means that the task vector is considered at joint variable $\theta[k]$, and the second argument shows that the desired x_d and Δx_d values are considered at the discrete time instant k, i.e.

$$t(\theta[k], k) = \Delta x_d[k] + \alpha\left(x_d[k] - f(\theta[k])\right). \tag{8}$$

The first step (7) of the CLIK algorithm is written with this terminology as

$$\Delta\theta[k] = J^{\#}(\theta[k])t(\theta[k], k) \tag{9}$$

where J is the task Jacobian. In the remaining sections we will suppose that the corresponding functions map to the task space, thus the application of the discussed methods does not depend on the task space.

3 Implicit and Second-Order Numerical Integration Algorithms

The tracking performance of the numerical solution of the inverse kinematics algorithm can be increased by using implicit or second-order numerical integration techniques instead of the explicit Euler method in (5). The authors in [9] considered the application of higher-order explicit methods. However, implicit methods may yield better tracking performance [10, 11], thus we consider mostly implicit methods here, i.e. the update law that replaces (5) depends on $\theta[k+1]$ as well. Let the general form of the update law be

$$\theta[k+1] = \phi(\theta[k], \theta[k+1]) \tag{10}$$

for some function ϕ. Some of the results (iteration to calculate the implicit solution, bounds for the convergence of the iteration) will be given for the general update law. However we will consider specific ϕ functions (standing for specific numerical integration techniques) in the simulations.

Note that an implicit update law depends on $\theta[k+1]$ that is the solution we are looking for (that makes the method implicit), and the underlying expressions are usually complex and nonlinear, so the update law can not be rearranged to express $\theta[k+1]$ explicitly, thus we need an iteration to calculate the implicit solution $\theta[k+1]$.

Suppose that the update law ϕ can be written in the form

$$\phi = \theta[k] + T_s\psi(\Delta\theta[k], \Delta\theta[k+1]). \tag{11}$$

Then an iteration to calculate the update law is shown in Algorithm 1 [11].

Algorithm 1. *Iteration for implicit solution with update law (11).*

1. *First, calculate* $\Delta\theta[k]$ *using the expression*

   $$\Delta\theta[k] = J^{\#}(\theta[k])t(\theta[k], k) \tag{12}$$

   and calculate $\Delta\theta[k+1]$ *using the expression*

   $$\Delta\theta[k+1] = J^{\#}(\theta[k])t(\theta[k], k+1), \tag{13}$$

   and compute $\tilde{\theta}[k+1]$ *using the update law (11).*

2. *Calculate the difference*

   $$\Delta\tilde{\theta}[k+1] = J^{\#}(\tilde{\theta}[k+1])t(\tilde{\theta}[k+1], k+1). \tag{14}$$

3. *Update* $\tilde{\theta}[k+1]$ *using the expression (11) as*

   $$\tilde{\theta}[k+1] = \theta[k] + T_s\psi(\Delta\theta[k], \Delta\tilde{\theta}[k+1]). \tag{15}$$

4. *Repeat steps 2 and 3 until the alteration of* $\tilde{\theta}[k+1]$ *is small enough or a certain number of iterations is reached.*

The following theorem gives an upper bound for the feedback gain α so that Algorithm 1 is convergent [11], i.e. the alteration of $\tilde{\theta}[k+1]$ becomes arbitrarily small after the appropriate number of iterations.

Theorem 1. Suppose, that the manipulator is far from singular configurations, i.e. it is moving in the connected subset U of the joint space, such that there exists a positive number $\eta > 0$ so that $\left\|J^{\#}(\theta)\right\|_\infty \leq \eta$ for all $\theta \in U$. Moreover, there exists a positive number ν so that

$$\max_i \left\|\partial_{\theta_i} J(\theta)\right\|_\infty \leq \nu \tag{16}$$

for all $\theta \in U$. Let $\Delta\theta[k+1]$ be the implicit difference and $\Delta\theta[k]$ be the explicit difference of joint variables. Suppose that ψ is a continuously differentiable function of $\Delta\theta[k+1]$. Then if α satisfies the inequality

$$\alpha < \frac{1}{T_s \left\|\partial_{\Delta\theta[k+1]} \psi(\Delta\theta[k], \Delta\theta[k+1])\right\|_\infty} - n\nu\eta \left\|\Delta\theta[k+1]\right\|_\infty \tag{17}$$

where n is the number of the joints of the robot, then $\theta[k+1]$ is the fix point of the function (10) with $\Delta\theta[k+1] = J^{\#}(\theta[k+1])t(\theta[k+1], k+1)$ and Algorithm 1 converges to this fixed point.

Proof. We will show that with the above conditions the mapping ϕ in (10) is a contraction mapping (in the ∞-norm), i.e. if the conditions of the theorem hold then there exists a number $0 \leq q < 1$ such that for all $a, b \in U$

$$\|\phi(a) - \phi(b)\|_\infty \leq q \|a - b\|_\infty . \tag{18}$$

Since ψ in (11) is continuously differentiable, the mapping (10) is also continuously differentiable due to the conditions of the theorem (since J is nonsingular thus, $J^{\#}$ exists and is continuously differentiable), so condition (18) is equivalent to the existence of a Lipschitz-constant q such that

$$\left\|\partial_{\theta[k+1]} \phi\right\|_\infty \leq q. \tag{19}$$

We will show that $\left\|\partial_{\theta[k+1]} \phi\right\|_\infty < 1$ implies (17) if the other conditions of the theorem hold. Applying the chain rule, the differential $\partial_{\theta[k+1]} \phi$ can be written as

$$\partial_{\theta[k+1]} \phi = T_s \partial_{\Delta\theta[k+1]} \psi(\Delta\theta[k+1]) \partial_{\theta[k+1]} \Delta\theta[k+1], \tag{20}$$

where we have omitted the argument $\Delta\theta[k]$ of ψ for clarity.

The derivative $\partial_{\theta[k+1]} \Delta\theta[k+1]$ is a matrix with its ith column being $\partial_{\theta_i[k+1]} \Delta\theta[k+1]$. For the sake of simplicity, in the remainder of the proof we will omit the argument $[k+1]$ and use the notations $\theta := \theta[k+1]$ and $\Delta\theta := \Delta\theta[k+1]$. Since $\Delta\theta$ is calculated as $\Delta\theta = J^{\#}(\theta)t(\theta, k+1)$, the derivative of $\Delta\theta$ with respect to the scalar θ_i is

$$\begin{aligned} \partial_{\theta_i} \Delta\theta &= \partial_{\theta_i} \left(J^{\#}(\theta) t(\theta, k+1)\right) \\ &= \left(\partial_{\theta_i} \left(J^{\#}(\theta)\right)\right) t(\theta, k+1) \\ &\quad + J^{\#}(\theta) \partial_{\theta_i} \left(t(\theta, k+1)\right). \end{aligned} \tag{21}$$

The differential of the task vector is

$$\begin{aligned}\partial_{\theta_i}(t(\theta,k+1)) &= \partial_{\theta_i}(\Delta x_d[k+1]+\alpha(x_d[k+1]-f(\theta))) \\ &= -\alpha\partial_{\theta_i}f(\theta) \\ &= -\alpha J(\theta)(\cdot,i), \end{aligned} \tag{22}$$

where $J(\theta)(\cdot,i)$ denotes the ith column of the matrix $J(\theta)$ with the notation used, e.g. in [14, 15]. Substituting this into the second term in (21) yields

$$\begin{aligned}J^{\#}(\theta)\partial_{\theta_i}(t(\theta,k+1)) &= J^{\#}(\theta)(-\alpha J(\theta)(\cdot,i)) \\ &= -\alpha e_i, \end{aligned} \tag{23}$$

where e_i is the ith unit vector of $\mathbb{R}^n$.

The differential of the Jacobian pseudoinverse is

$$\partial_{\theta_i}\left(J^{\#}(\theta)\right) = -J^{\#}(\theta)\left(\partial_{\theta_i}J(\theta)\right)J^{\#}(\theta), \tag{24}$$

so the first term in (21) becomes

$$\left(\partial_{\theta_i}\left(J^{\#}(\theta)\right)\right)t(\theta,k+1) = -J^{\#}(\theta)\left(\partial_{\theta_i}J(\theta)\right)\Delta\theta, \tag{25}$$

so (21) reduces to

$$\partial_{\theta_i}\Delta\theta = -J^{\#}(\theta)\left(\partial_{\theta_i}J(\theta)\right)\Delta\theta - \alpha e_i. \tag{26}$$

The norm of the function $\partial_\theta\phi$ can be bounded from above by

$$\|\partial_\theta\phi\|_\infty \le T_s\|\partial_{\Delta\theta}\psi\|_\infty\|\partial_\theta\Delta\theta\|_\infty \tag{27}$$

provided that $T_s > 0$. Since the ∞-norm of a matrix is its maximal absolute column sum,

$$\|\partial_\theta\Delta\theta\|_\infty = \max_i\left\{1_n\left|-\alpha e_i - J^{\#}(\theta)\partial_{\theta_i}J(\theta)\Delta\theta\right|\right\} \tag{28}$$

where 1_n is a row vector of length n whose each element is one and $|\cdot|$ is the element-wise absolute value function. Due to the triangle inequality

$$\|\partial_\theta\Delta\theta\|_\infty \le \alpha + \max_i\left\{1_n\left|-J^{\#}(\theta)\partial_{\theta_i}J(\theta)\Delta\theta\right|\right\}, \tag{29}$$

and since the absolute column sum is not greater than the product of the length of the column and the absolute value of the element of the column that has the greatest absolute value, the inequality becomes

$$\|\partial_\theta\Delta\theta\|_\infty \le \alpha + n\max_i\left\|J^{\#}(\theta)\partial_{\theta_i}J(\theta)\Delta\theta\right\|_\infty \tag{30}$$

from which we obtain

$$\|\partial_\theta\Delta\theta\|_\infty \le \alpha + n\left\|J^{\#}(\theta)\right\|_\infty\|\Delta\theta\|_\infty\max_i\partial_{\theta_i}J(\theta). \tag{31}$$

Substituting the bounds from the conditions of the theorem into (31), and substituting the result into (27) yields

$$\|\partial_\theta \phi\|_\infty \leq T_s \|\partial_{\Delta\theta} \psi\|_\infty (\alpha + n\nu\eta \|\Delta\theta\|_\infty). \tag{32}$$

This derivative is smaller than one and thus, ϕ is contractive and has a unique fixed-point θ if

$$\alpha < \frac{1}{T_s \|\partial_{\Delta\theta} \psi\|_\infty} - n\nu\eta \|\Delta\theta\|_\infty \tag{33}$$

that is the result we were looking for. □

The parameter q in (18) characterizes the speed of convergence, since the distance of the implicit solution and the approximate solution in the nth iteration is

$$\|\Delta\theta[k+1] - \Delta\tilde{\theta}[k+1]^{(n)}\| \leq \frac{q^n}{1-q} \|\Delta\tilde{\theta}[k+1]^{(0)} - \Delta\tilde{\theta}[k+1]^{(1)}\| \tag{34}$$

where $\Delta\theta[k+1]$ is the implicit solution and $\Delta\tilde{\theta}[k+1]^{(n)}$ is the solution resulting from Algorithm 1 after n number of iterations. Thus, the required number of iterations in Algorithm 1 depends on the value of q that depends on the value of α: if α is closer to the limit defined by Theorem 1, then q is closer to 1, so more number of iterations are required to get solutions that are sufficiently close to the real solution.

Condition (17) of Theorem 1 contains the norm of the partial derivative of the function Ψ in the update law that depends on the joint velocities. However, for specific numerical integration techniques $\left\|\partial_{\Delta\theta[k+1]} \psi\right\|_\infty$ is usually a constant as it will be shown in the upcoming subsections.

3.1 Implicit Euler Method

The update law in (10) in the case of implicit Euler integration becomes

$$\phi = \theta[k] + T_s \Delta\theta[k+1] \tag{35}$$

so the function ψ in (11) is

$$\psi(\Delta\theta[k], \Delta\theta[k+1]) = \Delta\theta[k+1], \tag{36}$$

and the ∞-norm of the differential of this function with regard to $\Delta\theta[k+1]$ is

$$\left\|\partial_{\Delta\theta[k+1]} \psi\right\|_\infty = 1. \tag{37}$$

Thus, the iteration described in Algorithm 1 converges for feedback gain α that satisfies

$$\alpha < \frac{1}{T_s} - n\nu\eta \|\Delta\theta\|_\infty \tag{38}$$

that is much smaller than the limit $2/T_s$ for the explicit Euler integration (since the quantities in the second term on the right-hand side of this inequality are all positive, so the limit is less than $1/T_s$), so the application of the implicit Euler method makes the CLIK algorithm unstable for smaller α values than in the case of explicit Euler integration. Note that if the CLIK algorithm becomes unstable for $1/T_s < \alpha < 2/T_s$ (and it does not become unstable if explicit Euler integration is used) it is because the iteration for the implicit solution becomes unstable since the conditions of Theorem 1 does not hold.

3.2 Trapezoid Methods

The update law in the case of trapezoid methods is the average of the explicit and implicit difference, i.e.

$$\phi = \theta[k] + \frac{1}{2}T_s\left(\Delta\theta[k] + \Delta\theta[k+1]\right). \tag{39}$$

The trapezoid method is called the explicit trapezoid method if the solution is approximated without iteration, so only the first step of Algorithm 1 is carried out.

If the iteration in Algorithm 1 is used, then the trapezoid method is called the implicit trapezoid method, and if the iteration is convergent, then the result of the algorithm converges to the implicit solution. The function ψ in the update law is

$$\psi(\Delta\theta[k], \Delta\theta[k+1]) = \frac{1}{2}\left(\Delta\theta[k] + \Delta\theta[k+1]\right) \tag{40}$$

and the ∞-norm of its derivative with respect to $\Delta\theta[k+1]$ is

$$\left\|\partial_{\Delta\theta[k+1]}\psi\right\|_\infty = \frac{1}{2}. \tag{41}$$

Thus the upper bound for the feedback gain α from the condition of Theorem 1 is

$$\alpha < \frac{2}{T_s} - n\nu\eta\,\|\Delta\theta\|_\infty \tag{42}$$

that is smaller than the limit $2/T_s$. However, it can be close to that limit if the second term on the right-hand side of the inequality is small enough.

3.3 Weighted Average or ϑ-Method

The update law in the case of the weighted average method is

$$\phi = \theta[k] + T_s\left((1-\vartheta)\Delta\theta[k] + \vartheta\Delta\theta[k+1]\right) \tag{43}$$

with $\vartheta \in [0,1]$, thus, the function ψ becomes

$$\psi(\Delta\theta[k], \Delta\theta[k+1]) = (1-\vartheta)\Delta\theta[k] + \vartheta\Delta\theta[k+1]. \tag{44}$$

Note that the three special cases of the weighted average method are

- $\vartheta = 0$ that corresponds to the explicit Euler method;
- $\vartheta = 1/2$ that corresponds to the implicit trapezoid method;
- $\vartheta = 1$ that corresponds to the implicit Euler method.

The ∞-norm of the derivative of (44) with respect to $\Delta\theta[k+1]$ is

$$\left\|\partial_{\Delta\theta[k+1]}\psi\right\|_\infty = \vartheta. \tag{45}$$

Thus, the upper bound for the feedback gain α from the condition of Theorem 1 is

$$\alpha < \frac{1}{T_s\vartheta} - n\nu\eta\,\|\Delta\theta\|_\infty \tag{46}$$

that depends on the value of ϑ. Note that as $\vartheta \to 0$, the result converges to the explicit Euler solution, and for the explicit Euler solution no iteration is needed, thus, the range of the convergence for the iteration tends to infinity. This inequality also shows that choosing $\vartheta < 0.5$ may give a bound for α that is higher than $2/T_s$, so the stability of the CLIK algorithm is not harmed. However, as we will see in the following section, $\vartheta = 0.5$ (which special case corresponds to the implicit trapezoid method) gives the best tracking performance, and different ϑ values result in worse tracking performance.

4 Simulation Results

The numerical integration techniques are tested on a benchmark problem where the solution of the inverse positioning problem of an elbow manipulator is considered; the manipulator consists of three revolute joints, the first two joint axes intersect each other and are perpendicular, while the second and third joint axes are parallel. This architecture is widely used in the practice. The three joint axes of the manipulator in the home configuration (i.e. in the configuration where $\theta = 0$) defined in a fixed frame are

$$\omega_1 = \begin{pmatrix} 0 \\ 0 \\ 1 \end{pmatrix} \quad \omega_2 = \begin{pmatrix} 1 \\ 0 \\ 0 \end{pmatrix} \quad \omega_3 = \begin{pmatrix} 1 \\ 0 \\ 0 \end{pmatrix}, \tag{47}$$

while some points on the joint axes 1, 2 and 3 respectively are

$$q_1 = \begin{pmatrix} 0 \\ 0 \\ 0 \end{pmatrix} \quad q_2 = \begin{pmatrix} 0 \\ 0 \\ 0 \end{pmatrix} \quad q_3 = \begin{pmatrix} 0 \\ 0 \\ l_1 \end{pmatrix}, \tag{48}$$

with $l_1 = 1$ being the length of the second segment of the manipulator, while the position of the end effector in the home configuration is

$$p(0) = \begin{pmatrix} 0 \\ 0 \\ l_1 + l_2 \end{pmatrix} \tag{49}$$

with $l_2 = 1$ being the length of the third segment of the manipulator. Based on these design parameters one can calculate the forward kinematics map in the task space and the task Jacobian in every configuration using techniques from, e.g. [1, 16].

The initial configuration of the robot arm was $\theta[0] = (0, 0, \pi/2)^\top$ that is a nonsingular configuration, i.e. $J(\theta[0])$ is regular. The desired end effector path and end effector velocity were

$$x_d[k] = \begin{pmatrix} 0 \\ -1 \\ 1 \end{pmatrix} + \frac{k}{N} \begin{pmatrix} 0 \\ 0.5 \\ -1 \end{pmatrix} \tag{50}$$

$$\Delta x_d[k] = \frac{1}{N} \begin{pmatrix} 0 \\ 0.5 \\ -1 \end{pmatrix}. \tag{51}$$

The number of iterations for the CLIK algorithm was $N = 30$, so in the simulations the discrete time steps $k = 0, 1, \ldots, N$ were considered, while the sampling time was $T_s = 0.1$ sec. The CLIK algorithm was solved for different α feedback gain parameters. The number of iterations in Algorithm 1 used for the implicit methods was chosen to depend on α as

$$M = \lfloor 5\,(1+\alpha) \rfloor \tag{52}$$

in order to ensure good convergence (note that as α increases and gets closer to the limit given in Theorem 1 the parameter q in (18) gets close to 1, so the speed of convergence decreases, and more iterations are required). However, this influences the computation time, since the implicit methods require approximately $1+M$ times more computation than the explicit methods.

For every value of α the tracking error was calculated and transformed into a specific coordinate system for each discrete time $k = 0, 1, \ldots, N$ whose basis vectors are:

1. The regular path direction, that is $\Delta x_d[k]$ after normalization for each $k = 0, 1, \ldots, N$; components of this basis are denoted by the subscript *reg*.

2. The first singular path direction, that is a unit vector perpendicular to $\Delta x_d[k]$ for each $k = 0, 1, \ldots, N$; components of this basis are denoted by the subscript $sin1$.

3. The second singular path direction, that is a unit vector perpendicular to $\Delta x_d[k]$ and the first singular path direction for each $k = 0, 1, \ldots, N$; components of this basis are denoted by the subscript $sin2$.

Note that for each value of α, the tracking error is a series in the three new components $\{e_{reg}[k]\}, \{e_{sin1}[k]\}, \{e_{sin2}[k]\}$ for $k = 0, 1, \ldots, N$, so along each component, the absolute value is taken and the maximal element is chosen. Thus, for each α we take the ∞-norms of the series $\{e_{reg}[k]\}$, $\{e_{sin1}[k]\}$ and $\{e_{sin2}[k]\}$ that are the values $\max \|e_{reg}\|$, $\max \|e_{sin1}\|$ and $\max \|e_{sin2}\|$. This way, we can characterize each simulation (i.e. the result of the CLIK algorithm for the desired path tracking task) with three numbers: the maximum absolute values of the tracking errors in the direction

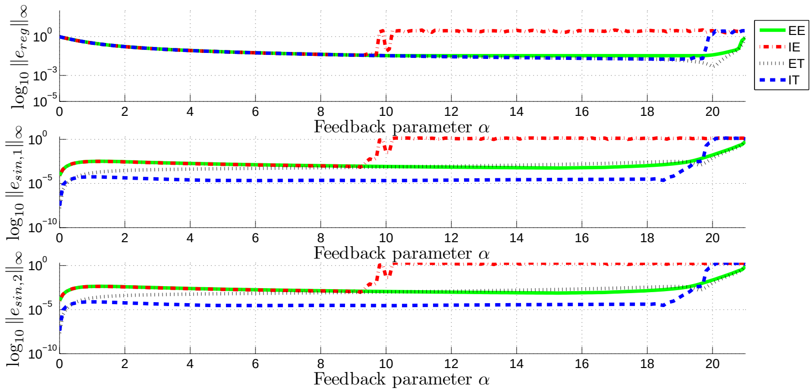

Figure 1
The logarithm of the maximal absolute values of the tracking errors along the regular and the two singular path directions for different values of the feedback gain parameter α, with the application of the explicit Euler (EE), implicit Euler (IE), explicit trapezoid (ET) and implicit trapezoid methods (IT)

of the desired movement (the regular path direction) and the two mutually orthogonal directions perpendicular to the direction of the desired movement (the singular path directions).

In the first case, the CLIK algorithm was solved using the explicit Euler [8], implicit Euler [10, 11], explicit trapezoid [9] and implicit trapezoid [10, 11] methods for different α feedback parameters. The initial value of α was zero, then it was increased by 0.1 in each step until it reached the value $\alpha = 21$. Note that since the sampling time was $T_s = 0.1$ sec, the stability limit for α in the case of the explicit Euler method is $\alpha = 2/T_s = 20$, so the explicit Euler method must become unstable if $\alpha \geq 20$.

The logarithm of the ∞-norms of the different error components for different feedback parameters are in Fig. 1. The tracking errors start to increase at $\alpha = 9.3$ for the implicit Euler method, since the iteration in Algorithm 1 becomes unstable for that value of α. The tracking errors start to increase for the implicit trapezoid method at $\alpha = 18.5$ for the same reason. The explicit methods provide stable operation for $\alpha < 20$ as expected.

All the four methods have similar performance in their stable region in the regular path direction, however there are differences in the singular path directions. The explicit and implicit Euler methods have same performance in the singular path directions as well until the implicit Euler method becomes unstable. For low values of α, the explicit trapezoid method has better performance in the singular path directions than the Euler methods, however for $\alpha > 6$ its performance becomes similar to the performance of the Euler methods. The implicit trapezoid method outperforms all the other methods, and has better performance with at least two orders of magnitude than the other methods (except for α close to zero, in this case the

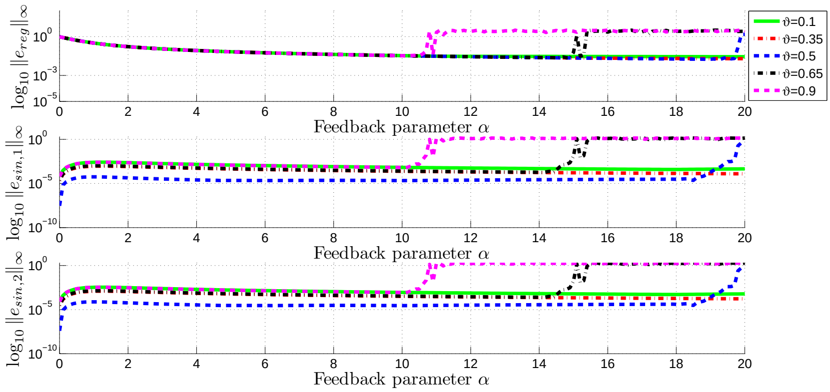

Figure 2
The logarithm of the maximal absolute values of the tracking errors along the regular and the two singular path directions for different values of the feedback gain parameter α, with the application of the weighted average method with $\vartheta \in \{0.1, 0.35, 0.5, 0.65, 0.9\}$

explicit trapezoid method has similar performance) until it becomes unstable for $\alpha > 18.5$. Thus, the implicit trapezoid method has the best tracking performance in the singular path directions for a wide range of α.

The CLIK algorithm was simulated with the application of the weighted average method as well, in order to find the optimal value of ϑ with which the algorithm has the best performance. The simulation results in this current situation showed that $\vartheta = 0.5$ has the best performance that corresponds to the implicit trapezoid method. The simulation results with $\alpha = 0, 0.1, 0.2, 0.3, \ldots, 20$ with five different ϑ values, i.e. $\vartheta \in \{0.1, 0.35, 0.5, 0.65, 0.9\}$ are in Fig. 2. Note that the results for the other values of ϑ are not depicted so that the data on the figure remain interpretable.

The figure shows that the $\vartheta = 0.5$ choice (i.e. the implicit trapezoid method) gave the best tracking performance. The differences are not relevant in the regular path direction, however the $\vartheta = 0.5$ solution has much better performance in the singular path directions. As the distance of the parameter ϑ from 0.5 increases, the tracking error in the singular path directions increases as well. For the pairs $\vartheta = \{0.1, 0.9\}$ and $\vartheta = \{0.35, 0.65\}$ (i.e. whose difference from 0.5 is the same), the performance is same in their stable region. For $\vartheta < 0.5$ the iteration in Algorithm 1 did not become unstable as it can be observed from (46) and since the tracking errors did not increase as the value $\alpha = 20$ was approached. However, for $\vartheta > 0.5$ the tracking errors started to increase for $\alpha < 20$ because the iteration for the implicit solution became unstable, i.e. for $\vartheta = 0.65$ the tracking error starts to increase at $\alpha = 14.5$ and for $\vartheta = 0.9$ the tracking error starts to increase at $\alpha = 10.2$. Note that as $\vartheta \to 1$, the ϑ-method tends to the implicit Euler method, and the value of α where the iteration becomes unstable tends to $\alpha = 9.3$, the stability margin for the implicit Euler method. Thus, the simulation results showed that the $\vartheta = 0.5$ choice gives the best results.

Conclusions

Application of second-order and implicit numerical integration methods in the CLIK algorithm were presented and the effect of the different integration methods on the tracking performance were examined. It turned out that the second-order methods give better tracking performance than the first order methods, and the implicit trapezoid method has the best performance. In order to explore if the implicit solution can be used more efficiently by taking its convex combination with the explicit solution, the application of the weighted average method has been considered as well and it turned out that the implicit trapezoid method (that is a special case of the weighted average method) has the best performance among all the possible choices.

An iteration was presented to calculate the implicit solutions, and the region of convergence for the iteration was given. Symbolic calculations showed that the implicit methods decrease the range of stability of the CLIK algorithm which was verified by simulations as well. Simulation results showed that the decrease of the stability margin in the case of implicit trapezoid method is small. However, the implicit Euler method greatly decreases the stability margin, while the decrease of the stability margin for the weighted average method depends on the parameter ϑ.

The results clearly show that the tracking performance of the CLIK algorithm can be increased by replacing the first-order numerical integration technique with a second-order one. Moreover, simulation results showed that implicit second-order methods give the best performance. The drawback of the implicit methods is that they require iteration to calculate the implicit solution that decreases the stability margin. As α tends to the stability margin for the iteration required to calculate the implicit solution, the number of required iterations increases as well. However, the results demonstrated that the decrease in the stability margin is relatively small, i.e. it does not affect the utility of the results, moreover, the increase in the computation time is only linear, thus do not harm real-time implementation criteria, while the increase in the tracking performance is significantly larger.

References

[1] Richard M. Murray, S. Shankar Sastry, and Zexiang Li. *A Mathematical Introduction to Robotic Manipulation*. CRC Press, 1994.

[2] Jon M. Selig. *Geometric Fundamentals of Robotics (Second Edition)*. Springer, 2005.

[3] Lorenzo Sciavacco and Bruno Siciliano. A solution algorithm to the inverse kinematic problem for redundant manipulators. *IEEE Transactions on Robotics and Automation*, 4(4):403–410, 1988.

[4] Bruno Siciliano, Lorenzo Sciavicco, Stefano Chiaverini, Pasquale Chiacchio, Luigi Villani, and Fabrizio Caccavale. Jacobian-based algorithms: A bridge between kinematics and control. In *Proceedings of the Special Celebratory Symposium In the honor of Professor Bernie Roth's 70th Birthday*, pages 4–35, 2003.

[5] Tomomichi Sugihara. Solvability-unconcerned inverse kinematics by the Levenberg-Marquardt method. *IEEE Transactions on Robotics*, 27(5):984–991, 2011.

[6] Yoshihiko Nakamura and Hideo Hanafusa. Inverse kinematic solutions with singularity robustness for robot manipulator control. *Journal of Dynamic Systems, Measurement, and Control*, 108(3):163–171, 1986.

[7] Fabrizio Caccavale, Stefano Chiaverini, and Bruno Siciliano. Second-order kinematic control of robot manipulators with Jacobian Damped Least-Squares inverse: Theory and experiments. *IEEE/ASME Transactions on Mechatronics*, 2(3):188–194, 1997.

[8] Pietro Falco and Ciro Natale. On the stability of closed-loop inverse kinematics algorithms for redundant robots. *IEEE Transactions on Robotics*, 27:780 –784, 2011.

[9] Emre Sariyildiz and Hakan Temeltas. Performance analysis of numerical integration methods in the trajectory tracking application of redundant robot manipulators. *International Journal of Advanced Robotic Systems*, 8(5):25–38, 2011.

[10] Dániel A. Drexler. Solution of the closed-loop inverse kinematics algorithm using the Crank–Nicolson method. In *Proceedings of the 2016 IEEE 14th International Symposium on Applied Machine Intelligence and Informatics (SAMI)*, Herlány, Slovakia, January 2016.

[11] Dániel A. Drexler and Levente Kovács. Second-order and implicit methods in numerical integration improve tracking performance of the closed-loop inverse kinematics algorithm. In *Proceedings of the 2016 IEEE International Conference on Systems, Man, and Cybernetics*, pages 3362–3367, 2016.

[12] Gordon D. Smith. *Numerical solution of partial differential equations: finite difference methods, Oxford applied mathematics and computing science series*. Oxford University Press, 1985.

[13] Uri M. Ascher and Chen Greif. *A First Course in Numerical Methods*. Society for Industrial and Applied Mathematics, 2011.

[14] Péter Érdi and János Tóth. *Mathematical Models of Chemical Reactions. Theory and Applications of Deterministic and Stochastic Models*. Princeton University Press, Princeton, New Jersey, 1989.

[15] Dániel A. Drexler and János Tóth. Global controllability of chemical reactions. *Journal of Mathematical Chemistry*, 54:1327–1350, 2016.

[16] Dániel A. Drexler and István Harmati. Regularized Jacobian for the differential inverse positioning problem of serial revolute joint manipulators. In *Proceedings of the IEEE International Symposium on Intelligent Systems and Informatics*, Subotica, Serbia, September 2013.

Robust Fractional Order Controllers for Distributed Systems

Eva-H. Dulf, Daniel Timis, Cristina-I. Muresan

Department of Automation, Technical University of Cluj-Napoca,
Memorandumului 28, 400114, Cluj-Napoca, Romania, e-mail:
eva.dulf@aut.utcluj.ro; daniel.timis@student.utcluj.ro; cristina.pop@aut.utcluj.ro

Abstract: An important step in any control system design is to account for the fault tolerance desired for the system at an early stage of development. It is not enough to test the fault tolerance after the implementation, as the tuning possibilities may be insufficient to ensure tolerance for an unexpected fault, it is better to monitor at the design phase. The control research community is interested in fault tolerant control system design, but only specific applications are addressed. The present paper deals with such a fault tolerant control system for a complex chemical process, the (13C) isotope separation columns cascade. To ensure the robustness to uncertainties of the designed system, the controller is a fractional order type, tuned using the particle swarm optimization method. The simulation results were obtained using the TrueTime Matlab toolbox.

Keywords: fault tolerant systems; distributed control system; fractional order controllers; robust control system

1 Introduction

Currently, the automatic control field is going through a continuous state of development. Research gives us new solutions and new control concepts. One of these is represented by cyber-physical systems, an interconnection between computers and physical systems. This modern type of system is embedding the computer into feedback loops, to monitor and control physical processes in various domains like: military and aeronautical systems, wastewater treatment, medical devices, manufacturing, automotive systems and so on. This approach gives us the chance to use preferred and efficient controller algorithms as opposed to old analog controllers, but the complexity of this approach increases. Because of this high level of complexity, we have to focus our attention towards the fault tolerance of the control system [1, 2]. To prevent critical failures we have to keep the local faults below a certain level. This represents an important objective to be pursued by researchers, who try to address it in the most efficient way.

Nowadays, fractional calculus is one of the most important and complex methods to be used in order to describe a complete behavior for a wide range of mathematical models from domains like: electrical and mechanical engineering, aeronautical engineering, computational mathematics, etc. A classic PID controller introduces three degrees of freedom, whereas a fractional PID controller has five degrees of freedom due to the fractional powers of the integrative and derivative effects. [3, 4]. The main disadvantage of the fractional controller design is caused by the complexity of the algorithm. By using classical tuning methods, it is hard to determine the fractional PID parameters needed to meet the given specifications. A solution for this disadvantage could be bio-inspired optimization algorithms [5].

This paper presents a simulation of a fault tolerant cyber-physical system, applied on a plant consisting of three (^{13}C) isotope separation columns, connected in a cascade structure. The used controllers are of fractional order, designed using the particle swarm optimization algorithm and implemented using a new continuous-to-discrete-time operator.

2 Control Structure

2.1 Robust Fractional Order Controller Design

A fractional order PID controller may be easily described in the Laplace domain as follows:

$$C_F(s) = K_P\left(1 + \frac{K_i}{s^{\lambda}} + K_d s^{\mu}\right), \tag{1}$$

where K_p, K_i, K_d are the proportional, integral and derivative gains, while λ and μ represent the fractional orders of integration and differentiation. The design of the fractional order PID controller in (1) follows the classical tuning rules for such type of controllers and it is carried out in the frequency domain [6, 7, 8]. To tune the parameters of the fractional order controller, three performance specifications are imposed to shape the closed loop response. These performance specifications refer to a gain crossover frequency and a phase margin, linked to a specific settling time and overshoot for the closed loop system, as well as the iso-damping property that allows for an increased robustness to open loop gain variations.

In mathematical terms, the three performance specifications may be easily described through the modulus and phase equations, while the iso-damping property is expressed using the derivative condition in the following equations:

$$\left|C_F(j\omega_{gc})\cdot G_P\left(j\omega_{gc}\right)\right| = 0\mathrm{dB} \tag{2}$$

$$\arg\left(C_F(j\omega_{gc})\cdot G_P\left(j\omega_{gc}\right)\right) = -\pi + \varphi_m \tag{3}$$

$$\left.\frac{d\arg\left(C_F\left(j\omega\right)\cdot G_P\left(j\omega\right)\right)}{d\omega}\right|_{\omega=\omega_{cg}} = 0 \tag{4}$$

where G_P stands for the transfer function of the process to be controlled, assumed here to be of the following form:

$$G_P\left(j\omega\right) = \frac{1}{A\left(j\omega\right)} = \frac{1}{\mathrm{Re}P(\omega) + j\mathrm{Im}P(\omega)} \tag{5}$$

Considering the following result:

$$\left(j\right)^r = \cos\left(\frac{r\pi}{2}\right) + j\sin\left(\frac{r\pi}{2}\right), r \in \Re \tag{6}$$

and denoting the modulus, phase and derivative conditions as function f_1, f_2 and f_3, respectively, the three performance specifications in (2)-(4) can be further expanded as indicated here:

$$f_1 = \frac{K_P\sqrt{1 + K_i\omega_{gc}^{-\lambda}a + K_d\omega_{gc}^{\mu}b + 2K_iK_d\omega_{gc}^{\mu-\lambda}\cos\left[\frac{(\lambda+\mu)\pi}{2}\right]}}{\sqrt{\mathrm{Re}P^2(\omega_{gc}) + \mathrm{Im}P^2(\omega_{gc})}} \tag{7}$$

$$f_2 = \frac{\omega_{gc}^{\mu}K_d\sin\left[\frac{\mu\pi}{2}\right] - \omega_{gc}^{-\lambda}K_i\sin\left[\frac{\lambda\pi}{2}\right]}{1 + \omega_{gc}^{\mu}K_d\cos\left[\frac{\mu\pi}{2}\right] + \omega_{gc}^{-\lambda}K_i\cos\left[\frac{\lambda\pi}{2}\right]} - \mathrm{tg}\left[-\pi + \varphi_m - \mathrm{arctg}\left[\frac{\mathrm{Im}P(\omega_{gc})}{\mathrm{Re}P(\omega_{gc})}\right]\right] \tag{8}$$

$$f_3 = \frac{c}{\left[1 + \omega_{gc}^{-\lambda}K_i\cos\left[\frac{\lambda\pi}{2}\right] + \omega_{gc}^{\mu}K_d\cos\left[\frac{\mu\pi}{2}\right]\right]^2} - \left.\frac{d\angle G_p(j\omega)}{d\omega}\right|_{\omega=\omega_{gc}} \tag{9}$$

where $a = 2\cos\frac{\lambda\pi}{2} + K_i\omega_{gc}^{-\lambda}$ and $b = 2\cos\frac{\mu\pi}{2} + K_d\omega_{gc}^{\mu}$

$c = c_1 + c_2 + c_3$, $c_1 = K_iK_d(\lambda+\mu)\omega_{gc}^{\mu-\lambda-1}\sin\left[\frac{(\mu-\lambda)\pi}{2}\right]$, $c_2 = K_d\mu\omega_{gc}^{\mu-1}\sin\left[\frac{\mu\pi}{2}\right]$ and $c_3 = K_i\lambda\omega_{gc}^{-\lambda-1}\sin\left[\frac{\lambda\pi}{2}\right]$.

Several techniques exist to solve the resulting system of nonlinear equations (2)-(4). In this paper, the proposed technique is based on a modified version of the Particle Swarm Optimization (PSO) algorithm as developed by Eberhart and Kennedy [9, 10]. In the PSO algorithm, the parameters of the controller transfer function in (1) are represented by a particle and each of these particles keeps track of its best solution, the personal best, and of the best value of any particle, the global best. Each particle modifies its position according to its current position, current velocity, the distance between its current position and the personal best and the distance between its current position and the global best. The PSO algorithm is based on finding the best values for all particles such as a fitness function is minimized. In this paper, the fitness function is selected to be the sum of the performance specifications as expressed in equations (7)-(9).

$$CF=\left|f_1(x)\right|+\left|f_2(x)\right|+\left|f_3(x)\right| \tag{10}$$

where $x=\begin{bmatrix} K_P & K_i & K_d \end{bmatrix}^T$ are the controller parameters.

To avoid falling into local optimal value and to ensure a fast convergence speed of optimization, the inertia weight [11] is used:

$$w=m-n\frac{1}{p^{gbest(i)}+1}+q\frac{1}{r^{bestf}+1} \tag{11}$$

where *m, n, p, q, r* are parameters selected according to the nonlinear equations, *gbest(i)* is the i^{th} global best and *bestf* is the standard deviation of all the i^{th} generation particles.

2.2 Discrete-Time Implementation of the Fractional Order PID Controller

In order to implement a fractional order PID controller, as given by the transfer function in (1), a new continuous-to-discrete-time operator is used:

$$s=\frac{1+\alpha}{T_s}\frac{1-z^{-1}}{1+\alpha z^{-1}} \tag{12}$$

with z^{-1} the backward shift operator, T_s the sampling period and $\alpha\in(0,1)$ – a weighting parameter that allows for an increased flexibility in ensuring a better fitting of the magnitude or phase curve of the original fractional order PID controller. The operator introduced in (12) is an interpolation between the Euler (α=0) and the Tustin (α=1) discretization rules [12].

The first step in the digital approximation consists in a continuous-time fitting of the fractional order PID controller, using a higher order rational transfer function. Because of its wide acceptance, simplicity and efficiency, the Oustaloup

Recursive Approximation [13] method is selected in this paper. The fitted continuous-time approximation of the fractional order PID controller is then given as:

$$G(s)=K_c\frac{{}_{j=1}^{m}\left(s\quad z_j^c\right)}{{}_{i=1}^{n}\left(s\quad p_i^c\right)} \tag{13}$$

where K_c is the gain, z_j^c are the continuous-time zeros, j=1,2,...,m and p_i^c are the continuous-time poles, i=1,2,…,n.

Once this continuous-time approximation of the fractional order PID controller in (11) has been obtained, the next step is to compute the discrete-time poles and zeros, using the inverse operator of (12):

$$z=\frac{1+\quad +\ sT_s}{1+\qquad sT_s} \tag{14}$$

The corresponding poles and zeros are then each computed according to the following rules:

$$p_i^d=\frac{1+\quad +\ p_i^cT_s}{1+\qquad p_i^cT_s} \tag{15}$$

$$z_j^d=\frac{1+\quad +\ z_j^cT_s}{1+\qquad z_j^cT_s} \tag{16}$$

Then, the discrete-time equivalent of the fractional order PID controller has the following form:

$$G(z)=K_d\frac{{}_{j=1}^{n}\left(z\quad z_j^d\right)}{{}_{i=1}^{n}\left(z\quad p_i^d\right)} \tag{17}$$

where the discrete-time gain K_d is computed based on the equivalency of the continuous-time and discrete-time transfer functions from (13) and (17) in steady state (s=0 and z=1):

$$K_d=K_c\frac{{}_{j=1}^{m}\left(\quad z_j^c\right){}_{i=1}^{n}\left(1\quad p_i^d\right)}{{}_{i=1}^{n}\left(\quad p_i^c\right){}_{j=1}^{n}\left(1\quad z_j^d\right)}. \tag{16}$$

Further details on the new operator (12) and on the effect of α can be found in [12] and in [14].

2.3 Fault Tolerant Distributed Control System

The modern control systems must be robust and adaptable for the system changes to be functioning, safe and fault tolerant, aspect which leads to the development of multi-agent systems. These systems have a number of independent agents, which possess capabilities such as: communication, computation, sensing and actuation. In the framework discussed in the present work, an agent is defined as an independent unit having specific functions. A Sensor agent is equipped with one or multiple redundant sensors of the same type to ensure fault-tolerance. The Actuator-agent is equipped with several redundant actuators that can provide the same functions. A Control-agent is capable of performing their own and their nearest neighbor control laws, being able to take over the functions of his neighbor in case of failure. The agents are distributed in the field, in order to complete the control system`s main task. In the case of a decentralized approach, any agent is free to manage and schedule its own activities and can exchange information with other controllers in its neighborhood, without any help from a coordinating agent. In the event of one agent`s failure, the resulting effect will not destabilize the process. Moreover, a neighboring agent could take over the task of a defective controller in order to keep the process near to the initial performances.

3 Case Study

The case study considered herein, consists in the distillation of carbon monoxide, in a train of three series columns, with the end purpose of enriching the natural concentration of the (^{13}C) carbon isotope. The enriching process is a difficult task, since there are very small differences in the nuclear characteristics of the two stable isotopes to be separated: the (^{12}C) and the (^{13}C). The actual equipment, as well as a schematic representation, are given in Figures 1 and 2. A great deal of papers have been published previously by the Authors describing the characteristics and operation of a single column or the cascade, the model of such a plant, as well as several control strategies [15-21].

The entire plant uses a common condenser cooled with liquid nitrogen. Three boilers, installed at the bottom of each column, ensure a gaseous upstream, while the liquid downstream is produced by condensing these vapors on the cold walls of the condenser. The system operates at approximately -190^{o}C, in order for both liquid and gaseous phases of (CO) to co-exist [16, 17, 22].

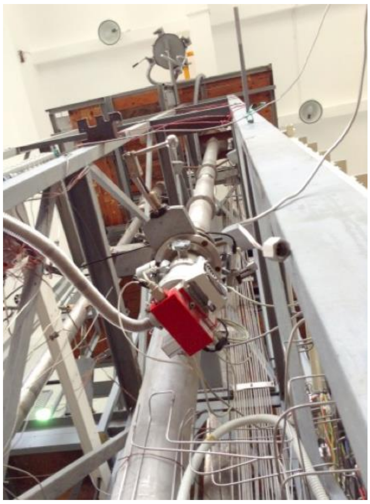

Figure 1
The (13C) isotope separation column cascade

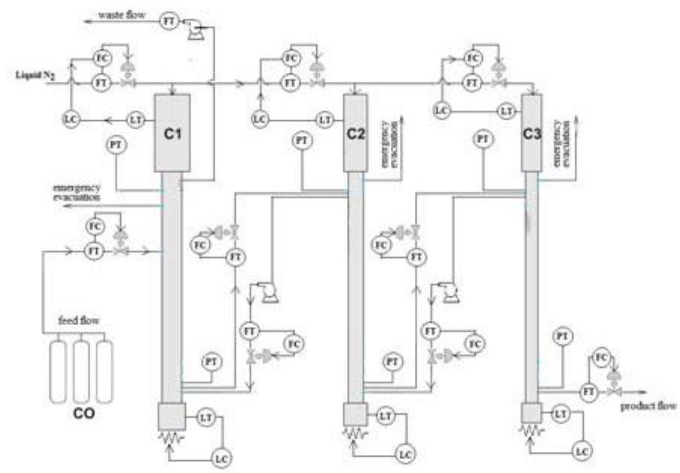

Figure 2
Schematic representation of the (^{13}C) isotopic separation column cascade

Several sensors and actuators, as pictured in Figure 3, are installed for monitoring and control purposes, such as: seven flow transducers, three pressure transducers at the top of the columns, three differential pressure transducers, three thermocouples for boiler temperature measurements, three dedicated liquid carbon monoxide level transducers in the bottom of the columns, three pumps to ensure the flow between the columns, as well as, a dedicated transducer for the liquid nitrogen level in condenser [23].

Figure 3
Sensors and actuators for the (^{13}C) isotopic separation column cascade

The TrueTime toolbox from Matlab [24] has been used to simulate the distributed system. A section of this system, including the communication between two agents, is presented in Figure 4. The whole system is much more complex, as can be seen in Figure 3, including a series of agents. Figure 4 highlights the communication layer in a subsystem: the "Plant" and the corresponding controller using the send message ("ttSendMsg") and get message ("ttGetMsg") blocks through TrueTimeNetwork. It is also included a disturbing node to simulate real scenarios of this highly critical system. [25]

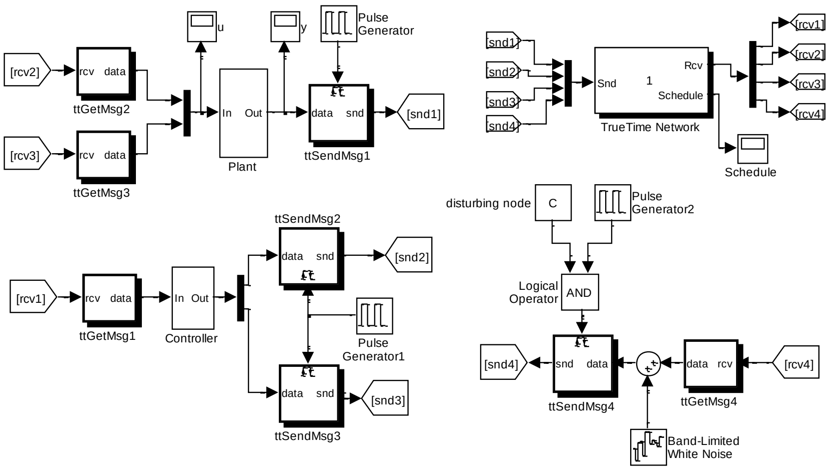

Figure 4
Communication between two agents as a section of the distributed control system of the (^{13}C) isotope separation cascade

In order to highlight the efficiency of the proposed control strategy, in this simulation stage, a subsystem having a simple first order transfer function $G_P(s) = \frac{1}{10s+1}$ is considered. This simplification does not affect the final results regarding fault tolerance. Imposing the gain crossover frequency of 15 [rad/sec], phase margin of 90^o, the above described particle swarm optimization method solves the controller design problem, using equations (7), (8) and (9). With a population size of 50 particles and considering the inertia weights: m=0.9; n=1.01; p=1.1; q=0.051 and r=1.01, the resulted controller's parameters are: K_p=71.51, K_d=0.012, K_i=16.5, λ=0.87 and μ=0.1. The Bode plot presented in Figure 5 proves the fulfillment of the imposed performances.

To highlight the proposed particle swarm optimization method efficiency, in Figure 6 are presented the particle evolutions after 5, 50, 100 and 150 iterations. It can be seen that the cost function value tends to zero after 50 iterations, Figure 6b, although this number depends on the initial conditions, Figure 6a. With 100 or 150 iterations, Figure 6c and Figure 6d, the accuracy can be improved.

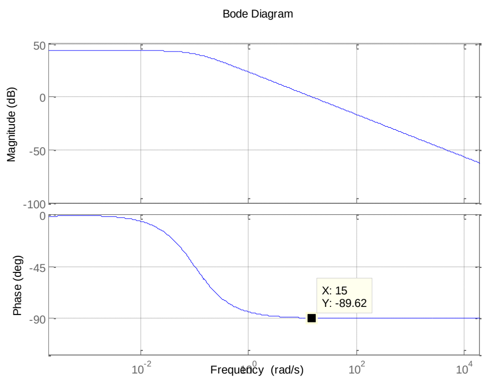

Figure 5

Frequency response of the system with the designed fractional order PID controller

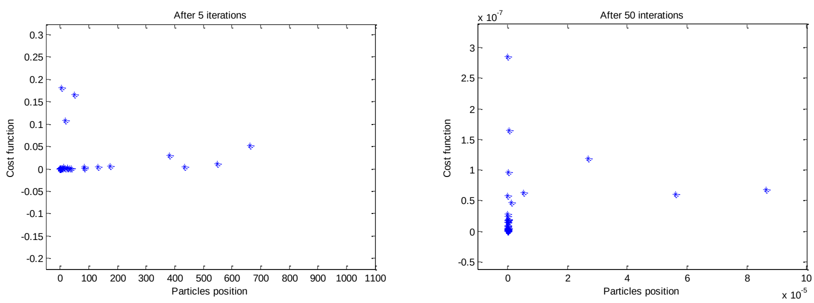

a) b)

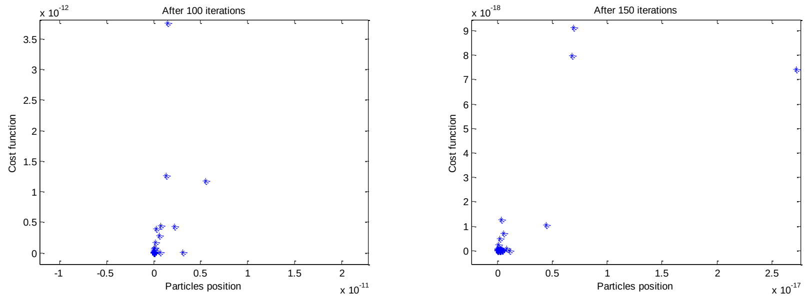

c) d)

Figure 6

Particle evolution in the optimization method, presented after: a) 5 iterations; b) 50 iterations; c) 100 iterations; d) 150 iterations

The continuous-time approximation of this fractional order PID controller has been obtained using the Oustaloup Recursive Approximation method within a low frequency bound ω_l=0.01 rad/s and a high frequency bound ω_h=100 rad/s. The order N=3 has been selected for the fitted continuous-time transfer function, yielding a total of 13 continuous-time poles and zeros. The discrete-time approximation has been obtained using the new continuous-to-discrete-time operator described in Section II.B, with α=0.9 and T_s= 0.0314 s. The Bode diagram in Figure 7 shows that a similar frequency response is obtained for the original fractional order PID controller, as well as its discrete-time approximation.

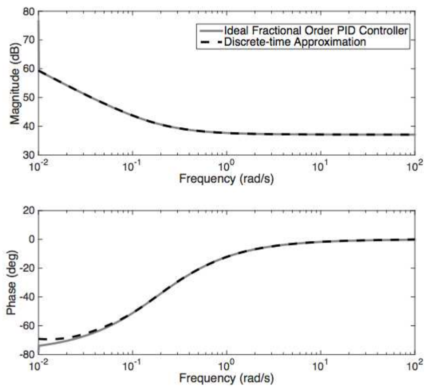

Figure 7

Frequency response of the ideal fractional order PID controller and of its discrete-time approximation

To test the robustness of the designed control structure, step responses were simulated using a +/-50% gain variation of the process transfer function. In Fig. 8, the step response of the simplified model is presented, highlighting no overshoot in all cases and settling time changes from 0.15 sec to 0.45 sec.

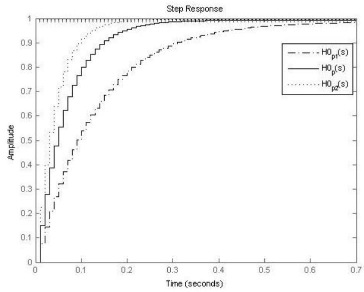

Figure 8

Step response of the closed loop system with nominal and +/-50% gain variation of the process

The next step in testing was the fault-tolerance test. Two schemes as the one, presented in Figure 4, have been used, in which each sensor- and actuator agent is equipped with two redundant sensors and actuators. Each control-agent is capable to perform their own and their nearest neighbor control laws, being able to take over the functions of his neighbor in case of failure. In Figure 9, the simulation results with the first controller failure are presented. If no fault tolerant control structure is implemented, the system output decreases from the steady-state value, Figure 9a. If the proposed strategy is implemented, when the controller fails, the neighboring controller detects this failure and takes over the responsibilities of the first one, obtaining the same steady-state value. The controller changes are not reflected in the system output; hence, the same closed loop system performance is obtained, Figure 9b.

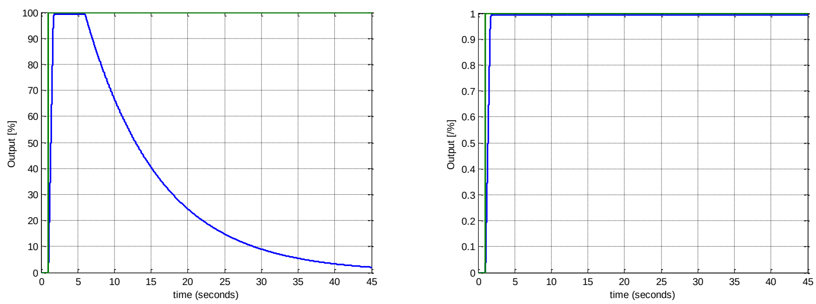

a) b)

Figure 9

Output signal of the subsystem in case of controller failure: a) without fault-tolerant structure; b) with fault-tolerant structure

The proposed fault-tolerance being based on the communication between two agents, the network effects on the control structure were tested. While taking into account the communication speed variations and the use of different network types, the step response of the system emphasizes the fact that the system is not affected. The packet loss probability has also been taken into account. Thus,

Figure 10 shows that even in the event of a 50% loss probability, the steady state value of the system remain the same, although the performance changes. In case of a packet loss probability greater than 50%, the second controller must take over the responsibilities of the first one, in order to have comparable performance.

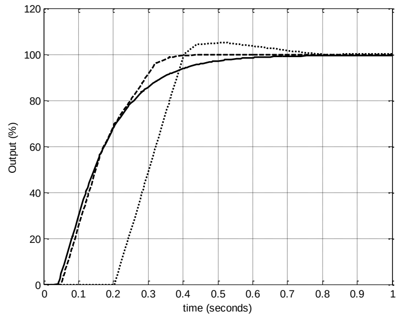

Figure 10

Step response of the closed loop system with different packet loss probabilities: 0% - solid line, 20% - dash line, 50% - dot line

Conclusions

The present paper uses an agent oriented approach for designing a fault tolerant control system, having the sensors, actuators and controllers communicating through a network. The design of the controllers ensures robustness to gain variations, while the communication between adjacent neighbor agents provides the fault tolerance of the system - in the event of a critical failure, the responsibility of the faulty agent will be passed on to the neighbor. This case study is an insight into the isotope separation columns, connected in a cascade structure, forming a highly critical cyber-physical system. The efficiency of the aforementioned control strategy is proven through simulation results and through the use of dedicated software for multi-agent systems. Future work will be in the area of implementation of this strategy, on a more detailed and complex system.

Acknowledgment

This work was supported by a grant of the Romanian National Authority for Scientific Research and Innovation, CNCS – UEFISCDI, project number PN-II-RU-TE-2014-4-1465, contract number 38/2015.

Cristina Muresan was supported by a grant of the Romanian National Authority for Scientific Research and Innovation, CNCS – UEFISCDI, project number PN-II-RU-TE-2014-4-0598, TE 86/2015.

References

[1] Xiaofeng Wang, Naira Hovakimyan, Lui Sha, “L1Simplex: Fault-Tolerant Control of Cyber-Physical Systems”, 2013 ACM/IEEE International Conference on Cyber-Physical Systems (ICCPS) pp. 41-50

[2] C. M. Krishna, I. Koren, "Adaptive Fault-Tolerance for Cyber-Physical Systems", 2013 International Conference on Computing, Networking and Communications, Workshops Cyber Physical System

[3] I. Podlubny, "Fractional-Order Systems and PIλDδ Controllers," IEEE Trans. On Automatic Control, 1999, Vol. 44, No. 1, pp. 208-213

[4] C. A. Monje, B. M. Vinagre, V. Feliu, Y. Q. Chen, "Tuning and Auto-Tuning of Fractional Order Controllers for Industry Applications," Control Engineering Practice, 16, 2008, pp. 792-812

[5] D. Floreano, C. Mattiussi, "Bio-inspired Artificial Intelligence: Theories, Methods, and Technologies" 2008, MIT Press, Cambridge

[6] Muresan, C. I., Dulf, E. H., Both, R., Vector-based Tuning and Experimental Validation of Fractional Order PI/PD Controllers, Journal of Nonlinear Dynamics, 2016, DOI: 10.1007/s11071-015-2328-2, Vol. 84, No. 1, pp. 179-188

[7] De Keyser, R., Muresan, C. I., Ionescu, C., A Novel Auto-Tuning Method for Fractional Order PI/PD Controllers, ISA Transactions, 2016, Vol. 62, pp. 268-275, DOI: 10.1016/j.isatra.2016.01.021

[8] Muresan, C. I., Dulf, E. H., Copot, C., De Keyser, R., Ionescu, C. M., Design and Analysis of a Multivariable Fractional Order Controller for a Non-Minimum Phase System, DOI: 10.1177/1077546315575433, Journal of Vibration and Control, 2016, Vol. 22, No. 9, pp. 2187-2195

[9] R. Eberhart, J. Kennedy, "A New Optimizer Using Particle Swarm Theory". In: Proceedings of the 6th International Symposium Micro Machine and Human Science (MHS) 1995, pp. 39-43, 1995

[10] Y. Shi and R. Eberhart, "A Modified Particle Swarm Optimizer," in Proceedings of the IEEE International Conference on Evolutionary Computation (ICEC '98) Alaska, USA, May 1998, pp. 69-73

[11] Y. Li, Y. Wei, Y. Chu, "Research on Solving Systems of Nonlinear Equations Based on Improved PSO", Mathematical Problems in Engineering, Vol. 2015, DOI: 10.1155/2015/727218

[12] De Keyser, R., Muresan, C. I., An Analysis of a New Continuous-to-Discrete Time Operator for the Approximation of Fractional Order Systems, Workshop on Women in Egineering, 2016 IEEE International Conference on Systems, Man, and Cybernetics (SMC 2016) Budapest, Hungary, 9-12 October 2016

[13] A. Oustaloup, F. Levron, B. Mathieu, F. M. Nanot, "Frequency-Band Complex Noninteger Differentiator: Characterization and Synthesis", IEEE Trans. Circuits Syst. I Fundam. Theory Appl., 2000, Vol. 47, No. 1, pp. 25-39

[14] S. Folea, R. De Keyser, I. R. Birs, C. I. Muresan, Experimental Results of a Fractional Order PD Controller for Vibration Suppression in Airplane Wings, Acta Polytechnica Hungarica, 2017, Vol. 14, No. 1, pp.

[15] E. H. Dulf, C. I. Pop, F. V. Dulf, “Fractional Calculus in C13 Separation Column Control”, Signal, Image and Video Processing, 2012, 6:479-485

[16] E. H. Dulf, F. V. Dulf, C.I. Pop, “Fractional Model of the Cryogenic (13C) Isotope Separation Column“, Chemical Engineering Communication, DOI: 10.1080/00986445.2014.968709, Volume 202, Issue 12, 2015

[17] Muresan, C. I., Dulf, E. H., Both, R., Comparative Analysis of Different Control Strategies for a Train of Cryogenic 13C Separation Columns, Chemical Engineering and Technology, 2015, Vol. 38, No. 4, pp. 619-631, DOI: 10.1002/ceat.201400550

[18] Dulf, E. H.; Pop, C. I.; Dulf, F., Systematic Modeling of the (13C) Isotope Cryogenic Distillation Process, Separation Science and Technology, 2012, 47 (8), 1234-1240

[19] Dulf, E. H; Festila, C.; Dulf, F. V.; Pop, C. I.; Both, R., Fractional Order Controller Design for 13 C Separation Column, Control & Automation (MED), 2011 19th Mediterranean Conference on, pp. 582-587

[20] Dulf, E. H.; Festila, C.; Baldea A., Stability of the 13 C Column Separation in Industrial Mode of Operation, Proceedings of Applied Computational Intelligence and Informatics (SACI) 2011 6th IEEE International Symposium on, pp. 41-44

[21] Dulf, E. H.; Both, R.; Dumitrache, D. C., Fractional Order Models for a Cryogenic Separation Column, Proceedings of Automation Quality and Testing Robotics (AQTR) 2010 IEEE International Conference on, pp. 1-6

[22] Both, R., Dulf, E. H., Muresan, C. I., Secara, M., Fractional Order PD Control of an Isotope Separation Columns Cascade, IEEE 10th Jubilee International Symposium on Applied Computational Intelligence and Informatics (SACI 2015) pp.193-196, DOI: 10.1109/SACI.2015.7208197, Timisoara, Romania, 21-23 May 2015

[23] R. A. Munteanu, E. H. Dulf, C. Festila, R. Munteanu, “Level Capacitive Cryogenic Transducer with Coplanar Plates for Liquid Nitrogen”, Patent proposal RO 128052

[24] A. Cervin, D. Henriksson, M. Ohlin, “TrueTime 2.0 beta 5 - Reference Manual". Dep. of Automatic Control, Lund University, Sweden, 2010

[25] Eva-H. Dulf, Daniel Timis, Lucian-Cristian Iacob, Cristina-I. Muresan, Roxana Both-Rusu, Fault Tolerant Distributed Control System with Robust Fractional Order Controllers, Proceedings of the 2016 IEEE International Conference on Systems, Man, and Cybernetics • SMC 2016 | October 9-12, 2016 • Budapest, Hungary, pp. 2501-2504

Novel Results for Asymmetrically Coupled Fractional Neurons

Carla M. A. Pinto

School of Engineering, Polytechnic of Porto, Center for Mathematics of the University of Porto, Rua Dr António Bernardino de Almeida, 431, 4200-072 Porto, Portugal, e-mail: cap@isep.ipp.pt

Abstract: We consider a fractional-order model of two asymmetrically coupled spiking neurons. The dynamical behavior of the two neurons is modeled by the fractional-order Hodgkin-Huxley equations. Simulations of the model for distinct values of the order of the fractional derivative, α, and of the coupling constants, k_1, k_2, show interesting features, such as relaxation oscillations, mixed-mode oscillations, small oscillations, and localized solutions. Moreover, α adds extra complexity to the dynamics of the model. These differences may explain certain differences in processing similar tasks in the human brain.

Keywords: asymmetric; coupled; neurons; fractional Hodgkin-Huxley equations

1 Introduction

In 1952, Hodgkin and Huxley [1] conducted experiments, in the squid axon, aimed at a better understanding of the mechanisms and rules governing the flow of the electric current in a nerve cell, during an action potential. The derived equations, known as the Hodgkin-Huxley (HH) equations, have had a decisive influence on the understanding of the neuronal function since then [2], [3], [4], [5]. Phenomena such as in-phase synchronization, anti-phase synchronization, bursting, localization, small oscillations, mixed-mode oscillations, have been modeled by the HH equations.

Synchronization is observed in specific areas of the brain in patients suffering from epilepsy and Parkinson's disease [6]. On the other hand, tasks such as processing sensory information, only occur in synchronized neurons. Localized solutions in oscillatory systems are associated with a partition of the oscillators in two distinct sets. One set is described by oscillators with high amplitudes and the other by oscillators with small amplitudes [7]. These types of patterns may be good approximations for the dynamics of working memory, in a biologically reasonable parameter region [8]. Relaxation oscillations are solutions defined by long periods of quasi-static behavior interspersed with short periods of rapid transition. They are analyzed in the context of the canard phenomenon [9]. A solution showing a combination of traits of relaxation oscillations and small oscillations is defined as a mixed mode oscillation. The later may also be generated by the canard mechanism.

In [2] the authors simulate an integer-order asymmetrically coupled system of two HH equations. They find localized solutions, small oscillations, relaxation oscillations, and mixed-mode oscillations, for certain values of the coupling constants. Localized solutions are seen for negative values of the two coupling constants and when the ratio $\frac{k_1}{k_2}$ between the two constants is far from to -1. Relaxation oscillations occur when this ratio is close to -1, and mixed mode oscillations are the states in between.

Keeping the aforementioned ideas in mind, in this paper, we propose a fractional order model for the dynamics of two asymmetrically coupled HH equations, for variation of the order of the fractional derivative and various temperatures. We consider that the coupling is diffusive and is only done in the voltage term. This is, to our best knowledge, not been the issue of any previous research. In Section 2, we introduce the FO model of asymmetrically coupled HH equations. In Section 3 we show and discuss the outcomes of the simulations of the model. In the last section, we conclude our work.

1.1 Non-Integer Order Differentiation

Non-integer order, aka fractional order (FO), differentiation and integration are generalizations of the well-known differentiation and integration of integer order. FO systems have been widely applied, for a couple of decades now, to solve problems in engineering, biology, physics, to name a few [10, 11, 12, 13, 14].

There are several definitions of FO derivatives. The most commonly used are the Caputo, the Grünwald-Letnikov, and the Riemann-Liouville derivatives [10]. The GL derivative is given by the equation (1).

$$ {}_{a}^{GL}D_t^{\alpha} f(t) = \lim_{h\to 0} \frac{1}{h^{\alpha}} \sum_{0}^{\left[\frac{t-a}{h}\right]} (-1)^k \binom{\alpha}{k} f(t-kh), t > a, \alpha > 0 \quad (1) $$

In 2015, Caputo and Fabrizio (CF) [15] proposed a new definition for the fractional order derivative. The update with respect to previous definitions is the new non-singular kernel operator. This novel derivative has been used in groundwater and thermal problems. Moreover, Atangana *et al.* apply the CF derivative to find the solutions of the Fisher's reaction-diffusion equation and of the Baggs-Freedman model [16, 17].

2 The Fractional-Order Asymmetrically Coupled System of Two HH Equations

The Hodgkin-Huxley equations (1) are a system of 4 × 4 ordinary differential equations (ODEs). They were derived by Hodgkin and Huxley in 1952 [1] to model the electrical behavior of the squid axon. The first equation refers to the trans-membrane potential dynamics, $v(t)$, for a single neuron, in response to an external stimulus I, and as a function of the ion currents. The ion currents are mostly three, one for the sodium (Na^+), one for the potassium (K^+), and one for a leakage current, associated with other ions, where calcium is included. The ions' conductance's are described by the other three equations of the model.

$$
\begin{aligned}
\frac{C_m dv}{dt} &= f(v,m,n,h) - I \\
\frac{dm}{dt} &= \Phi(\alpha_m(v)(1-m) - \beta_m(v)m) \\
\frac{dn}{dt} &= \Phi(\alpha_n(v)(1-n) - \beta_n(v)n) \\
\frac{dh}{dt} &= \Phi(\alpha_h(v)(1-h) - \beta_h(v)h)
\end{aligned}
\tag{2}
$$

where $C_m$is the membrane capacitance, $\Phi = 3^{\frac{\mathrm{T}-6.3}{10}}$, is the temperature compensating factor. The function f is defined as:

$$f(v,m,n,h) = -g_L(v - V_L) - g_{Na}m^3h(v - V_{Na}) - g_K n^4(v - V_k)$$

The functions $\alpha_i(v)$ and $\beta_i(v), i = m,n,h$, are given in [1] as:

$$\alpha_m(v) = \psi\left(\frac{v+25}{10}\right),\ \alpha_n(v) = 0.1\psi\left(\frac{v+10}{10}\right),\ \alpha_h(v) = 0.07\psi\left(\frac{v}{20}\right)$$

$$\beta_m(v) = 4e^{\left(\frac{v}{18}\right)}, \beta_n(v) = \frac{1}{8}e^{\left(\frac{v}{80}\right)}, \beta_h(v) = \left(1 + e^{\left(\frac{v+30}{10}\right)}\right)^{(-1)}$$

and $\psi = \begin{cases} \frac{x}{e^x - 1}, & x \neq 0 \\ 1, & x = 0 \end{cases}$.

The asymmetrically coupled system of two fractional-order HH equations is thus given by:

$$
\begin{aligned}
\frac{C_m d^\alpha v_1}{dt^\alpha} &= f(v_1, m_1, n_1, h_1) - I - k_1(v_1 - v_2) \\
\frac{dm_1}{dt} &= \Phi\big(\alpha_{m_1}(v_1)(1-m_1) - \beta_{m_1}(v_1)m_1\big) \\
\frac{dn_1}{dt} &= \Phi\big(\alpha_{n_1}(v_1)(1-n_1) - \beta_{n_1}(v_1)n_1\big) \\
\frac{dh_1}{dt} &= \Phi\big(\alpha_{h_1}(v_1)(1-h_1) - \beta_{h_1}(v_1)h_1\big) \\
\frac{C_m d^\alpha v_2}{dt^\alpha} &= f(v_2, m_2, n_2, h_2) - I - k_2(v_2 - v_1)
\end{aligned}
\tag{3}
$$

$$\frac{dm_2}{dt} = \Phi\big(\alpha_{m_2}(v_2)(1-m_2) - \beta_{m_2}(v_2)m_2\big)$$

$$\frac{dn_2}{dt} = \Phi\big(\alpha_{n_2}(v_2)(1-n_2) - \beta_{n_2}(v_2)n_2\big)$$

$$\frac{dh_2}{dt} = \Phi\big(\alpha_{h_2}(v_2)(1-h_2) - \beta_{h_2}(v_2)h_2\big)$$

where k_1, k_2 are the coupling constants, and α is the order of the fractional derivative.

3 Numerical Simulations

In this section we show simulations of the FO asymmetrically coupled HH equations model (4), for several values of the order of the fractional derivative, α, and distinct coupling constants, $k_1,\ k_2$. In Table 1, we list the values of the HH parameters fixed in the simulations. In Table 2, can be found the initial conditions and the values for the varied parameters. The symmetrically coupled FO HH equations model is studied in [18].

Table 1

Values of the Hodgkin-Huxley parameters used in the simulations

Parameters	Values	Units
C_m	1.0	$\mu F/cm^2$
T	6.3, 16.0, 26.0	^oC
V_{Na}	-115.0	mV
V_K	12.0	mV
V_L	-10.599	mV
g_{Na}	120.0	mS/cm^2
g_K	36	mS/cm^2
g_L	0.3	mS/cm^2

Table 2

Initial conditions and parameter values used in the simulations

Fig.	Initial conditions	T, I	$k_1,\ k_2$
1, 2, 3	(-22.18,0.43,0.65,0.07, -20.81,0.38,0.63,0.08)	$26^oC, 155$	$-0.2, -2.01$
4, 5, 6	(-10.67,0.17,0.56,0.17, -18.91,0.67,0.74,0.05)	$16^oC, 60$	$0.7, -1.1$
7, 8, 9	(-16.21,0.36,0.60,0.10, 1.39,0.04,0.52,0.28)	$16^oC, 60$	$0.5, -1.1$
10, 11, 12	(-26.01,0.48,0.64,0.07, -7.43,0.12,0.63,0.10)	$20^oC, 155$	$-0.1, -2.0$

Figures 1-3 depict small oscillations of the FO coupled system (3), for $T = 26.0, I = 155$, and $\alpha = 1.0, 0.8, 0.4$, respectively. One can observe a decrease in the amplitude of the periodic orbits with the order of the fractional derivative, α, and a slight increase in the spiking frequency. Faster transients are observed for smaller α. In Figures 4-6, we show relaxation oscillations of the model (3), for $T = 16.0, I = 60$, and $\alpha = 1.0, 0.8, 0.4$, respectively. As α is decreased the spiking frequency of the two neurons increases. In Figures 7-8, we show mixed-mode oscillations of the model (2), for $T = 16.0, I = 60$, and $\alpha = 1.0, 0.8$, respectively. Fixing all other parameters and decreasing only α to 0.4, the mixed-mode oscillations are lost, and a relaxation oscillation appears, see Figure 9. Thus, α, causes a, non-expected, change in the behavior of the system (3). Localized solutions are shown in Figures 10-12, for $T = 20.0, I = 155$, and $\alpha = 1.0, 0.8, 0.4$, respectively. Moreover, we note a decrease in the amplitude and an increase in the spiking frequency of the neurons as α decreases from 1.

As it can be observed from the numerical simulations, the asymmetrically coupled FO model of two HH equations has a rich dynamical behavior. Mixed-mode oscillations, relaxation oscillations, small oscillations, and localized solutions, are common in specific regions of the coupling constants. These regions agree with the results of paper [2], for most values of α. This means that localized solutions are seen for negative values of the two coupling constants and when the ratio $\frac{k_1}{k_2}$ between the two constants is far from to -1. Relaxation oscillations occur when this ratio is close to -1, and mixed mode oscillations are the states in between. Nevertheless, the value of the fractional order derivative, α, adds extra complexity to the behavior of the model. We saw in Figure 9 an `expected' mixed-mode oscillation tend towards a relaxation oscillation, when all other parameters `suggested' a mixed-mode oscillation. This `complexity' may be associated with differences in the human brain, when processing and storing information [8, 7], when responding to certain stimuli, amongst others. Further study is needed in order to infer the importance of the order of the fractional derivative in these models of spiking neurons.

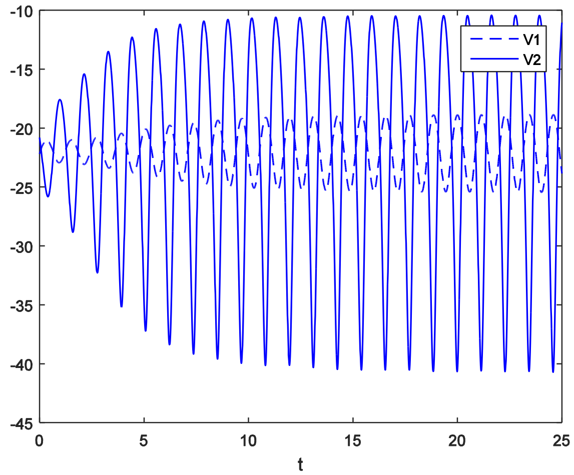

Figure 1
Small oscillations of the FO model (2) for T=26.0, I=155, and α=1.0

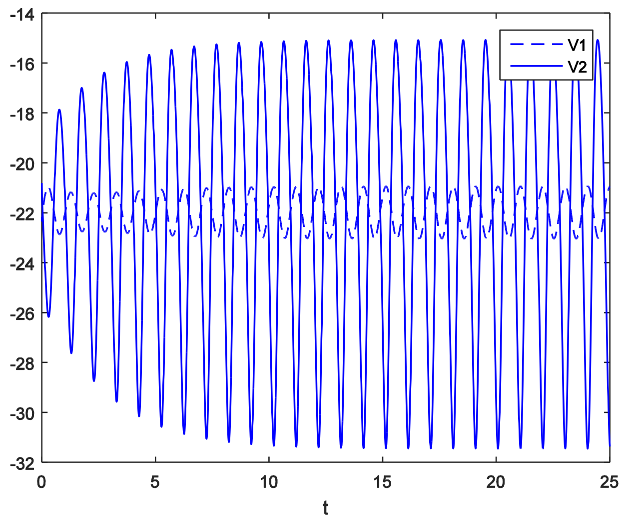

Figure 2
Small oscillations of the FO model (2) for T=26.0, I=155 and α=0.8

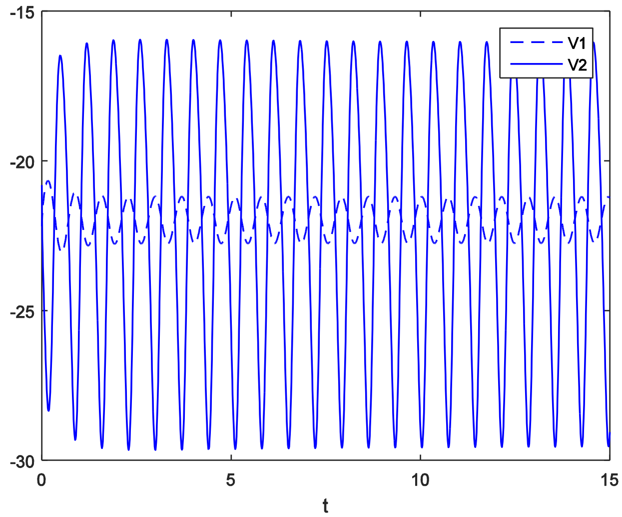

Figure 3
Small oscillations of the FO model (2) for T=26.0, I=155, and α=0.4

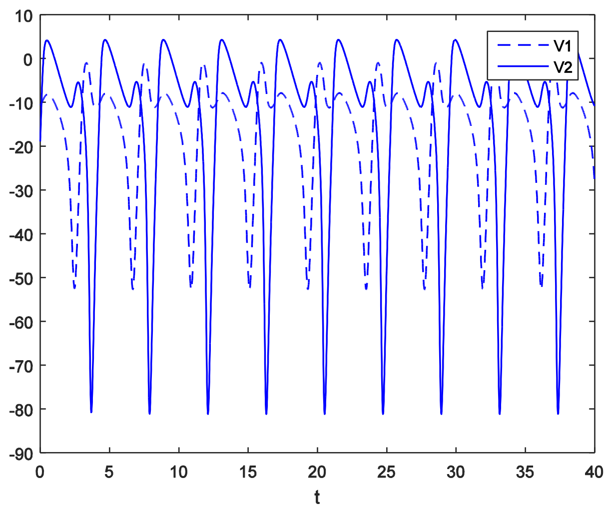

Figure 4
Relaxation oscillations of the FO model (2) for T=16.0, I=60, and α=1.0

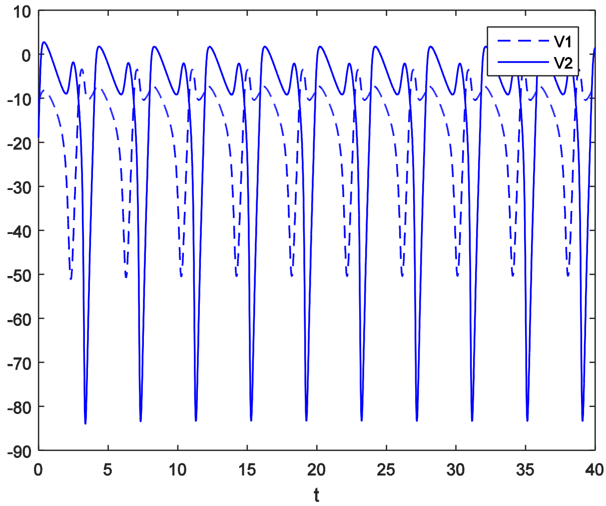

Figure 5
Relaxation oscillations of the FO model (2) for T=16.0, I=60, and α=0.8

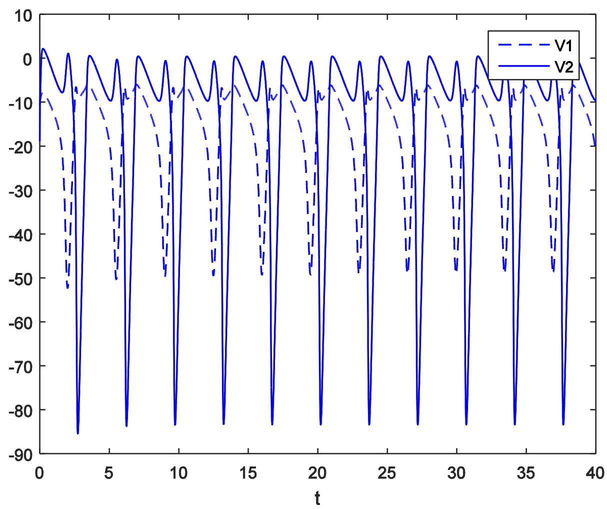

Figure 6
Relaxation oscillations of the FO model (2) for T=16.0, I=60, and α=0.4

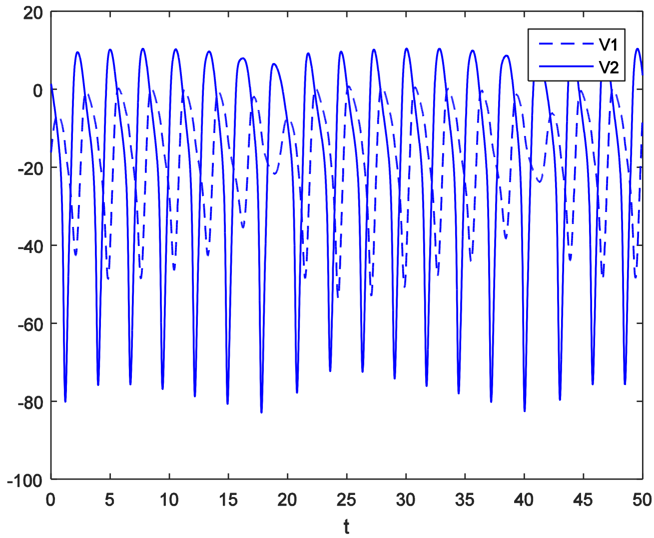

Figure 7
Mixed-mode oscillations of the FO model (2) for T=16.0, I=60, and α=1.0

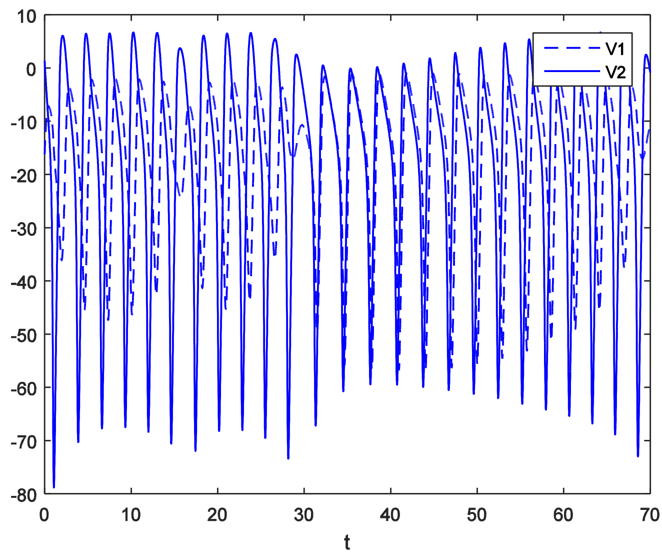

Figure 8
Mixed-mode oscillations of the FO model (2) for T=16.0, I=60, and α=0.8

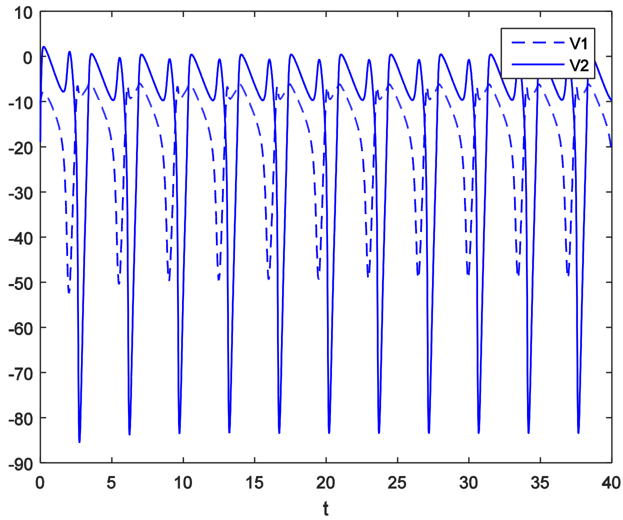

Figure 9
Relaxation oscillations of the FO model (2) for T=16.0, I=60, and α=0.4

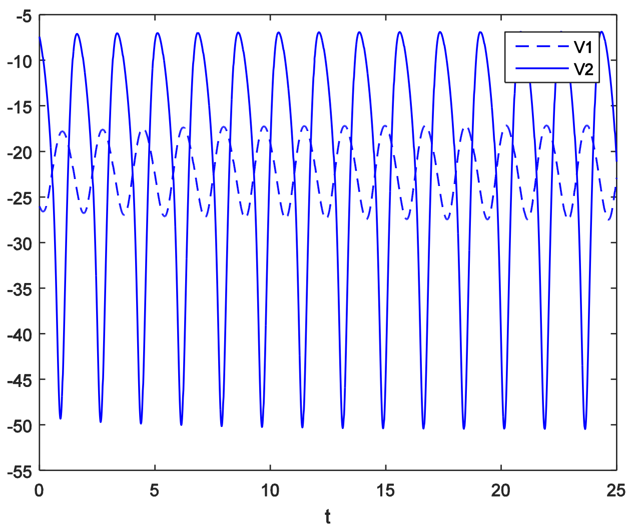

Figure 10
Localized solutions of the FO model (2) for T=20.0, I=155, and α=1.0

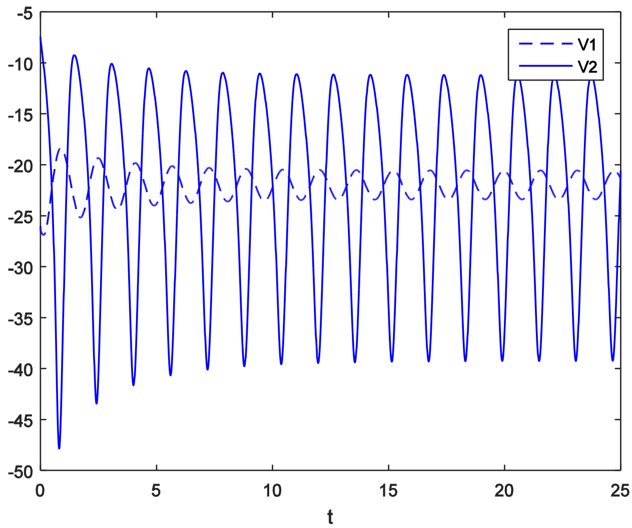

Figure 11
Localized solutions of the FO model (2) for T=20.0, *I*=155, and α=0.8

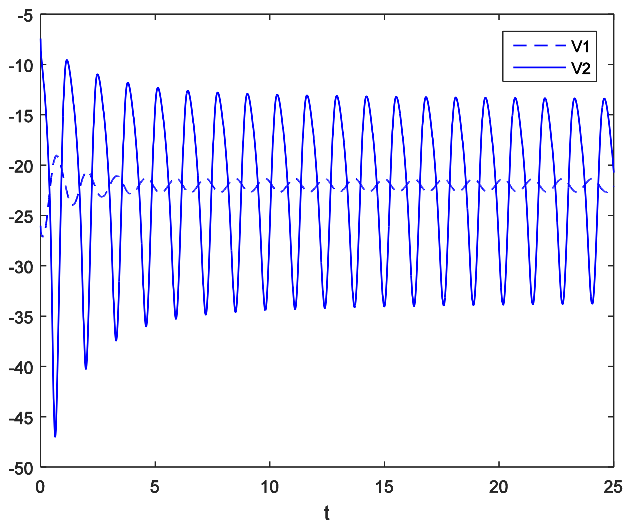

Figure 12
Localized solutions of the FO model (2) for T=20.0, *I*=155, and α=0.4

Conclusions

Herein we observed an asymmetrically coupled model of two FO HH equations. The model is rich in terms of diversity of dynamic patterns. One can distinguish mixed-mode oscillations, small oscillations, relaxation oscillations and localized solutions for certain parameters (coupling constants) regions. Moreover, the value of the order of the fractional derivative comprises more complexity to the coupled FO model. This may be used to explain differences in the human brain when storing and processing memories or when reacting to the same stimuli. More work is needed in order to fully understand the vast diversity of patterns in the model.

Acknowledgement

The author was partially supported by CMUP (UID/MAT/00144/2013), which is funded by FCT (Portugal) with national (MEC) and European structural funds (FEDER), under the partnership agreement PT2020 and by PAPRE-Programa de Apoio à Publicação em Revistas Científicas de Elevada Qualidade from Polytechnic Institute of Porto.

References

[1] Hodgkin, A. L., Huxley, A. F., A Quantitative Description of Membrane Current and Its Application to Conduction and Excitation in Nerve. In *J Physiol* (Lond), Vol. 117, 1952, pp. 500-544

[2] M. Krupa and C. M. A. Pinto, Curious Phenomena in Two Coupled Neurons. In *Proceedings of the 26th IASTED International Conference on Modelling, Identification and Control*, 2007, pp. 387-390

[3] I. S. Labouriau and C. M. Alves-Pinto, Loss of Synchronization in Partially Coupled Hodgkin-Huxley Equations. In *Bulletin of Mathematical Biology*, Vol. 66, 2004, pp. 539-557

[4] H. H. Sherief, A. M. A. El-Sayed, S. H. Behiry, W. E. Raslan, Using Fractional Derivatives to Generalize the Hodgkin–Huxley Model. In: *Fractional Dynamics and Control*, New York, NY: Springer New York, 2012, pp. 275-282

[5] A. M. Nagy and N. H. Sweilam, An Efficient Method for Solving Fractional Hodgkin–Huxley Model. In *Physics Letters A*, Vol. 378, 2014, pp. 1980-1984

[6] J. Modolo, B. Bhattacharya, R. Edwards, J. Campagnaud, A. Legros, A. Beuter, Using a Virtual Cortical Module Implementing a Neural Field Model to Modulate Brain Rhythms in Parkinson's Disease. In *Frontiers of Neuroscience,* Vol. 4, Article 45, 2010, p. 11

[7] H. G. Rotstein, N. Kopell, A. M. Zhabotinsky, I. R. Epstein, A Canard Mechanism for Localization in Systems of Globally Coupled Oscillators. In: *SIAM J. Appl. Math*, Vol. 63(6), 2003, pp. 1998-2019

[8] C. P. Fall, T. J. Lewis, J. Rinzel, Background-Activity-Dependent Properties of a Network Model for Working Memory that Incorporates Cellular Bistability, In: *Biol. Cybern.*, Vol. 93(2), 2005, pp. 109-118

[9] Krupa M, Szmolyan P. Relaxation Oscillations and Canard Explosion. In: *J Diff Equations*, Vol. 174, 2001, pp. 312-368

[10] A. A. Kilbas and H. M. Srivastava and J. J. Trujillo. *Theory and Applications of Fractional Differential Equations* 204, North-Holland Mathematics Studies, Elsevier, Amsterdam, 2006

[11] F. Mainardi, Fractional Relaxation-Oscillation and Fractional Diffusion-Wave Phenomena. In *Chaos Solitons & Fractals*, Vol. 7, 1996, pp. 1461-1477

[12] D. Baleanu, S. I. Muslih, Lagrangian Formulation of Classical Fields within Riemann–Liouville Fractional Derivatives In *Phys. Scr.*, Vol. 72(2-3), 2005, 119-121

[13] R. De Keyser, C. I. Muresan, C. M. Ionescu, A Novel Auto-Tuning Method for Fractional Order PI/PD Controllers. In *ISA Transactions*, Vol. 62, 2016, pp. 268-275

[14] C. M. A. Pinto, A. R. M. Carvalho, New Findings on the Dynamics of HIV and TB Coinfection Models. In *Appl. Math. Comput.*, Vol. 242, 2014 36-46

[15] M. Caputo, M. Fabrizio, A New Definition of Fractional Derivative without Singular Kernel, In *Progr. Fract. Differ. Appl.,* Vol. 2, 2015, 73-85

[16] A. Atangana, On the New Fractional Derivative and Application to Nonlinear Fisher's Reaction–Diffusion Equation. In *Appl. Math. Comput.*, Vol. 273, 2016, 948-956

[17] A. Atangana, I. Koca, On the New Fractional Derivative and Application to Nonlinear Baggs and Freedman Model. In *J. Nonlinear Sci. Appl.,* Vol. 9, 2016, 2467-2480

[18] C. M. A. Pinto, Coupled Fractional Spiking Neurons. In: *Proceedings of 2016 IEEE International Conference on Systems, Man, and Cybernetics*, February 2017, 000487-000491

Discrete-Time Implementation and Experimental Validation of a Fractional Order PD Controller for Vibration Suppression in Airplane Wings

Silviu Folea*, Robin De Keyser, Isabela R. Birs*, Cristina I. Muresan*, Clara Ionescu****

* Department of Automation, Technical University of Cluj-Napoca, Memorandumului 28, Cluj-Napoca, Romania, e-mails: Silviu.Folea@aut.utcluj.ro, Isabela.Birs@aut.utcluj.ro, Cristina.Muresan@aut.utcluj.ro

** Department of Electrical energy, Systems and Automation, Ghent University, Technologiepark 914, Gent, Belgium, e-mail: Robain.DeKeyser@UGent.be

Abstract: Vibrations in airplane wings have a negative impact on the quality and safety of a flight. For this reason, active vibration suppression techniques are of extreme importance. In this paper, a smart beam is used as a simulator for the airplane wings and a fractional order PD controller is designed for active vibration mitigation. To implement the ideal fractional order controller on the smart beam unit, its digital approximation is required. In this paper, a new continuous-to-discrete-time operator is used to obtain the discrete-time approximation of the ideal fractional order PD controller. The efficiency and flexibility, as well as some guidelines for using this new operator, are given. The numerical examples show that high accuracy of approximation is obtained and that the proposed method can be considered as a suitable solution for obtaining the digital approximation of fractional order controllers. The experimental results demonstrate that the designed controller can significantly improve the vibration suppression in smart beams.

Keywords: fractional order controller; novel indirect discretization method; smart beam; vibration attenuation; experimental results

1 Introduction

A cantilever beam equipped with sensors and actuators is considered to be “smart” since its dynamics are always known. This offers countless possibilities to control the amplitude and frequency of the beam’s movement, while also eliminating undesired vibration. The advantages of such an approach have endless practical uses, especially in the case of an airplane wing, which is continuously subjected to random, unwanted vibrations caused by turbulences, engine vibration and trajectory changes [1].

The displacement of the free end of the beam can be successfully reduced with a variety of controllers, from fractional order to integer order PI, PD and PID, from Fuzzy Logic to Linear Quadratic Regulator, from adaptive to robust; and any hybrid combination between them [2]. In addition, optimization algorithms to compute the controller's parameters such as Particle Swarm Optimization and Genetic Algorithms haven't been neglected in the study of vibration suppression [3]. A tuning procedure based on reducing the resonant peak on the frequency magnitude plot is successfully presented in [4]. Apart from classical tuning procedures and optimization techniques, using neural networks is also a viable approach [5], [6].

Over previous decades, the popularity of the fractional order controllers has increased considerably. The fractional order approach represents a generalization of differentiation and integration to an arbitrary order. Compared to the integer order controllers, the fractional order ones offer increased flexibility and can honor more closed loop performance constraints simultaneously [7]. For this reason, a fractional order PD controller has been previously designed for a similar cantilever beam, as the case study in this paper, and the experimental results demonstrated the advantages of using a fractional order PD controller instead of the classical integer order PD [8], [9].

One of the key characteristics of fractional order systems is the hereditary effect, which offers an accurate mathematical representation of the dynamics of several phenomena. However, at the same time, because of their unlimited memory, fractional order systems cannot be exactly implemented [10] and thus, they require a proper rational approximation [11], [12], [13] in a limited frequency range [14]. In this paper, a fractional order PD controller is designed for vibration suppression. Its implementation, on a real time controller, requires the discrete-time approximation of the ideal fractional order control algorithm. To achieve this, the indirect discretization method proposed in [14] is used. First, the well-known Oustaloup Recursive Approximation method is employed to obtain a continuous-time approximation for the fractional order controller. Next, to obtain the discrete-time approximation, a new continuous-to-discrete time operator is proposed as an interpolation between the Euler and Tustin rules, allowing for the possibility of shaping the discrete-time transfer function through the use of a weighting parameter to better approximate the original fractional order system phase or magnitude. The purpose of this paper is to show that the proposed discrete-time approximation method is simple and efficient, not just in simulation environments, but also for real-time implementation of fractional order controllers and even for processes that exhibit a fast dynamic.

The paper is structured as follows. Section II presents the tuning procedure for a fractional order PD controller for vibration suppression in a smart beam. Section

III presents the proposed continuous-to-discrete-time operator, as well as the inverse operator. The mapping between the continuous-time and discrete-time poles/zeros is given, as well as numerical examples to show the flexibility, as well as the problems that can be avoided through the use of the new operator, compared to the classical Tustin rule. Section IV consists in the case study: the vibration attenuation in a smart beam, and details the design and discrete-time implementation of a fractional order controller. Experimental results are also provided. The last section includes the concluding remarks.

2 Tuning of a Fractional Order Controller for Vibration Suppression

To suppress unwanted vibrations that may occur in a smart beam, a fractional order PD controller is designed:

$$H_{FO-PD}(s) = k_p(1 + k_d s^{\mu}) \tag{1}$$

where k_p and k_d are the proportional and the derivative gains, respectively, while $\mu\epsilon[0,1]$ is the fractional order of differentiation. The frequency domain representation of (1) is obtained as:

$$H_{FO-PD}(j\omega) = k_p\left[1 + k_d\omega^{\mu}\left(cos\left(\frac{\pi\mu}{2}\right) + jsin\left(\frac{\pi\mu}{2}\right)\right)\right] \tag{2}$$

The design of the fractional order controller in (1) is based on imposing three different frequency domain specifications [15], [16], regarding the gain crossover frequency ω_{cg}, the phase margin of the open loop system φ_m and the iso-damping property. The three performance specifications are mathematically expressed as:

$$\angle\left(H_{open-loop}(j\omega_{cg})\right) = -\pi + \varphi_m \tag{3}$$

$$\left|H_{open-loop}(j\omega_{cg})\right| = 1 \tag{4}$$

$$\left.\frac{d\left(\angle H_{open-loop}(j\omega)\right)}{d\omega}\right|_{\omega=\omega_{cg}} = 0 \tag{5}$$

Assuming the smart beam is mathematically modeled through a transfer function G(s), then the equations (3)-(5) can be further described as:

$$\left|k_p\left[1 + k_d\omega_{cg}^{\mu}\left(cos\left(\frac{\pi\mu}{2}\right) + jsin\left(\frac{\pi\mu}{2}\right)\right)\right]\right| = \frac{1}{|G(j\omega_{cg})|} \tag{6}$$

$$\frac{k_d\omega_{cg}^{\mu}sin\left(\frac{\pi\mu}{2}\right)}{1+k_d\omega_{cg}^{\mu}cos\left(\frac{\pi\mu}{2}\right)} = tg\left(-\pi + \varphi_m - \angle G(j\omega_{cg})\right) \tag{7}$$

$$\frac{\mu k_d\omega_{cg}^{\mu-1}sin\left(\frac{\pi\mu}{2}\right)}{1+2k_d\omega_{cg}^{\mu}cos\left(\frac{\pi\mu}{2}\right)+k_d^2\omega_{cg}^{2\mu}} = -\left.\frac{d(\angle G(j\omega))}{d\omega}\right|_{\omega=\omega_{cg}} \tag{8}$$

Equations (7) and (8) can then be used to determine the controller parameters k_d and μ based on a graphical approach [15, 16, 17], in which the derivative gain is computed as a function of the fractional order according to (7) $k_{d1}=f(\mu)$ and according to (8) $k_{d2}=g(\mu)$. Then, the two functions f and g are plotted, with the final values for k_d and μ determined as the intersection point of f and g. The proportional gain k_p can be determined afterwards based on the modulus equation in (6).

3 The Proposed Approximation Method

To implement the fractional order PD controller in (1), an indirect discretization method is proposed [14]. The approximation method consists in two steps: the first one involves the continuous-time fitting of the ideal fractional order PD controller with a higher order rational transfer function, while the second step requires the discretization of this fitted continuous-time approximation using any of the well know discretization techniques [13]. Even though a lot of continuous-time approximation methods have been developed, in this paper the Oustaloup Recursive Approximation method [19] is used because of its wide acceptance and efficiency. According to this method, the continuous-time rational transfer function is obtained as follows:

$$C(s) = K_c \frac{\prod_{j=1}^{m}\left(s-z_j^c\right)}{\prod_{i=1}^{n}\left(s-p_i^c\right)} \tag{9}$$

where K_c is the gain, z_j^c are the zeros, j=1,2,...,m and p_i^c are the poles, i=1,2,…,n. The poles and zeros are obtained based on a recursive distribution between a low and a high frequency, at well-chosen intervals, such that a constant ratio is obtained between two consecutive poles and zeros [19].

To obtain the digital approximation of the fractional order PD controller, the second step implies the discretization of (9). Instead of using the classical discretization rules, such as Euler, Tustin, Simpson, Al-Alaoui, etc., a new continuous-to-discrete-time operator is applied [14]:

$$s = \frac{1+\alpha}{T}\frac{1-z^{-1}}{1+\alpha z^{-1}} = \frac{1+\alpha}{T}\frac{z-1}{z+\alpha} \tag{10}$$

with the inverse operator obtained directly from (10):

$$z = \frac{1+\alpha+\alpha sT}{1+\alpha-sT} \tag{11}$$

where T is the sampling time. The proposed operator is an interpolation between the Euler and the Tustin discretization rules, with $\alpha \epsilon [0,1]$ being a weighting parameter. The Euler discretization rule is obtained if α=0, while α=1 leads to the Tustin rule.

The poles, p_i^d, and zeros, z_j^d, of the discrete-time transfer function in (14) are computed according to the inverse operator in (11):

$$p_i^d = \frac{1+\alpha+\alpha p_i^c T}{1+\alpha-p_i^c T} \tag{12}$$

$$z_j^d = \frac{1+\alpha+\alpha z_j^c T}{1+\alpha-z_j^c T} \tag{13}$$

Then, the discrete-time equivalent of (9) has the form:

$$C(z) = K_d \frac{\prod_{j=1}^{n}\left(z-z_j^d\right)}{\prod_{i=1}^{n}\left(z-p_i^d\right)} \tag{14}$$

where K_d is the corresponding discrete-time transfer function gain and it is computed based on the equivalency of the continuous-time and discrete-time transfer functions from (9) and (14) in steady state (s=0 and z=1):

$$K_d = K_c \frac{\prod_{j=1}^{m}\left(-z_j^c\right)\prod_{i=1}^{n}\left(1-p_i^d\right)}{\prod_{i=1}^{n}\left(-p_i^c\right)\prod_{j=1}^{n}\left(1-z_j^d\right)} \tag{15}$$

Remarks [14]*:*

1) To calculate the discrete-time gain K_d using (15) it is necessary to remove first all pure integrators and differentiators.

2) A continuous-time transfer function with dead time can be converted in two steps. The rational part is converted using (12), (13) and (14), while the dead time is converted separately to the nearest integer number of samples: $e^{-s\tau_d} \leftrightarrow z^{-d}$ with $\tau_d \cong dT$.

3) If $m<n$, then $(n\text{-}m)$ continuous-time zeros at $-\infty$ are converted into discrete-time zeros at $-\alpha$. In this case, $(n\text{-}m)$ zeros are added in discrete-time: $z_j^d = -\alpha$ with $j = \overline{m+1,n}$.

Figs. 1 a) and b) show the frequency response of the ideal continuous-time fractional order system $s^{-0.35}$, as well as the discrete-time approximations. The Oustaloup Recursive Approximation method has been used to compute the continuous-time rational transfer function, with the maximum and minimum frequency bounds taken as ω_h=10 and ω_l=10^{-2}, with a total of 5 poles and zeros. The sampling time used in the discretization is T=0.314 s and the weighting parameter has been taken as α=0.9 in Fig. 1a) and α=0.2 for Fig. 1b).

The frequency responses in Fig. 1 demonstrate that the lower the value for α, the better the discrete-time approximation of the magnitude curve. On the other hand, a higher value for α improves the approximation of the phase curve. However, if α is selected close to 1, problems could arise in the discrete-time approximation. The next numerical example demonstrates this issue.

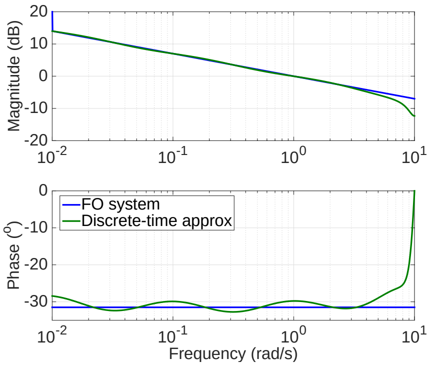

a)

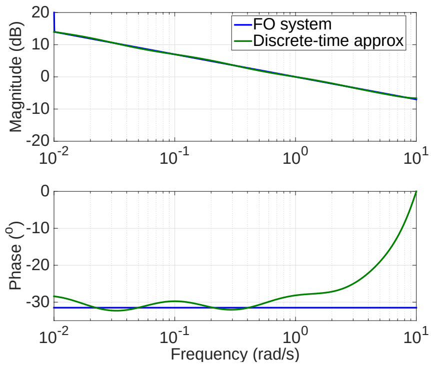

b)

Figure 1

Frequency responses of $s^{-0.35}$ for a) α=0.9; b) α=0.2

Consider the fractional order PID controller:

$$H_{FO-PID}(s) = 10 + 20s^{-0.2} + 2s^{0.7} \tag{16}$$

The Oustaloup Recursive Approximation method, with 5 poles and zeros and within the frequency interval $\omega\epsilon(10^1, 10^2)$, is used to approximate the fractional order integrator and differentiator in (16). The discrete-time approximation is then computed with a sampling time T=0.0314 and two different values for the weighting parameter, α=0.3 and α=1, respectively. Fig. 2 shows the frequency responses of the ideal fractional order controller in (16), along with the two discrete-time approximations corresponding to the two different choices for α. The step responses of the two controllers are given in Fig. 3. As indicated here, when α=1, the ringing phenomenon occurs. Ringing of the controller output is usually unwanted in practice because of its wear effect on the actuators.

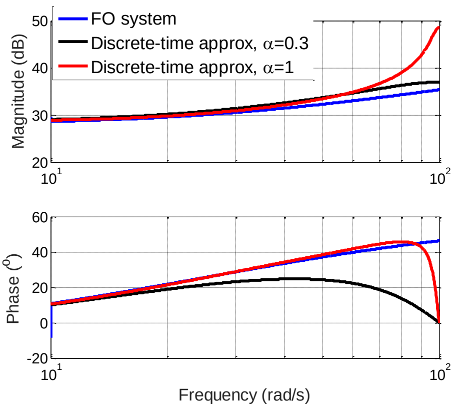

Figure 2

Frequency responses of a fractional order PID controller: ideal vs. discrete-time approximations using the proposed method

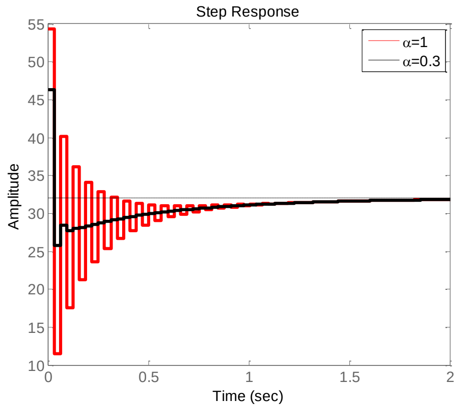

Figure 3

Step responses of the discrete-time approximations of a fractional order PID controller using different values for α

As a conclusion, it is usually bad practice to convert a continuous-time fractional order system (obtained according to the Oustaloup Recursive Approximation method) to its discrete-time equivalent by taking the weighting parameter α close to 1. A fortiori, taking α=1 (Tustin) should be avoided. A theoretical explanation of the cause of the ringing phenomenon is given in [14].

4 Case Study

A smart beam system is considered, in this paper, as the case study. An experimental laboratory scale smart beam unit was developed and built at the Technical University of Cluj-Napoca in Romania, (Fig. 4).

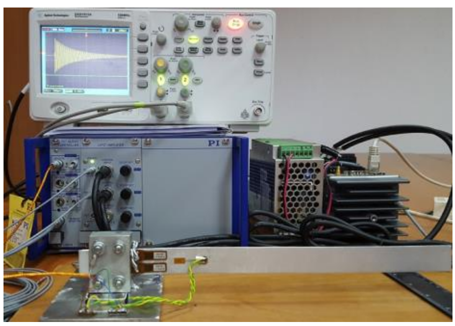

Figure 4

The experimental stand

4.1 Hardware Setup

The block diagram of the system, including the programmable automation controller and a dedicated system with power amplifier (E503.00), the signal processing module (E509.X3), chassis (E501.00), the smart beam, two actuators PZT (P-878.A1) and two piezo resistive sensors (1-LY11-3/120) placed on both sides of the smart beam is presented in Fig. 5.

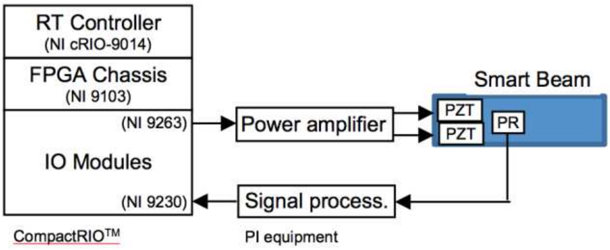

Figure 5
Block diagram of the experimental stand

The PAC embedded system used for implementation is a reconfigurable control and acquisition system providing high performance and reliability. The device includes a real time controller (NI 9014), a chassis with FPGA (NI 9103), two extension modules with analog input lines (NI 9230) and analog output lines (NI 9263).

The architecture of the embedded system is built around two chips: the first one, which runs the VxWorks real-time operating system and is programmable with LabVIEWTM Real Time, and the second which is programmable through LabVIEWTM FPGA.

The real time controller is used for control purposes and is based on an industrial 400 MHz Free scale processor for deterministic and reliable real-time applications. An advantage of this processor is the support for floating point calculations, which is necessary for the control algorithm chosen, having 128 MB of DRAM memory and 2 GB of nonvolatile storage.

The programmable chassis module harbors the user-programmable Virtex II FPGA, which will be used to implement all time critical operations and data acquisition. The input module provides connections for three differential analog input channels. It includes a 24-bit analog-to-digital converter (ADC), is dedicated for piezoelectric sensors and is compatible with TEDS sensors. The NI 9263 provides 4 analog output channels and is used for the command signal applied to the power amplifier and PZT.

4.2 System Identification

The transfer function of the process was determined experimentally by applying a sine wave excitation to the two actuators attached near the fixed end of the beam. By applying a swept sine with varying frequency between 5 and 100 Hz, it was experimentally observed that the largest vibration amplitude is obtained around 14.5 Hz which is the resonant frequency characterizing the first flexural mode.

A second order model for the process was determined exciting the beam with a sine wave of amplitude 1V and 14.5 Hz.

$$G(s) = \frac{78.35}{s^2+1.221\,s+8222} \tag{17}$$

Figs. 6, 7 and 8 show the experimental data used in the identification, as well as a zoomed view of the transient and steady state responses. A 93.22% fit over the experimental data has been obtained using the mathematical model in (17). Obtaining such a high similarity between the identified model and the experimental data doesn't justify the effort necessary to approximate the dynamics of the process with a higher order model.

A swept sine of 1V amplitude and a frequency range between 12 and 16 Hz has also been applied to the smart beam. The simulated and experimental data in Fig. 9 show a good accuracy for the mathematical model with a 73.66% fit.

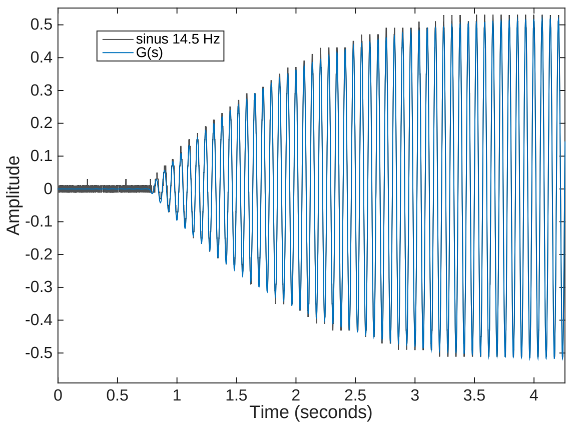

Figure 6

Validation of the identified transfer function on a sine excitation with amplitude 1 and frequency 14.5 Hz

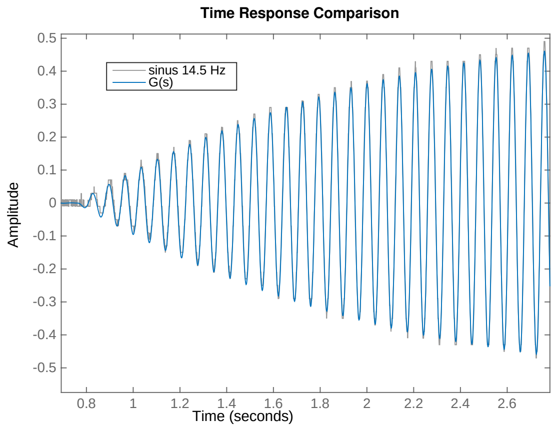

Figure 7
Zoomed transient regime

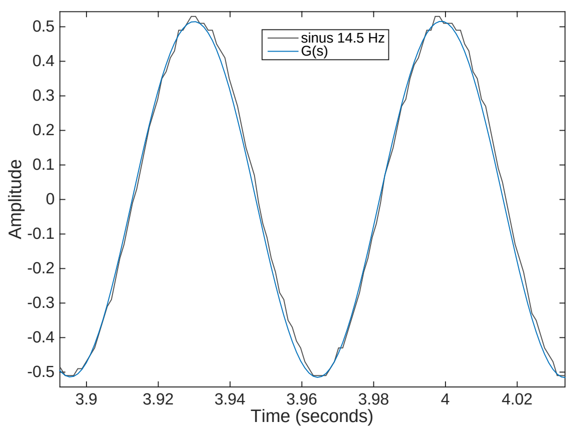

Figure 8
Zoomed steady-state regime

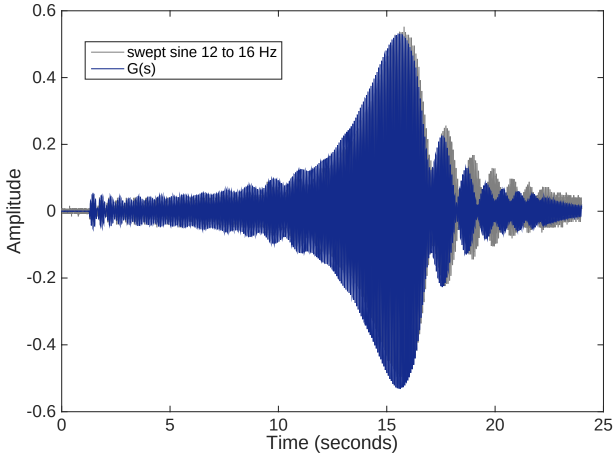

Figure 9
Comparison of actual smart beam response and mathematical model for a swept sine response

4.3 Controller Tuning and Experimental Results

To tune the fractional order PD controller for the smart beam modeled as indicated in (17), the following performance specifications are imposed: a) a gain crossover frequency ω_{cg}=105 rad/s, b) the phase margin φ_m=60$^{\text{o}}$ and the iso-damping property. The graphical solution for equations (7) and (8) is given in Fig. 10. The intersection point in Fig. 10 gives k_d=0.0308 and μ=0.9043. Based on the modulus condition in (6), the proportional gain k_p =14.736. The transfer function of the fractional order PD controller is then:

$$H_{FO-PD}(s) = 14.736(1 + 0.0308s^{0.9043}) \quad (18)$$

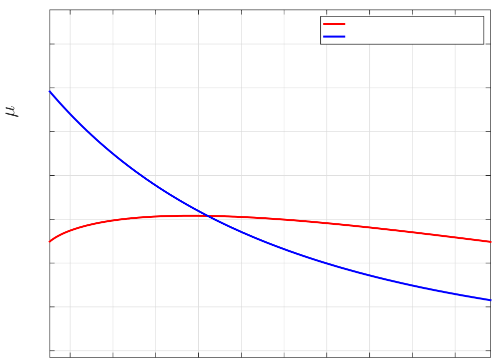

Figure 10
Graphical solution for fractional order PD controller parameters: k_d and μ

The Oustaloup Recursive Approximation method is used to obtain the continuous-time rational transfer function, within the frequency range ω∊(0.0638, 628):

$$C(s) = \frac{1248.8\,(s+468.3)\,(s+58.64)\,(s+18.23)\,(s+1.368)\,(s+0.08718)}{(s+5505)\,(s+347.3)\,(s+21.92)\,(s+1.383)\,(s+0.08725)} \tag{19}$$

The discrete-time approximation, based on the proposed method, is obtained with α=0.2 and a sampling time T=0.005 seconds:

$$G(z) = 77.175\frac{(z-0.206)(z-0.764)(z-0.915)(z-0.993)(z-0.9996)}{(z+0.15)(z-0.29)(z-0.89)(z-0.993)(z-0.9995)} \tag{20}$$

The Bode diagrams of the ideal fractional order PD controller in (18), along with its discrete-time approximation in (20), are given in Fig. 11 showing a good similarity between the two frequency responses. The discrete-time controller in (20) is then implemented on the smart beam. The experimental results considering a tip displacement of the beam's free end are given in Fig. 12, while Fig. 13 shows the free response of the beam considering the same initial tip displacement. The settling time for the free response is 6.88 seconds; as indicated in Fig. 12, the settling time for the controlled response is reduced to 2.92 seconds, which is less than a half.

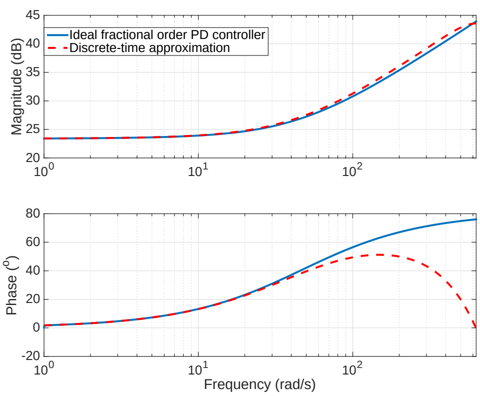

Figure 11

Bode diagrams of the ideal fractional order PD controller and its discrete-time approximation

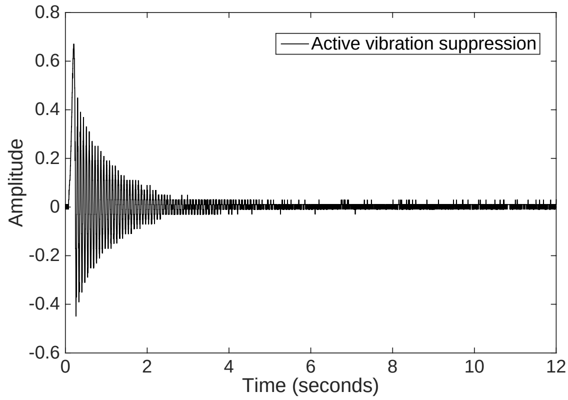

Figure 12
Vibration attenuation using fractional order PD controller

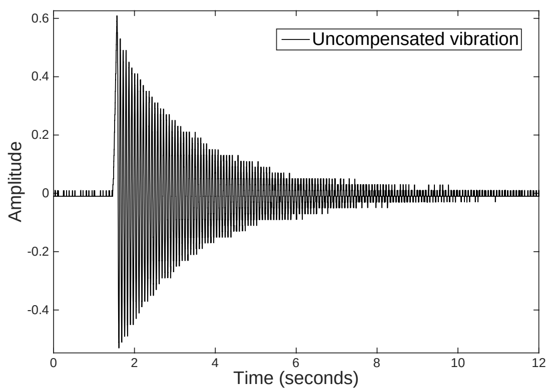

Figure 13
Free response of the smart beam

Conclusions

Suppressing unwanted vibrations are a key concern in numerous industrial domains, including the aerospace industry. Smart structural beams are generally considered an accurate means of studying the behavior of airplane wings. Numerous active vibration control strategies have been proposed, analyzed and experimentally tested, with a new focus on fractional order control algorithms. In this paper, a fractional order PD controller is designed for such a purpose. The major disadvantage of such controllers is that their unlimited memory causes problems when it comes to the actual implementation of the controllers on real environments. The solution to this problem consists in the proper, rational approximation of these fractional order controllers.

In this paper, a novel indirect approach to compute a rational discrete-time approximation of the fractional order PD controller is used. The preliminary results of using this new method have been presented in [14]. The first step consists in obtaining a rational continuous-time transfer function according to the Oustaloup Recursive Approximation method. Then, the new continuous-to-discrete-time operator is used to compute the digital transfer function. The new operator is an interpolation between the Euler and Tustin rules, which ensures an increased flexibility in guaranteeing a better fitting of the magnitude or phase curve of the original fractional order controller. Numerical examples are provided to point out the advantages of this new operator.

Furthermore, this paper presents and demonstrates that the proposed discrete-time approximation method is simple and efficient, not just in simulation environments, but also for real-time implementation of fractional order controllers and even for processes that exhibit a fast dynamic. In this regard, the case study presented shows that the use of this new operator in the approximation of a fractional order PD controller leads to a discrete-time rational transfer function that can be further implemented on the dedicated real time control device. The experimental results, obtained using this discrete-time approximation of the fractional order PD controller, demonstrate the efficiency of the designed algorithm, providing for a 57.5% improvement in the vibration suppression.

Acknowledgement

This work was supported by a grant of the Romanian National Authority for Scientific Research and Innovation, CNCS – UEFISCDI, project number PN-II-RU-TE-2014-4-0598, TE 86/2015.

References

[1] H. A. Abdulameer, H. R. Wasmi: “Vibration Control Analysis of Aircraft Wing by Using Smart Material”, Innovative Systems Design and Engineering, Vol. 6, No. 8, pp. 7-42, 2015

[2] I. Birs, S. Folea, D. Copot, O. Prodan, C. I. Muresan: “Comparative Analysis and Experimental Results of Advanced Control Strategies for Vibration Suppression in Aircraft Wings”, The 13th European Workshop on Advanced Control and Diagnosis, Lille, France, November 17-18 2016

[3] M. Marinaki, Y. Marinakis, G. E. Stavroulakis, "Fuzzy Control Optimized by PSO for Vibration Suppression of Beams”, Control Engineering Practice, Vol. 18, No. 6, pp. 618-629, 2010

[4] I. Birs, C.I. Muresan, S. Folea, O. Prodan, L. Kovács: “Vibration Suppression with Fractional-Order PIλDμ Controller”, Proceedings of the 2016 IEEE International Conference on Automation, Quality and Testing, Robotics (AQTR), Cluj-Napoca, Romania, May 19-21 2016

[5] Z. Qiu, X. Zhang, C. Ye: "Vibration Suppression of a Flexible Piezoelectric Beam using BP Neural Network Controller," Acta Mechanica Solida Sinica, Vol. 25, No. 4, pp. 417-428, 2012

[6] O. Abdeljaber, O. Avci, D. J. Inman, "Active Vibration Control of Flexible Cantilever Plates using Piezoelectric Materials and Artificial Neural Networks", Journal of Sound and Vibration, Vol. 363, pp. 33-53, 2016

[7] C. A. Monje, Y. Q. Chen, B. M. Vinagre, D. Xue, V. Feliu, “Fractional order Systems and Controls: Fundamentals and Applications”, Springer-Verlag, London, 2010

[8] I. R. Birs, C. I. Muresan, S. Folea, O. Prodan: “A Comparison between Integer and Fractional Order PDμ Controllers for Vibration Suppression”, Applied Mathematics and Nonlinear Sciences, Vol. 1, No. 1, pp. 273-282, 2016

[9] Cristina Muresan, Isabela Birs, Silviu Folea, Ovidiu Prodan; “Experimental Results of a Fractional Order PDλ Controller for Vibration Suppresion”, 14th International Conference on Control, Automation, Robotics and Vision, ICARCV 2016, November 13-15, Phuket, Thailand

[10] Charef, T. Bensouici, “Design of Digital FIR Variable Fractional Order Integrator and Differentiator”, Signal, Image and Video Processing, Vol. 6, No. 4, pp. 679-689, 2012

[11] T. Krishna, “Studies on Fractional Order Differentiators and Integrators: A Survey”, J. Signal Proc., Vol. 91, No. 3, pp. 386-426, 2011

[12] G. Maione, “Closed-Form Rational Approximations of Fractional, Analog and Digital Differentiators/Integrators”, IEEE Journal On Emerging And Selected Topics In Circuits And Systems, Vol. 3, No. 3, pp. 322-329, 2013

[13] R. El-Khazali, “Discretization of Fractional-Order Differentiators and Integrators”, Preprints of the 19th World Congress, Cape Town, South Africa. August 24-29, pp. 2016-2021, 2014

[14] De Keyser, R., Muresan, C. I., An Analysis of a New Continuous-to-Discrete Time Operator for the Approximation of Fractional Order Systems, Workshop on Women in Egineering, 2016 IEEE International Conference on Systems, Man, and Cybernetics (SMC 2016), Budapest, Hungary, 9-12 October 2016

[15] Copot, C., Muresan, C. I., Ionescu, C. M., De Keyser, R. (2014), Fractional Order Control of a DC Motor with Load Changes, 14th International Conference on Optimization of Electrical and Electronic Equipment OPTIM, pp. 956-961, DOI: 10.1109/OPTIM.2014.6850964, May 22-24, Bran, Romania

[16] C. I. Muresan, S. Folea, G. Mois, E. H. Dulf, "Development and Implementation of an FPGA Based Fractional Order Controller for a DC Motor", Journal of Mechatronics, Vol. 23, no. 7, pp.798-804, 2013

[17] Muresan, C. I., Dulf, E. H., Both, R. (2016) Vector-based Tuning and Experimental Validation of Fractional Order PI/PD Controllers, Journal of Nonlinear Dynamics, DOI: 10.1007/s11071-015-2328-2, Vol. 84, No. 1, pp. 179-188

[18] Petras, "Tuning and Implementation Methods For Fractional-Order Controllers", Fractional Calculus and Applied Analysis, Vol. 15, No. 2, pp. 282-303, DOI: 10.2478/s13540-012-0021-4, 2012

[19] Oustaloup, A., F. Levron, B. Mathieu, F. M. Nanot, "Frequency-Band Complex Noninteger Differentiator: Characterization and Synthesis", IEEE Trans. Circuits Syst. I Fundam. Theory Appl., Vol. 47, No. 1, pp. 25-39, 2000

Fractional Order Impedance Model to Estimate Glucose Concentration: in Vitro Analysis

Dana Copot, Robin De Keyser, Jasper Juchem, Clara M. Ionescu

Ghent University, Research group on Dynamical Systems and Control
Technologiepark 914, 9052 Ghent, Belgium
{dana.copot,claramihaela.ionescu,robain.dekeyser,jasper.junchem}@ugent.be

Abstract: This paper uses tools from fractional calculus such as Cole-Cole and fractional order impedance models for estimation of glucose concentration. The measured impedance is compared with two fractional order models and the simulation results show that Cole-Cole model has limitation and cannot capture the dynamics of the simulated environment. On the other hand, the fractional order model can follow the changes in impedance for several study cases. Model parameters are correlated with various conditions of the test environment. The results of these study cases show that the fractional order model is a suitable candidate for this particular application. The hypothesis tested in this paper provides new tools for glucose concentration monitoring and measurement.

Keywords: Fractional Order Impedance Models; Diabetes; Modeling; Cole-Cole Model

1 Introduction

Due to the increase in diabetes severity, this disease has become a serious health problem at a worldwide level representing teh main cause of death in the age category 20-79 years. Hence, the research comunity has focused on developing more reliable and accurate devices for glucose measurement [1]. In this research area the main challenge to tackle is the design of non-invasive devices. Although, the non-invasive idea dates already from the 70s many of the proposed technologies are still at an early stage of development [2].

Several techniques such as electromagnetic sensing, infrared spectroscopy, polarimetry were considered in order to enable the design of new methodologies for glucose concentartion measurement. Worldwide, this area is intensively explored and efforts are being made towards the development of stabe, reliable and accurate measurement devices (e.g. BioSensors, Cnoga Medical C8 MediSensors, etc.).

Although there are several devices available on the market, they are not yet working at the desired capacity and there is ongoing research for upgrade. Moreover, the documentation released by the research groups is limited and also validation of this devices on large groups is still missing [3]. The main disadvantage of the current devices is that they are relatively poor in signal-to-noise-ratio. Therefore, up to now no device can be considered fully reliable and clinically validated. Given that non-invasive techniques are still at an early stage of development there is still room for improvements [3].

Therefore, focus on developing systems such as artificial pancreas to control insulin delivered to patients with diabetes has increased. the current standards in clinical practice consist of blood glucose measurements based on finger-prick technique. However, when this method is used for most patients is an unpleasant procedure due to the protocol of taking blood samples. Moreover, recent studies show that on long term there is the risk of fingerprint damage [4]. In figure 1 an overview of the methods used for blood glucose monitoring and control are presented.

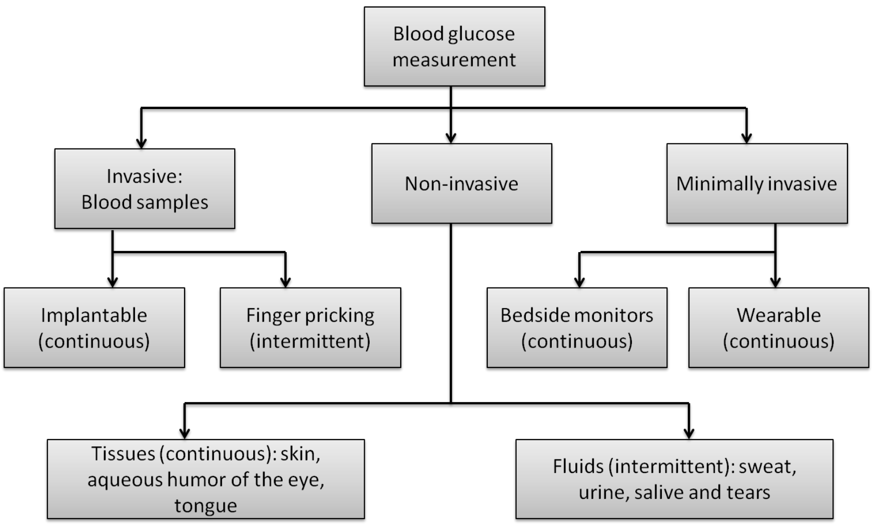

Figure 1
An overview of the method used for blood glucose measurement

Considering all the aspects presented above the advantages of non-invasive technology is easily motivated. Nowadays, the use of nano-technology is the new approach towards the improvement of the health sector. For example, nanorobots are used to deliver a drug to a precise location. This will result in a faster effect and also will reduce the risks of secondary effects. Blood can be characterized as a non-newtonian fluid and therefore when designing such a device this aspect needs to taken into account [5]. In order to deal with difficulties encountered (from a modeling and control approach) new techniques need to be investigated.

Therefore, this paper discusses the use of fractional calculus since it is able to make a trade off between linear theory (Newtonian) and non-linear theory (Non-Newtonian) fluids.

More specifically, fractional order impedance is a suitable tool to estimate, measure and evaluate the glucose levels. FC is of key importance in modeling of phenomena in several areas of research (e.g. chemistry, physics, engineering, etc.) [6, 7]. From

the perspective of biomedical engineering fractional order calculus has been only recently introduced [8].
In the biomedical engineering research community the interest on using tools from fractional calculus in this area has increased considerably in the last years [9–11]. Fractional order concept refers to dynamical systems for which the structure consist of arbitrary-order derivatives and integrals [12]. A detailed description of fractional order integrals and derivatives can be found in [13].
In this paper the hypothesis wheter or not fractional calculus is a suitable candidate to measure, estimate and evaluate the level of glucose. For this, electrochemical impedance spectroscopy has been employed and preliminary analysis (in vitro) has been performed. EIS is used in several fields of research (e.g. batteries, fuel cells, biological systems, etc.) [14–18] EIS has been succesfully applied to estimate and analyze the impact of glucose in erythrocytes [19, 20], effect of glucose in aqueous solutions [21,22], etc. This paper proposes a new approach, i.e. the use of fractional order impedance models to characterize changes in glucose concentration (in vitro analysis). At the same time, analysis on how the model parameters are changing as a function of the concentration will be also investigated. The preliminary results indicate that the proposed fractional order model can detect and differentiate changes in glucose concentration.
The paper is organized as follows: In section II A brief description of the tools proposed in this paper is given followed by Section III where the measurement device and the methodology employed are introduced. The outcome of the proposed hypothesis is given in section IV. The main outcome of this study is summarized in section V.

2 Theoretical Background

2.1 Cole-Cole Impedance Model

Fractional order elements are present in many areas of engineering [23]. When an electrochemical system is modelled usually a constat phase element is chosen since a non-homogenuous surface is present [23]. Impedance (when a CPE is used) is obtained using the following formula:

$$Z(j\omega) = \frac{1}{C_\alpha (j\omega)^\alpha} \tag{1}$$

where C_α represents the capacitance of order α, with $0 \le \alpha \le 1$.
Electrical properties of cell membrane have been modelled by means of impedance measurements in the 1940 by Cole. Recently, the work of Magin presented a generalization of the Cole-Cole expression by means of fractional calculus [16, 17]. This model consist of 3 main elements: a low frequency resistor R_0, a high frequency resistor R_∞ and a CPE_α [24].
The developed circuit can be visualised as two serial connected elements: one is R_∞ and the second one is $(R_0 - R_\infty)||CPE_\alpha$. The complex impedance described by Cole

model is given by the following equation (Cole 1940):

$$Z_\alpha(\omega) = R_\infty + \frac{R_0 - R_\infty}{1 + (j\omega\tau_\alpha)^\alpha} \tag{2}$$

with τ_α the characteristic relaxation time.
Previous work of the authors have aslo employed Cole-Cole model fro characterization of several simulated environment (i.e. simulating different concentrations of glucose) and the obtained results are presented in [24].

2.2 Fractional Order Impedance Model

The Cole-Cole model has several limitation (as described in [24]) in terms of capturing the dynamics of the real data. Next, tools from fractional calculus have been employed and an augmented fractional order model has been used to characterize the glucose concentration profile. Given the structure of the fractional order model electrical analogy with ladder networks can be considered [10]. It has been shown that the values of the complex impedance are increasing as a function of the number of neural networks.
A conceptual scheme of such a ladder network is depiceted in the following Figure. The total admittance of such a ladder is given by the continued fraction expansion.

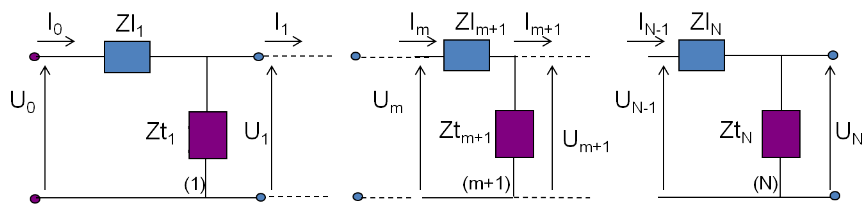

Figure 2
Schematic representation of a ladder network characterizing the neuron transmission model [10]

$$Y_N(s) = \cfrac{1/Zl_1}{1 + \cfrac{Zt_1(s)/Zl_1(s)}{1 + \cfrac{Zt_1(s)/Zl_2(s)}{1 + \cfrac{Zt_2(s)/Zl_3(s)}{1 + \cfrac{\cdots}{1 + \cfrac{Zt_{N-1}(s)/Zl_N(s)}{1 + Zt_N(s)/Zl_N(s)}}}}}} \tag{3}$$

In previous work of the authors it has been demonstrated that this structure of the ladder network results in the appearance in lumped form of a fractional order parameter dependent on the structure and fucntionality of the ladder elements [10]:

$$\gamma = \frac{log(a)}{log(a+b)} \tag{4}$$

where a and b represent the specific property parameters. Then, the lumped admittance model can be expressed as:

$$Y(s) \approx Ks^{\gamma} \tag{5}$$

or equivalently, the impedance:

$$Z(s) \approx \frac{k}{s^{\gamma}} \tag{6}$$

When interpreting the model at a micro scale level, the model refers to the diffusion process of glucose molecules in teh simulated environment. Independently, the lumped impedance model has been shown to be of the form:

$$Z(s) = Ds^{\delta} \tag{7}$$

where D represents the diffusion parameter and δ represents the fractional order parameter value related to the diffusion rate. The complete fractional order model is expressed as:

$$Z(j\omega) = R + \frac{k}{s^{\gamma}} + Ds^{\delta} \tag{8}$$

When this model is employed there are 5 parameters which need to be estimated for every impedance measurement.
The reasoning behind developing such a model is to enable the design and development of a nanoscale robot for continuous evaluation of glucose levels. Such a technology would lead to a better monitoring of patients with diabetes by means of an accurate and reliable tool.

3 Experimental Setup and Methodology

3.1 Solutions

To test the proposed methodology, simulated solutions of different glucose concentration have been used for analysis. It is well known that the composition of plasma consits in 92% water and dissolved solutes of 8% such a electrolytes, proteins, organic wastes and nutrients. Electrolytes are responsible with the transmission of electrical signals. The major electrolytes in plasma are Sodium (Na^{+}), Potassium (K^{+}) and Chloride (Cl^{-}) and these are responsible to ensure stable concentrations and to charge differences across cell membranes. For teh study cases presented in this paper aquaous solution of KCl with a concentration of 80 mmol/L have been used. In order to simulate the real life situation this baseline solution has been diluted in other 5 concentration levels, i.e. 5, 10, 15, 20 and 40 mmol/L. To ensure that the analysis performed is as close as possible to real life teh sample concentration have been chosen based on the data presented in Table 1.

Table 1
Overall glucose level and the medical interpretation.

mmol/L	mg/dL	Medical interpretation
2.0	35	very low, danger of unconsciousness
3.0	55	marginal insulin reaction
4.0 - 6.0	70 -100	normal value before meal in nondiabetic patient
8.0	150	normal value after meal in nondiabetic patient
10.0	180	maximum after meal in nondiabetic patient
15	270	high to very value
16.5 - 20.0	300 - 360	danger
22	400	extremely high

In clinical practice the following glucose levels have been defined (recommended): prior a meal (preprandial) it is indicated that the level of glucose is less than 100 mg/dL (5.5 mmol/L) in plasma and 89 mg/dL (4.9 mmol/L) in whole blood capillary; after meal (postprandial) the value cannot exceed 140 mg/dL (7.8 mmol/L) in plasma and 125 mg/dL (6.9 mmol/L) in whole blood or capillary as shown in table 1, based on which the samples concentration has been selected.

3.2 Instrumentation

Impedance measurements have been performed using an electrochemical device i.e. a Solatron modulabXm impedance analyzer (Solatron Analytical, UK), see Figure 3. The experimental procedure consist in sending a sinusoidal voltage to the electrodes connected to the analyzed sample. The impedance has been evaluated in the frequency interval 1Hz-1MHz. The measurement cell is a small cylindrical tank (inner diameter of 20 mm and a length of 30 mm) and the electrodes used to aquired the measured data are screen-printed electrodes. These electrodes are suitable for repeatable measurements but also they exhibit high electrochemical activity.

3.3 Methodology

Mostly, the electrochemical impedance spectrocopy method is done by means of a single frequency. However, this a time-consuming procedure and it is more difficult to eliminate the transient. Another posibility is to use a random signal which will decrease the amount of time rquired for analysis, but, in this situation leakage migt introduce error in the frequency response function estimation [21]. Therefore, it is important to preserve linearity and to ensure this small amplitude signals need to be send to the analyzed probe and this will result in a poor signal to noise ration. To overcome these multisine exciattion signals are a suitable choice. These signal are able to ensure a short measurement time due to their ability to perform broadband excitation. Also, in case of multisine signals leakage is not an issue since it is a periodic signal. For the analysis performed in this paper a multisine exictation signal

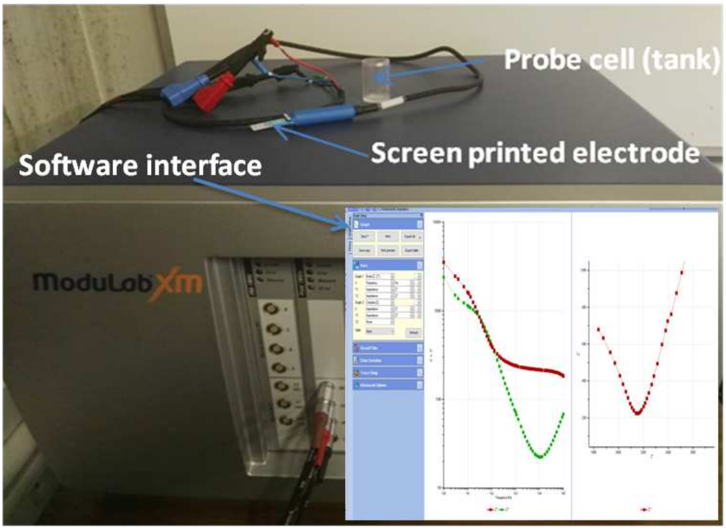

Figure 3
Solatron ModulabXm impedance analyzer

(i.e. voltage) has been sent to the probe and the corresponding current signals have been aquired. This method has the advantage of proving a good analysis of the noise and at the same time of the bias present in the analyzed data. This enables extraction of teh best linear approximation from the measured data. For identification, the non-parametric best linear approximation method has been employed. More details about this method can be found in [10]. The outcome of teh identification procedure is a complex impedance which can be expresssed as real and imaginary part for each excited frequency point. This is a graphical interpretation of the analyzed data which allows us to extract a parametric representation. More speciffically, to the extracted data is compared with the parametric model described in section 2. This results in a parameterization of the analyzed data. In previous work the authors showed that the method employed in this paper is equally good as a full optimization procedure [10]. In Figure 3 a typical measurement output is depicted.

4 Results

In this section the experimental results obtained for different glucose concentrations solution are presented and discussed. Using the device described in section 2 and employing the metodology describe in the paper analysis of multiple simulated solutions has been performed and the results are presented in figures 4-10. The reasoning of the analysis performed in this paper has been described in 3.2. First, the measured data has been fitted to the Cole-Cole model. For this, it is necessary to identify the values of the five model parameters (R_0, R_∞, τ, α, β) for the Cole-Cole model. This model proved not be able to capture the dynamics of measured impedances. In figure 4 the results obtained for concentration of 5mmol/L and 10mmol/L glucose are presented.

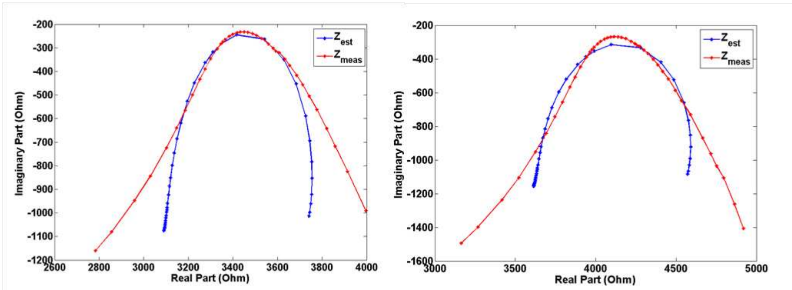

Figure 4
Results of tge measured and estimated impedance using Cole-Cole approach. Blue line: model; Red line: measured data. Left: 0 mmol/L glucose; Right: 5 mmol/L. The measurement were performed in the ferquency range 1Hz-0.1Mh

As it can be noticed from Figure 4 the obtained results are not satisfactory. More specifically, it can be seen that the typical ellipsoid shape of the estimated impedance does not comply with the somewhat skewed polar plot of the calculated impedance from voltage-current measurements. Therefore, we have moved one step further and tools from fractional calculus have been employed.
For the fractional order impedance model the following parameters have to be estimated R, L, D, α, β. The identified values for every parameter are given in table 2. From table 2 it can be noticed that three model parameters are well caharacterized while two parameters are yet to be identified. For this two parameters the right experiment has not been yet found but there is ongoing work. The real and imaginary part of the measured impedance for the in vitro tests performed are shown in Figure 5.

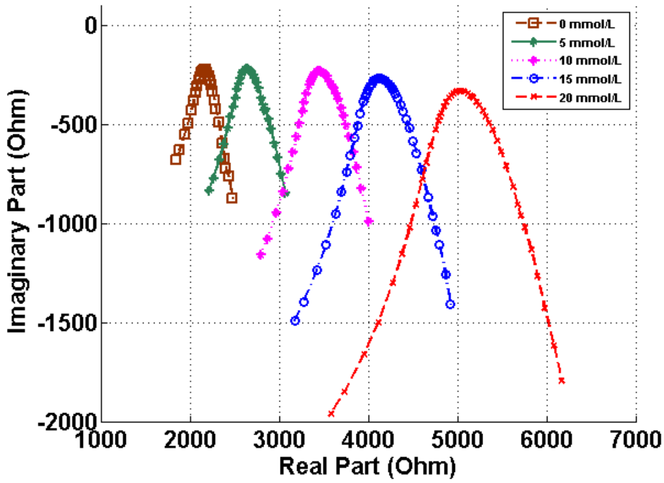

Figure 5
Relevant part of the measured signal used for further analysis

Table 2
Fractional order impedance model parameters estimation.

R	L	D	α	β
0.1512	0.2862	2.9583	0.0017	0.00009
0.1568	0.1700	2.6854	0.00011	0.00009
0.1658	0.0180	2.1128	0.0013	0.00009
0.2164	0.1210	2.6358	0.00012	0.00009
0.2358	0.3521	2.2657	0.0015	0.00009
0.2688	0.0130	1.8598	0.00015	0.00009

In Figures 6-10 the results obtained for different glucose concentration are presented and it can be noticed that a good fit between measured and estimated impedance has been obtained. As it can be noticed from the model parameters also, there si still room for improvement and research with respect to the model performance is ongoing. More specifically, tests to understand the changes of the impedance at high frequencies as well as why at higher concentration a good fitting is not obtained anymore are being investigated.

Conclusions

In this paper the concept of fractional calculus and electrochemical impedance spectroscopy has been used to estimate and measure the impedance of several aqueous glucose solutions. The results show that the electrochemical impedance spectroscopy can be used as a basis for detection of glucose. However, there is still room for improvement in order to obtain a better correlation between the estimated and measured impedance.

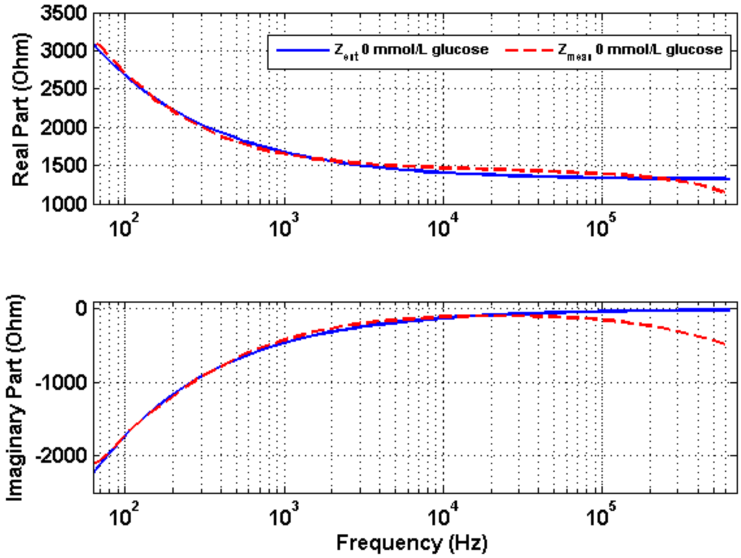

Figure 6
Model (o) against measured impedance (+) at a concentration of 0 mmol/L glucose in the frequency range 1Hz-0.1 MHz

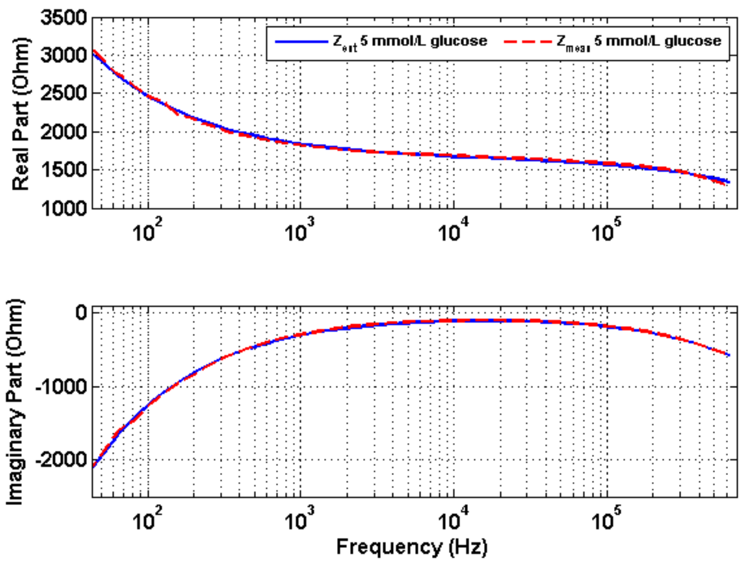

Figure 7
Model (o) against measured impedance (+) at a concentration of 5 mmol/L glucose in the frequency range 1Hz-0.1 MHz

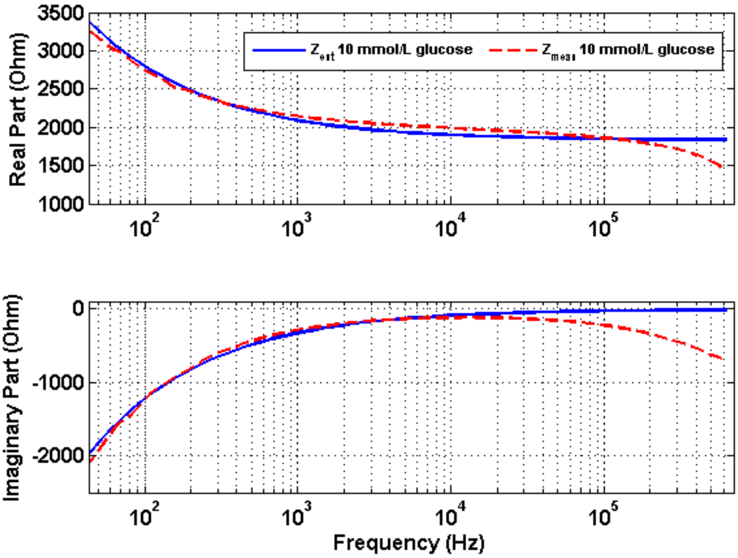

Figure 8
Model (o) against measured impedance (+) at a concentration of 10 mmol/L glucose in the frequency range 1Hz-0.1 MHz

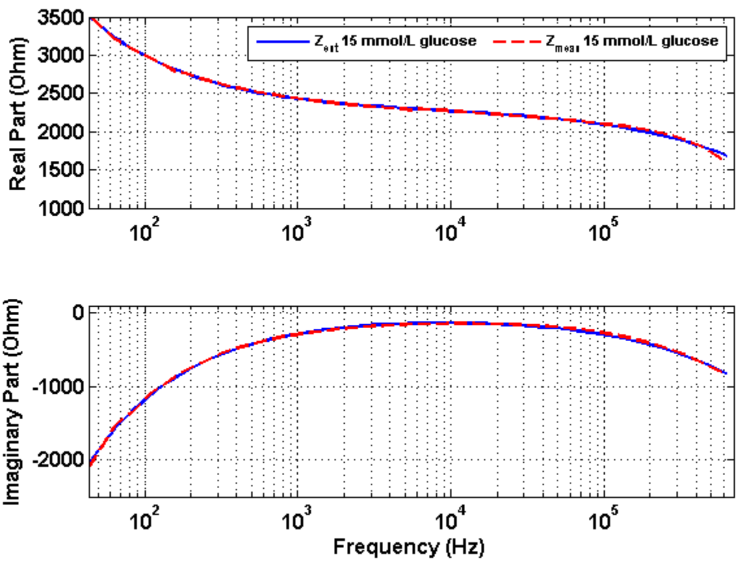

Figure 9
Model (o) against measured impedance (+) at a concentration of 15 mmol/L glucose in the frequency range 1Hz-0.1 MHz

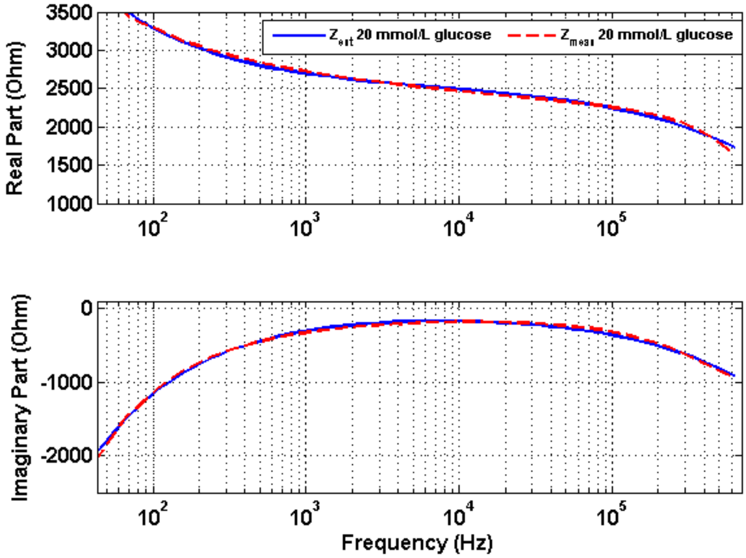

Figure 10
Model (o) against measured impedance (+) at a concentration of 20 mmol/L glucose in the frequency range 1Hz-0.1 MHz

Acknowledgement

This work is financially supported by Flanders Research Centre, grant nr 12B3415N, G008113N and G026514N.

References

[1] S. Vashist, Constinuous glucose monitoring systems: A review. Diagnostics, 3, 385-412, 2013.

[2] O. Khalil, Non-invasive glucose measurement technologies: an update from 1999 to the dawn of the new millennium. Diabetes Technology Therapy, 6(5), 660–697, 2004.

[3] C. So, K. Choi, T. Wong, J. Chung, Recent advances in noninvasive glucose monitoring. National Center for Biotechnology Information, doi:10.2147/MDER.S28134, 2012.

[4] V. Sgurev, R. Yager, J. Kacprzyk and K. Atanassov. Recent contributions in intelligent systems. Springer International Publishing Switzerland, 2017.

[5] C. Ionescu, A memory-based model for blood viscosity. Communications in Nonlinear Science and Numerical Simulation, 45, 29-34, 2017.

[6] R. L. Magin. Fractional Calculus in Bioengineering, Begell House Publishers, 2006.

[7] E. Gutierrez, J. Mauricio Rosario and J. T. Machado. Fractional Order Calculus: Basic Concepts and Engineering Applications, Mathematical Problems in Engineering, 2010.

[8] B. J. West. Fractal physiology and chaos in medicine, Studies of nonlinear phenomena in life sciences, vol.1. Singapore: World Scientific, 1990.

[9] G. A. Losa, D. Merlini, T. F. Nonnenmacher and E. R. Weibel. Fractals in Biology and Medicine, vol IV. Berlin: Birkhaser, 2005.

[10] C. Ionescu, The human respiratory system: an analysis of the interplay between anatomy, structure, breathing and fractal dynamics, Springer, Series in BioEngineering ISBN 978-1-4471-5387-0, Online ISBN 978-1-4471-5388-7, 2013.

[11] C. Ionescu, Phase Constancy in a Ladder Model of Neural Dynamics. IEEE TRANSACTIONS ON SYSTEMS MAN AND CYBERNETICS PART A-SYSTEMS AND HUMANS, 42(6), 1543-1551, 2012.

[12] A. Oustaloup. La derivation non entiere. Hermes, Paris, 1995. (in French)

[13] I. Podlubny. Fractional differential equations, San Diego: Academic Press,1999.

[14] F. Mansfeld, W.J. Lorenz, Electrochemical impedance spectroscopy; applications in corrosion science and technology, in R. Varma, J.R. Selman (Eds.) , Techniques for Characterization of Electrodes and Electrochemical Processes, Wiley, New York, 581-647, 1999.

[15] A. Lasia, Electrochemical impedance spectroscopy and its applications, in R.E. White, B.E. Conway, J.O'M. Bockris (Eds.), Modern Aspects of Elec-

trochemistry, vol. 32, Kluwer Academic/Plenum Press, New York, 143-248, 1999.

[16] R. Magin, Fractional calculus in bioengineering 1. Critical Reviews in Biomedical Engineering, 32, 1-104, 2004.

[17] R. Magin, Fractional calculus in bioengineering 2. Critical Reviews in Biomedical Engineering, 32, 105-194, 2004

[18] H. Fricke, Theory of electrolytic polarization. Philosophical Magazine, ed. Tailor and Francis, 14, 310-318, 1932.

[19] R. Lisin, B. Ginzburg, M. Schlesinger, Y. Feldman, Time domain dielectric spectroscopy study of human cells. I. Erythrocytes and ghosts. Biochimica et Biophysica Acta, 1280(1), 34-40, 1996.

[20] A. Caduff , L. Livshits , Y. Hayashi, Y. Feldman, Cell Membrane Response on d-Glucose Studied by Dielectric Spectroscopy. Erythrocyte and Ghost Suspensions. Journal of Physical Chemistry, 108(6), 13827-13830, 2004.

[21] Park, J.H. Kim, C.S. Choi, B.C. Ham, Biosens. Bioelectron. 19 (4), 321–324

[22] A. Tura, S. Sbrignadello, S. Barison, S. Conti, G. Pacini, Impedance spectroscopy of solutions at physiological. Journal of Physical Chemistry glucose concentrations, 129(2-3), 235-241, 2007.

[23] E. Barsoukov, J. Macdonald, Impedance spectroscopy theory, Experiment and Applications. New Jersey: John Wiley and Sons, 595p, 2005.

[24] D. Copot, C. Muresan. R. De Keyser, C. Ionescu, Fractional order modeling of diffusion processes: a new approach for glucose concentration estimation. International Conference on Automation, Quality and Testing, Robotics, Cluj Napoca, Romania, 19-21 May, 2016 (accepted).

[25] R. Kadara, N. Jenkinson, C. Banks, Characterisation of commercially available electrochemical sensing platforms. Sensors and Actuators B: Chemical, 138(2), 556-562, 2009.

Modelling Tumor Growth Under Angiogenesis Inhibition with Mixed-effects Models

Tamás Ferenci, Johanna Sápi, Levente Kovács

Research and Innovation Center of Óbuda University, Physiological Controls Group
Óbuda University, Kiscelli utca 82, Budapest, H-1032, Hungary
Email: {ferenci.tamas,sapi.johanna,kovacs.levente}@nik.uni-obuda.hu

Abstract: Angiogenesis inhibitors offer a promising new treatment modality in oncology. However, the optimal administration regimen is often not well-established, despite the fact that it might have substantial impact on the outcome. The aim of the present study was to investigate this issue. Eight weeks old male C57Bl/6 mice were implanted with C38 colon adenocarcinoma, and were given either daily (n $= 9$*) or single (n* $= 5$*) dose of bevacizumab. Outcome was measured by tracking tumor volume; both caliper and magnetic resonance imaging was employed. Longitudinal growth curves were modelled with mixed-effects models (with correction for autocorrelation and heteroscedasticity, where necessary) to infer on population-level. Several different growth models (exponential, logistic, Gompertz) were applied and compared. Results show that the estimation of the exponential model is very reliable, but it prevents extrapolation in time. Nevertheless, it clearly established the advantage of the continuous regime.*

Keywords: mixed effects models; tumor growth; angiogenesis inhibition; dosing regimen

1 Introduction

Biomedical experiments aim to investigate and understand physiological and pathophysiological processes. There are three main types of the biomedical experiments: *in vivo*, *in vitro* and *in silico* experiments. *In vivo* studies use living organisms for the experiment, these are animal studies and clinical trials. *In vitro* studies examine biological processes in a controlled environment but outside of a living organism. Finally, *in silico* studies are performed on computer or via computer simulation. It is clear that in vivo experiments describes most precisely the real processes and as a result, we can observe the overall effects of an experiment on a living organism. The drawback, however, is the use and sacrifice of animals (in case of animal experiments), and according to the principles of the 3Rs (replacement, reduction and refinement) [1] we should avoid or replace the use of animals (replacement), and minimize the number of animals used per experiment (reduction).

In our experiment, we used 14 mice in total (in order to fulfill the principle of reduction), nevertheless the obtained results are satisfactory to carry out statistical modelling (which is a replacement method since in the future these models can be used for further investigation instead of the use of mice).

In cancer treatment, a novel approach is identifying cancer-specific mechanisms and develop therapies based on these key points or targets. These targeted molecular therapies [2] contain several different specific treatment types. Knowing that angiogenesis (namely the formation of new blood vessels) has a key role in tumor growth, inhibiting angiogenesis could lead to slowed tumor growth or, in particular, it can cease the whole growth process [3]. Hahnfeldt et al [4] carried out a tumor growth model which describes the growth process under antiangiogenic therapy; however, the biological fundamentals of this model have become outdated.

In particular, the aim of our study was to determine whether the continuous administration of an antiangiogenic inhibitor offers advantages over the more conservative (higher dose – less frequent administration) approach.

1.1 Tumor Growth Models

While tumor growth involves many complicated biological mechanisms, its overall nature – in terms of weight, size or volume – often follows surprisingly simple patterns. This was recognized decades ago (especially following the landmark paper of Laird in 1964 [5]) and has been utilized – in spite of their limitations – ever since both to understand the biological foundations and to provide modelling, for instance in preclinical studies of drug candidates using xenograft tumors implanted in test animals.

These models might be purely empirical, like the Gompertzian growth discussed by Laird, or they might involve considerations about the underlying biological mechanisms (mechanistic and semi-mechanistic models), like the exponential-linear model by Simeoni [6].

Empirical models will be used in the present study. While some models (e.g. [7]) directly incorporate the effect of drugs (making them at least semi-mechanistic), now the same – empirical – growth model is assumed to apply in both the control and the treated groups; the drug exerts its effects by altering the parameters of the curve.

1.1.1 Exponential Growth (Inital Phase, No Plateau)

One of the earliest observations about tumor growth modeling was that in many cases, the growth – both in vivo and in vitro – exhibits exponential nature in its earliest period. Biologically, it corresponds to the phase where the resource-limitation is not apparent, and in that sense the tumor can ”freely” grow, limited only by its own size which defines the pool of cells that can divide.

The growth thus obeys the following ordinary differential equation (DE):

$$\frac{\mathrm{d}V(t)}{\mathrm{d}t} = aV(t); \tag{1}$$

the solution of which is the well-known exponential growth formula:

$$V(t) = V_0 e^{at}, \tag{2}$$

where $V(t)$ is the tumor volume (or any dimension of the tumor, in the general case), with $V_0 = V(0)$.

In almost every practical case, this model can only describe the early phase of tumor growth. In particular, it always leads to an infinite growth, the reason being that the effect of the appearence of growth-limiting factors is not accounted for.

As measurements in the present study were made in such initial period, apparently even the exponential growth provides adequate fit. However, these models are still problematic, even in this case, simply because they offer no possibility to extrapolate in time. Even if the plateau is not yet apparent, we might try to model it (or it might be an especially important task in such case) using only pre-plateau information – this is not possible with the exponential model.

1.1.2 Sigmoid Growth (Plateau Accounted For)

The typical solution to this problem is the application of sigmoid-like growth curves. Such models can capture the asymptotical phase, and thus the plateau can be estimated – even from data collected before reaching the plateau. The question will be, of course, the reliability if the observations are far from the plateau-phase.

We will use two popular sigmoid models in the present study, for a review of the alternatives, see [8, 9, 10].

Note that many such model is a special case of the DE

$$\frac{\mathrm{d}V(t)}{\mathrm{d}t} = aV(t)^{\alpha} - bV(t)^{\beta}, \tag{3}$$

which is usually called the generalized two-parameter model, with appropriate choice of the a, α, b, β parameters. (As a matter of fact, even the exponential model is a special case with $a = 1$, $\alpha = 1$, $b = 0$.)

Gompertz growth One of the earliest such model (used already by Laird in 1964 [5]), and perhaps the most widely used even today, is the Gompertz growth. It is governed by the following DE:

$$\frac{\mathrm{d}V(t)}{\mathrm{d}t} = aV(t) - bV(t)\ln V(t), \tag{4}$$

giving rise to the Gompertz growth curve:

$$V(t) = e^{\frac{a}{b} - \left(\frac{a}{b} - \ln V_0\right)e^{-bt}}. \tag{5}$$

(This is also the limiting case of Equation 3 when appropriate definitions are used [11].)

In the current study, the following – equivalent – parametrization will be used:

$$V(t) = Ae^{-b_2 \cdot b_3^t}, \tag{6}$$

where A represent the asymptote (level of the plateau), while b_2 and b_3 determine the transition.

One well-known property of Gompertz growth is that the derivative at the initial rising period is higher than at the period before reaching the asymptote, i.e. the two transitions are not symmetric.

Logistic growth The logistic growth is another well-known sigmoid model; as opposed to the Gompertz curve, it is symmetric in both transitions.

It obeys the following DE:

$$\frac{\mathrm{d}V(t)}{\mathrm{d}t} = aV(t) - bV(t)^2 \tag{7}$$

giving rise to the logistic growth curve:

$$V(t) = \frac{a/b}{1-(1-\frac{a}{bV_0})e^{-at}}. \tag{8}$$

(This is also a special case of Equation 3 with $\alpha = 1$ and $\beta = 2$.)

In the present study, the following – equivalent – parametrization will be used:

$$V(t) = \frac{A}{1+e^{\frac{t_m-t}{s}}}, \tag{9}$$

where A represent the asymptote (level of the plateau), t_m is the mid-point (time to reach half of the plateau level), and s determines the steepness of the growth.

2 Material and Methods

2.1 Experimental Setting

2.1.1 Mouse and Tumor Type

Fourteen eight weeks old male C57Bl/6 mice were implanted with C38 colon adenocarcinoma. A piece of tumor was transplanted subcutaneously in the recipient animal on the 1st day of the experiment.

2.1.2 Treatment

We investigated the effect of bevacizumab which is an angiogenic inhibitor [12]. Two groups were created to compare the effectiveness of the prescribed, one large dose protocol and a daily, quasi-continuous treatment. The control group contained 5 mice, each one received 200 μg bevacizumab dose intraperitoneally on the -1st day and on the 17th day of the experiment (this bolus was designed for an 18-day treatment). By contrast, mice in the case group (9 mice) received 1.11 μg bevacizumab intraperitoneally every day from the -1st day until the last day of the experiment (the total period was 20 days); that is to say, one-tenth dose of control dose spread over 18 days.

The above dosage was selected based on the fact that the recommended administration of bevacizumab is $5-10\ mg/kg$ dose for 2-3 weeks [13]. We have administered 10 mg/kg body weight intraperitoneally, which means 200 μg bevacizumab per a mouse, since the mass of the mice in the experiment was approximately 20 g.

2.1.3 Tumor Volume Measurement

Tumor volume was measured with digital caliper and small animal MRI as well.

Due to the subcutaneous localization, two dimensions of the tumor can be measured with digital caliper. The third dimension should be estimated, and assuming a certain shape, tumor volume can be approximated. Based on different estimation methods, we obtained three different tumor volume values for each measurement point [14]. Measurements with caliper were made on the 0th, 2nd, 4th, 6th, 8th, 10th, 12th, 14th, 16th, 18th and 19th days of the experiment.

In order to verify our estimation methods based on caliper measurements, we used small animal MRI for tumor volume determination as well, since MRI provides much more precise volume measurement. Measurements with small animal MRI were carried out on the 0th, 4th, 7th, 11th, 14th and 19th days of the experiment. Figure 1 shows tumor volumes using all the estimation methods.

Mice were sacrificed at the end of the treatment, in strong accordance with the 3Rs principles.

2.2 Statistical Tools

First, individual curves were fitted for each test animal (using each measurement method) with all three models. Fitting was performed with nonlinear least squares (NLS) [15, 16]. Gauss-Newton algorithm turned out to be incapable of converging in every case (sigmoid growth curves were problematic, when even the end of the observed data was far from reaching the plateau). Thus, Levenberg-Marquardt algorithm [17] was employed, which successfully converged for all three models for every growth curve.

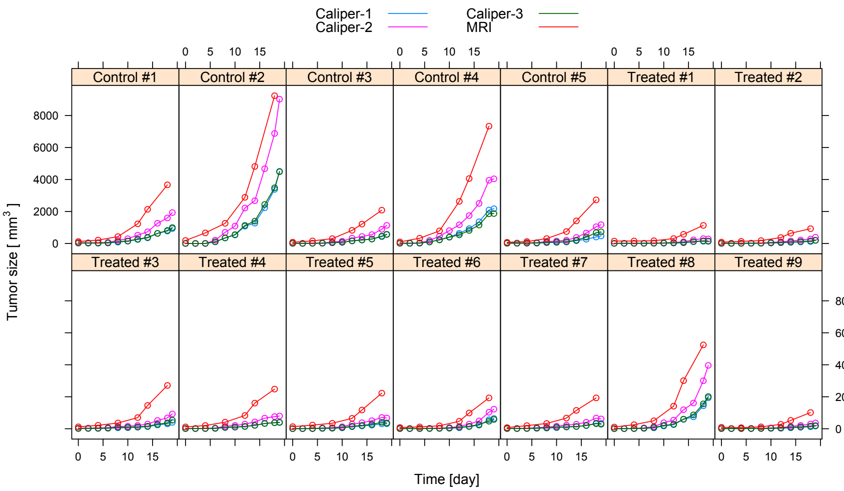

Figure 1
Measured tumor volumes (with all measurement methods).

This approach provides the best fit as it estimates individual parameters for all subject and measurement method, but this is also the very reason that prevents generalization: we have separate models, thus it is not possible to infer on a higher level (i.e. the population of parameters). As we are now primarily interested not in these particular subjects, but rather on the population from which they are coming, a model will be used which explicitly incorporates this aspect: the mixed effects model [18, 19].

These models assume that parameters are not fixed values, but rather realizations of a random variable, most typically normal random variate; this is called a random effect. These are characterized by mean and variance (and possibly covariance for different such distributions). Therefore the estimation focuses not on the individual parameters, but rather on these parameters of the population.

To formalize: denoting the tumor volume of the ith subject at measurement number j with V_{ij} we have

$$V_{ij} = f(\boldsymbol{\phi}_{ij}, t_{ij}) + \varepsilon_{ij}, \quad \varepsilon_{ij} \sim \mathcal{N}(0, \sigma^2), \tag{10}$$

where f represents the nonlinear functional form – in the present study, exponential, Gompertz or logistic – of time (t_{ij} being the time when the $j$the measurement was made on the ith subject) determined the parameters $\boldsymbol{\phi}_{ij}$, the dimensionality of which corresponds to the number of parameters in the growth curve (2 or 3 in our cases).

Now we assume that these parameters depend on whether the test animal belongs to the treated or to the control group and on the measurement method, that is

$$\boldsymbol{\phi}_{ij} = (\boldsymbol{\beta}_0 + \mathbf{b}_i) + \boldsymbol{\beta}_{\mathrm{Group}}\mathrm{Group}_i + \boldsymbol{\beta}_{\mathrm{MeasMeth}}\mathrm{MeasMeth}_i, \tag{11}$$

where random effects $\mathbf{b}_i \sim \mathcal{N}(\mathbf{0}, \boldsymbol{\psi})$ and $\boldsymbol{\beta}$s are vectors containing the fixed effects for each parameter of the growth curve. (In this case $\boldsymbol{\phi}_{ij}$ only depends on i, in other words, we had no time-varying covariates.) For instance, exponential growth curve, using the more usual notation, is modelled as

$$V_i(t) = \left(V_0 + b_{V_0,i} + \beta^{(V_0)}_{\text{Group}}\text{Group}_i + \beta^{(V_0)}_{\text{MeasMeth}}\text{MeasMeth}_i\right) \cdot \\ \cdot e^{\left(a + b_{a,i} + \beta^{(a)}_{\text{Group}}\text{Group}_i + \beta^{(a)}_{\text{MeasMeth}}\text{MeasMeth}_i\right)t} + \varepsilon_{i,t}. \tag{12}$$

We assumed that $\boldsymbol{\psi}$ is diagonal, i.e. the random effects are uncorrelated. Residual (within-group) error ε_{ij} is assumed to be independent and independent from all random effects too.

To sum up, we assume that these covariates act by altering the parameters of the – same – functional form. In particular, this means that the effect of drug is incorporated by assuming that the tumor growth obeys the *same* law under treatment, but with *different* parameters.

This model assumes, among others, that

- the variance of the error terms is a constant (i.e. no heteroscedasticity present),
- the error terms are uncorrelated (i.e. no residual autocorrelation present).

These assumptions were checked by plotting the standardized residuals versus the time – the only covariate in the models – and the autocorrelation function of the residuals, respectively. In case of violation, appropriate weighting functions and within-subject autocorrelation functions – with autoregressive, moving average (ARMA) models – were included in the models [18]. Models were characterized with Akaike's Information Criterion (AIC), among others.

This analysis updates a previous one [20] with more elaborate individual curve fitting and a more rigorous mixed-effects modelling.

2.3 Programs Used

R statistical program package [21] (version 3.3.2) was used with libraries minpack.lm [22] (version 1.2-0) and nlme [23] (version 3.1-128) to carry out the calculations using a custom script developed for this purpose that is available at the corresponding author on request. Visualizations were created with the lattice library [24] (version 0.20-34).

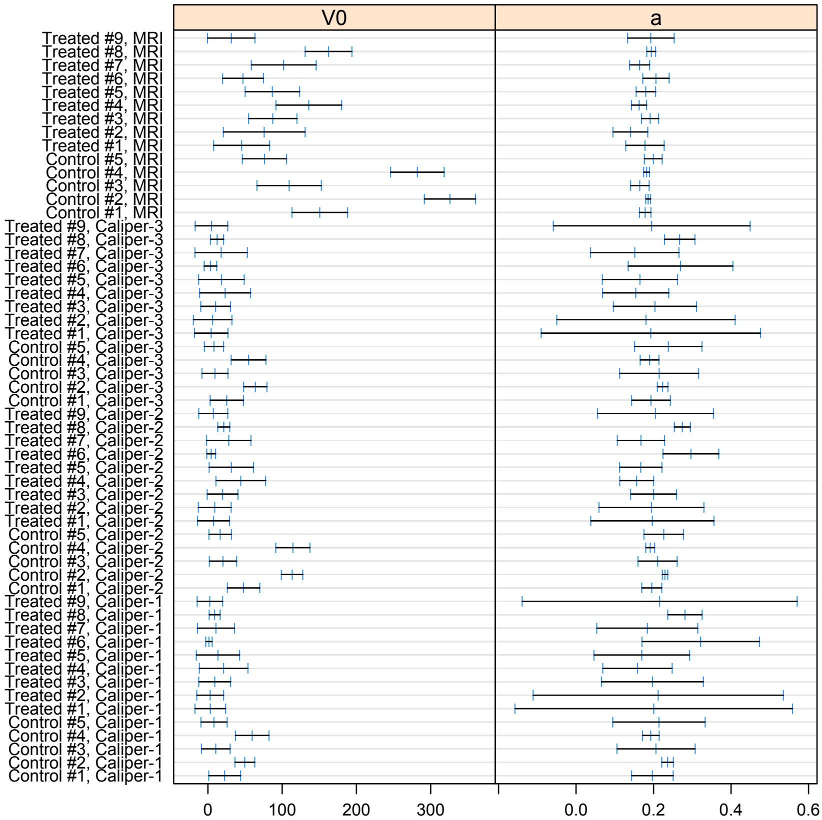

Figure 2
Point estimates with 95% confidence intervals for the parameters of the individual exponential model (for each animal using each measurement method).

3 Results

3.1 Individual Fitting

Results obtained with the exponential model are shown – for each subject and measurement method – on Figure 2.

a parameters are rather homogeneous, but V_0 shows substantial heterogeneity (with a clear tendency of MRI measurements being higher than any of the caliper measurements).

The fitting of sigmoid models is much more complicated. Figure 3 shows that the parameteres associated with the plateau can be estimated only with extreme uncertainty in certain cases. (Note the logarithmic scale of the Figure.) The reason is that the data gives information only on the early phase of the growth, far from the plateau, which makes extrapolation very hard.

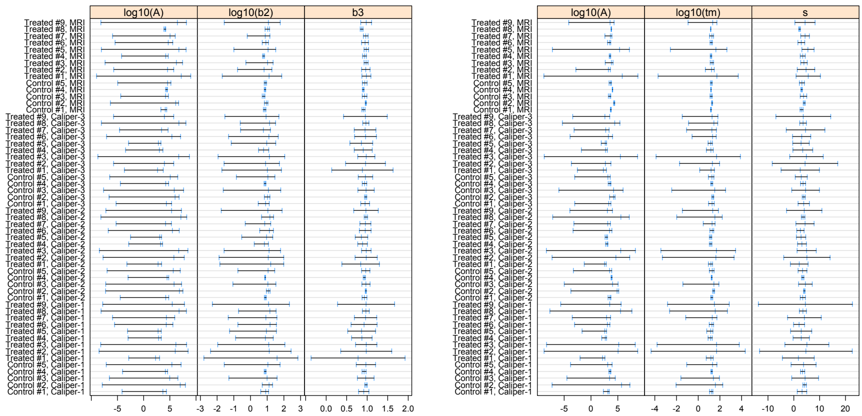

(a)
Gompertz growth

(b)
Logistic growth

Figure 3
Point estimates with 95% confidence intervals for the parameters of the individual sigmoid models (for each animal using each measurement method). Note the logarithmic scale for certain parameters.

3.2 Population-level Mixed Model

3.2.1 Exponential Growth

Residuals of the exponential model showed no substantial dependence on time, but were definitely heteroskedastic in terms of measurement method (Figure 4), so different variances were assumed for each measurement method.

The autocorrelation function (Figure 5) showed significant residual autocorrelation. As it was not disappearing even at higher lags, it was assumed to be basically MA-process; finally ARMA(1,4) specification turned out to be practically removing residual autocorrelation.

In this – now diagnostically correct – model, the standard deviation of the random effect for the V_0 was 13.14565, for the a it was 0.02614131. The residual standard deviation and AIC is shown in Table 1.

Table 1
Residual standard deviations and AICs of different population-level models

Model	Residual standard deviation	AIC
Exponential	113.2	6474
Logistic	86.6	6602
Gompertz	660	8677

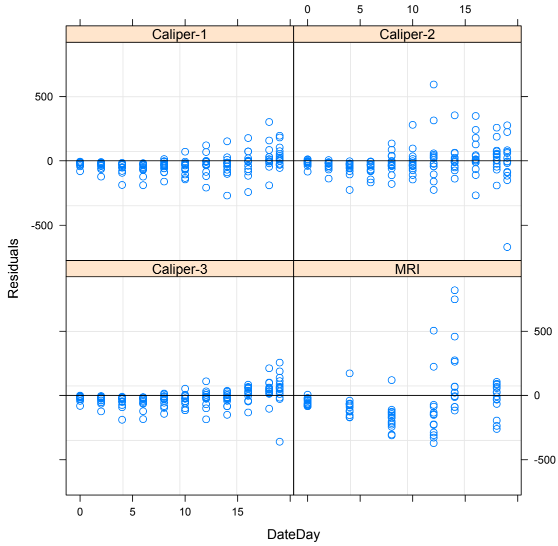

Figure 4
Residuals of the exponential model plotted as a function of day, by measurement method.

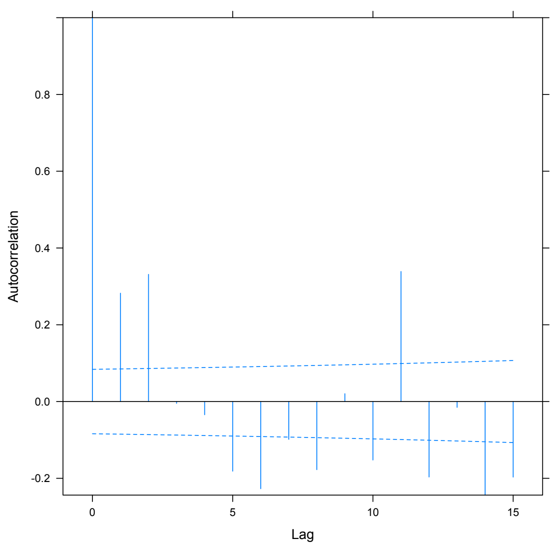

Figure 5
Autocorrelation function of the residuals from the exponential model, with critical values at 5% significance level.

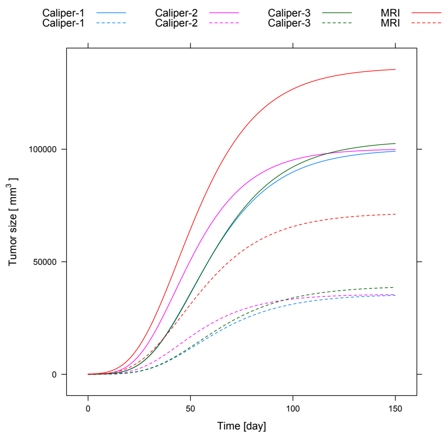

(a)
Gompertz growth

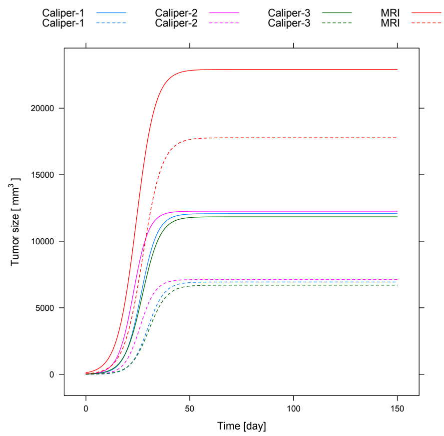

(b)
Logistic growth

Figure 6
Predicted growth (on population-level) of the tumor volume for Days 0 to 150. Different colors indicate different measurement methods (see legend), solid line indicates control group, while dashed line indicates treated group.

In this model, the intercept of V_0 is 40.5 with MRI measurement having significantly higher values than caliper measurements (+275.2 compared to Caliper-1). The intercept of a is 0.18349, but now MRI measurements are having significantly lower a (−0.04342 compared to Caliper-1), Caliper-2 however exhibits significantly higher a (+0.02894).

The treatment's effect is very interesting: it does slightly significantly alter V_0 (−18.05230, $p = 0.0354$), but it does have a more significant effect on a, being associated with −0.03746 change ($p = 0.0197$). I.e. the continuous regimen decreases the rate of growth – which shows the benefit of this dosing regimen.

3.2.2 Sigmoid Growth

Sigmoid growth models were barely approximable (as already expected from the results of the individual fitting), so no attempt was made to include special variance or autocorrelation function.

The results of the mixed models are shown (Figure 6) as – population-level – predicted tumor volumes for Days 0 to 150 (for each measurement type and for the treated/control groups). Note that the original data spanned from Days 0 to 19, so this exemplifies the extrapolation with the models.

The residual standard deviations and AICs are shown in Table 1.

The effect of treatment was significant for the mid-point parameter of the logistic growth ($p = 0.0228$), but it was not significant for any parameter of the Gompertz growth. In particular, the asymptotic levels were substantially lower in both cases

(-5136 with the intercept being 12071 for the logistic model, -64657 with the intercept being 100263 for the Gompertzian model), but these were insignificant, as they were very hard to estimate, as expected (also note the extreme difference between the two models in asymptotic levels).

The asymptotic level in the logistic model was significantly – and substantially – higher with MRI ($+10841$, $p < 0.001$).

4 Discussion

It was possible to reliably estimate all parameters of the exponential growth model, indicated by the consistent and rather narrow confidence intervals in the individual fits and the acceptable residual standard deviation in the mixed model. The results show the effect of the treatment; already demonstrated in an earlier research [25].

In contrast, the estimates for the sigmoid-growth models were exceedingly variable evidenced by the very wide confidence intervals. The population level model exhibited extremely poor fit, with enormously high residual deviations. Nevertheless, it could concluded that the logistic modell still provided better fit than the Gompertzian.

In short, it was not possible to reliably estimate these models, the reason being the rather short observation period that was available, showing only the very early period of tumor growth. Notwithstanding, results point out the possibility to estimate the plateu phase, which is a very interesting and promosing parameter – in additional to the initial rate of growth, already captured by the exponential model –, but trusthworthy estimation of this requires more observation.

Results also highlight the differences between the measurement devices, clearly showing that measurements made with MRI are systematically higher than any of the caliper measurements.

One strength of our approach was that it integrates all factors (treatment and measurement device) into one single model, allowing us to investigate both the effect of the treatment and the effect of the applied measuring method at the same time. Also, the mixed effects approach allows a smooth and elegant usage of the individual measurements to create a population-level model. In addition to that, we have the possibility to test several potentional functional forms; with some of them, we are also able to extrapolate in time, and capture clinically relevant parameters.

The most important limitation was the rather small number of test subjects, and the too short observation period to estimates some of the models.

Conclusion

The exponential model could be estimated in a robust manner, both individually, and in the population-level with the mixed effects model. Results confirm the effect of the treatment, and make it possible to quantify this.

In contrast, the sigmoid-like growth curves were almost impossible to estimate, revealing the limitations of our data. Nevertheless, the possibility to estimate such models – making extrapolation possible – presents a promising opportunity.

Acknowledgement

This project has received funding from the European Research Council (ERC) under the European Union's Horizon 2020 research and innovation programme (grant agreement No. 679681). In addition, Tamás Ferenci was supported by the UNKP-16-4/III New National Excellence Program of the Ministry of Human Capacities. The authors say thanks to the Physiological Controls Group's (`http://physcon.uni-obuda.hu/`) members for their support.

References

[1] R. M. A. Parker and W. J. Browne. "The Place of Experimental Design and Statistics in the 3Rs". In: *ILAR Journal* 55.3 (2014), pp. 477–485.

[2] I. Petersen. "Antiangiogenesis, anti-VEGF(R) and outlook". In: *Recent Results In Cancer Research, Targeted Therapies in Cancer*. Ed. by M. Dietel. Springer – Verlag, 2007.

[3] G. Bergers and L. E. Benjamin. "Tumorigenesis and the angiogenic switch". In: *Nat Rev Cancer.* 3(6) (2003), pp. 401–410.

[4] P. Hahnfeldt et al. "Tumor development under angiogenic signaling: A dynamical theory of tumor growth, treatment response, and postvascular dormancy". In: *Cancer research* 59 (1999), pp. 4770–4775.

[5] A. K. Laird. "Dynamics of tumour growth". In: *British Journal of Cancer* 18.3 (1964), p. 490.

[6] M. Simeoni et al. "Predictive pharmacokinetic-pharmacodynamic modeling of tumor growth kinetics in xenograft models after administration of anticancer agents". In: *Cancer Research* 64.3 (2004), pp. 1094–1101.

[7] S. Yamazaki et al. "Pharmacokinetic-pharmacodynamic modeling of biomarker response and tumor growth inhibition to an orally available cMet kinase inhibitor in human tumor xenograft mouse models". In: *Drug Metabolism and Disposition* 36.7 (2008), pp. 1267–1274.

[8] P. L. Bonate. "Modeling tumor growth in oncology". In: *Pharmacokinetics in drug development*. Springer, 2011, pp. 1–19.

[9] R. P. Araujo and D. L. S. McElwain. "A history of the study of solid tumour growth: the contribution of mathematical modelling". In: *Bulletin of mathematical biology* 66.5 (2004), pp. 1039–1091.

[10] S. Benzekry et al. "Classical mathematical models for description and prediction of experimental tumor growth". In: *PLoS Comput Biol* 10.8 (2014), e1003800.

[11] M. Marušić et al. "Analysis of growth of multicellular tumour spheroids by mathematical models". In: *Cell proliferation* 27.2 (1994), pp. 73–94.

[12] European Medicines Agency. *Scientific discussion of Avastin*. Available: http://www.ema.europa.eu. Accessed 10 April 2016. 2005.

[13] Genentech. *Prescribing information of Avastin (Bevacizumab)*. Available: http://www.gene.com/download/pdf/avastin_prescribing.pdf. Accessed 10 December 2016. 2013.

[14] J. Sápi et al. "Tumor Volume Estimation and Quasi-Continuous Administration for Most Effective Bevacizumab Therapy". In: *PLoS ONE* 10.11 (Nov. 2015), pp. 1–20. DOI: 10.1371/journal.pone.0142190.

[15] D. M. Bates and D. G. Watts. *Nonlinear regression analysis and lts applications*. Wiley, 1988.

[16] C. Ritz and J. Streibig. *Nonlinear Regression with R*. Use R! Springer New York, 2008. ISBN: 9780387096162.

[17] J. J. Moré. "The Levenberg-Marquardt algorithm: Implementation and theory". In: *Numerical Analysis: Proceedings of the Biennial Conference Held at Dundee, June 28–July 1, 1977*. Ed. by G. A. Watson. Berlin, Heidelberg: Springer Berlin Heidelberg, 1978, pp. 105–116. ISBN: 978-3-540-35972-2. DOI: 10.1007/BFb0067700. URL: http://link.springer.com/chapter/10.1007%2FBFb0067700.

[18] J. Pinheiro and D. Bates. *Mixed-Effects Models in S and S-PLUS*. Statistics and Computing. Springer New York, 2000. ISBN: 9780387989570.

[19] G. Verbeke and G. Molenberghs. *Linear Mixed Models for Longitudinal Data*. Springer Series in Statistics. Springer New York, 2009. ISBN: 9781441902993.

[20] T. Ferenci, J. Sápi, and L. Kovács. "Modelling xenograft tumor growth under antiangiogenic inhibitation with mixed-effects models". In: *Systems, Man, and Cybernetics (SMC), 2016 IEEE International Conference on*. 2016, pp. 3912–3917.

[21] R Core Team. *R: A Language and Environment for Statistical Computing*. R Foundation for Statistical Computing. Vienna, Austria, 2016. URL: https://www.R-project.org/.

[22] T. V. Elzhov et al. *minpack.lm: R Interface to the Levenberg-Marquardt Nonlinear Least-Squares Algorithm Found in MINPACK, Plus Support for Bounds*. R package version 1.2-0. 2015. URL: https://CRAN.R-project.org/package=minpack.lm.

[23] J. Pinheiro et al. *nlme: Linear and Nonlinear Mixed Effects Models*. R package version 3.1-128. 2016. URL: http://CRAN.R-project.org/package=nlme.

[24] D. Sarkar. *Lattice: Multivariate Data Visualization with R*. ISBN 978-0-387-75968-5. New York: Springer, 2008. URL: http://lmdvr.r-forge.r-project.org.

[25] J. Sápi et al. "Tumor Model Identification and Statistical Analysis". In: *Systems, Man, and Cybernetics (SMC), 2015 IEEE International Conference on*. 2015, pp. 2481–2486. DOI: 10.1109/SMC.2015.434.